THÈSE

En vue de l'obtention du

DOCTORAT DE L'UNIVERSITÉ DE TOULOUSE

Délivré par : *l'Université Toulouse 3 Paul Sabatier (UT3 Paul Sabatier)*

Présentée et soutenue le *21/07/2015* **par :**

EDNA MAGDALENA HERNÁNDEZ GONZÁLEZ

High Spatial Resolution Investigation of Spin Crossover Phenomena using Scanning Probe Microscopies

JURY :

DANEL RUIZ-MOLINA Professeur, Centro de Investigación en Nanociencia y Nanotecnología	Rapporteur
WOLFGANG LINERT Professeur, Technische Universität Wien	Rapporteur
BRUNO DOMENICHINI Professeur, Université de Bourgogne	Examinateur
PHILIPPE DEMONT Professeur, Université Toulouse III Paul Sabatier	Examinateur
MA. DEL PILAR CARREÓN CASTRO Professeur, Universidad Nacional Autonoma de México	Examinatrice
AZZEDINE BOUSSEKSOU Directeur de Recherche, Laboratoire de Chimie de Coordination CNRS	Directeur de thèse
GÁBOR MOLNÁR Directeur de Recherche, Laboratoire de Chimie de Coordination CNRS	Codirecteur de thèse

École doctorale et spécialité :

SDM : Physique de la matière - CO090

Unité de Recherche :

Laboratoire de Chimie de Coordination (UPR 8241)

Directeurs de Thèse :

Azzedine BOUSSEKSOU et *Gabor MOLNAR*

Acknowledgments

When I arrived to Toulouse, I had a meeting with Azzedine and Gábor. During that meeting they told me that studying this materials with SPM was a challenge. I answered immediately "I love challenges". Three years later looking backwards, I found that they were right. This work was a very interesting and accelerating challenge. I enjoyed and learned in each step of the process, mostly due to the nice environment on the team which drives you to do your best.

I would like to thank Daniel Ruiz-Molina and Wolfgang Linert for accepting being referees of my work, reeding and judging this work. I would also want to thank Bruno Domenichini, Philippe Demont and Ma. del Pilar Carreón for participating as jury of my thesis. I would like to thank all of them for their comments and corrections.

I specially would like to acknowledge my thesis director Gábor Molnár for all our fruitful discussions which greatly helped me during my PhD thesis. I learned a lot about oral and writing communication and all the different aspects of research thanks to him. I would like to thank him for pushing me to be better and do my best. I would also like to thank Azzedine Bousseksou for accepting me into this amazing group. I would like to express my gratitude to both of them for all their support. They always found a way to give me what I needed to succeed and for that I am very grateful.

I would like to thank Lionel Salmon for helping me to find the right samples to analyze by SPM. I also would like to express my gratitude to William Nicolazzi for all our discussions that helped me to understand the mechanisms behind the different phenomena I studied. I would like to thank both of them for their moral support and their help in day to day issues. To all the members and ex-members of the "Switchable Molecular Materials" team I would like to thank you for all the jokes, support, discussions, extra curricular activities and so on. You made this three years one of the happiest, more accelerating and amazing of my life.

I would like to recognize the technical support of the laboratory for their excellent work. In particular, I would like to thank Lionel Rechignat and Marine Tasse.

I would like to express my gratitude to all our collaborators for all their help. From LAAS I would like to recognize to Christian Bergaud for his help in the thermodynamical studies, Christophe Thibault for forming me in AFM technique and for giving me access to

LAAS, as well as to the technical services there, Franck Carcenac for all his work in e-beam and photolithography and Benjamin Reig for helping me to keep the Dimension Icon AFM up to date and functional. From Universiteit Leiden I would like to show my appreciation to Sylvestre Bonnet and his student Siepeng Zheng for providing [Fe^{II}(bapbpy)$(NCS)_2$] crystals. From UNAM I would like to recognize Víctor Velázquez for our discussions. His questions allowed me to understand better spin crossover phenomena. I would also like to acknowledge Mickaël Febvre and Emmanuel Paris from Bruker Nano for their technical guidance and generous access to the AFM equipment.

Finally I would like to thank my family for all their kind and encouragement words, even 10 000 km away I could count with them. To the closest to my heart Arturo Curiel I would like to thank him for making life easier so I could concentrate in my PhD work.

I am grateful to the CONACYT for the Ph.D grant (No. 3101095). This work was financially supported by the project ANR-Thermospin and LIA Franco-Mexicain

Contents

General Introduction

At the nanometric scale the physical and chemical properties of materials are frequently very different from those in bulk. One can cite different examples, such as the melting point depression in metallic nanoparticles, the band gap opening and associated color change in quantum dots, superparamagnetic phenomena in ferromagnetic nanoparticles and Coulomb blockade effects in nanosized junctions. Besides the size dependent properties, merely the confinement and organization of matter at the nanoscale can give access to new or enhanced properties. For example, the thermodynamical properties of liquids confined in nanotubes are known to be strongly altered. These various nanoscale phenomena provide a very appealing scope for fundamental research and technological innovations in different fields of science. Indeed in the past few decades tremendous efforts have been devoted to the elaboration of nanosized materials and the investigation of size reduction effects on their properties and functions. Of course an important driving force of this research comes from the microelectronic industry, which produces devices with continuously smaller and smaller sizes. Other fields, such as catalysis, biomedicine and food industry are using also more and more nanomaterials. These different fundamental and technological advances have been also associated with the continuous development of novel characterization tools specific to this size range, such as electron and scanning probe microscopies.

In this thesis we focus on Spin Crossover (SCO) nanomaterials. SCO compounds are inorganic complexes which display phase change behavior in the bulk form between the so-called high spin (HS) and low spin (LS) states. As in any material, the phase stability and transformation kinetics are size dependent. In particular it was shown that the spin transition temperature (or more generally speaking the phase diagram) and the completeness of the transformation are strongly affected at the nanoscale. The experimental and theoretical investigations of the underlying physical mechanisms are relatively recent and demand further efforts. On the other hand, the outstanding properties of SCO nanomaterials make them very interesting for several technological applications. Indeed the spin state switching in SCO nanoobjects (nanoparticles, thin films, nanopatterns, etc.) is accompanied by a spectacular change of various material properties, including magnetic, optical, electrical and mechanical ones, providing scope for applications in na-

noelectronic, spintronic, nanophotonic and nanomechanical devices. For example, they have been proposed for diffractive gas sensors [1, 2], micro and nanoelectromechanical actuators (MEMS, NEMS)[3, 4], thermocromic pigments [5], photonic waveguides [6], switchable THz filters [7] and nanothermometers [8, 9].

Conventional experimental approaches used to characterize bulk SCO materials (magnetometry, X-ray diffraction, calorimetry, Mössbauer, electronic and vibrational spectroscopies), are often not well adapted to investigate nanoscale SCO objects, generally due to the low amount of matter, and new technics are needed to characterize them. In particular, there is a need for high spatial resolution microscopy tools as well as for high sensitivity methods able to detect molecular spin-state changes in very small amounts of matter, ideally in a single, isolated nano-object. Beyond their high resolution and/or high sensitivity, these new experimental approaches can provide also information on material properties, which are either difficult to access by conventional methods or not so relevant at other size ranges. Far-field optical microscopy techniques have already been employed with success to monitor the spin state changes in a single nanometric object. For example, single SCO nanoparticles were studied using fluorescence, Raman and differential interference contrast microscopy. On the other hand, nanometric thin films of SCO complexes were analyzed by different photonic methods (ellipsometry, surface plasmon resonance, etc.). In order to surmount the rather limited spatial resolution of far-field optical methods one may use electron or X-ray beams, which can provide structural and spectroscopic information with high spatial resolution. In the case of relatively brittle molecular SCO materials care must be taken, however, due to the invasive nature of these techniques: sample heating and radiation damage are in fact frequently encountered. These problems have been largely decreased in a very recent work, which used aperture-based time-resolved electron microscopy to follow the spin transition in individual nanoparticles [10]. Another possible approach, which we explored in this thesis work, is based on scanning probe microscopies (SPM). Although SPM has been already used to study phase transition in different materials, SPM studies on spin crossover materials are very scarce. Actually only scanning tunneling microscopy (STM) has been used in this field, but STM is more relevant in the context of single molecule studies than nanomaterials which are the scope of our work. Indeed, the principal objective of this work is to explore the possible use of SPM techniques to characterize and manipulate the spin state of SCO complexes at the nano- and micrometric scales. We focused on two SPM methods: near-field scanning optical microscopy (NSOM) and atomic force microscopy (AFM). This latter was used either for imaging sample topography or mechanical properties.

The manuscript is organized as follows:

In chapter 1 a general introduction to the molecular spin crossover phenomenon and scanning probe microscopy techniques is provided in order to introduce the reader to both subjects. First a brief history of spin crossover research is presented, followed

by basic ligand-field theoretical and thermodynamical aspects of the phenomenon. Then, two current hot topics of the SCO field, research on the spatiotemporal dynamics and size reduction effects, are overviewed. In fact, these two topics have provided the primary motivation for this thesis work. In the second section the different scanning probe microscopy approaches are briefly reviewed and the principal notions of atomic force microscopy and near-field scanning optical microscopy are described.

In chapter 2 we present our near-field scanning optical microscopy (NSOM) studies on spin crossover thin films. First we provide details about our NSOM set-up and also about an original methodology we developed for temperature dependant NSOM measurements using metallic nanowire heaters. Then, using NSOM in luminescence mode, the first successful subwavelength resolution imaging of the spin transition in thin films of the SCO compound $[Fe(hptrz)]_3(OTs)_2$ doped with Rhodamine 110 is presented. In the next section simultaneous far-field and near-field reflectivity studies of the same compound as well as the complex $[Fe(Htrz)_2(trz)]BF_4$ are exposed. Finally the possibility of triggering the spin transition with high spatial resolution using the NSOM tip is demonstrated.

A study of the mechanical properties of spin crossover materials using atomic force microscopy (AFM) is presented in chapter 3. In the beginning of the chapter a state of the art of the different AFM modes providing information about sample mechanical properties is presented. This is followed by the discussion of preliminary tests on PMMA films which were carried out in order to put in place the experimental set-up and explore different AFM modes. In the following sections thermomechanical measurements on $[Fe(hptrz)]_3(OTs)_2$ films along the spin transition curve are presented and the spin-state dependance of the viscoelastic properties of this sample is discussed. Finally, a comparison of different AFM mechanical modes using this sample is presented.

Chapter 4 is dedicated to the investigation of the spatio-temporal dynamics of the spin transition in single crystals of the complex $[Fe(bapbpy)(NCS)_2]$. Following the general description of the sample, nucleation and growth phenomena associated with the first-order spin transition in this compound are put in evidence by conventional optical far-field microscopy and Raman spectroscopy. The AFM investigation of the spin transition in this system proved to be difficult due to severe thermal and possible electrostatic interactions between the sample and the AFM probe. Nevertheless, changes in the topography of the crystals due to spin transition were detected. On the other hand probe-sample interactions were found useful to manipulate locally the nucleation and propagation of spin domains.

The manuscript ends with the general conclusions and some perspectives for future work as well as annexes.

Chapter 1

Introduction

1.1 Introduction to the Spin Crossover Phenomenon

In 1931 Cambi et al. observed for the first time an anomalous magnetic behavior in a series of Fe^{III} dithiocarbamate compounds [11]. This phenomenon would be later known as spin crossover (SCO), also called spin conversion or spin transition. The first spin transition with an Fe^{II} complex was observed by Baker and Bobonich [12] in 1964. In the same year the notion of spin crossover was introduced by Ewald et al [13], where the authors make use of ligand field theory to propose that the change of spin state is possible when the ligand field energy is comparable to the average energy of electron pairing in the orbitals *d*. Up to now this vision of the phenomenon has not been changed and can be found in several articles and textbooks. This phenomenon has been observed in compounds with metallic centers with electronic configuration $3d^4$-$3d^7$ coordinated with ligands in octahedral symmetry. Metallic centers which can present SCO are: Fe^{III} [14–17], Co^{II} [18–21], Co^{III} [22–24], Mn^{II} [25, 26], Mn^{III} [27, 28], Cr^{II} [29, 30] and Fe^{II}. This latter ion presents the highest number of studies.

During the spin transition phenomena the physico-chemical properties of the material change. The spin crossover is associated with a variation of the thermodynamic quantities like the enthalpy ΔH and the entropy ΔS of the system which can be detected by calorimetry. The change in the spin state modifies obviously the magnetic properties of the material. Hence, the magnetic susceptibility ($\chi(T)$) is a key property to characterize the spin transition. The change of electronic configurations produces also a change in the optical absorption properties of the material. Indeed in most cases the spin transition can be detected with the naked eye, as a color change of the sample. The hyperfine interactions between the electronic cloud and the nucleus are observed as a modifications of the Mösbauer absorption spectrum. König and Madeja were the first to observe the change of the Mössbauer absorption spectrum of $[Fe(phen)_2(NCS)_2]$ due to a spin state change [31]. Using this technique Köing and Ritter studied for the first time the evolution of the

Lamb-Mössbauer factor during the spin transition [32]. Their study allowed to relate the elastic properties of the material with its spin state, using Debye's model [33]. Another important effect of the spin transition is the increase of the molecular volume when going from the low spin to the high spin state, which can be characterized by X-ray diffraction methods [34].

Most conveniently the spin transition is triggered by a variation of the temperature. However, it has been shown that this phenomenon can be produced by several other external stimuli as well [35]. The difference of volume between the two spin states makes possible to trigger the spin transition by applying an external pressure. As the pressure increases the low spin state is favored since it has a lower size, so the equilibrium temperature moves to higher values. Several pressure studies on mononuclear, dinuclear and polymeric spin crossover systems have been performed and this tendency has been confirmed in most cases, even if remarkable exceptions have been found highlighting the complexity of pressure effects [36]. Another way to trigger the spin transition is through light irradiation. Mc Garvey and Lawthers observed for the first time the possibility to convert the spin state of iron complexes in solution by light irradiation [37]. A little later, Decurtins et al. detected the same effect in the solid state [38, 39], which they called Light Induced Excited Spin State Trapping (LIESST). It consists in converting a stable low spin state(LS) into a metastable high spin state (HS) at low temperatures using light irradiation. Later on, Hauser reported the reverse-LIESST effect, where light is used to convert the HS state into the LS state [40]. The LIESST technique allowed also to investigate in a convenient manner the kinetics of the spin state interconversion. Another external stimulus that can trigger spin transition is the application of a magnetic field. This has been studied for the first time on $[Fe(phen)_2(NCS)_2]$ by Gütlich et al.[41]. Afterwards Bousseksou et al studied the effect of a pulsed magnetic field on the same compound [42].

In diluted systems (solutions, etc.) the thermal spin crossover is always gradual and follows Boltzmann statistics. However, in bulk solids abrupt (discontinuous) transitions can be also observed, with or without hysteresis. These first order phase transition phenomena are explained by the intermolecular elastic interactions [43], which arise due to the difference of volume between the two spin states. Slichter and Drickamer developed a thermodynamic model that takes into account these interactions in a phenomenological manner using a nonlinear term of the free enthalpy [44]. From the microscopic point of view, the Ising model was adapted to simulate spin transitions with intermolecular interactions. A more explicit theory of elastic interactions was proposed by Spiering [45] based on continuum mechanics.

Up to now several hundreds of spin crossover complexes (either molecular or coordination networks) have been synthesized and characterized. In the following sections we will briefly summarize the most important theoretical concepts of SCO including crystal

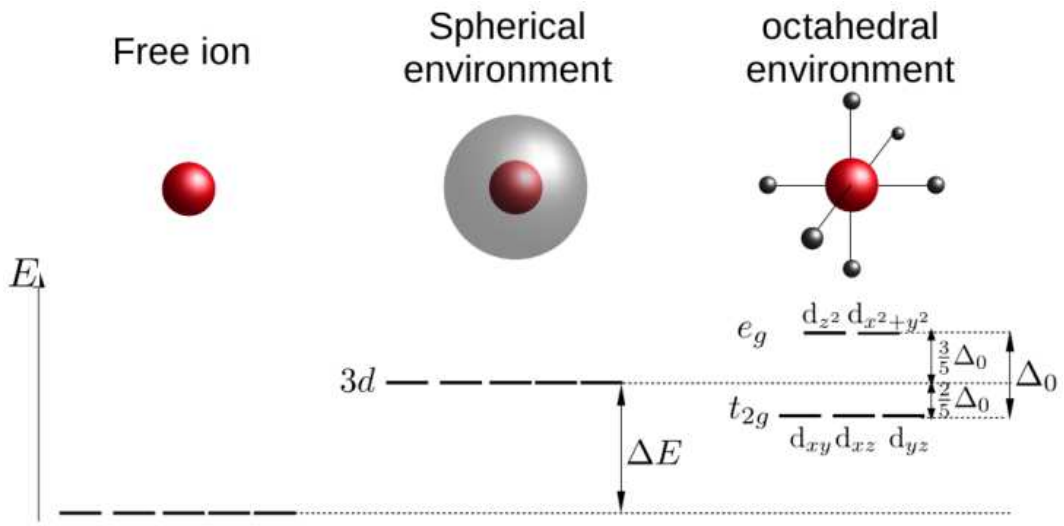

Figure 1.1: Influence of a spherical or octaedric environment on 3d orbitals.

field theory and thermodynamical aspects. Then, we will highlight two current hot topics in the field: investigation of the spatio-temporal dynamics of SCO and the development of nanoscale spin crossover objects.

1.1.1 Crystal field theory

Crystal field theory allows to explain in a simple way the SCO phenomenon. This theory considers that the interaction between the metallic center and the ligand is purely electrostatic. The metallic ion is positively charged meanwhile the the ligands have a negative charge. This model describes the electron distribution in the d or f orbitals of a metallic ion under different symmetries [46]. In the case of the free Fe^{II} ion, the energy levels of the five 3d orbitals are degenerated. If the metallic ion is localized in a spherical field the energy levels of the orbitals will be $E_{sph} = E_{free} + \Delta E$, where E_{free} is the energy of the free Fe^{II} ion, see figure 1.1. In an octahedral environment, which has a lower symmetry than the sphere, the five 3d orbitals suffer a lift of degeneracy, leading to a low energy level t_{2g} which contains the degenerated orbitals d_{xy},d_{xz},d_{yz} and a higher energy level e_g with the degenerated orbitals d_{z^2},$d_{x^2-y^2}$. The energies of the high energy and the low energy levels will be $E_{e_g} = E_{sph} + 3/5\Delta_0$ and $E_{t_{2g}} = E_{sph-2/5\Delta_0}$, where Δ_0 is the energy difference between the two levels, i.e. the crystal field energy. Δ_0 depends both on the nature of the ligands and the metallic ion.

In a weak ligand field configuration, in other words when Δ_0 is lower than the electron spin pairing energy (Π), the electrons in the complex follow Hund's rule of maximum multiplicity. In this case, the number of unpaired electrons is maximized and the electrons fill also the high energy orbitals, see figure 1.2 right. In this case the total spin is S = 2 for Fe^{II}. This paramagnetic state is called high spin state (HS), represented by

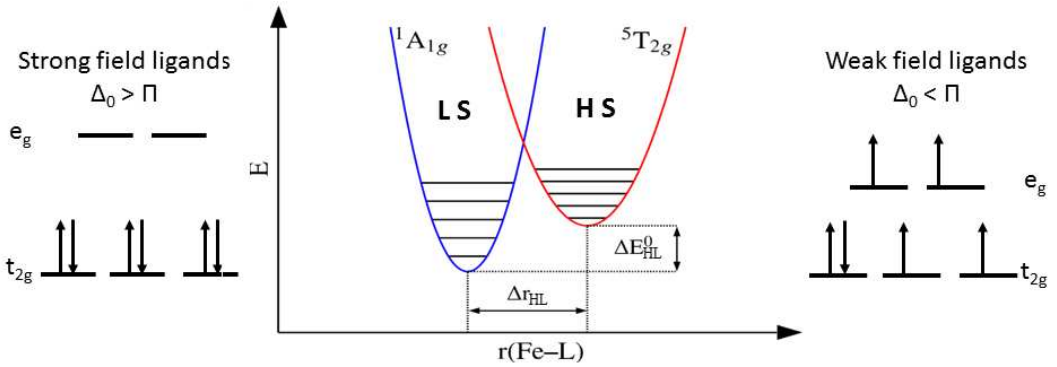

Figure 1.2: Electronic configuration for the two possible ground states following crystal field theory and simplified schematic representation of the configurational diagram of two molecular spin states (HS and LS).

the spectroscopic term $^5\mathrm{T}_{2g}$.

On the other hand, in a strong ligand field configuration, when Δ_0 is higher than Π, the electrons do not follow Hund's rule. The electrons occupy the lowest energy level (t_{2g}), maximizing the number of paired electrons. In this case the total spin for $\mathrm{Fe^{II}}$ is $S = 0$. This diamagnetic state is called low spin state (LS), represented by the spectroscopic term $^1\mathrm{A}_{1g}$.

The origin of these two stable states can be observed in the Tanabe-Sugano diagrams. For example, the diagram in figure 1.3 gives the energy of the spectroscopic terms of d^6 ions in an octahedral environment and shows the ground and excited states as function of the ligand field strength. The free electron ground state is ^{5}D. Under the influence of a ligand field this state splits into two, the new ground state $^5\mathrm{T}_{2g}$ (HS state) and an excited state $^5\mathrm{E}_g$. The state $^5\mathrm{T}_{2g}$ remains the ground state until $\Delta_0 \approx \Pi$. Let's call this value Δ_{crit}. For higher values of Δ_0, the $^1\mathrm{A}_{1g}$ (LS state) becomes the new ground state.

One important aspect of the spin transition is the change in the metal-ligand distance (Δr_{HL}). In the HS state the metal-ligand distance ($r_{Fe\mathrm{II}_{-L}}$) is higher than in the LS state due to the presence of two electrons in the anti-bonding e_g orbitals that repel the ligand electronic orbitals. In the case of Fe^{II} Δr_{HL} is typically 0.2 Å, which implies a strong change of the ligand field strength, since this latter depends on the metal-ligand distance as ($\Delta \approx r^{-n}$, where $n = 5 - 6$) [46]. From a classical point of view, using the approximation of a unique harmonic vibrational mode, it is possible to represent both molecular states as a double potential well in a configurational coordinate diagram along the metal-ligand distance [22]. The elongation of the metal-ligand distance in the HS state leads to lower force constants, reflected by different concavity of the potential well, and to lower vibrational frequencies, reflected by the higher density of vibrational states (figure 1.2). From this diagram we can also infer that for triggering spin transition it is necessary that the energy difference between the minima of the two potential wells

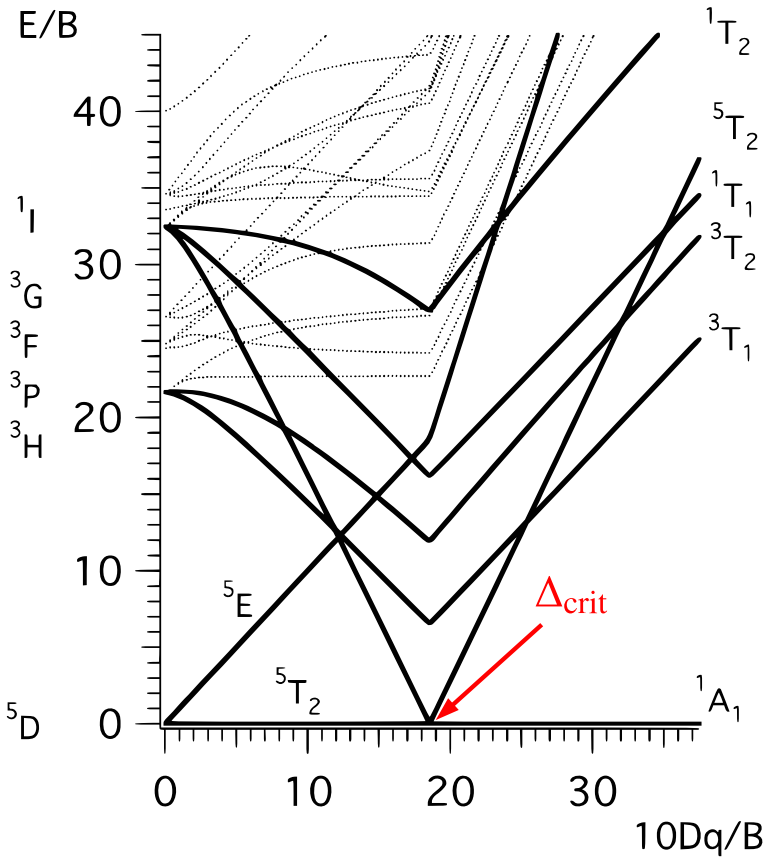

Figure 1.3: Tanable-Sugano diagram for a transition metal ion with six d electrons [47].

($\Delta E^0_{HL} = E^0_{HS} - E^0_{LS}$) is in the magnitude of the thermally accessible energies (i.e. $\Delta E^0_{HL} \approx k_B T$).

1.1.1.1 Thermodynamical aspects of spin crossover

Spin transition can be described using a simple thermodynamical model as an equilibrium between two phases, if we consider a system constituted by an assembly of isolated, non-interacting SCO molecules. In normal experimental conditions the pressure and the temperature of the sample can be external control parameters, so the pertinent thermodynamical function is the Gibbs free energy, G. At constant pressure, the free enthalpy difference between the HS and the LS state is written as:

$$\Delta G = G_{HS} - G_{LS} = \Delta H - T\Delta S \tag{1.1}$$

where ΔH and ΔS are the enthalpy difference ($H_{HS} - H_{LS}$) and the entropy difference ($S_{HS} - S_{LS}$), respectively. As ΔH and ΔS are always positive, an equilibrium temperature ($T_{1/2}$) can be defined as the temperature when the proportion of HS molecules (N_{HS}) is equal to the proportion of LS molecules (N_{LS}) [48]. In this case $\Delta G = 0$, so $T_{1/2}$ can be written as:

$$T_{1/2} = \frac{\Delta H}{\Delta S} \tag{1.2}$$

ΔH can be divided into two contributions, an electronic part (ΔH_{el}) and a vibrational contribution (ΔH_{vib}). Apart from a few specific cases (the so called equienergetic situation [49]), for most SCO complexes the main contribution to ΔH is given by ΔH_{ef}.

On the contrary the entropy variation ΔS has in most cases a main contribution from the vibrational part(ΔS_{vib}). During the spin transition the electronic part (ΔS_{el}) is attributed to the change of total spin momentum S, and the change of the angular orbital momentum L. These can be written as:

$$\Delta S^{spin}_{el} = N_a k_B ln\left(\frac{2\mathrm{S}_{HS}+1}{2\mathrm{S}_{LS}+1}\right) \tag{1.3}$$

$$\Delta S^{orb}_{el} = N_a k_B ln\left(\frac{2\mathrm{L}_{HS}+1}{2\mathrm{L}_{LS}+1}\right) \tag{1.4}$$

where N_a is Avogadro's number and k_B is the Boltzmann constant. If the ligand field has a perfect octahedral symmetry, then we need to consider both electronic contributions. However, in most cases the symmetry of the ligand field is lower than O_h. As a consequence there is no significant contribution from ΔS^{orb}_{el}, i.e. $\Delta S_{el} \approx \Delta S^{spin}_{el}$. In the case of a spin transition of $\mathrm{Fe^{II}}$ between the $^1\mathrm{A}_1$ and $^5\mathrm{T}_2$ states, $\Delta S^{spin}_{el} = 13.38$ J·K^{-1}·mol^{-1} [50]. However, heat capacity measurements in $\mathrm{Fe^{II}}$ based SCO complexes highlighted that ΔS values are typically between 40 J·K^{-1}·mol^{-1} and 80 J·K^{-1}·mol^{-1} [51–53]. This

important difference between ΔS and ΔS_{el} is attributed to the vibrational part of the entropy difference. The intramolecular vibrational modes are considered to be the main contributors to ΔS_{vib} (ΔS_{vib}^{intra}) due to the difference in the metal-ligand distance between the HS and LS states.

From equations 1.1 and 1.2 we can draw the following conclusions:

- $T < T_{1/2} \rightarrow \Delta H > T\Delta S \leftrightarrow G_{LS} < G_{HS}$ The enthalpy is dominant and the stable state is the LS state.
- $T > T_{1/2} \rightarrow \Delta H < T\Delta S \leftrightarrow G_{LS} > G_{HS}$ The entropy becomes dominant and now the stable state is the the more degenerated spin state, i.e. the HS state.
- $T = T_{1/2} \rightarrow \Delta H = T\Delta S \leftrightarrow G_{LS} = G_{HS}$ The enthalpy and entropy are equivalent and there is an equilibrium between the two phases.

1.1.1.2 Different spin transition behaviors

In a diluted SCO system, the intermolecular interactions can be neglected hence the change of the spin state of the system can be described as a sum of the conversions of isolated molecules. In this case the spin state change statistics follows Boltzmann distribution. On the other hand, in the case of a bulk solid the intermolecular interactions and the crystal packing of the material will play an important role. When a molecule switches from the LS to the HS state there is an increase of volume of the molecule that will change the energy of the other molecules in the solid due to elastic stress and strain. In addition this increase in volume is associated with a decrease of the intermolecular forces of the material that is translated in an increase of its compressibility. These elastic mechanisms are denoted globally as the cooperativity of the SCO material.

By convention the thermal spin transition curve is obtained by plotting the high spin fraction (n_{HS}) as function of the temperature. In a SCO material composed by N molecules, there are N_{HS} molecules in the HS state and $N_{LS} = N - N_{HS}$ molecules in the LS state. Then, n_{HS} is defined as:

$$n_{HS} = \frac{N_{HS}}{N} \tag{1.5}$$

All spin crossover curves observed until 1960 where gradual [54, 55] like the one shown in figure 1.4 panel a. These compounds have weak cooperativity. In this case we call the phenomenon as spin equilibrium or spin conversion or spin crossover.

In 1964 the first abrupt spin transition was observed by Baker & Bobonich for the compound [Fe(phen)$_2$(NCS)$_2$] [12], and confirmed in 1967 by König & Madeja [56]. This first order transition is represented in figure 1.4, b. The abrupt transition is a consequence of the intermolecular interactions of elastic origin. This complex presents

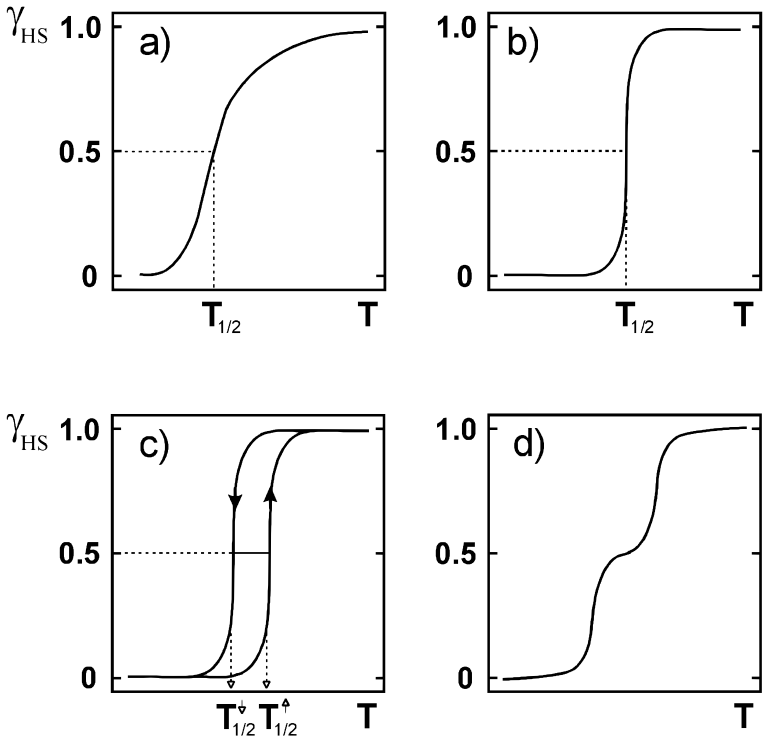

Figure 1.4: Principal types of thermal spin transitions, representing in a schematized way the HS fraction as function of the temperature: (a) gradual spin transition, (b) abrupt spin transition, (c) spin transition with hysteresis and (d) double step spin transition.

strong cooperativity and by convention we denote this phenomenon as spin transition, though the general term "spin crossover" is also used by the community. For highly cooperative systems the hysteresis associated with the first order spin transition becomes more pronounced, as the one represented in figure 1.4 c. The temperatures $T_{1/2}^{\uparrow}$ and $T_{1/2}^{\downarrow}$ are the transition temperatures ($n_{HS} = 1/2$) on warming and cooling, respectively. The first observation of a hysteresis cycle was reported for the [Fe(4,7-$(CH_3)_2$-phen)$_2$$(NCS)_2$] compound in 1976 by König & Ritter [57].

The spin transition can also take place in several steps, as it is shown by the figure 1.4 d. This phenomenon was observed for the first time in 1981 in a Fe^{III} complex of 2-bromo-salicylaldehyde-thiosemicarbazone [58]. Such multi-step transition may appear for different reasons. For example, it may occur when the metal ions occupy two or more different lattice sites in the material [59]. In the second case the spin transition in one metal atom may render the transition less favorable in a nearby metal ion. This type of spin transition can be also observed in systems where all metal ions are equivalent. In this case it is the preferential formation of HS-LS pairs (ordering) due to a competition between short range and long range interactions in the progress of the transition that produces the double step transition [60]. The first example of this situation was reported in a binuclear system [61].

1.1.1.3 Thermodynamical approach of the cooperativity in SCO solids

a) Non cooperative systems

Lets consider a spin transition material in contact with a pressure and thermal reservoir, constituted by N molecules, where the intermolecular forces are negligible. If we denote G_{HS} and G_{LS} as the free Gibbs energy in the HS and in the LS states respectively, the Gibbs energy of this system can be written as:

$$G(T, P, N) = n_{HS}G_{HS} + (1 - n_{HS})G_{LS} - TS_{mix} \tag{1.6}$$

where S_{mix} is the mixing entropy representing the different distribution possibilities of the HS and LS populations for N molecules in the material. In an isolated system where the molecules are indistinguishable in the HS state and in the LS state, but the sites are distinguishable then S_{mix} can be written as:

$$S_{mix} = k_B ln\left(\frac{N!}{N_{HS}!N_{LS}!}\right) \tag{1.7}$$

Using the Stirling approximation ($ln(N!) \approx Nln(N) - N$) we obtain that

$$S_{mix} = -Nk_B[n_{HS}\ln(n_{HS}) + (1 - n_{HS})\ln(1 - n_{HS})] \tag{1.8}$$

At a given P and T the thermodynamical equilibrium is achieved when $\left(\frac{\partial G}{\partial n_{HS}}\right) = 0$.

$$\frac{\partial G}{\partial n_{HS}} = \Delta H - T\Delta S + Nk_B Tln(\frac{n_{HS}}{1 - n_{HS}}) = 0 \tag{1.9}$$

So we can write the temperature of the system as a function of the high spin fraction:

$$T = \frac{\Delta H}{\Delta S + Nk_B ln(\frac{1-n_{HS}}{n_{HS}})} \tag{1.10}$$

The transition temperature can be retrieved from equation 1.10 by substituting $n_{HS} = 0.5$.

$$T_{1/2} = \frac{\Delta H}{\Delta S} \tag{1.11}$$

b) Cooperative systems

As already stated in section 1.1.1.2, in the solid state intermolecular interactions play an important role in the spin transition. The most widely used model that takes the intermolecular interactions into account was introduced by Sclitchter and Dickramer [44]. They introduced a phenomenological nonlinear interaction term $G_{int} = \Gamma n_{HS}(1 - n_{HS})$

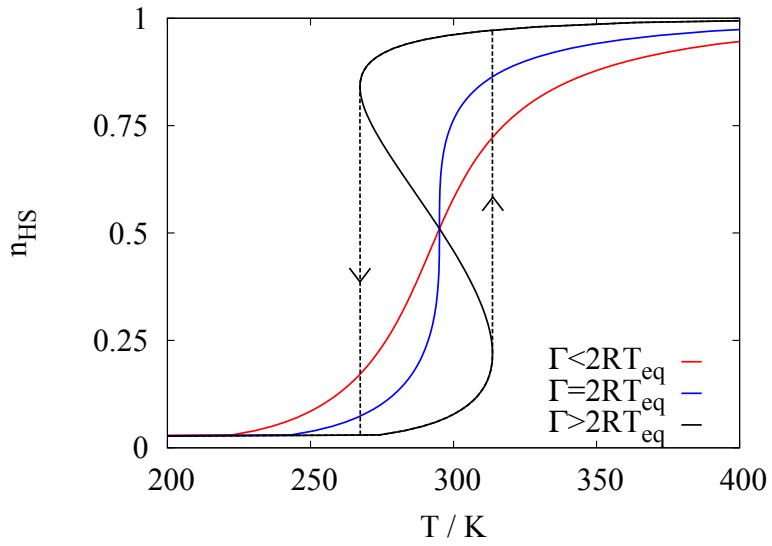

Figure 1.5: Plots of the temperature vs the high spin fraction for different values of the cooperativity (Γ) calculated with equation 1.14. The dotted lines correspond to the hysteresis phenomenon due to the presence of metastable states.

in equation 1.6. The free energy can be expressed as:

$$G = n_{HS}G_{HS} + (1 - n_{HS})G_{LS} + \Gamma n_{HS}(1 - n_{HS}) - TS_{mix} \tag{1.12}$$

were $\Gamma(P, T)$ is an effective parameter, which describes the strengths of the intermolecular interactions, i.e. the cooperativity. It represents the tendency for a molecule or an active center in a given spin state to be surrounded by molecules or active centers with the same spin state. This term generates a hysteresis without changing the Gibbs energy values. As in the previous case, the temperature as function of the high spin fraction is calculated by obtaining the partial derivative of the free enthalpy.

$$\frac{\partial G}{\partial n_{HS}} = \Delta G + \Gamma(1 - 2n_{HS}) + Nk_BT \ln\left(\frac{n_{HS}}{1 - n_{HS}}\right) \tag{1.13}$$

In thermal and pressure equilibrium $\partial G/\partial n_{HS}|_{P,T} = 0$ then we can write T as function of n_{HS}:

$$T = \frac{\Delta H + \Gamma(1 - 2n_{HS})}{Nk_B ln(\frac{1-n_{HS}}{n_{HS}})} \tag{1.14}$$

For simplicity it is better to work in J·mol^{-1}, hence Nk_B is substituted by R the perfect gas constant.

We can distinguish three situations:

- $\Gamma < 2RT_{eq}$ Here $\frac{dT}{dn_{HS}} > 0$ and there is a gradual conversion without hysteresis typical of weak molecular interactions.

- $\Gamma \approx 2RT_{eq}$ In this case $\frac{dT}{dn_{HS}} > 0$ but it is zero when $n_{HS} = 0.5$, so there is a discontinuity, i.e. a sharp transition without hysteresis. The materials that present this kind of behavior are called cooperative.

- $\Gamma > 2RT_{eq}$ The curve presents a local minimum and a local maximum, so there is a sharp transition with hysteresis, present when there are strong molecular interactions.

The influence of the cooperativity on the spin transition curves is shown in figure 1.5.

1.1.2 Spatiotemporal dynamics

Up to now we have not considered the dynamics of the spin transition. The first time-resolved measurements on SCO systems were carried out in solution [37, 62]. These studies addressed the intramolecular kinetics of spin crossover and were based in a first time on temperature jump and ultrasonic perturbation techniques and later on laser photo-perturbation methods. A further important step in the investigation of spin crossover dynamics was the discovery of light-induced excited spin state trapping (LIESST) phenomenon. Indeed the possibility to generate long-lived metastable spin states by light irradiation allowed for a detailed investigation of the relaxation dynamics of these states, as well as the study of different physico-chemical parameters (temperature, pressure, metal substitution, etc.) on the dynamics [63, 64]. Thanks to these studies, in diluted systems the spin state interconversion rates are today well understood.

In bulk materials the dynamics are further complicated by spatially heterogeneous phenomena. Sorai and Seki were the first to suggest that first-order spin transitions should consist in one or several nucleation points followed by a heterogeneous phase separation and domain growth [51]. This behavior has been first evidenced by X-ray diffraction and more recently observed by optical microscopy in some SCO crystals. Several theoretical models have been also proposed to describe these spatio-temporal phenomena [65–69]. Nevertheless there are many open questions: How many nuclei form? What are the control parameters for the growth of the new phase? How the nucleation and growth phenomena depend on the morphology and structure of the sample? What is the minimum size of the crystal where phase separation can still be observed? In a natural nucleation point how many molecules should transit to trigger the transition of the whole crystal? What is the size and the nature of the phase boundary? To answer some of these questions the existing experimental methods are not sufficient and we need new techniques able to detect the spin transition with high spatial resolution.

In this work we will go into this direction and investigate the spatio-temporal dynamics with submicrometric resolution. Therefore in the following section a state of the

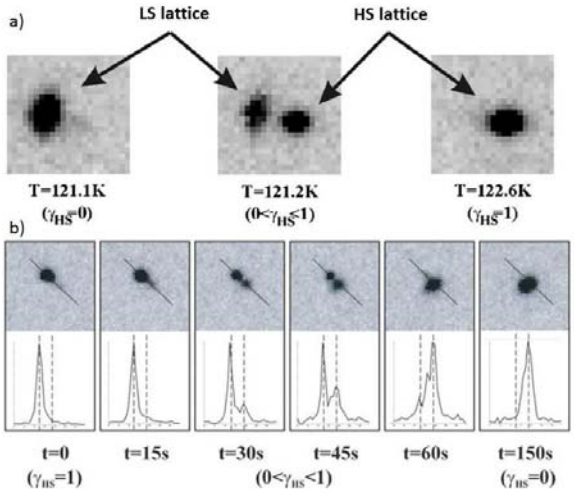

Figure 1.6: a) Thermally induced transition in the heating mode: Temperature dependence of the (063) reflection in the x-ray diffraction pattern [70]. b)Dynamics of the spin crossover for a single crystal of $[Fe(btr)_2(NCS)_2H_20]$ at T = 117.2 K. Each picture corresponds to the instantaneous (at t = 0, 15, 30, 45, 60, 150 s) 2D diffraction profile of the reflection (upper part) and intensity line profile (lower part) along the radial direction [72].

art of the current experimental approaches to study the spatio-temporal dynamics on SCO compounds is presented.

1.1.2.1 X-ray diffraction

The difference in the lattice parameters in the HS and LS phases enable the possibility to follow the spin transition by X-ray diffraction or neutron diffraction. The first systematic studies were carried out by König on powder samples [34]. Later on these results were extended to single crystals [70, 71]. The experimental resolution is related to the coherence length (L_c) of the incident light, i.e. the propagation distance over which a coherent wave maintains a specified degree of coherence ($L_c \approx \lambda/\Delta\lambda$, where λ is the wavelength of the incident light). The volume of the material that diffracts the beam in a coherent manner is directly related to the coherent length.

In SCO materials that present a gradual spin transition, the volume and lattice parameters of the material change in a continuous manner. This is observed in the diffractograms as a gradual shift of the Bragg peaks in the reciprocal space and the diffraction is independent of the illuminated volume.

In strongly cooperative materials, the nucleation of the new phase occurs in seeds that grow to form domains. While the domains do not outgrow the coherence length, Bragg peaks of both phases will be observed in the reciprocal space. This splitting of

the Bragg peaks was reported in highly cooperative materials like $[Fe(btr)_2(NCS)_2H_20]$ and $[Fe(2\text{-pic})_3]Cl_2EtOH$ [70–72]. An example of X-ray diffraction pattern in a highly cooperative SCO compound is shown in the figure 1.6.

X-ray diffraction allowed to confirm the existence of a structural phase separation and investigate the kinetics of nucleation and growth, but the lack of imaging capability has strongly limited the information content of this technique. This problem was recently solved using electron microscopy providing access to high spatial and temporal resolution information both in the real (conventional transmission electron microscopy image) and the reciprocal (electron diffraction) spaces [10].

1.1.2.2 Optical imaging

Optical microscopy is a non invasive method that is capable to give spatiotemporal information on the spin transition phenomena. Even though the spatial resolution is limited to the optical diffraction limit, it is a very interesting tool to study the dynamics of the transition.

The optical imaging of the spin transition in single crystals was performed for the first time by Jeftic in 1999 on the $[Fe(ptz)_6(BF_4)_2]$ compound [73]. One year later other optical images were taken by Ogawa on crystals of the $[Fe(2\text{-pic})_3Cl_2EtOH]$ compound during the photoswitching process [74]. In both papers the formation and growth of domains with a clear phase separation was reported. Optical microscopy was fully recognized as a powerful quantitative approach to study spin transition materials after the absorbance studies of Goujon in 2008 [75].

Optical microscopy using different imaging approaches (bright field, dark field, transmission, reflection, crossed polarizers, etc.) allowed to obtain information about the development in time of the spin fractions with micrometric resolution [66, 68, 74–87]. The main results are consistent with the general expectation in that the spin transition in cooperative systems occurs via heterogeneous nucleation and growth mechanism (figure 1.7), while the spin crossover in weakly cooperative systems is a spatially rather homogeneous transformation. Remarkably, in high quality, cooperative crystals a very reproducible nucleation and growth of a single macroscopic domain with a well-defined "transition front" was reported. The nucleation points were localized around structural defects in the crystals (usually on the surface) and the domain growth was reported directional in many cases. The specific orientation and movement of the phase boundary seems to be governed by the minimization of the elastic energy between the HS and the LS structures [67]. The speed of propagation of the new phase (HS or LS) was usually measured between 1-40 $\mu m{\cdot}s^{-1}$. This low value is probably related to the accumulation of mechanical stress and/or latent heat during the boundary motion. Unfortunately, the mechanical effects accompanying the spin transition associated with the brittleness of the crystals have

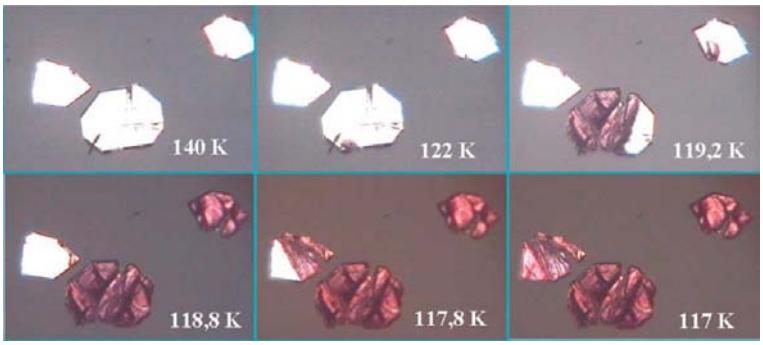

Figure 1.7: Optical images of five crystals of $[Fe(btr)_3(NCS)_2]\cdot H_2O]$ at different temperatures in cooling mode. The sample is colorless in the HS and violet in the LS states.

led in several cases to irreversible damage of the crystals (formation of cracks and other defects) over repeated cycling. The limited number of robust, high-quality single crystals represents thus a major obstacle for the deeper investigation of the spatio-temporal dynamics of the spin transition by microscopy techniques.

To obtain more detailed structural information optical microscopy imaging can be extended towards microscopic imaging using vibrational spectroscopies (Raman or FTIR). Microspectroscopy not only enables to study nucleation and growth mechanisms with micrometric spatial resolution, but it allows also to detect local changes in the crystal structure and elastic properties of the material. The first vibrational spectroscopic studies that were focused on the coexistence of the two spin states in solid SCO materials were carried out by Baker & Bobonich in 1964, but without imaging [12]. In highly cooperative crystals the coexistence of HS and LS spectroscopic markers is observed around the transition temperature, as shown in figure 1.8 (a) and (b). The imaging of spin domains and their propagation was then achieved using Raman microspectroscopy on different compounds [79, 88]. Nevertheless confocal Raman microscopy remains still limited by the diffraction of light.

1.1.2.3 High resolution microscopy

In all previous techniques the highest resolution that can be obtained is limited by the Abbe diffraction limit ($d = \lambda/(2\text{N.A.})$, where N.A. is the numerical aperture. This limit is not much better than the micrometer for far-field optical microscopy. In order to surmount the rather limited spatial resolution of optical microscopes, one may either employ instruments using high energy photons, electrons or other particles, wherein one does not overcome, but reduces the diffraction limit, such in the case of the electron microscopy study of Van der Veen et al. [10]. The other alternative is the use of Scanning Probe Microscopy (SPM). SPM refers to a family of surface analysis methods, which use a nanometric probe in interaction with a sample surface and a scanner, which allows to

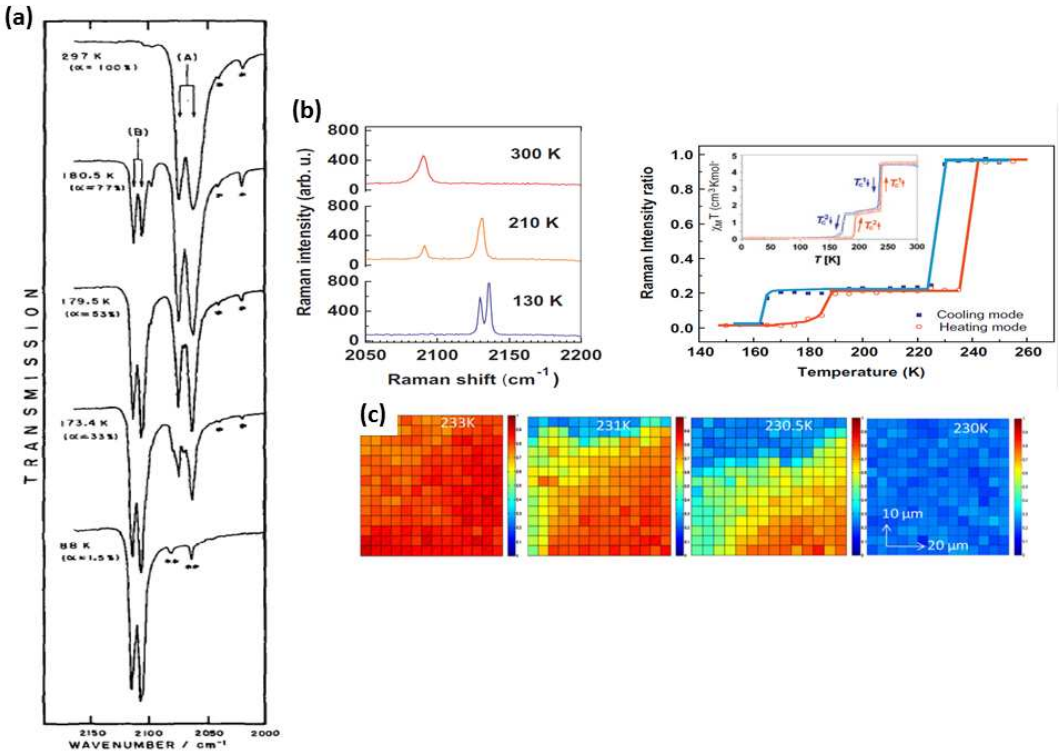

Figure 1.8: Infrared spectra for different temperatures of $[Fe(phen)_2(NCS)_2]$ in the region of C-N stretching frequencies [51]. (b) Left: Raman spectra of the HS (300 K), intermediate phase (IP) (210 K) and LS (130 K) phases in the CN stretching (νCN) mode region of $[Fe(bapbpy)(NCS)_2]$. Right: the thermal spin transition curve of a single crystal of $[Fe(bapbpy)(NCS)_2]$ (c) Point-by-point Raman spectral mapping of the spin fractions in a region of 76 x 70 μm of the crystal at different temperatures in the cooling mode. The red color is associated with the HS phase and blue with an intermediate phase [79].

control with nanometric precision the position of the probe with respect to the surface, both laterally and vertically. SPM techniques are today widely used in different fields of science and technology for investigating sample surface properties from the micrometer down to the atomic scale. Beyond their surface imaging capabilities they provide also access to various material properties, such as surface charge and electro-magnetic field distributions, elastic moduli, thermal conductivity, etc. SPM, and in particular AFM (Atomic Force Microscopy), is extensively used for surface topography imaging of SCO films and other nano-objects, but rarely to probe the molecular spin state changes. Until now, most of the published results [89–91] have been obtained using Scanning Tunneling Microscopy (STM), which probes the local electronic structure of a surface with atomic resolution. While STM is an extraordinary tool to investigate the spin transition at the molecular level it is inadequate for the investigation of the spatio-temporal dynamics of an insulating crystal. In this respect, AFM studies on SCO compounds appear somewhat more promising, though still very challenging, mainly for the need for using external stimuli (temperature, pressure, etc.) to trigger the SCO. In addition, the interaction between the tip and the sample may be difficult to analyze in a quantitative manner. Chong et. al. made the first study on spin transition crystals at room temperature, they studied the wetting properties of two different SCO crystals [92]. The first spin transition curves and study in both phases using atomic force microscopy and Near-field Scanning Optical Microscopy (NSOM) were performed by Lopes et al. in our team [93]. We studied the change in the surface roughness and other topographic features of Fe(pyrazine)[$Pt(CN)_4$] crystals across the spin transition. We found that is possible to to record thermal spin transition curves with high spatial resolution using these techniques, showing details that were not visible in optical microscopy. Based on these first results this thesis aims for investigating the potential of AFM and NSOM methods in the study of spatio-temporal dynamics of SCO single crystals.

1.1.3 SCO nano-objects

Kahn was the first to evoke the interest in fabricating SCO materials at nanometric scale, so that they could be used in high density information storage media [94]. The two key properties that have to be controlled are the transition temperature and the hysteresis width in SCO nanoparticles. Indeed, the phase stability and the transformation kinetics are in general highly dependent on the object size. In spin crossover compounds, size effects may lead to a loss of the hysteresis (bistability) properties, a shift of the transition temperature or the occurrence of an incomplete transition, but also a reappearance of the hysteresis at the extreme size reduction (1-4 nm). To investigate size reduction phenomena in SCO materials, considerable efforts have been made in the last ten years to synthesize and characterize spin transition materials at nanometric scale including nanoparticles

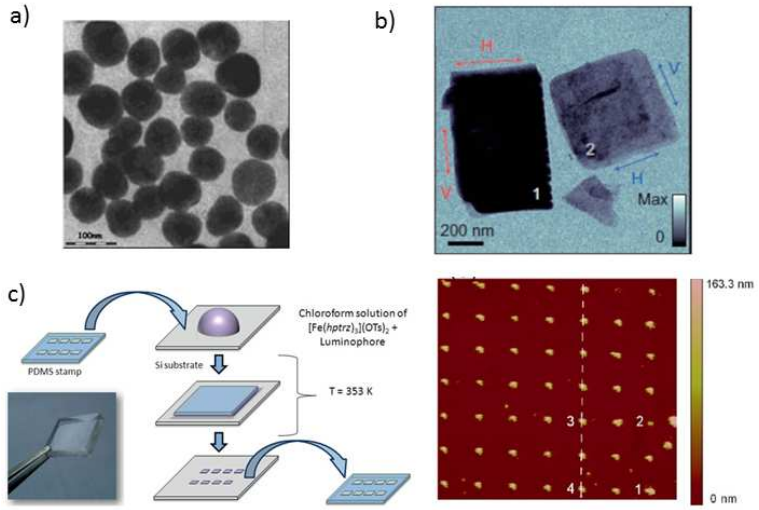

Figure 1.9: (a) TEM image of $[Fe(NH_2\text{-}trz)_3](Br)_2 3H_2O$ nanoparticles [98]. (b) Bright-filed electron microscopy image of two SCO nanocrystals [10]. (c) Fabrication process for arrays of SCO nanodots. [9].

and continuous or nanopatterned thin films [4, 62, 95]. Beyond the fundamental scientific questions these switchable nano-objects are also interesting candidates for applications in nano-optical, nano-electronic and/or nanomechanical devices [96].

Spin transition nanoparticles were prepared by the first time by the group of Jean-François Létard (Bordeaux) using the reverse micelle technique [5, 97, 98]. Later several other methods have been published for the synthesize of SCO nanoparticles [4]. It is interesting to note that most of the spin transition nanoparticles reported up to now consist of coordination networks, and only a few "genuine" molecular nanoparticles were fabricated [99]. Spin crossover thin films were also deposited by different techniques: spin coating [100, 101], layer by layer assembly [102], thermal evaporation [103, 104], etc.

Besides the synthesis the characterization of SCO materials at the nanoscale raises also new problems. A large ensemble of nanoparticles can be studied using classic characterization techniques, such as magnetic susceptibility measurements and Mössbauer spectroscopy. However, ensemble averaging in these methods leads for difficulties to achieve proper size - property correlations. In addition particle - particle interactions might also occur. To avoid these artifacts it would be desirable to investigate single, isolated SCO objects. It is, however, delicate to detect the spin transition by standard techniques on thin films or single nano-objects due to the small amount of probed material. In order to overcome this problem new detection techniques have been developed, based on the change of different physical properties of the material. Many of them are based on the change or the optical properties [105]. For example the detection of spin transition in thin films has been achieved using Surface Plasmon Resonance (SPR) [6, 106] and optical diffraction [2]. Fluorescence techniques have also been implemented to study single objects [9]. As

mentioned above electronic microscopy has been also used to detect the spin transition in a single particle [10]. In this context SPM methods appear also advantageous. Although SPM has been already used to study phase transitions in different materials [107–113], it has not yet been used in the context of SCO nano-objects. Hence the second aim of this theses is the development of SPM approaches to study spin transition at nanometric scale.

1.2 Introduction to Scanning Probe Microscopy

Scanning Probe Microscopy (SPM) is a branch of microscopy that was created to reach resolutions below the optical diffraction limit. It consists of a sharp tip that moves accurately over the sample surface with nanometric or subnanometric precision. This may be compared with the act of sensing with a finger over a surface, or like an old-fashioned record player with a metallic needle on a vinyl record. With this technique it is possible to obtain three-dimensional (3D) images of solid surfaces with atomic resolution.

This family of microscopy methods was founded with the scanning tunneling microscope (STM), invented by Binnig and Rohrer in 1982 [114]. With the STM it became possible to image single atoms on flat surfaces. In parallel the near-field scanning optical microscope (NSOM) was invented, which allowed microscopy with light below the optical resolution limit [115, 116]. STM can only be used to study conducting or semiconducting surfaces. Based on the STM Binnig et al. developed the atomic force microscope (AFM) in 1986 [117], to overcome the disadvantage of STM. AFM is able to measure very small forces (less than 1 nN), between the tip and the sample on either conductive or insulating surfaces. These microscopes have initiated a real revolution in the fields of surface and colloid science and are commonly used to characterize micro and nanomaterials.

The capability to investigate surfaces with unprecedented resolution using this technology promoted the development of numerous related techniques, which use different kinds of probes and observation modes resulting in different tip-sample interactions. The resolution varies from one technique to the other, it spans from some tens of nanometers to atomic resolution. This capability is mainly due to the ability of the piezoactuators to execute motions with a precision and accuracy better than 1/10 of nanometer. The most used scanning probe microscopy methods are:

- Atomic Force Microscopy (AFM): Besides topographical images, AFM is a mean to study the mechanical properties of the sample such as the Young's modulus, adhesion forces [118, 119], as well as friction forces [120].

- Electrostatic Force Microscopy (EFM): Local charges on the tip or surface lead to electrostatic forces between the tip and the sample, which allows to study the distribution of charges in the sample [121].

- Near-field Scanning Optical Microscopy (NSOM): NSOM is a method for nano-scale optical imaging that achieves subwavelength resolution by detecting the evanescent wave fields accessible in the near-zone of a scattering object. [107, 122].

- Magnetic Force Microscopy (MFM): If the tip is coated with a magnetic material e.g. iron, that has been magnetized along the tip axis,the magnetic domains in ferromagnetic materials can be studied [121, 123].

- Scanning tunneling microscopy (STM): An applied voltage difference between a conducting tip and sample, which are brought very close together can allow electrons to tunnel through the vacuum between them. With this technique the local electronic structure can be obtained [124, 125].

- Chemical Force Microscopy (CFM): By modifying the AFM tip chemically it is possible to probe various chemical properties (hydrophobicity, chemical or biological affinities, etc.) of the sample [126, 127]

- Kelvin probe force microscopy (KPFM): In KPFM the contact potential difference between the sample surface and the tip is measured with high spatial resolution. The work function of a broad range of materials can be studied with this method [128, 129].

- Conductive atomic force microscopy (C-AFM): The conductivity of a sample is obtained by applying a voltage between the tip and the sample when they are in contact [130].

- Piezoresponse microscopy (PFM): A sharp conductive probe is brought into contact with a ferroelectric surface. By applying an alternating current bias to the probe tip the ferroelectric domains can be imaged and manipulated [131].

This list is not exhaustive, for example we did not described the existing methods to study the mechanical properties of the materials with high spatial resolution, since they will be discussed in chapter 3.

Among these various SPM techniques two approaches seem particularly adequate to study SCO compounds: (1) NSOM since the index of refraction of SCO materials changes during the spin transition and (2) the different mechanical modes of AFM, since the stiffness varies from one spin state to the other[1]. In the following sections we will thus provide a brief introduction to Atomic Force Microscopy (section 1.2.1), and Near-Field Scanning Optical Microscopy (section 1.2.2). AFM gives information about the

[1]MFM is not suitable to study SCO compounds. As already mention SCO compounds are paramagnetic in the HS state and diamagnetic in the LS state. However the paramagnetization of the compound is very weak. For this reason we believe that the MFM signals might be very small.

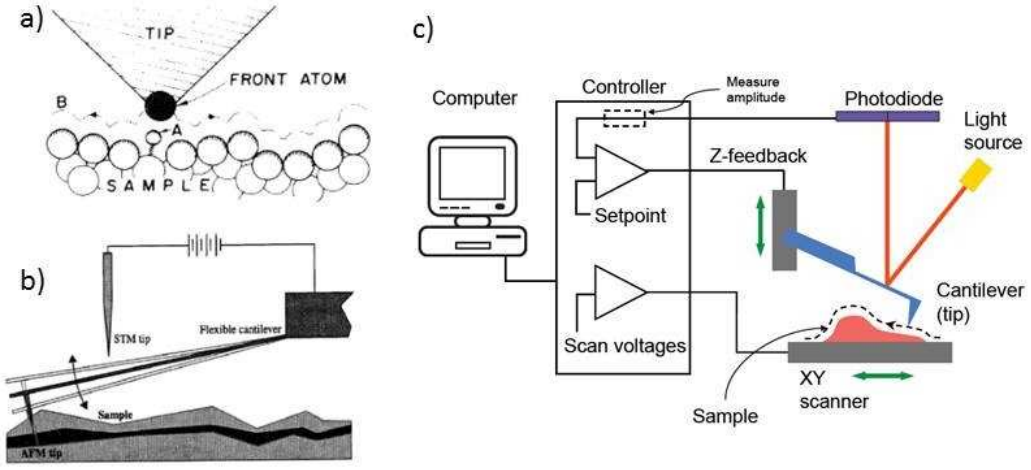

Figure 1.10: a)Scheme of the tip interacting ideally with the sample surface through a single atom at the apex. b) The first AFM set-up [117] where an STM is used to detect the cantilever deflection. c) Actual AFM model using optical beam deflection system.

topography of the sample and its mechanical properties, such as elasticity, adhesion and viscosity. On the other hand, NSOM gives us information about the optical properties of the sample surface with subwavelength resolution.

1.2.1 Atomic Force Microscopy

The Atomic Force Microscope (AFM) was invented by Bining, Quate and Gerber in 1986 [117] to overcome a basic drawback with Scanning Tunneling Microscope (STM). In fact STM can only image conducting or semiconducting surfaces, while AFM can image non conductive materials as well. Similar to STM, the AFM relies on a scanning technique to produce a 3D image of the surface. High resolution is achieved by minimizing the interaction volume between the probe and the object. For this reason the probe takes the form of a sharp tip glued to a cantilever where only the very apex of the probe is responsible for the interaction, see figure 1.10 a.

In the first AFM design, an STM probe was used to measure the normal force [117]. This force was maintained at a constant level with a feedback mechanism (see figure 1.10 b). One disadvantage of this first model was the complex alignment necessary to make it work. In addition force measurements were much affected by thermal drift. In 1989 Gunther et al introduced the tuning fork into the field of scanning probe microscopy [132]. The idea is to place a tip in the end of a tuning fork which is forced to oscillate at its resonant frequency. When the tip approaches to the surface the tuning fork will react to the force that the sample applies on the tip and consequently the amplitude and the phase of the oscillation will change. The topography of the sample is obtained by maintaining the amplitude or phase constant through the scan. Today the tuning fork is still used

in many devices, since it has proven to be a very stable system and it does not involve the use of light for the detection of the probe position. However, only the dynamic (AC) modes of AFM can be used with this set-up. In 1990 Meyer and Amer introduced an optical beam deflection system [133], which is the most widely used nowadays. In this system a laser beam is reflected from the back of the cantilever onto a position-sensitive detector (photodiode). The backside of the cantilever is normally covered with a thin metal layer to enhance its reflectivity. Depending on the mode chosen by the user the system will measure the force between the tip and the sample, F_{ts} (contact mode) or the frequency / amplitude of an oscillating cantilever, ω/A (AC mode). Independently of the AFM mode, the chosen property will be measured by monitoring the deflection of the cantilever with a feedback loop. This later is used to control the tip-sample distance. In this way the chosen property (F_{ts}, ω or A), is kept constant.

1.2.1.1 Contact mode

In contact mode the force between the tip and the sample is kept constant by controlling the deflection of the cantilever (Z_c). As a consequence the tip is always in contact with the sample. The tip is mounted on a soft cantilever with a spring constant (k_c) usually lower than 1 N/m. In this case one can assume that the probe will not move the atoms on the surface. The forces between the surface and the tip (typically in the order of piconewtons) cause the cantilever to bend in the vertical direction, which is discerned by a detector. When the cantilever bends and the reflected light-beam moves through an angle equal to twice the change of the endslope dZ_c/dX. The signal of the detector is used to vertically adjust the tip position with respect to the sample surface, so the deflection, i.e. the position of the laser in the detector is fixed in the same value. This allows to record the height of the sample as function of the x and y position, and thus the topography of the surface is built up into a three dimensional image with nanometric or even with atomic resolution [117].

In this mode there is a direct control over the force applied to the sample. It is therefore possible to plot the force applied by the tip vs the distance between the tip and the sample at a given (x, y) position. Such force-distance curves give information about the local elasticity, adhesion and deformation of the surface.

In figure 1.11 a force-distance curve is shown where the different interactions between the tip and the sample are marked with numbers (1-4). When the tip is far from the sample, there are no forces between the tip and the sample (1). As the cantilever comes close to the surface van der Waals and capillary forces in air become significant compared with the spring constant of the cantilever, the tip jumps into contact with the surface and the cantilever is deflected downwards (2). When we continue the approach repulsive forces arise between the tip and the sample and the cantilever is deflected upwards (3). When

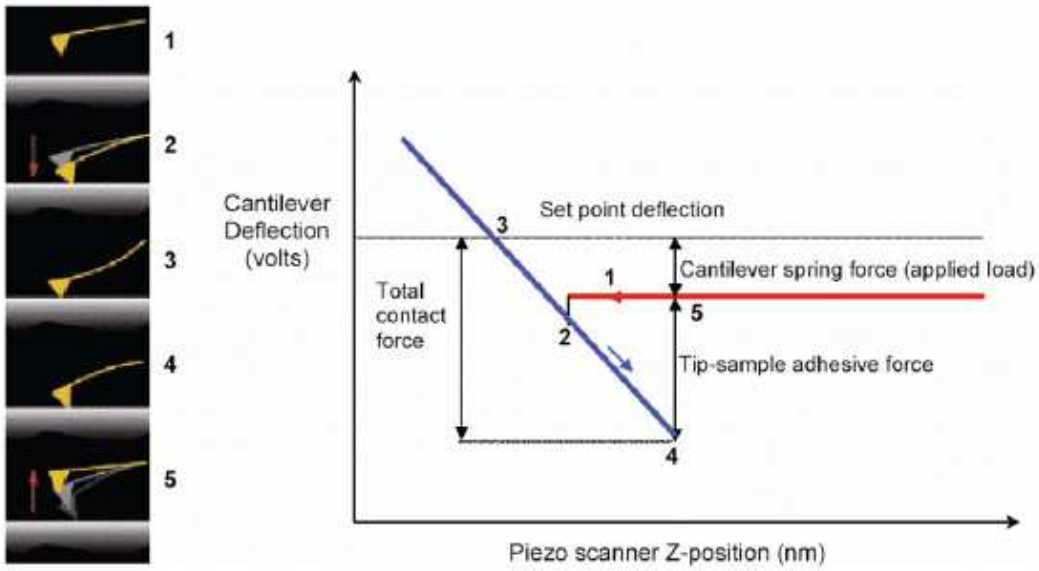

Figure 1.11: Force-Distance curve obtained with and AFM. The approach (red) and withdraw (blue) curves are shown in the right. The deflection of the cantilever corresponding to the different parts of the force-distance curve is shown on the left.

working in air there is usually adhesion from capillary forces between the tip and the sample. For this reason when the cantilever is retracted from the surface the tip remains in contact with the surface due to the adhesion forces and the cantilever is deflected downwards, until the tip is suddenly released from the surface (4).

From this curve it is possible to obtain information about the adhesion, the Young's modulus, the sample deformation and dissipation (see section 3.1.2).

Contact mode imaging is carried out by simply keeping the setpoint (point 3 in figure 1.11) constant, while scanning the sample. This mode is reasonably easy to operate, but contact mode has the inherent drawback that the lateral force exerted on the sample can be considerably high. In many cases this can lead to a degradation of the sample or the tip. As a solution to this problem the AC mode was invented.

1.2.1.2 AC mode

If the tip interacts with the sample for a very small time in each pixel of the scanned image, high lateral forces observed in contact mode can be avoided while maintaining high lateral resolution. In AC mode a stiff cantilever is forced to oscillate near its resonant frequency with a free amplitude A_f. This amplitude is typically some tens of nanometers, i.e. very small compared to the cantilever length. When the tip is approached to the sample a shift in the frequency, amplitude and phase of its oscillation is observed. Using a feedback loop the system maintains constant either the frequency (FM, frequency modulation) or the phase (PM, phase modulation) or the amplitude (AM, amplitude modulation) during

the scan, but in most conventional systems the latter is implemented. The AC mode reduces the damage to the sample by decreasing the lateral forces. It allows therefore to analyze soft samples as well. The risk of contaminating the tip and the wear of the tip decreases also in this mode [134, 135]. The tip-sample interactions in AC mode can be classified in two regimes: non-contact mode and intermittent contact (tapping) mode [136].

In non-contact mode, the amplitude of oscillation is a few or a few tens of nanometers and the tip feels mainly the van der Waals forces. (The tip is approached up to 1nm or 10 nm above the surface.). In this case there is no degradation of the tip or the sample so it is preferred for soft samples. In rigid samples the intermittent contact and non contact mode images should look the same. However, if a thin monolayer of fluid is laying on the sample the image may be quite different and it will become impossible to determine the true dimension of the sample.

The intermittent contact mode (also known as tapping mode) uses a cantilever or a tuning fork oscillating with an amplitude A_f above ca. 60 nanometers. The tip registers a combination of the van der Waals and the repulsive forces. In this case the tip exerts a pressure on the sample, so it can pass through a thin layer of fluid. This mode is normally used for hard and moderately soft samples. When working with soft samples there could be an apparent decrease in height since the tip indents the sample.

Assuming that air damping is the dominant factor, the movement of the cantilever can be described using the driven damped harmonic oscillator model [137, 138].

$$F(t) = m_e \frac{\partial^2 Z_c}{\partial t^2} + b\frac{\partial Z_c}{\partial t} + k_c Z_c \tag{1.15}$$

where $F(t)$ is the driving force, m_e is the effective mass of the cantilever (i.e. $m_e = 0.2427m_c + m_t$; where m_c is the real mass of the cantilever and m_t is the mass of the tip [138]), Z_c is the deflection of the cantilever and k_c is the spring constant of the cantilever. Considering that a periodic force $F(t) = F_0 \sin(\omega t)$ is applied on the cantilever and that $\tan(\phi) = b\omega/(k_c - m_e\omega^2)$, equation 1.15 is solved in steady-state by:

$$Z_c(t) = A_0 \sin(\omega t - \phi) \tag{1.16}$$

where A_0 is the free amplitude of the oscillation and is defined as:

$$A_0(\omega) = \frac{F_0}{\sqrt{(k_c - m_e\omega^2)^2 + b^2\omega^2}} = \frac{F_0}{m_e\sqrt{(\omega_0^2 - \omega^2)^2 + (\omega\omega_0/Q)^2}} \tag{1.17}$$

where $Q = \omega_0/b$ is the quality factor and $\omega_0 = \sqrt{k_c/m_e}$. The maximum amplitude

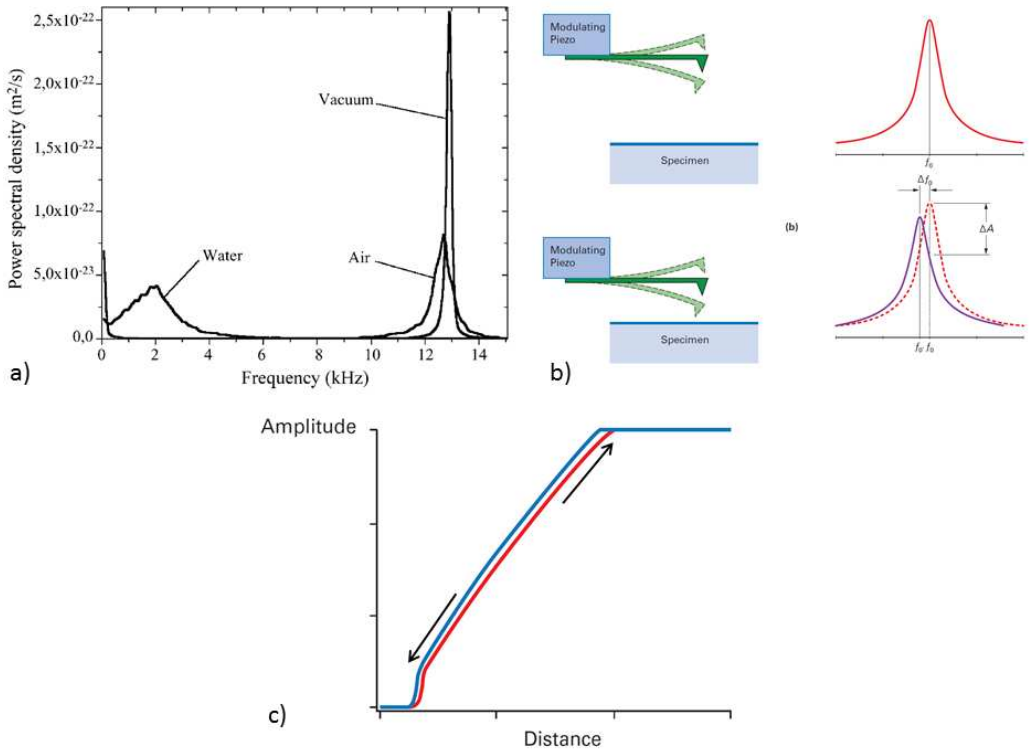

Figure 1.12: a) Power spectral density as a function of the frequency for a cantilever immersed in different media [138]. b) Scheme of the tip in AC mode and illustration of the change of frequency, amplitude and phase when the oscillating tip approaches the surface. c) Amplitude vs distance plot during approach (blue) and retract (red).

of oscillation (resonance) is reached when

$$\omega = \sqrt{\frac{k_c}{m_e} - \frac{b}{2m_e}} \tag{1.18}$$

The behavior of the tip will vary in different media. When the cantilever is submerged in liquid the effective mass of the cantilever increases, because the cantilever drags the surrounding liquid. On the other hand, in a gaseous media ω will be near the resonant frequency because the damping coefficient is relatively low, as shown in figure 1.12 a.

As the tip approaches to the sample the interaction between the tip and the sample becomes apparent, the cantilever is not free anymore. This interaction is translated into a shift of the resonance frequency, amplitude and phase as shown in figure 1.12 b. When the force between the tip and the sample is mostly an attractive force, the resonance frequency is reduced, on the other hand if the force is mostly a repulsive force the resonance frequency increases. When the tip approaches to the sample it is possible to measure the amplitude of oscillation as a function of the distance as shown in figure 1.12 c. This curve gives information of the reduction of the cantilever amplitude. Each point

represents an average value of the tip-sample interactions, so there is no unambiguous process to transform an amplitude-distance curve in a force-distance curve [138, 139]. Nevertheless, qualitative information about the mechanical properties of a sample can be obtained.

Additionally forces can vary when going away from a steady-state situation. This occur while scanning rough surfaces as the amplitude error at the sharp edges can correspond to interaction forces one order of magnitude higher than that of steady-state. Amplitude error incurred force is the leading cause of tip damage and such damage occurs because the feedback is not directly controlling interaction forces. On samples with high adhesion forces, a high tip amplitude has to be selected to ensure that the tip leaves the sample surface before tapping on it again.

1.2.2 Near-field Scanning Optical Microscopy

Extending optical perception to increasingly finer scales permitted early scientists to discover natural laws otherwise invisible. Over nearly 4 centuries the basic design of a microscope did not really change conceptually. Then, a few decades ago a new microscope, the Near-field Scanning Optical Microscopy (NSOM) was developed in an effort to overcome the diffraction limit of optical imaging.

In 1883, Abbe and Rayleigh derived a criterion for the minimum distance (d_{min}) between two point sources at which they can still be unambiguously distinguished as two separated sources [140].

$$d_{min} = \frac{\lambda}{2n\sin(\theta_{max})} \tag{1.19}$$

where λ is the wavelength of the incident light, n is the index of refraction of the surrounding medium and θ_{max} is the maximum collection angle of the optical system. The denominator $n\sin(\theta_{max})$ is called the numerical aperture (NA). The maximum value that NA can reach is between 1.4 and 1.6. Hence, considering a green incident light with $\lambda \approx 500$ nm the maximum resolution that can be achieved is roughly 250 nm. In contrast, NSOM offers higher resolution (few tens of nanometers) for the same wavelength. In addition NSOM provides simultaneous measurements of the topography and optical properties.

In 1928 the first mention of near-field microscopy appeared in an article of Synge [141]. Synge suggested that the diffraction limit could be overcome by reducing the illuminating light source to a volume smaller than the wavelength. In his article he established the bases of modern near field optics introducing the notions of superresolution, local detection and evanescent waves detection. Near-fields are usually tightly confined in the vicinity of matter so their detection is not easy and needs nanometer accuracy actuators capable of moving a suitable sensor or light source a few nanometers from the sample.

Therefore, the invention of the STM in 1982 was a significant instrumental progress for near-field optics, since the probe rasters the sample a few nanometers above the surface.

The first evidence of the existence of near-fields was done by Newton who discovered an anomaly in light behavior with his famous "Two prism experiment" carried out at the end of the 17th century [122, 142]. In his experiment Newton studied the total reflection of a light beam inside a glass prism. By fastening a second identical prism against the first one, the light beam could be transmitted from the first to the second prism without major perturbations, even before the two flat prism surfaces were in contact, i.e. before the continuity of the material was ensured between the two glass surfaces.

Another evidence of the existence of near-fields is found when developing the electric field of a linear electric dipole using the Hertz vectors or potential functions [143]. In this case the electrical field of the dipole varies as function of the distance r as $1/r$, $1/r^2$ and $1/r^3$, from its center. The fist term (r^{-1}) is associated with a propagating field obeying the energy conservation law. The other terms (r^{-2} and r^{-3}) cannot be explained simply, they carry no energy and therefore they do not propagate. However, they cannot be neglected in near-field optics, since it is one of the basis of subwavelength resolution.

Near-field optics is based on two important concepts: one is the existence of evanescent waves and the second is the notion of non-propagating fields.

1.2.2.1 Near-field optics insight

A source is called non-radiative if it does not produce any power flow across a close surface of infinite radius, centered on a point in the source region. The dark zones of an interference pattern are an example of a non-radiative source. The evanescent waves studied in this thesis are partial non-radiative sources, since they propagate in the x and y direction, but not in the z direction.

The description of the field in the vicinity of the sample is composed of both non-propagating (evanescent) components and propagating ones [144]. This physical duality of the field has the merit of being simple, but it conceals the fact that these components cannot be dissociated, since the propagating field exists because the non-propagating terms exist. Only the propagating components can be defined without ambiguity in the far-field. In general we can say that the electric field of evanescent waves propagates in the x, y plane, but is exponentially attenuated in the z direction.

There are three important phenomena where evanescent waves are formed: total internal reflection, subwavelength diffraction and surface plasmon resonance. In the next paragraphs these three examples will be presented briefly. More details can be found in [122, 143, 145, 146]

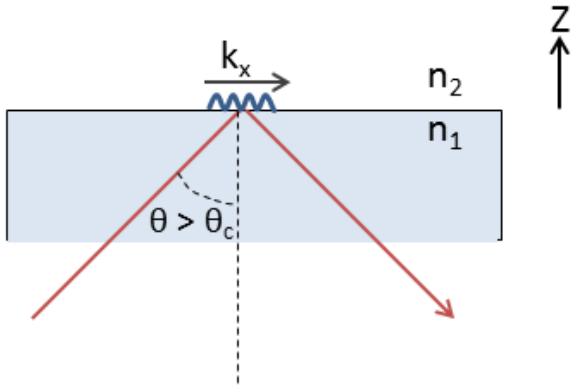

Figure 1.13: Total internal reflection scheme where an evanescent wave propagates parallel to the interface.

a) Total internal reflection

Total internal reflection occurs in a medium 1 denser than medium 2, when the incident angle (θ_i) exceeds the value of the critical angle (θ_c) defined as:

$$\sin(\theta_c) = \frac{n_2}{n_1} \tag{1.20}$$

where n_i is the refractive index in the medium i, and $n_1 > n_2$. From the Snell-Descartes relation the transmitted angle $\sin(\theta_t) = \frac{n_1 \sin(\theta_i)}{n_2}$. When θ_i reaches the critical value θ_c the transmitted angle θ_t tends towards 90° and the light beam propagates along the boundary surface.

From Maxwell's equations it is possible to deduce the electric field. If v_i is the velocity of the electromagnetic wave in the medium i, we obtain:

$$\mathbf{E(x,z)} = \mathbf{E_0} \exp -\mathbf{i}\omega \left(\mathbf{t} - \frac{\mathbf{x} \sin \theta_\mathbf{i}}{\mathbf{v_1}} \right) \mathbf{exp} - \frac{\omega \mathbf{z}}{\mathbf{v_2}} \sqrt{\frac{\mathbf{n_2 sin^2 \theta_i}}{\mathbf{n_1}} - \mathbf{1}} \tag{1.21}$$

In addition from Fresnel's formulae we find that the total reflected components equal to the incident components. This means that no energy is lost during the reflection process. Hence, the field lying on the boundary between the two media does not propagate, it oscillates harmonically without any energy flow and it vanishes rapidly in the z direction over a distance of a few hundreds of nanometers. However, the energy conservation is broken when some scattering centers are present at the interface.

The non-propagating character of the evanescent wave is somewhat disconcerting because the only way to detect the evanescent field consist in converting this field into a propagating one. Therefore, equation 1.21 is no longer fulfilled and the detector must be taken into account in the electromagnetic interaction. Although in certain cases it is possible to ignore the coupling between the collector/emitter and the sample.

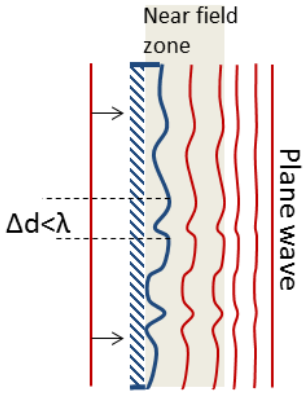

Figure 1.14: Interaction of a plane wave with a sub-wavelength structure. The field is perturbed in the near-field zone, while in the far-field it is a plane wave similar to the incident wave.

b) Sub-wavelength diffraction

We have seen that in the case of total internal reflection, it is possible to generate an evanescent wave for angles above a critical angle. In a similar way in the case of diffraction a non propagating field can be formed when the half angle of diffraction reaches 90°.

A plane wave intercepted by a sub-wavelength structure will be strongly perturbed in the vicinity of the structure, but the light beam after a few nanometers will be reconstructed in such a way that the emerging wave will be a plane wave as shown in figure 1.14. Any field distribution characterized by details smaller than the incident light wavelength will be expanded into propagating and evanescent waves. The amount of evanescent waves depends on the amount of details smaller than λ. The weight of the evanescent contribution depends on the size (Δd) and the nature of the dispersive objects. The smaller $\Delta d/\lambda$ is the bigger the evanescent contribution is.

c) Surface Plasmon Resonance

A surface plasmon polariton (SPP)is an electro-magnetic wave propagating along a metal-insulating surface. Optical excitation of the SPP can be achieved using the Kretschmann configuration (figure 1.15), where p-polarised, collimated light beam undergoes total internal reflection at a dielectric/metal/dielectric interface. The magnitude of the wave vector of the SPP (k_{SPP}) is related to the dielectric constants of both the medium 2 and the gold film. For non-absorbing media, the dielectric constant equals the square of the refractive index, $\epsilon = n^2$, where ϵ is the dielectric constant and n is the refractive index. Therefore, k_{SPP} is defined as:

$$k_{SPP} = \frac{2\pi}{\lambda}\sqrt{\frac{n_2^2 n_m^2}{n_2^2 + n_m^2}} \tag{1.22}$$

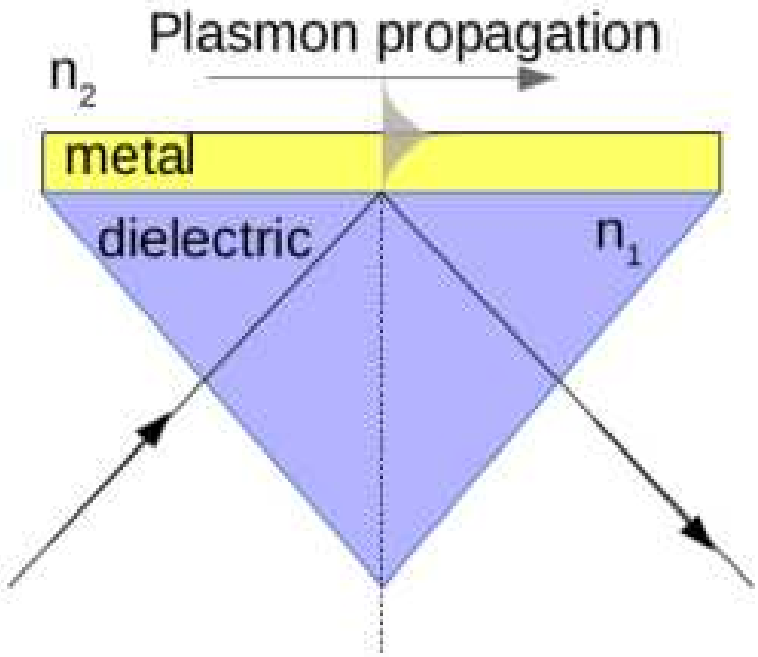

Figure 1.15: Kretschmann's configuration for generating surface plasmons.

where n_2 is the refractive index of medium 2 at the vicinity of the interface and n_m is the refractive index of the metal thin film.

When the surface plasmon is non radiative, the solutions of the Maxwell's equations are non-homogeneus. Then, the surface plasmon can be excited by the evanescent waves and this phenomenon is called surface plasmon resonance (SPR). When a gold film with suitable thickness is placed at the interface, the evanescent wave is enhanced, penetrating the gold film and existing in the medium 2. The magnitude of the parallel wave vector of the evanescent wave, k_{ew}, is expressed as:

$$k_{ew} = \frac{2\pi}{\lambda} n_1 \sin(\theta) \tag{1.23}$$

where n_1 is the refractive index of the prism.The angle at which the resonance occurs is obtained when $k_{SP} = k_{ew}$ and is extremely sensitive to any change in n_2 when n_1 and n_m are fixed. Therefore, the monitoring of the resonance peak angle θ_{SPR} can be used to analyze any change in the refractive index of media 2.

Thanks to its high spatial resolution NSOM has become an interesting tool to study the surface plasmon resonance of gold nanowires, nanopatterns, etc [147–150]

1.2.2.2 Main Near-field Microscope Configurations

The evanescent waves can not be detected by the objective of a classical microscope, since they decay exponentially in the z direction. The variations of the field in the

immediate vicinity of the object have to be collected to achieve subwavelength resolution. The collection is achieved by transforming the evanescent waves into propagating ones. Evanescent waves can be converted to propagating radiation by local scattering. The smaller the scatterer is and the closer it is placed near the surface of an object the better the conversion will be. This is why the invention of SPMs was essential in the development of near-field optical microscopy.

According to Babinet's principle [143], the diffraction pattern from an opaque body is identical to that from a hole of the same size and shape. This means that the small details of an object can be accessed by either scattering the evanescent fields created by the object with a small scattering center or by illuminating the object with evanescent fields created by a local source. Both process lead to similar results although they are phenomenologically different.

In NSOM the optical interaction between probe and sample is confined in a small (subwavelength) volume. Thanks to Babinet's principle many experimental configurations can be employed to obtain near-field information of the sample. The probe can be used either as a source and/or as a detector of evanescent waves. NSOM set-ups are usually divided in two categories:

- Apertureless NSOM: They use metal tips usually made of tungsten or gold. They locally scatter the evanescent waves and the near-field information is discriminated from the far-field signal using specific detection systems, such as lock-in amplifiers. In some cases it is even possible to benefit from the enhancement of the electric field created by plasmon resonance and/or antenna effects close to a sharp metal tip under laser illumination.

- Apertured NSOM: They use optical fiber tips with an aperture whose diameter is smaller than the used wavelength. A metal coating is used to prevent the light to spread out of the fiber. These sources can be used as local scatterers or as nanosources of evanescent waves. Their guiding properties allow to control polarization which is helpful in the interpretation of data.

Since in this work we only used apertured tips, we will only discuss apertured NSOM configurations. The most common ones are shown in figure 1.16.

It is possible to work in transmission (figure 1.16 a-c) or in reflection (figure 1.16 d-e), exciting with the tip and collecting in far-field (figure 1.16 a,d), illuminating from far-field with standard optics and collecting light with the tip (figure 1.16 b, e), exciting and detecting with the tip (figure 1.16 d) or using total internal reflection (figure 1.16 f).

It is important to remark that illuminating the object with evanescent waves created by total internal reflection (TIR) drastically reduces the background far-field light. This technique emphasizes the fact that a near-field probe frustrates the evanescent field.

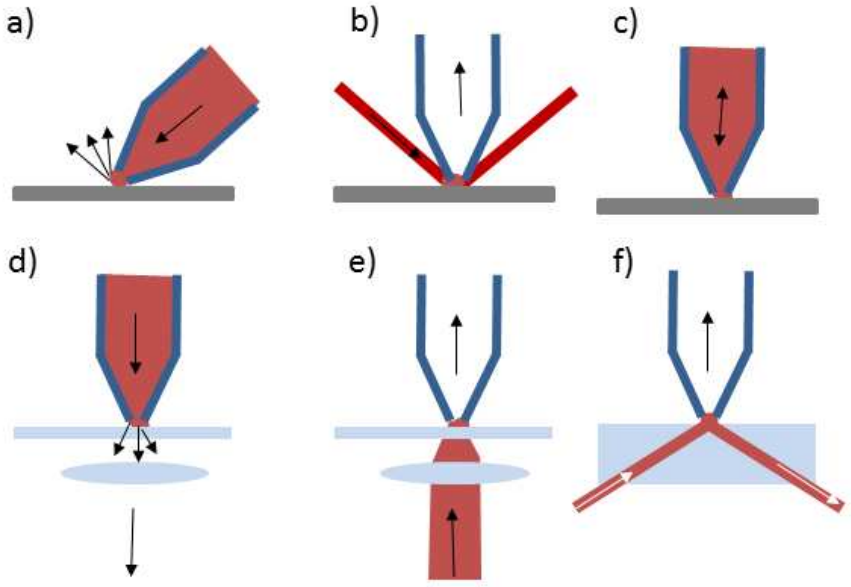

Figure 1.16: Different NSOM configurations in reflection (a-c) and transmission (d-f). Exciting with the tip and collecting in far-field (a, d), illuminating from far-field with standard optics and detecting with the tip (b,e), exciting and detecting with the tip c) or using total internal reflection f)

Chapter 2

Near-field Scanning Optical Microscopy (NSOM)

As mentioned in section 1.1, the SCO phenomenon is accompanied with a change of the optical properties of the material.

For example, the change of the electronic configuration of the SCO compounds between the HS and the LS states leads to a change of the absorption spectra. In fact the spin state changes can be followed by the metal-centered d-d (ligand -field) transitions positioned in the visible and the near infrared or by the charge transfer bands usually located in the ultra violet [46]. Nevertheless absorbance changes accompanying the SCO can be hampered by the weak oscillator strengths of the electronic transitions [151]. One way to enhance the optical contrast between the two spin states can be achieved through luminescent doping. In this case, the luminophore must be selected in such a way that its luminescence is selectively quenched in only a given spin state due to a radiative or resonant energy transfer process [9].

SCO materials exhibit also an important change in the real part of the complex refractive index ($n^* = n + ik$) through the whole UV-vis-IR spectral ranges primarily due to the mass density change accompanying the SCO phenomenon. The volume of the octahedron defined by the six bonding nitrogen atoms around the iron(II) ion is typically 25-30% higher in the HS state leading to a unit cell expansion $\Delta V_{HL}/V$ usually between 1 and 10%, depending on the nature of the compound. As a consequence of this significant density change, one should expect a variation of the real part of the refractive index, upon SCO, in the range between $\Delta n_{HL} = 0.01 - 0.1$. In addition to this material density change, one shall consider the change of the electronic polarizability of the complex. This effect will be particularly important for wavelengths in the vicinity of intense charge transfer transitions [151]. The change of the refractive index during the SCO phenomenon have already been analyzed using optical diffraction [2, 152], ellipsometry [2] and surface plasmon resonance spectroscopy [6, 106]. However, the spatial resolution that can be

achieved through these methods is limited by the wavelength of the light. To overcome this problem, our team has explored the use of NSOM to detect the spin crossover with sub-wavelength spatial resolution on singe crystals [93]. Here, we extended our efforts to the SCO detection on thin films.

NSOM studies can be performed in transmission and in reflectivity configurations (see section 1.2.2 for more details). The change in the real part of the refractive index suggests that the reflection configurations might be very promising. On the other hand, the observation of the spin transition phenomenon using transmission configurations could be very challenging due to the low optical density of the material and thus limiting the type of samples and experimental set-ups that can be used.

In the first part of this chapter we present the instrumentation we used and an original methodology we developed for temperature dependent SPM measurements. Then, fluorescence and reflectivity data obtained using NSOM on fluorescent SCO thin films at different temperatures are analyzed.

2.1 Instrumentation

A Nanonics Multiview 2000^{TM} system was used to perform simultaneous AFM topography (AC mode) as well as near-field (NSOM) and far-field optical imaging thanks to the excellent coupling between the AFM and the optics in this instrument. This system includes two piezo scanners which allow to perform either sample scanning or tip scanning, by moving either the sample or the probe in the x, y and z directions. This gives flexibility for using a wide range of possible configurations. In our instrument, the AFM is located inside an environmental chamber that allows to work under vacuum or a controlled atmosphere. The temperature of the sample can be controlled either with a thermoelectrical heating-cooling stage (temperature range from 253 K to 353 K) or with a resistive heating stage (from room temperature to 473 K). Additionally, it is fully integrated with an upright and an inverted (Olympus) optical microscopes. The ensemble of the system is placed on an active vibrational isolation table and we have also fabricated an acoustic enclosure around it using a specific phonic isolation foam (SE50 from the company Solutions Elastomères). This enclosure serves also to isolate the system from external light sources.

In the optical measurements (near-field or far-field) light is collected with a Mitutoyo objective (either 20x magnification and numerical aperture N.A.=0.42 or 50x magnification and N.A.=0.55) and it is sent to a high sensitivity CCD camera (Andor Technology Clara) and/or a photomultiplier tube (MP900 from Perkin Elmer), which can be used independently. Different filters and accessories can be easily integrated to the microscope depending on the experiment. One thing that makes this microscope unique is that it is

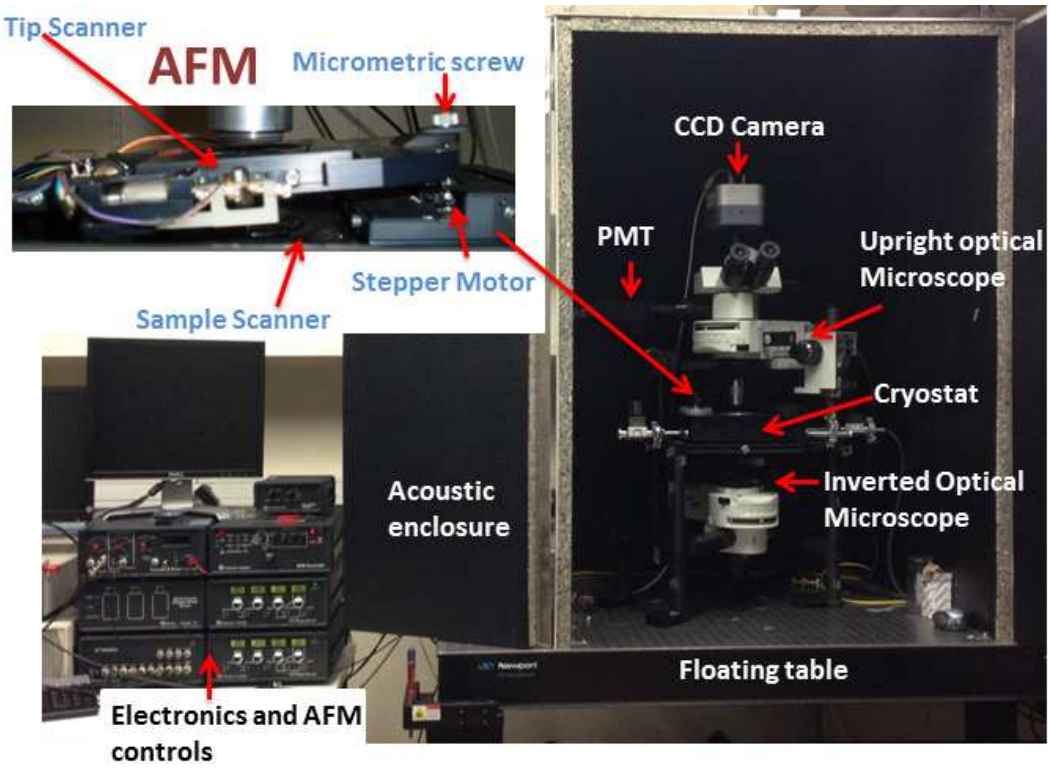

Figure 2.1: Nanonics Multiview 2000 atomic force microscope at the LCC-CNRS.

optically an open system. The tips are made of a bent fiber of glass or fused silica (see figure 2.2). The architecture of this instrument is conceived in such a way that the optical path from the sample to the detectors is not obstructed either by the probe or the SPM detection system. As a consequence, the optical access to the sample remains excellent in both transmission and reflection modes even when the tip is engaged.

This microscope uses a tuning fork instead of a beam deflection system. Hence, this AFM works only in AC mode. The probe is mounted on a tuning fork which is excited by an AC voltage near its resonant frequency; the oscillations are then sensed with a electrical detection scheme [153]. Contrary to beam deflection systems, in tuning fork systems there is no optical perturbation due to an additional laser signal, they present higher amplitude and phase sensitivities and a higher mechanical quality factor Q, which allows a better control of the system.

NSOM tips consist of a bent silica optical fiber (length $\approx$ 3 m) which is coated with Cu and Au. Therefore, light can be transmitted to the aperture with the same efficiencies and polarization properties as those of conventional, straight near-field optical elements. In this work tips with an aperture of $\approx$ 200 nm were used, unless otherwise mentioned. This relatively large aperture reduces the achievable optical resolution, but allows to collect more signal. The quality factor of the probes we used varied between 400 and 1900, the frequency of resonance was $\approx$ 33 kHz, the length of the tip was between

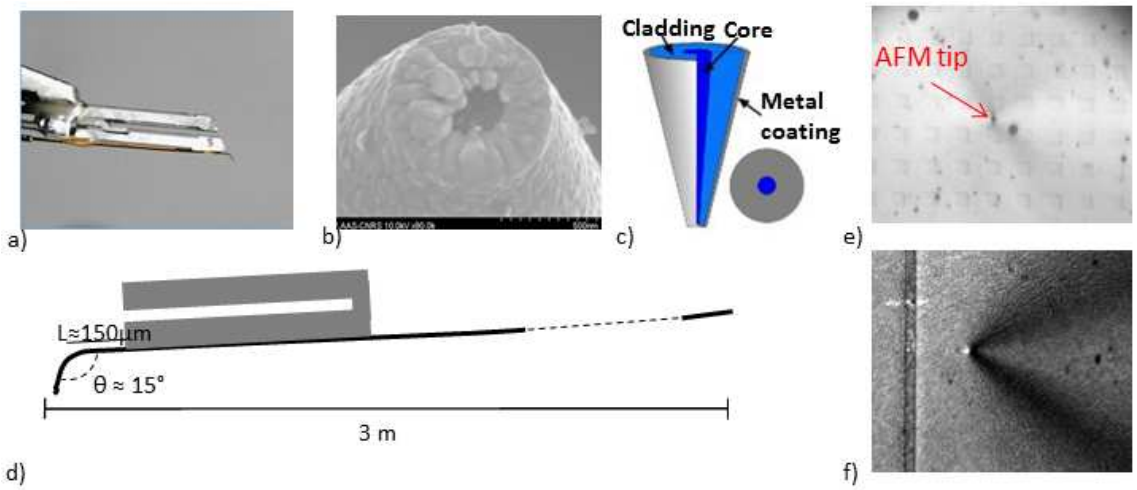

Figure 2.2: a) Photograph of a fiber tip glued to a tuning fork cantilever. b) Scanning electron microscope image of the very apex of the tip, showing a circular hole of around 200 nm. c) Scheme of the fiber tip and its coating. d) Scheme of a fiber tip mounted on a tuning fork. Optical images of e) an AFM tip engaged on a Si surface and f) and NSOM tip engaged to a sample.

150 - 300 μm, the length of the fiber was $\approx$ 3 m, the angle of the bending was ca. 15-20 degrees.

A blue line (488 nm) of an argon laser (Melles Griot) was coupled to a multimode fiber using an Olympus objective lens (20x magnification and N.A. = 0.4). At the end of the multimode fiber a series of lenses (collimation package F810FC from Thorlabs) helps to collimate the light and then it is injected to the tip fiber using an Olympus objective lens (4x magnification, N.A.=0.1). The multimode fiber allows us to place the laser on a separated table, reducing the propagation of mechanical vibrations to the AFM table. In certain cases, the continuous (CW) laser beam was modulated by a mechanical chopper (SR540, Stanford Research Systems) which allowed us to put in place a synchronized detection using a lock-in amplifier (720 DSP, EG&G Instruments). This detection scheme is used to improve the signal to noise ratio. The lock-in amplifier can be also used to achieve synchronization with the oscillating tip in order to better separate the near-field contribution from the far-field. Nevertheless, for our set-up this latter approach gave rarely a satisfactory signal.

Before performing any AFM-NSOM experiments, it is important to calibrate the piezos using a characterization grid, assure that the table is floating and reduce any source of vibration like suspended cables or other instruments. Check that all the different parts are well fixed (i.e. microscope, probe, probe holder, upper scanner, etc.). Each time a new tip is mounted, it is necessary to check that a good connection is achieved between the probe and the instrument (i.e. the measured quality factor should be near the one given by the manufacturer) and verify the integrity of the tip using optical microscopy.

The error signal before the tip engage should be between 0.2 and 0.3. If the engage is well done, this value reduces to ≈0.01. In NSOM experiments the fiber should be placed in such a way that it bends the less abruptly possible to avoid loose of power at the end of the tip. The maximum laser power that can be used without melting the tip is 15 mW. The laser aligment can be done using the CCD camera to determine the point when the maximum light intensity exits the fiber[1]. It is important to remark that any vibration of the fiber will certainly affect output power at the end of the NSOM tip due to losses when the fiber is deformed. Thus, during an NSOM measurement, the whole body of the fiber must be fixed to a surface in order to avoid artifacts in the detected signal.

2.2 Methodology

Up to now there is only one NSOM study that has been done on SCO compounds [93] and generally speaking NSOM studies on phase change materials are scarce as well. While a few qualitative investigations have been reported in the literature [154], quantitative NSOM imaging across a phase transition remains a challenge. Of course it is essential to avoid topography artifacts and separate the near-field from the far-field contribution as much as possible (see appendix A). In our case, further complications arise since images are acquired during the thermal cycling of the sample. In general, changing the temperature leads to rotations and translations of the sample due to thermal expansion and even due to the spin transition itself. In addition the properties of the probe (spring constant, size, resonance frequency, etc.) evolve also with temperature (see section 4.3.1). Independently of the temperature change, the mere fact that in most of our experiments we need to perform several tens of successive scans in a quantitative manner is a considerable technical challenge for most SPM modes because both the sample and the tip can suffer unwanted degradation. For these reasons, the simultaneous detection of the spin crossover by other means is necessary to determine whether the changes observed by SPM do not come from other phenomena. As mentioned above, the SCO phenomenon involves a drastical change of optical properties; hence, probably the most convenient way to follow the spin transition during an SPM experiment is provided by far-field optical microscopy. The AFM-optical coupling in the Nanonics system allows to capture near-field and far-field signals at the same time with great flexibility. In this thesis we used several far-field optical configurations such as luminescence microscopy and bright field microscopy (both in reflection and transmission modes) to infer the spin state of the sample in-situ during the SPM measurements.

Whenever it is necessary to compare several images in a quantitative manner while

[1] As the fiber is moved in front of the laser beam, it becomes brighter, this means that the laser is entering in the border of the fiber and that the coupling is not well done.

working with NSOM or any other SPM it is convenient to have a reference area in the scan zone that is not expected to change. This reference area can give us information about the tip wear or tip-sample interaction changes. This could allow us to correct the data in a reliable manner and assure a better interpretation of our results. However, while using conventional SPM heater or cooler devices it is almost impossible to achieve such reference area since the entire image is affected by thermal effects. In order to overcome this problem, we implemented an original strategy wherein we change the sample temperature only in a small area. This was achieved by means of a Joule heated metallic nanowire. In the next section we discuss in more details this nanoheater approach, which we developed in collaboration with Christian Bergaud (LAAS-CNRS, Toulouse).

2.2.1 Nanowires for Heating Purposes

Metallic wires can be heated using an electrical current as it is described by Joule's laws of heating. In particular, nanowires can be heated using a low electrical current flow due to their low dimensions and low heat capacitance. For the same reasons, the temporal response of the nanowires can be very high. For example, in the case of the nanowire devices used in this thesis, the steady-state temperature can be reached within a few hundreds of nanoseconds (Figure 2.3). Fast heating is an interesting feature when it is combined with an AFM, since it becomes possible to change the temperature (i.e. applied current) in a controlled manner between two scan lines. A further interesting asset of the nanowire heater is that the ΔT can be confined in a very small volume - using an appropriate design. For instance, while using identical nanowires, the heated area is much smaller on silicon than on glass substrates due to the significantly higher thermal conductivity of silicon. Figure 2.3 b shows a finite elements simulation of a gold microwire heater on a silicon substrate. It can be seen that the induced ΔT is tightly confined to the wire and the temperature distribution is very homogeneous along its long axis. This means that only a few micrometers away from the wire the sample temperature remains unaffected and this sample area can be used as a reference zone in each scan. In addition, contrary to the usual heating stages proposed by AFM manufacturers, such nanowire heaters do not induce any discernible thermal drift of the sample and the properties of the AFM tip can remain nearly unaffected by the sample temperature changes (depending on the experimental details). Since the heated area is very small any convection effect due to a difference of temperature between the heater and the probe or the probe holder is minimized.

The thermal design of these heating elements is a critical step. The performance of a heating platform is largely dependent not only on the size of the system, but also on the materials used and the geometry of the different components.

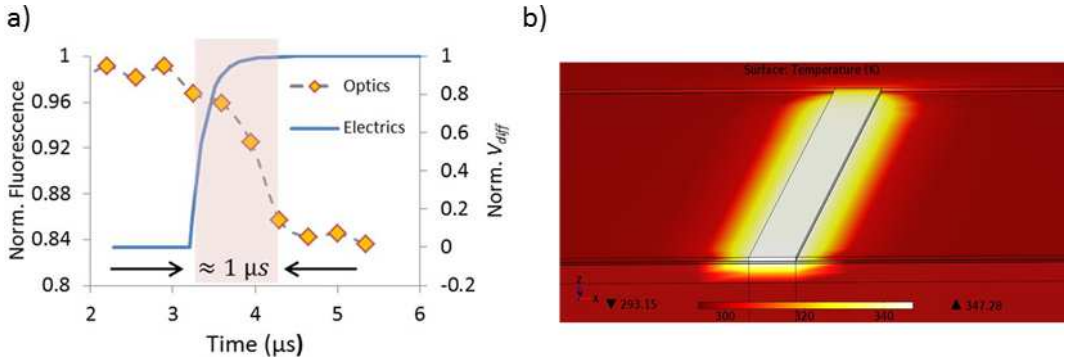

Figure 2.3: a) Electrical and optical transient heating response of a set of five gold nanowire heaters (thickness = 50 nm, width= 500 nm, length 80 μm) covered with a thin layer of Rhodamine B as function time. The response time of the nanowire is in the order of a few hundred nanoseconds [155]. b) COMSOL finite element simulation that shows the confinement of the heat of a nanowire (thickness = 50 nm, width = 1 μm and length = 80 μm) [156].

2.2.1.1 Nanowire fabrication

Gold micro- and nanowires were fabricated by Carlos Quintero at LAAS-CNRS on silicon and glass substrates either by stepper photolithography or by electron beam lithography (EBL) with subsequent metal deposition and lift-off process. An additional photolithography process is necessary to build micrometric electrodes that connect the nanowires to an external circuit.

The substrates used for Au nanowire fabrication were 500 μm thick glass or <100> p-type silicon wafers passivated with a SiO_2 layer (200-500 nm thick). Si wafers were cleaned using a Piranha solution that consists of a 1:3 mixture of H_2O_2 and H_2SO_4.

In the first method gold nanowires (length 40 μm, thickness 50 nm and width 0.5-1 μm) were fabricated by stepper photolithography with a subsequent metal deposition and lift-off process. A photo sensitive negative resist (NLOF) was spin coated and selectively exposed to UV radiation. Then, the sections that were not exposed to UV radiation are removed while immersing the wafer in the MIF20CD developer solution during 30 seconds. Here, the different designs of the wires are engraved into the resist in the form of cavities. Then, a Ti/Au metallization with a respective thickness of 10 nm / 40 nm was performed on the wafer. (The Ti layer works as an adhesive layer between the gold and SiO_2.) Last, a lift off in acetone medium is done in order to remove the remaining resist leaving only the metal that was in touch with the surface, i.e. the nanowires.

In the second method, 50 nm thick, 80 μm long and 500 nm or 1 μm wide gold wires were fabricated by means of electron beam lithography (EBL). A positive EBL resist layer (PMMA, Polymethylmethacrylate) was spin coated and then it was selectively exposed with a RAITH - 150 EBL writer. Here, a focused electron beam is used to pattern the nanowires on the PMMA film. The irradiated zones become soluble in a 1:3 solution

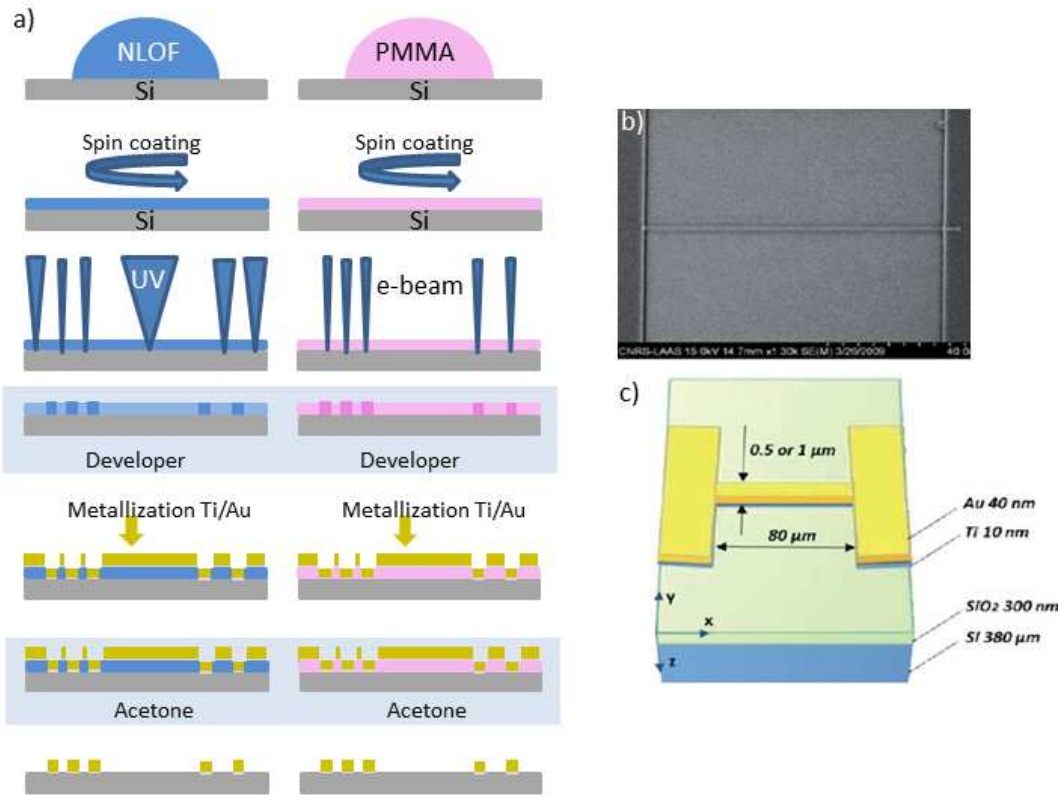

Figure 2.4: (a) Schematic steps of the fabrication process of the microwires and nanowires by e-beam lithography (right) and photolithography (left). Scanning Electron Microscopy image (b) and schematic drawing (c) of a 50nm x 1μm x 80 μm Au nanoheater device.

of MIBK (Methyl isobutyl ketone) and IPA (Isopropyl alcohol). After immersing the wafer in this solution, cavities with the form of the nanowires are created in the layer. Afterwards, a Ti/Au metallization with a respective thickness of 10 nm and 40 nm was performed. Finally, by means of a lift off process in acetone the resist is removed from the surface leaving only the metal that was in contact with the substrate.

In both cases the connecting gold pads and micrometric wires (thickness = 250 nm, width = 1-4 μm, length = 1 mm) were fabricated using standard photolithography.

2.2.1.2 Nanowire calibration

The temperature calibration of the gold nanowires was performed by combining two electrical measurements. First, the resistance of the wires was measured as a function of the temperature using a heating stage. Second, the resistance was measured as a function of the applied electrical current. Assuming that the resistance variation mainly comes from the change of the temperature in the nanowire, it is possible to relate the two measurements to obtain a calibration of the mean temperature of the wire as a function of the applied current and find the quadratic relationship that relates both of them (Figure

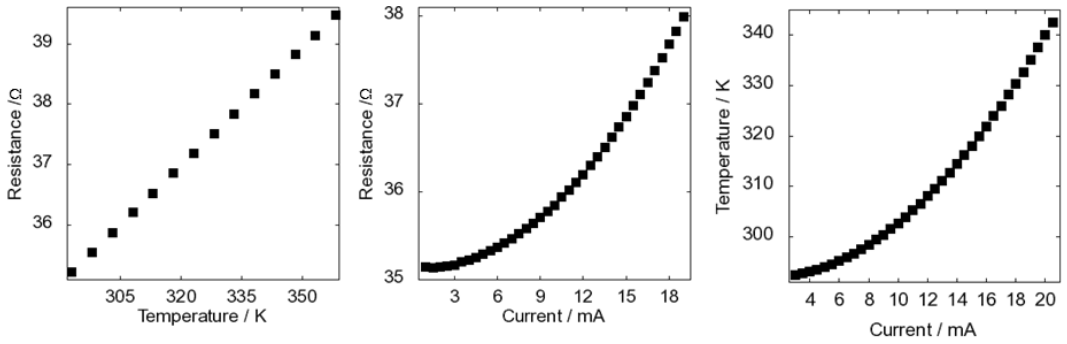

Figure 2.5: Characterization of a gold nanowire heater (thickness= 50 nm, width = 1 μ m, length 40 μm), a)Resistance as function of the temperature obtained by heating the substrate with a heating stage, b) Resistance as a function of the applied current, c) Mean temperature of the nanowire as a function of the applied current. This plot is obtained from a and b.

2.5).

2.2.2 Samples combining Spin Crossover and Luminescence

In the past few years, a few hybrid materials combining luminescence and spin crossover (SCO) properties have been reported in the literature with the aim of achieving luminescence signal modulation resulting from the spin state switching phenomenon [9]. Indeed, the SCO phenomenon involves very drastic changes in the electronic configuration and the crystal structure of the material. Thus, if a luminescent probe is introduced in the material, the changes accompanying the spin state switching can also affect the luminescent properties of the probe.

Luminescence can be modulated by changes in the density of the lattice or in the electronic configuration of the SCO material. In the first case, the mechanical coupling between the luminophore and the host lattice can affect both the wavelength and the intensity of the luminescence. A purely electronic coupling is also possible when there is a close match between the energy levels of the luminophore and those of the SCO compound in a given spin state. In other words, if the excitation or emission spectra of the luminophore overlaps with either the LS or the HS absorption spectrum of the SCO compound, a quenching of the luminescence occurs in that spin state [8].

While combining SCO with luminescence there are several important issues that must be taken into account. For instance, if the SCO center is too close to the luminophore the luminescence could be quenched in both spin states resulting in a non radiative compound. Furthermore, the luminophore should not be sensible to the stimuli which is used to trigger the spin transition. For example, in the case of thermal SCO the luminophore should not present an important thermal quenching in the temperature range of the SCO phenomenon. This way the changes in the luminescence can be related

directly to the spin transition.

In the literature, there are basically two synthetic strategies: (i) combining the luminophore and the SCO centers into a single entity or (ii) doping the SCO material with luminescent entities.

The first case can be achieved either by generating luminescent ligands or counterions. However, changing the SCO molecule to include a luminescent moiety may lead to the loss of one or both properties in an unpredictable manner. Another complication with this kind of systems is the high concentration of fluorescent centers which may result in self-quenching [2] and the loss of the luminescent signal in both states. Even though in an ideal condition one should have one luminophore for each SCO molecule to monitor the phenomenon, such situation could be detrimental for the overall luminescent response.

In the second case (doping), the luminophores are in uncertain positions of the lattice, therefore the interaction between SCO centers and luminophores is more difficult to elucidate. The luminophore is used as a structural probe, where only part of the SCO material is probed by some luminescent entities. Hence, the luminescent signal may not characterize the ensemble of the system. On the other hand, since the dopant is present in low quantities, the probability of altering spin transition properties decreases. Moreover, since each component is independent, the properties of one element can be modified without altering the other one.

2.2.2.1 $[Fe^{II}(hptrz)]_3(OTs)_2$ doped with Rhodamine 110

This hybrid material has been developed in our team and used as a test sample in many cases. Thin films are prepared by spin coating a chloroform solution of $[Fe^{II}(hptrz)_3](OTs)_2$ (hptrz=4-heptyl-1,2,4-triazole, OTs=tosylate) and Rhodamine 110 [9]. The resulting thin film is homogeneous (roughness, Ra $\approx$ 5 nm) and can be deposited on any surface. As shown in figure 2.6. The spin transition occurs not far from room temperature. For these reasons we identified this compound as a good candidate for SPM studies.

a) Synthesis

The compound was synthesized as described by Quintero et al. [9]. The mother solution of the complex was prepared by mixing two solutions; the 1st containing iron(II) tosylate hexahydrate (30 mg, 0.06 mmol, 1 equiv.) and p-toluenesulphonic acid monohydrate (4 mg, 0.02 mmol) in ethanol (150 μl) and the second containing 4-heptyl-1,2,4-triazole (60-100 mg, 0.36 mmol, 2 equiv.) in $CHCl_3$ (4 ml). For spin coating 50 μl of

[2] When the absorption and emission bands of the luminophore overlap there could be an energy transfer between luminophores and travel long distances without emission, witch ends in a loss of the luminescent signal.

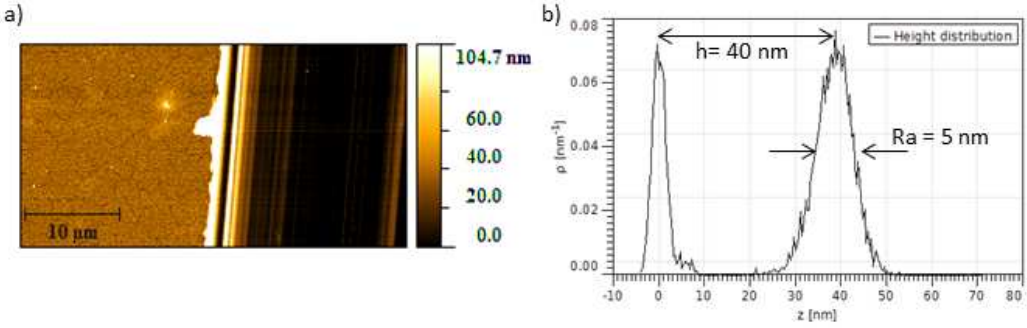

Figure 2.6: a)AFM image acquired around a scratch made on a thin film of $[Fe^{II}(hptrz)_3](OTs)_2$. b) Height histogram corresponding to the AFM image.

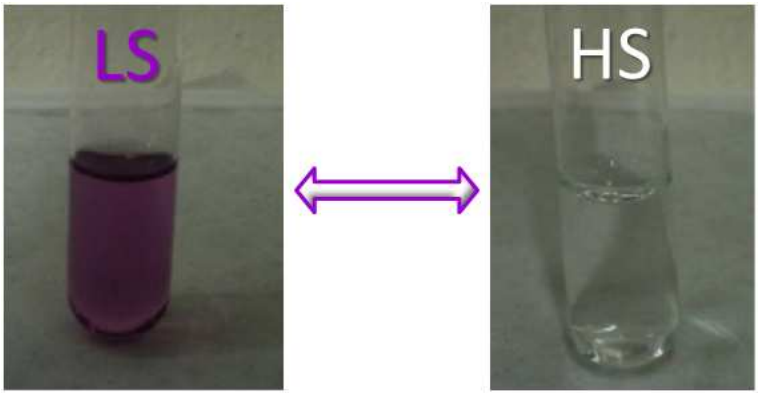

Figure 2.7: Photographs of undoped $[Fe(hptrz)_3](OTs)_2$ in chloroform solution in the low spin and high spin states.

the mother solution of the complex was mixed with 0.66 mM ethanol solution of rhodamine 110 (0.2% mol of luminophore per iron atom). Thin films of this compound were deposited on the substrates by spin coating the solution with the following parameters: speed = 5000 rpm, acceleration = 4000 rpm^2 and time = 30 s. Under these conditions the spin coated films measured ca. 80 nm thickness with a roughness of $\approx$ 5 nm, as shown in figure 2.6. Thicker films were obtained by increasing the amount of ligands in the mother solution.

b) Characterization

Un-doped $[Fe(hptrz)_3](OTs)_3$ in chloroform forms very small particles (6.5+/-2 nm) which remain stable for a few hours [151]. This solution is violet in the LS state and transparent in the HS state as shown in figure 2.7. The spin transition occurs near room temperature at $T_{1/2}^{\uparrow} \approx 315$ K on heating and $T_{1/2}^{\downarrow} \approx 307$ K on cooling, i.e. with a small hysteresis.

Figure 2.8 (a) shows the absorption spectra of the solution in the high spin and low spin states. In the LS state one can observe an absorption peak around 540 nm, which

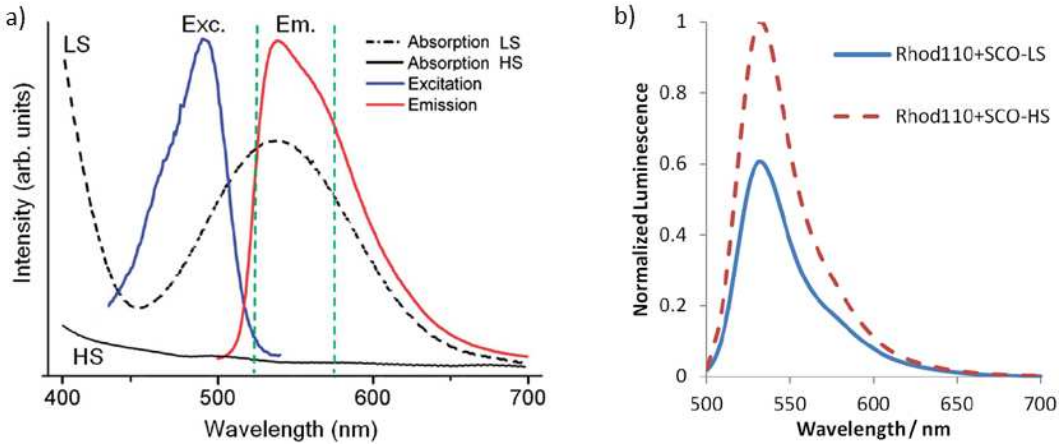

Figure 2.8: a) High spin and low spin absorption spectra of $[Fe^{II}(hptrz)_3](OTs)_2$ in the visible range[9] displayed together with the excitation and emission spectra of Rhodamine 110. b) Normalized luminescence spectra at 293 K (LS) and 315 K (HS) of a chlorophorm solution of $[Fe^{II}(hptrz)_3](OTs)_2$ doped with Rhodamine 110. (The sample was excited with blue light (450 nm) selected with a band pass filter.)

corresponds to the $^1A_1 \rightarrow ^1T_1$ transition. In the HS state the solution is completely transparent in the visible range. We have chosen Rhodamine 110 as a luminescent probe for two principal reasons. First, its emission peak overlaps perfectly with the LS absorption peak of $[Fe(hptrz)_3](OTs)_3$ (figure 2.8 a). Second, it does not present considerable thermal quenching in the range of temperatures that we are interested in. Figure 2.8 (b) displays the luminescence emission spectra recorded at 293 K (LS state) and at 315 K (HS state) for a $[Fe(hptrz)_3](OTs)_3$ chloroform solution doped with Rhodamine 110. An increase of the luminescence is observed when going from the LS to the HS state. The lower luminescence intensity in the LS state can be rationalized by an energy transfer from the excited luminophore to the LS complex.

Even though the optical density of these films is negligible in the visible range [9], they provide a considerable modulation of the luminescence due to spin transition. Figure 2.9 shows the thermal variation of the luminescence of this film monitored in far-field using conventional fluorescence microscopy in air or under N_2 atmosphere. The samples were cycled several times at a rate of 2 K/min from room temperature to 350 K. While going from the LS to the HS state, the fluorescence intensity increases in a rather abrupt manner. This observation corresponds closely to the results obtained with the sample in chloroform solution (Figure 2.9). Fluorescence is modulated as a function of the temperature due to a change of the spin state of the compound. The spin transition temperature shifts up to ten degrees depending on the atmosphere around the film. This phenomenon is well known in the literature: the more hydrated is the sample (i.e. ambient air), the higher is the transition temperature.

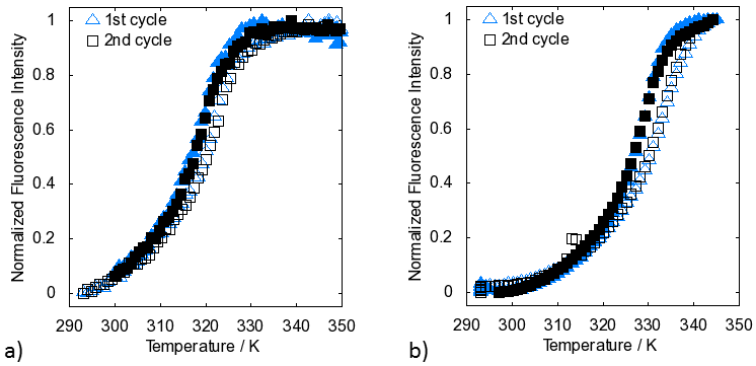

Figure 2.9: Fluorescence intensity as a function of temperature of a $[Fe(hptrz)_3](OTs)_2$ thin film doped with Rhodamine 110 (excitation at 450 nm and detection at 550 nm) recorded under N_2 (a) or in air (b) atmospheres during two successive thermal cycles. (Heating mode: open symbols, cooling mode: closed symbols.)

2.3 NSOM fluorescence

The first NSOM experiments on $[Fe^{II}(hptrz)]_3(OTs)_2$ were performed using fluorescent detection. The sample was irradiated with a blue line (488 nm) of an argon ion laser (Melles Griot) coupled to the tip fiber as mentioned in section 2.1. When the tip is near the sample, evanescent waves generated near the apex of the tip excite the fluorophores in a very small volume. The light emitted and reflected by the sample is then collected by a Mitutoyo objective (50x magnification, N.A.=0.55). Then, this light is filtered with a dichroic mirror (Semrock FF510-Di02) that reflects the light below 510 nm and a band pass filter centered at 550 nm (F1). The signal is then detected by a photomultiplier tube (PMT). As a protection, a Notch filter centered at 488 nm (F2) was placed in front of the photomultiplier tube (Figure 2.10). The laser intensity at the entrance of the NSOM fiber was varied between 1 and 7 mW depending on the fluorescence signal of the sample. NSOM scans were carried out while acquiring the AFM topography as well. The feedback signal was provided by the phase channel of the AFM.

Before and after each near-field scan we have systematically recorded a far-field fluorescence image of the sample as well. For far-field fluorescence measurements the microscope was equipped with a charge coupled device (CCD) camera. In this case the sample was excited using a halogen lamp and a band pass filter centered at 450 nm. The emitted photons were collected with the same 50x Mitutoyo objective and fluorescence was separated from the excitation light using the same filters as in NSOM.

Several factors that are not related to the spin transition can affect the luminescent intensity of the sample. For example, photobleaching, wear and contamination of the tip, etc. In thermal studies where several SPM scans have to be performed, a good reference area can help to compare different scans.

In a first approach we made a narrow scratch on a thin film ($\approx$ 150 nm) of

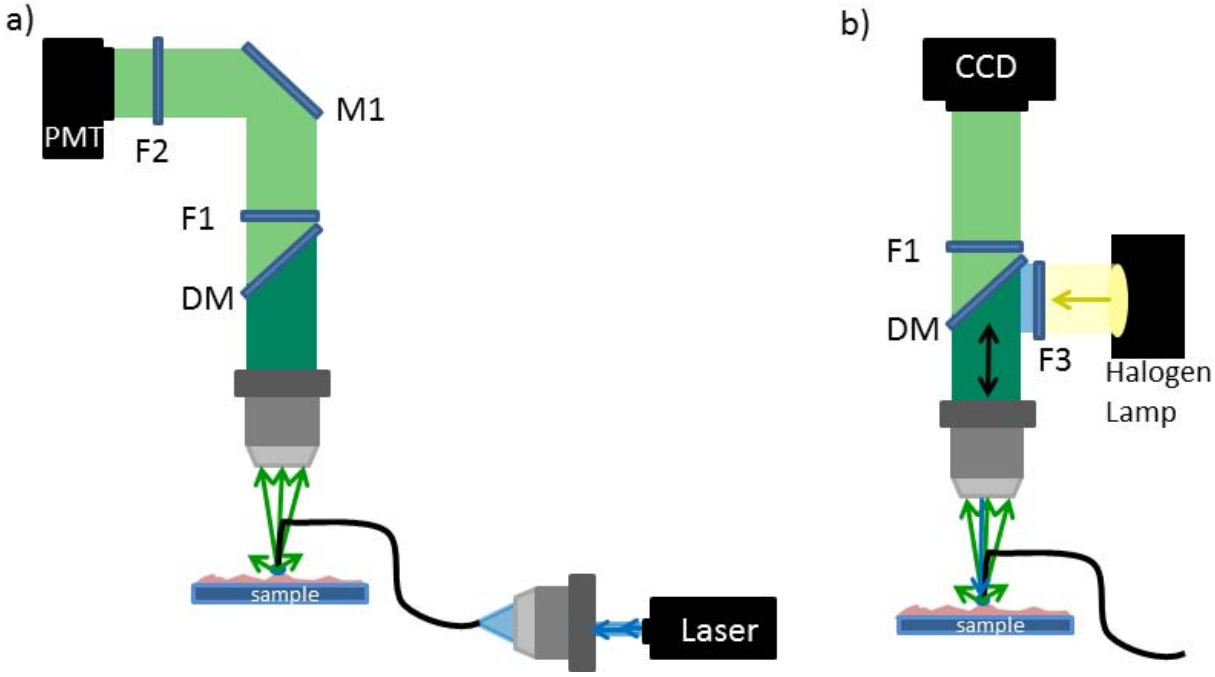

Figure 2.10: Experimental set-ups for obtaining the fluorescent signal in a) NSOM and b) far field. DM stands for dichroic mirror (510 nm), F1 for a band pass filter centered at 550 nm and F2 for a notch filter centered at 488 nm.

$Fe^{II}(hptrz)]_3(OTs)_2$ spin coated on a silicon substrate. The absence of fluorescent material in the scratch should be observed as a dark area in the NSOM image and it should have the same intensity in all the NSOM maps. In figure 2.11, an image of the topography of the thin layer obtained with an NSOM tip is presented. Each scan consists of 128 X 42 points acquired at a rate of 12 ms per point. Even though the tip aperture is relatively large ($\approx$ 200 nm) we can observe that the layer is constituted by grains which measure some hundreds of nanometers. After dehydrating the sample at 353 K for 30 min under nitrogen flux, successive scans were performed in nitrogen atmosphere at different temperatures. In panel c the average cross sections of the topography for different temperatures (from 293 K to 343 K) are presented. The topography does not show any significant variation, i.e. the volume change related to the spin transition. This is not surprising since the average unit cell parameter expansion in this compound is only around 1% [157]. As it can be observed in this figure, the stability of the topography signal in temperature dependent measurements is not enough to observe such small volume changes. Nevertheless we can consider that the reproducibility of the scans is quite satisfactory.

The laser intensity during these scans was decreased as much as possible to avoid laser induced destruction of the luminophores, i.e. to minimize the photobleaching. Nevertheless, to obtain a good signal to noise ratio allowing the observation of details in the sample, the intensity must be adjusted so as the PMT detects between 100 and 600 photons per second as shown in figure 2.11 b. In other words a compromise must be found

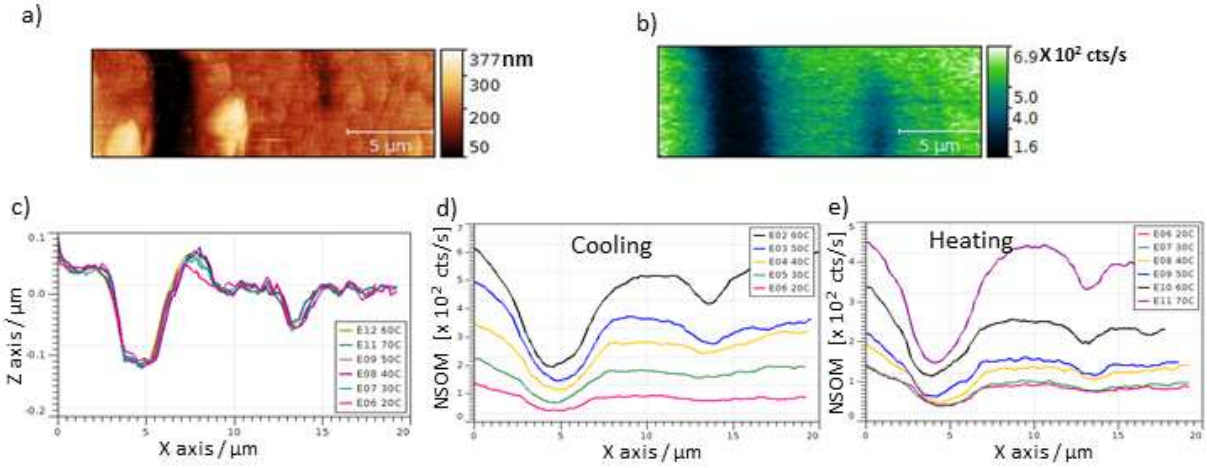

Figure 2.11: Simultaneous AFM topography and NSOM scans around a scratch made in a thin layer ($\approx$ 150 nm) of $[Fe^{II}(hptrz)]_3(OTs)_2$ spin coated on silicon. (The scratch appears as a black area in the images.) a) Topography, b) near-field fluorescence scan, c) cross section of topography at different temperatures. Cross section of near-field fluorescence signal at different temperatures while cooling (d) and heating (e).

between signal intensity and sample stability. Average cross sections of the NSOM maps at different temperatures are presented in panels d and e of figure 2.11 upon cooling and heating, respectively. As expected the fluorescence intensity increases at higher temperatures, which is the opposite phenomena of ordinary thermal quenching and thus we can tentatively attribute it to the spin transition in the sample. However, the fluorescence signal also changes in the scratched area. Assuming that the increase of fluorescence in this area is due to the pollution of the tip, more realistic values can be obtained by subtracting this "dark signal" from the signal of the sample at each temperature. The resulting fluorescence intensity is plotted as function of the temperature in figure 2.12.

Figure 2.12 shows also a far-field image at room temperature. The red square in this image indicates the zone scanned in near-field. In the NSOM map we observe some grains, that can not be resolved in the far-field image. In panel b a comparison of the fluorescence intensity between the near-field and far-field data as a function of the temperature is presented. Far-field data is plotted for both, the scanned area and another "virgin" area which was not scanned in near-field. While heating the sample from room temperature to 343 K, the fluorescence intensity in far-field increases quite monotonously, but the most important change seems to occur between 303 and 313 K. On cooling, the signal remains constant down to 313 K, then it decreases to its initial value at room temperature. A hysteresis between heating and cooling is observed. These results compare reasonably well with those shown in figure 2.9 and can be thus attributed to the spin transition of the sample. The difference between the far-field intensity in and out of the scanned area remains small through the whole temperature cycle. This

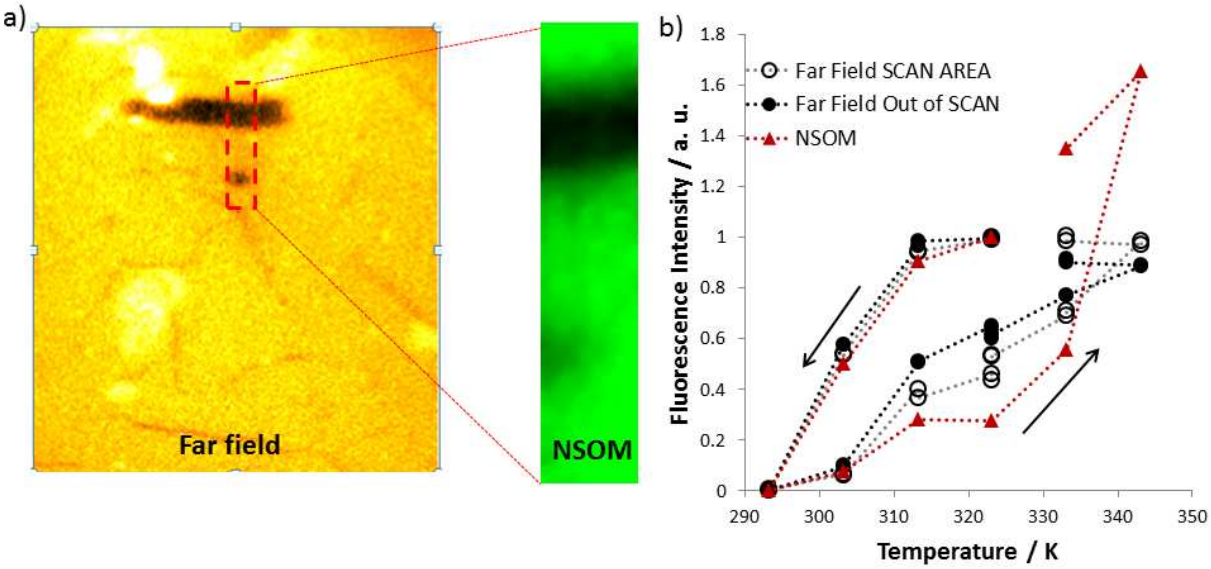

Figure 2.12: a) Fluorescence signal in far field and in near-field of a layer ($\approx$ 150 nm) of $[Fe^{II}(hptrz)]_3(OTs)_2$ spin coated on silicon. b) Fluorescence signal as function of temperature of the same layer in far-field and in near-field. Far-field data is plotted both for the scanned area (shown by the red rectangle in (a)) and another area which was not scanned in near-field.

observation as well as the reversibility of the signal indicates that photobleaching effects remain negligible in this experiment. There is also a fairly good correspondence between the temperature dependence of the far-field and near-field fluorescence signal, in particular at the beginning of the thermal cycle. At the end, the difference between near-field and far-field data increases considerably. This difference can be most probably associated to a change of the tip (wear, contamination, etc.). It should be noted that recording the complete thermal cycle, including 20 far-field and 10 near-field images, took approximately 7 hours. Despite these severe experimental constraints we can conclude that the spin transition is observable through the near-field fluorescence signal.

To further improve the measurement protocol, the use of a fluorescent reference area can help to discriminate different artifacts such as photobleaching or the change of the properties of the tip. In principle, the fluorescence signal intensity in the reference area will decrease if the laser photobleaches the sample, but the changes related to tip wear are less predictable. In any case the changes will be, at least partially, irreversible. As mentioned before, under certain conditions a metallic nanowire can heat a very localized area that can easily be surpassed in a single scan. Furthermore, the temperature of the nanowire stabilizes in less than a microsecond. This allows to change the current applied to the nanowire between two scan lines. In optimal conditions, i.e. if the substrate is well fixed, only one or two scans are needed to determine if the spin transition can be detected with a given experimental set-up.

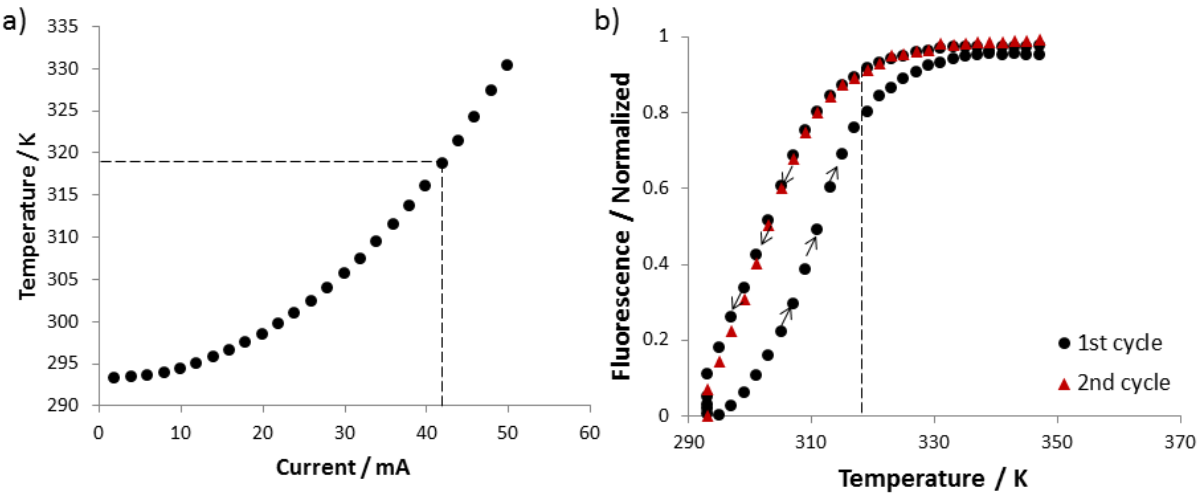

Figure 2.13: a) Temperature as function of the applied current of a gold microwire (thickness=250 nm, width=8 μm, length=1 mm) on glass substrate. b) Temperature dependence of the far-field fluorescence signal of a layer ($\approx$ 60 nm) of $[Fe^{II}(hptrz)]_3(OTs)_2$ spin coated on the microwire device. Heating and cooling modes are indicated by arrows.

To test these ideas, we have fabricated gold microwires on a glass substrate using the method presented in section 2.2.1.2. The temperature vs current characteristic of the device is shown in figure 2.13 (a). Then, a fresh solution of $[Fe(hptrz)]_3(OTs)_2$ doped with Rhodamine 110 was spin coated on the device. The fluorescence signal of this sample as a function of temperature (recorded in air) is shown in figure 2.13. Even though the SCO property of the sample is clearly inferred from this figure, the transition temperature differs somewhat from the one shown in figure 2.9. In this sample the spin transition is detected at $T^{\downarrow}_{1/2}$ = 303 K upon cooling and at $T^{\uparrow}_{1/2}$ = 312 K upon heating. This reproducibility problem with this sample is well known in the literature and it is probably related to its high sensitivity to humidity. Nevertheless, this issue does not represent a serious drawback for our experiments because we can continuously monitor the spin state of the system by far-field measurements. From the graphs shown in figure 2.13 we can determine that the current needed to trigger the complete spin transition is 42 mA.

The topography of the film of $[Fe^{II}(hptrz)]_3(OTs)_2$ spin coated on the microwire is shown in figure 2.14 a. The microwire, colored in yellow, is not centered in the image in order to be able to observe a large reference area within the scan. Similar to the previous sample, we observe a granular film with an average grain size of 250 nm. In panel b, the NSOM signal recorded at room temperature is presented. In NSOM configuration the light that arrives to the detector has been dispersed by the tip and by features in the topography of the sample. This artifact is particularly visible at the border of the microwire. It is also important to notice that the distribution of the luminescent probes in the sample is not uniform, since some areas are more luminescent than others and the

topography indicates that there is nearly the same amount of material everywhere on the wire.

In the next step we acquired AFM and NSOM images while applying different currents (2 mA and 42 mA) to the wire. From figure 2.13 we can infer that the sample is in the low spin (high spin) state at 2 (42) mA. The average cross sections of the topography and the NSOM signal in the two spin states are presented in figure 2.14 c and d, respectively. The topography is very well reproducible from one scan to the next and no significant effect of the spin transition can be detected. The NSOM average cross section shows some differences as shown in figure 2.14 d. We can make two important observations here. First, the fluorescence intensity of the sample on the wire is significantly higher in the high spin state in agreement with the far-field results. On the other hand, the signal intensity changes also far from the wire (more than 30 μm away) where the sample temperature and thus its spin state should be the same. We have therefore made an image treatment with the hypothesis that far from the wire the signal intensity is the same in each scan. Each cross section was thus divided by the average value obtained far from the wire. The result, shown in figure 2.14 e, is not satisfactory because scans recorded in the same conditions do not overlap. Different reasons, either related to the tip or to the sample degradation, can explain this observation. In order to reduce these problems, we decided to change the acquisition strategy and we changed the applied current during a single scan.

Figure 2.15 displays this type of scan where the current applied to the wire was successively switched between two values (2 mA and 42 mA) after 14 scan lines, which corresponds to ca. 5 μm. As result, a NSOM map with dark areas (low spin state) and bright areas (high spin state) was obtained (panel c). In panel d the cross section of the different areas corresponding to the two different current values is shown. Cold and neutral colors represent low current areas and warm colors represent high current areas. There is a very obvious increase of the luminescence on and around the wire when the high current is applied. Unfortunately, the inhomogeneity of the luminescence of the sample does not allow to make a more quantitative analysis based only on this image. However, by subtracting the NSOM image recorded in the LS state (figure 2.14 b) from the NSOM image presented in figure 2.15 c, we obtain an image which contains information only (or chiefly) about the effect of the current switching on the NSOM signal (figure 2.15 e). In panel f, the cross sections of the different areas corresponding to the two different current values are shown for this figure. As it can be expected the substraction for the zones with I = 2 mA (LS state) leads to values close to zero even if the error becomes non-negligible in the highly fluorescent part of the sample. On the other hand, the cross sections for the areas where I = 42 mA (HS state) reveal higher intensities on top and in the proximity of the wire while the difference tends towards zero when the tip moves away from the wire. This figure puts in evidence the spin transition in a repeatable manner

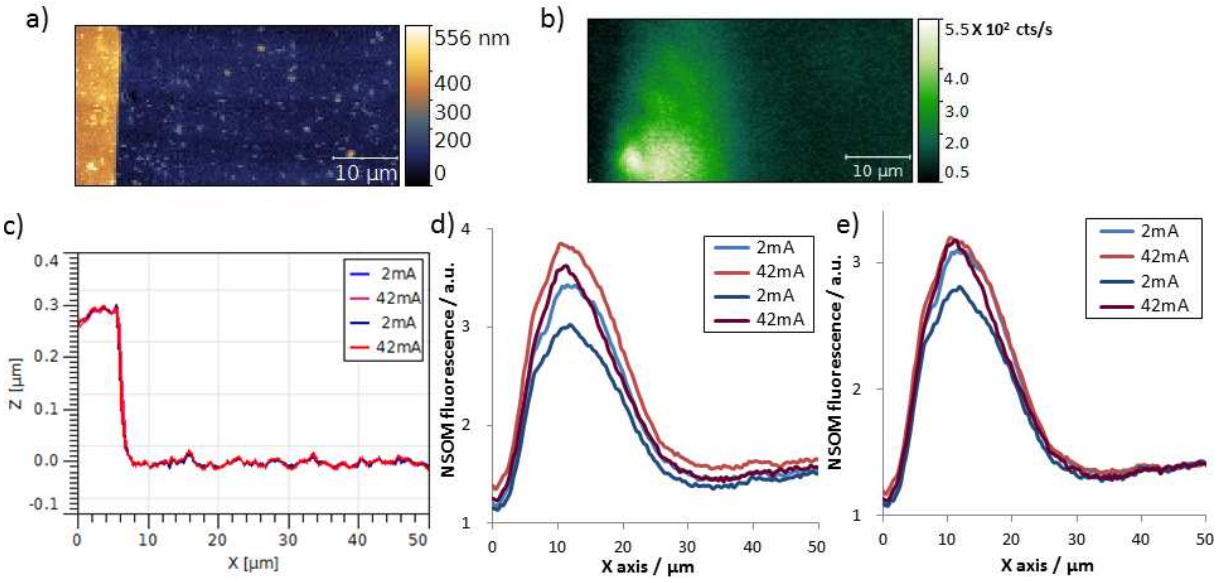

Figure 2.14: Room temperature topography (a) and NSOM fluorescence images (b) of a thin layer ($\approx$ 60 nm) of $[Fe^{II}(hptrz)]_3(OTs)_2$ spin coated on a gold microwire (thickness=250 nm, width=8 μm, length=1 mm, glass substrate). Images were recorded without any applied bias on the wire. Average cross sections of c) topography, d) NSOM fluorescence signal and e) corrected NSOM signal for successive scans performed by applying different currents (2 and 42 mA) on the wire.

in the area heated by the wire. It shows also that far form the wires there is no spin transition. We can conclude therefore that NSOM fluorescence can be used to detect the spin transition. On the other hand, it is practically impossible to transform the NSOM fluorescence intensity image into a high spin fraction image for two reasons. First of all, the intensities measured in different points of the sample can not be compared because the NSOM signal is strongly influenced by different parameters such as sample topography, the nature of the substrate, etc. This problem is particularly evident in our data when comparing the sample deposited on gold (i.e. the wire) or on glass. The second problem is photobleaching. When repeating several times the experiment shown in figure 2.15 the difference between the HS and LS signal intensity becomes smaller and smaller due to photobleaching. The far-field fluorescence image recorded after this experiment(figure 2.16) shows clearly that NSOM scans (i.e. the dark areas) produce severe photobleaching.

As stated above, the laser intensity was kept in all cases at the minimum intensity necessary to obtain an NSOM map. The use of other detection systems such as an avalanche photodiode with higher quantum efficiency might help to reduce the intensity of the laser and thus to reduce photobleaching. However, the signal to noise ratio is smaller in an avalanche photodiode than in a PMT, hence the small variations in the luminescence due to SCO phenomena could be more difficult to observe.

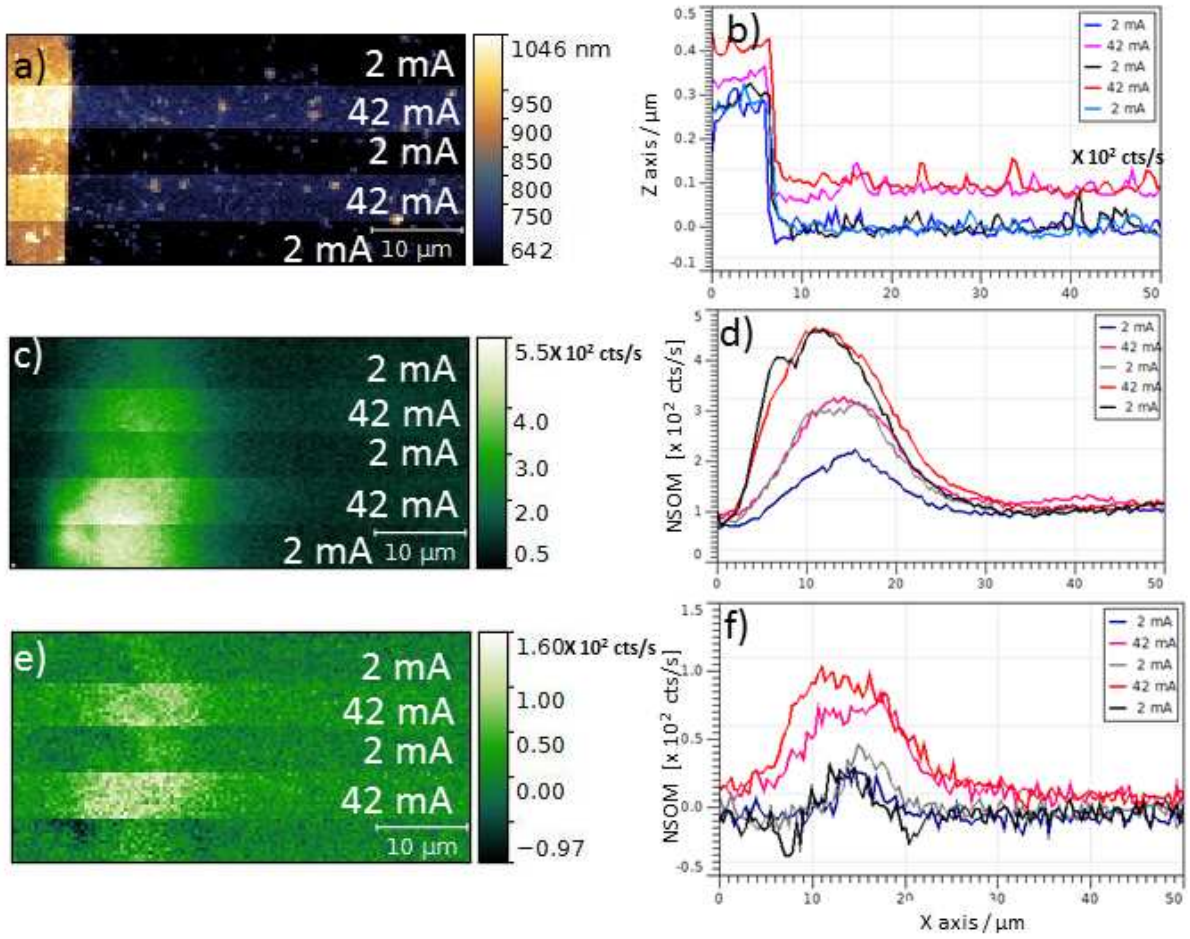

Figure 2.15: AFM topography (a) and NSOM fluorescence images (c) of a thin layer ($\approx$ 60 nm) of $[Fe^{II}(hptrz)]_3(OTs)_2$ spin coated on a gold microwire (thickness=250 nm, width=8 μm, length=1 mm, glass substrate). During image acquisition the current flowing in the wire was successively switched between 2 mA and 42 mA as indicated in the images. Cross sections of the scanned areas corresponding to the two different current values in the topography image (b) and in the NSOM fluorescence image (d). e) Corrected NSOM fluorescence image obtained by substracting the image in figure 2.14 b) from the NSOM image presented in figure 2.15 c. f) Cross sections of the scanned areas corresponding to the two different current values in the corrected NSOM image (e).

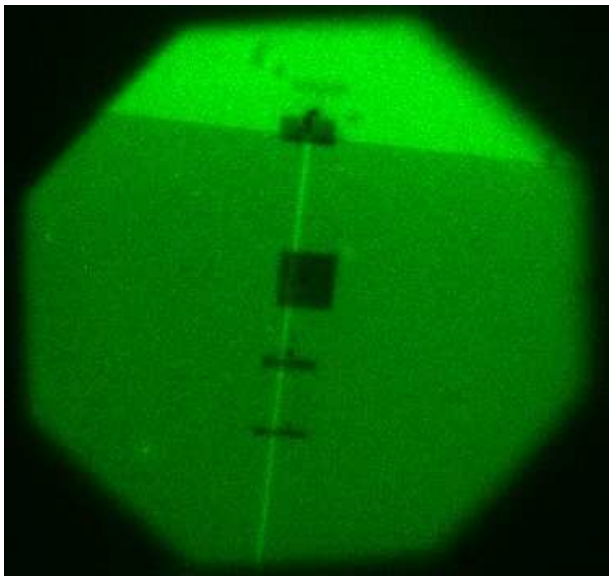

Figure 2.16: Far-field fluorescence image recorded following a series of NSOM scans in different parts of the sample around the gold wire. The black squares were produced by photobleaching while scanning the surface with the NSOM tip.

2.4 NSOM reflectivity

Opposed to fluorescence measurements, NSOM reflectivity experiments provide several advantages. First of all the higher photon counts are translated into a higher signal to noise ratio. This allows us to place several beam-splitters before the NSOM detector in order to carry out simultaneous far-field and near-field measurements as shown in figure 2.18. This is particularly important so as to control continuously the good focusing of the sample. The second important advantage is that photobleaching can be neglected in reflectivity measurements. The disadvantage is that the spin transition in thin films can not be easily detected in the far-field without the contrast enhancement provided by the luminescence.

In the case of nanometric thin films the change of the reflectivity signal due to the spin crossover is primarily related to the change of the real part of the refractive index (n). (I.e. the optical density of such thin films is negligible.) Figure 2.17 shows the variation of the real part of the refractive index as a function of the wavelength for the compound $[Fe(hptrz)]_3(OTs)_2$ as reported in [2]. The thermal variation of n (presented in figure 2.17 b) is virtually linear far from the spin transition as expected for ordinary thermal expansion. Around the spin transition n shows a discontinuity. The variation of the real part of the refractive index between the low spin and high spin states for $[Fe(hptrz)]_3(OTs)_2$) is $\Delta n_{HL} = 0.015$ ($\lambda = 660$ nm) [2]. We expect to observe a similar behavior using near-field scanning optical microscopy and a hysteresis should be also observed around 320 K. Since there are no singularities in the refractive index in the

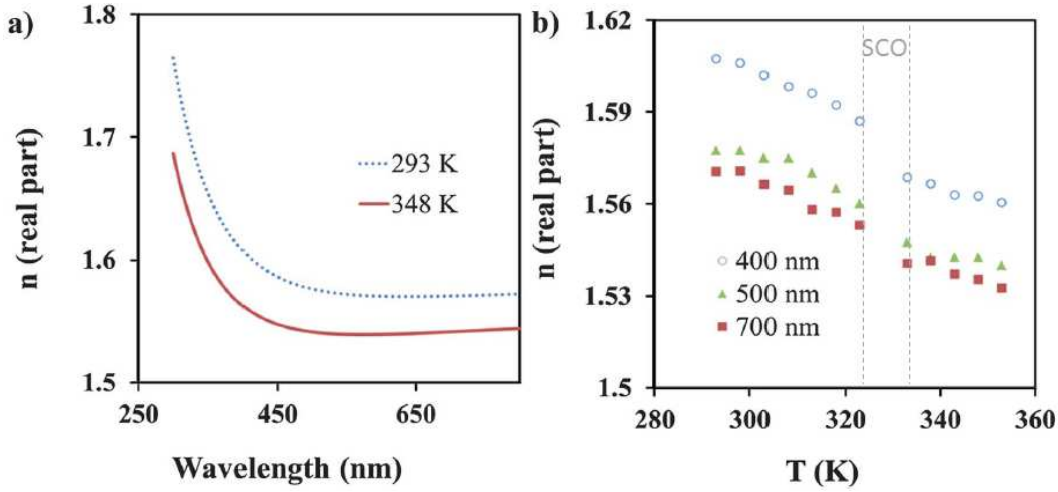

Figure 2.17: Spectroscopic ellipsometry results obtained on a thin layer (thickness = 80 nm) of $[Fe(hptrz)]_3(OTs)_2$): a) refractive index spectra recorded at 348 K (HS state) and at 293 K (LS state) in air and b) temperature dependence of the real part of the refractive index in the heating mode at different wavelengths [2].

visible wavelengths, any laser wavelength in the visible region can be used to excite the sample and observe the spin transition. In particular, we can use the blue ($\lambda = 488$ nm) argon laser line.

The set-up for NSOM reflectivity experiments (figure 2.18) is similar to the fluorescence configuration. For far-field reflectivity detection the sample is illuminated with blue light from a halogen lamp selected with a band pass filter (450 ± 22.5 nm). The light reflected by the sample is then detected by a CCD camera. For near-field reflectivity measurements, a blue line (488 nm) of an argon laser (Melles Griot) is coupled to the tip fiber as mentioned in section 2.1. The evanescent waves produced at the end of the tip are diffracted by the sample and collected by a Mitutoyo objective (20x magnification, N.A.=0.4). A beam splitter (50/50) sends the collected light to a band pass filter (500 ± 25 nm) to filter out the light from the halogen lamp. Finally the reflected laser light is detected by a PMT.

The reflectance of gold for wavelengths between 400 and 500 nm is below 40%, therefore when illuminated with blue light it provides a dark contrast on glass substrates, which was observed in both far-field and near-field configurations (figure 2.19 b and d, respectively). The dispersion effect produced by the edges of the nanowire is considerably diminished, which is important since we are interested in observing differences in intensity between the film deposited on the wire and on the substrate.

Figure 2.20 displays the AFM topography and NSOM reflectivity images of a thin layer (≈ 60 nm) of $[Fe^{II}(hptrz)]_3(OTs)_2$ spin coated on a gold microwire (thickness=250 nm, width=8 μm, length=1 mm). Similar to the strategy we used in NSOM fluorescence, the current applied to the wire was switched several times between 2 and 42 mA during

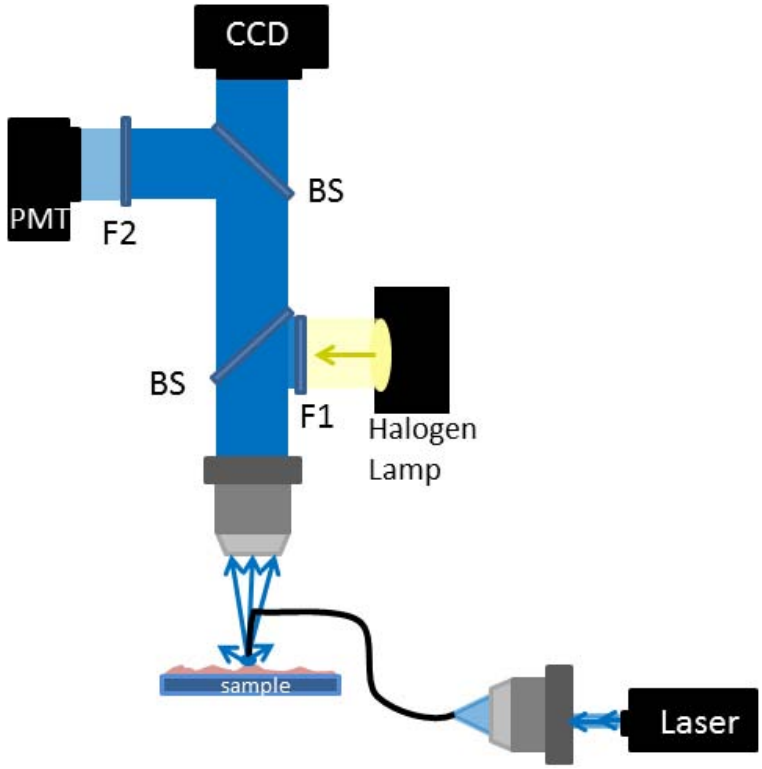

Figure 2.18: Experimental scheme of the NSOM reflectivity set-up with simultaneous near-field (PMT) and far-field (CCD) detection. F1 and F2 are band pass filters with a transmission window of 450±22.5 nm and 500 ±25 nm, respectively. BS stands for beam splitter.

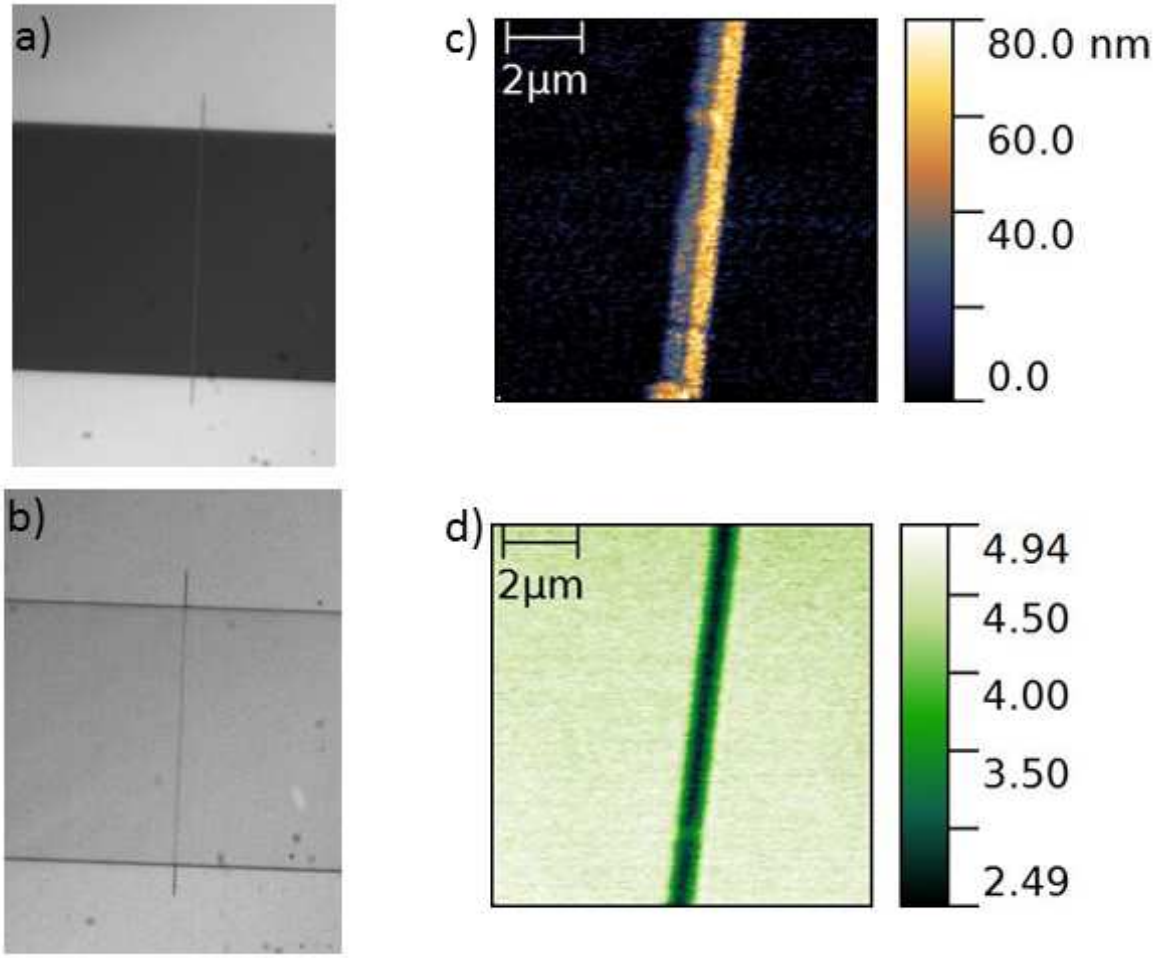

Figure 2.19: (a,b) Far-field reflectivity images of a gold nanowire (thickness = 50 nm, width = 1 μm length = 40 μm) on a glass substrate obtained using a) white light or b)blue light. (c, d) AFM-NSOM scan of a gold nanowire on a glass substrate: c) Topography, d) NSOM reflectivity (488 nm).

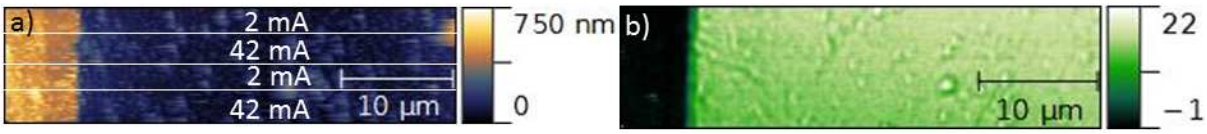

Figure 2.20: AFM and NSOM images of a thin layer (≈ 60 nm) of $[Fe^{II}(hptrz)]_3(OTs)_2$ spin coated on a gold microwire (thickness=250 nm, width=8 μm, length=1 mm, glass substrate): a) Topography and b) NSOM reflectivity. During image acquisition the current flowing in the wire was successively switched between 2 mA and 42 mA as indicated in the figure.

the scan . No obvious effect of the current intensity change was observed in these images. The intensity difference between the reflectance of the glass and the gold is very high, therefore any small variation in the reflectance due to the spin transition might be difficult to detect. The contrast between the wire and the substrate can be reduced using a silicon substrate. A close up of the topography and the reflectivity NSOM maps of a gold microwire on silicon substrate is presented in figure 2.21. NSOM images were obtained for two different applied currents (2 mA and 92 mA). In this case, some intensity difference between the scans with high and low applied currents can be observed at the beginning, but these changes are not reproducible. It is difficult to determine the origin of this problem, but we believe that the sample properties change under laser illumination. We did not continue working with this sample, because during the course of this work a new SCO thin film was developed in the team by Iurii Suleymanov, which presented more appealing properties for our NSOM reflectivity studies.

2.5 Reflectivity measurements on $[Fe(Htrz)_2(trz)]BF_4$

$[Fe(Htrz)_2(trz)]BF_4$ (Htrz=1,2,4-triazole, trz=1,2,4 triazolato) nanoparticles (≈ 180 nm) were synthesized by Iurii Suleimanov in the team. This compound presents a LS-HS spin transition at temperatures higher than ambient, with a wide thermal hysteresis (≈ 40 K), shown in figure 2.22. In the first cycle the compound is hydrated, therefore it presents a wider hysteresis, but from the second cycle it displays a reproducible spin transition around $T^{\uparrow}$=393 K on heating and $T^{\downarrow}$=353 K on cooling. This compound is violet in the low spin state and white in the high spin state. The change of color is very abrupt and easy to follow by reflectivity measurements in far-field. The refractive index and its change with the SCO has not yet been determined for this compound, but taking into account the Gladston-Dale equation [158] the very important density change between the two spin states (≈ 11.5 %) must lead also to a significant refractive index change of ca. 0.1.

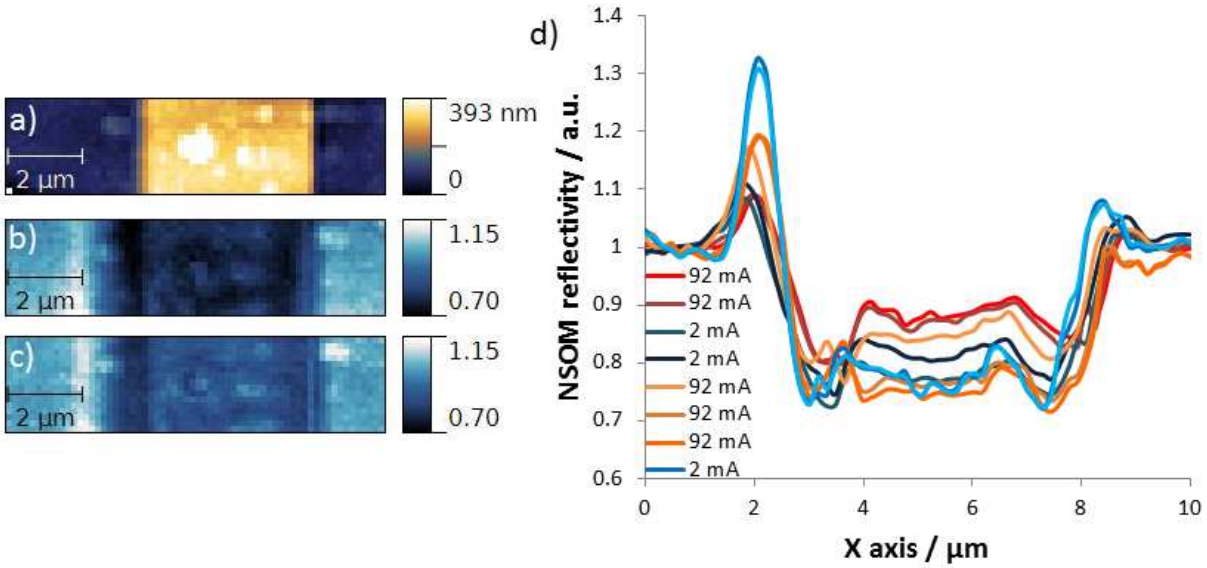

Figure 2.21: AFM images of a thin layer ($\approx$ 60 nm) of $[Fe^{II}(hptrz)]_3(OTs)_2$ compound spin coated on a gold microwire (thickness=250 nm, width=8 μm, length=1 mm, silicon substrate): a) Topography, b) NSOM reflectivity map for 2 mA current and c) NSOM reflectivity map for 92 mA current. d) Average cross sections of the NSOM images for successive experiments with different applied currents.

NSOM and far-field reflectivity measurements were performed with the same configuration as the one presented in section 2.4. A solution of $[Fe(Htrz)_2(trz)]BF_4$ particles (50 mg) in 2 ml ethanol was spin coated over the gold nanowires (speed=4500 rpm, acceleration = 4000 rpm^2, time = 30 s). The particles were distributed homogeneously on the surface, as shown in figure 2.22. However, when the wire is too thick (>100 nm), the particles were not deposited in its proximity.

Reflectivity tests in far-field were carried out by fixing the temperature of the sample stage at 378 K. The transition from the low spin to the high spin state was induced by Joule heating using a gold microwire heater. Figure 2.23 shows pictures of a $[Fe(Htrz)_2(trz)]BF_4$ film on a gold wire taken before and after applying a 92 mA current pulse to the wire. This current pulse induces a transient heating Δt = 1 min in the film that brings the complex to the HS state, which is evidenced by the increase of the reflectance. When the heat is dissipated the complex remains in the high spin state because the temperature of the sample stage (378 K) falls within the hysteresis region. Thanks to the tight confinement of the ΔT induced by the heater, the particles on the Si substrate remain in the LS state and only those on the wire change their spin state. To demonstrate more clearly this change, the normalized reflectance difference is presented in figure 2.23 b. The reflectance difference between the two spin states is only 6 % on the gold wire and 0% on the Si substrate, as shown in the cross section of the difference image.

In addition to the far-field images, NSOM scans were also performed before and after

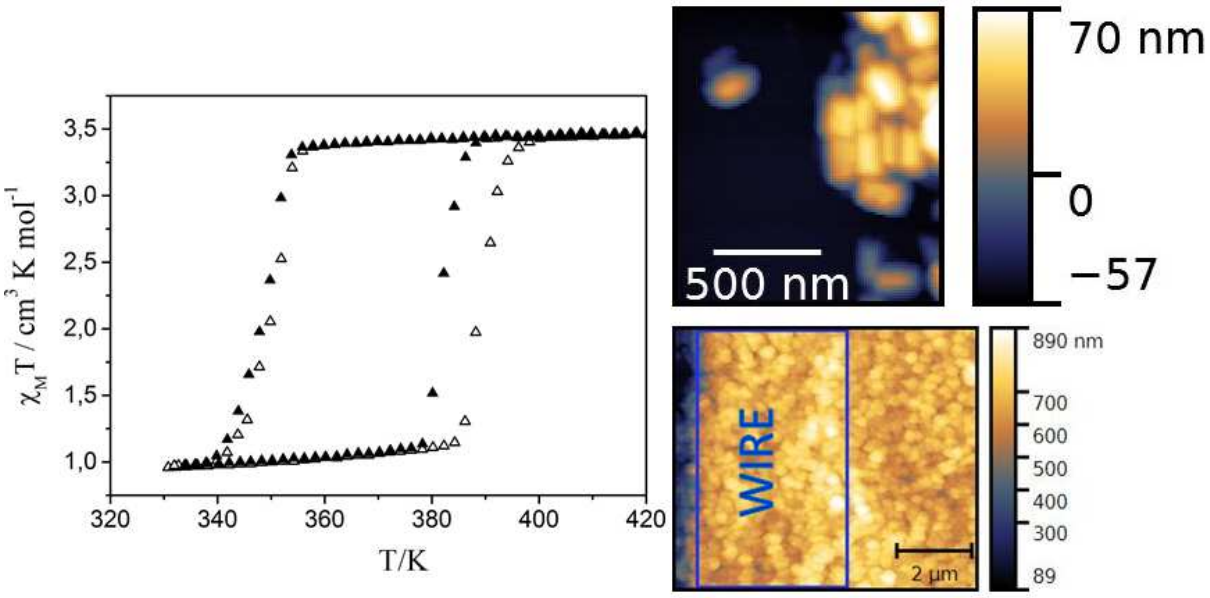

Figure 2.22: a)Temperature dependence of $\chi_m T$ product (χ_m= molar magnetic susceptibility and T = temperature) of the $[Fe(Htrz)_2(trz)]BF_4$ complex and AFM images of the deposited particles on a silicon substrate and on a gold wire.

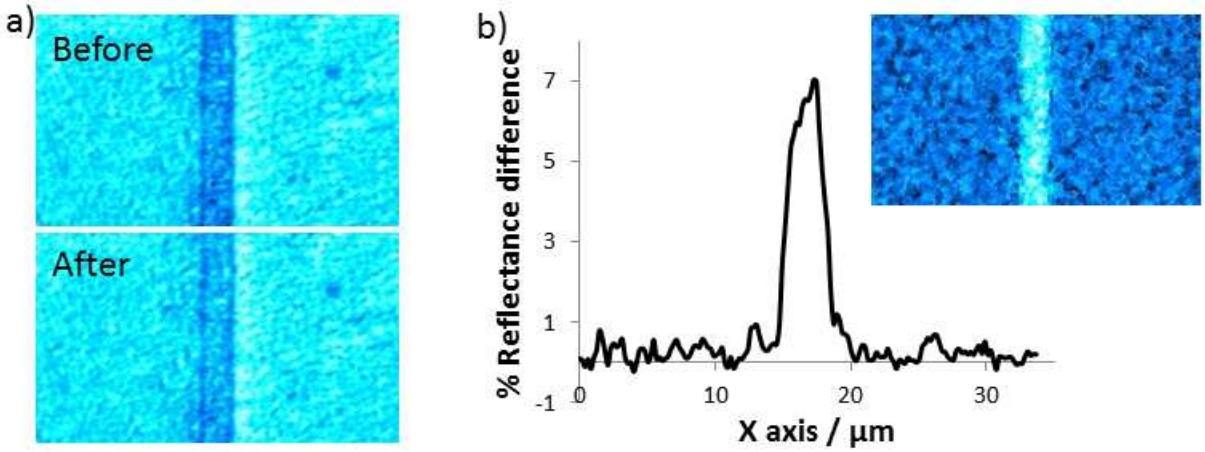

Figure 2.23: a) Far-field images of a $[Fe(Htrz)_2(trz)]BF_4$ film on a gold wire (Si substrate) at 378 K before and after applying a 92 mA current pulse to the wire (pulse duration 1 min). b) Image and average cross section of the reflectance difference between the two images in (a), i.e. the reflectance change induced by the heating of the wire.

heating the sample with the wire. It may be worth noting that each scan was carried out in the same thermal conditions. The tip aperture was of 70 nm. We chose a small aperture because when the sample topography and the tip have the same size, tip motion artifacts are more prominent [159]. The power of the laser at the entrance of the tip fiber was fixed at 500 μW to assure that the material will not change its spin state due to local laser heating. The NSOM images present details with a resolution below the wavelength (488 nm) as shown in figure 2.24. After heating the material on the wire, the NSOM reflectivity signal should increase on the wire. On the other hand, on the Si substrate the optical properties (i. e. the NSOM signal) should be the same, since the temperature of the material is not modified by the applied current. Based on this assumption, supported by the far-field data, we have normalized the NSOM images using a reference area far from the wire. The result of this treatment is shown in figure 2.24. The cross sections in panel c show that the normalized NSOM reflectance remains unchanged on the whole Si substrate (i.e. not only in the reference area) providing strong support for the validity of our data treatment. We observe an increase of the NSOM reflectance after the current pulse only on the wire (see panel d). This increase (ca. 7%) is comparable with the far-field result (ca. 6%). Overall there is a very good agreement between the far-field and near-field results. The signal to noise ratio of the latter is of course less good, but it provides high resolution details, which are obviously not accessible in far-field.

After a few scans the NSOM reflectance images were difficult to reproduce. In many cases a brighter zone, corresponding to the scanned area, was observed in the far field images, as shown in figure 2.25. Taking a closer look to the topography, we observed several holes in the SCO film. The appearance of these holes in the topography image indicates that the tip moved the particles while scanning the surface. Decreasing the interaction between the tip and the sample by modifying the gain, the oscillation amplitude and the setpoint did not completely solve this problem. Besides tip-sample interactions, long exposures to light and high temperatures in ambient air also affect the sample integrity. Therefore, after a couple of days of continuous manipulation the reflectance intensity difference between the HS and LS states decreases until it is no longer detectable.

Up to now we have performed NSOM experiments in AFM feedback, i.e. following the topography of the sample. It is also possible to carry out NSOM measurements at a constant height. This method has the advantage that tip-sample mechanical interactions are considerably reduced. Several authors have compared the two methods [159, 160]. They found that high contrast images can only be obtained in feedback, but the NSOM images include artifacts mainly due to the crosstalk with the topographic signal.

When working at a constant height, it is necessary to perform a preliminary topography scan to determine the highest point of the topography. In this way, a minimum safe distance can be defined and thus avoid any damage of either the sample or the tip. It is

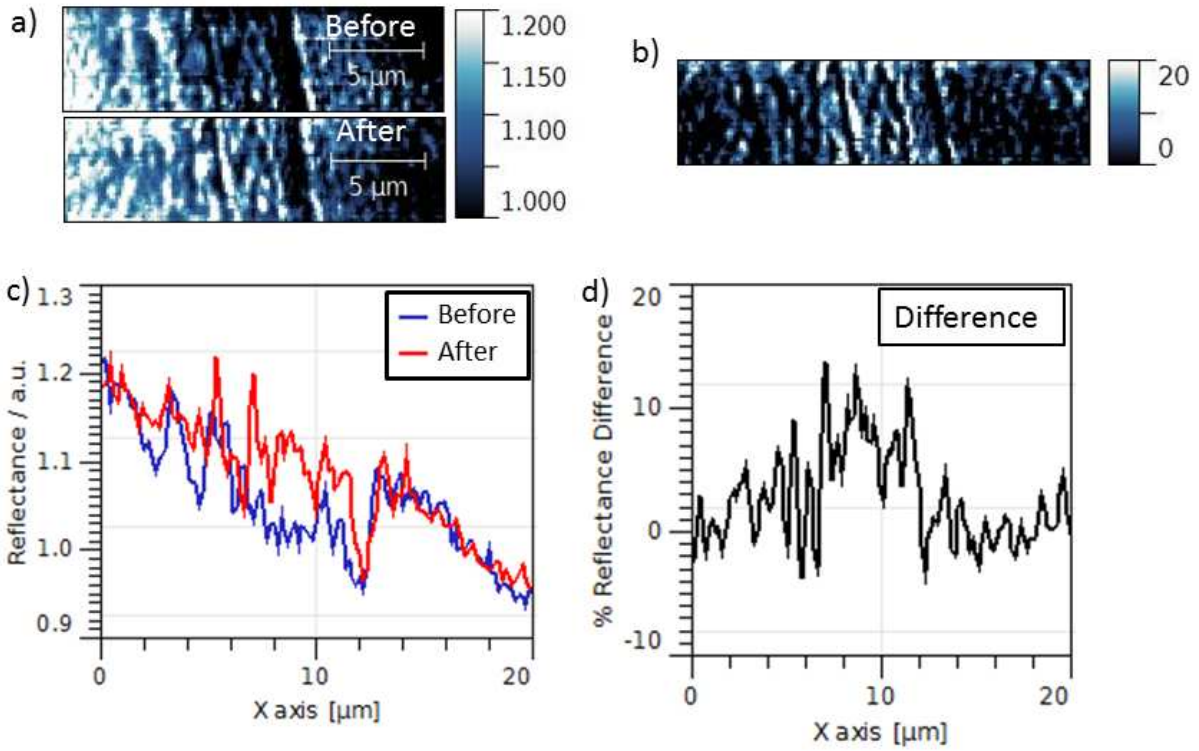

Figure 2.24: a) NSOM map of a $[Fe(Htrz)_2(trz)]BF_4$ film on a gold wire (thickness 250 nm, length 1 mm, width 4 μm, Si substrate) before and after applying a 92 mA current pulse through the wire. b) Normalized reflectance difference between the two images shown in panel (a). c) and d) Average cross sections of the images in panels (a) and (b), respectively.

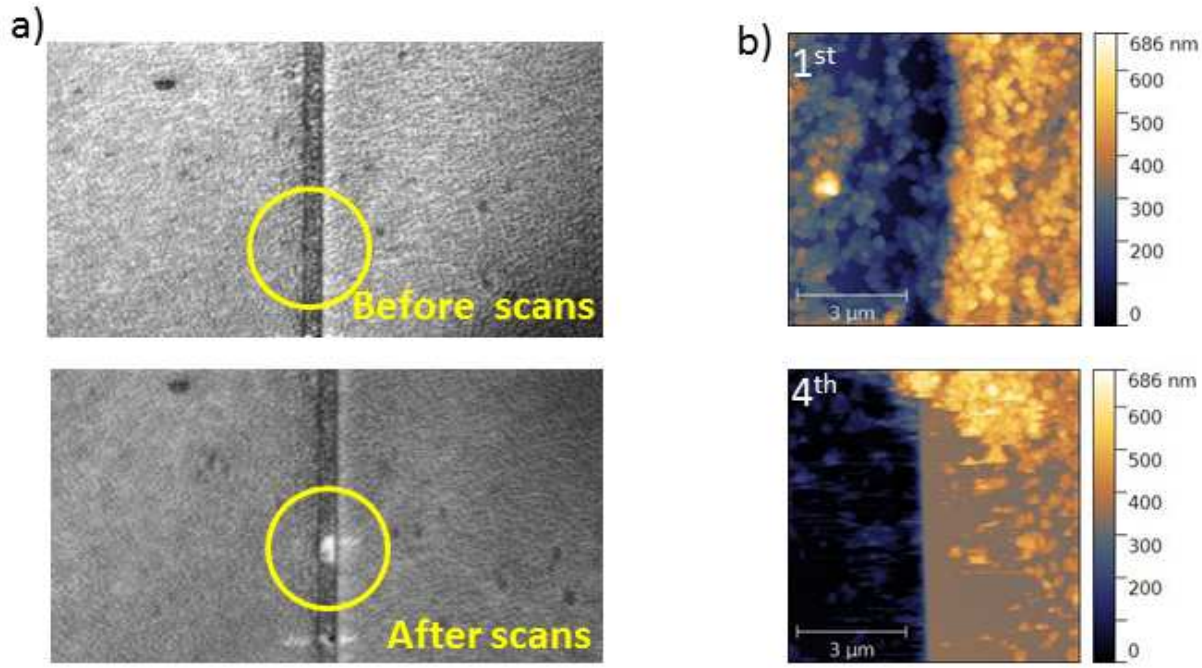

Figure 2.25: Images of a film ($\approx$ 250 nm) of $[Fe(Htrz)_2(trz)]BF_4$ on a wire (thickness = 250 nm, length = 1 mm, width = 4 μm) a) Far-field pictures before scans and after scans and b) near-field maps of the first and fourth scans. A damage in the sample is observed after scanning.

also important to compensate the inclination of the sample in both the x and y directions. The distance at which the high spatial frequency components can be observed depends on the size of the aperture of the tip and the used wavelength.

Constant height NSOM reflectivity measurements were carried out on a new sample prepared in the same conditions. The gold wire used here had a different geometry: thickness 250 nm, length 1 mm, width 8 μm. The experimental set-up for combined near-field and far-field reflectivity measurements was the same as used for the previous experiments. First, we have recorded the reflectivity in far-field (see figure 2.26). The results are similar to those obtained with the previous sample (cf. figure 2.23), but in this case the reflectance change upon applying a 190 mA current pulse, i.e. between the LS and HS states, is only 3 %. The smaller reflectance change is probably related to the different sample thermal history and / or to the different sample thickness. One should also note the different current used to heat the sample - this is simply due to the different widths of the wires used in the two experiments.

Topography tests on the sample revealed that the roughness of the sample is ca. 45 nm and the highest point was found always below 55 nm on a relatively flat area. In order to carry out NSOM measurements at a constant height around a gold wire, the approach of the tip to the sample was always performed on the wire. Then, the tip was retracted 5 steps, (i.e. 60 nm away from wire and 310 nm away form the silicon substrate)

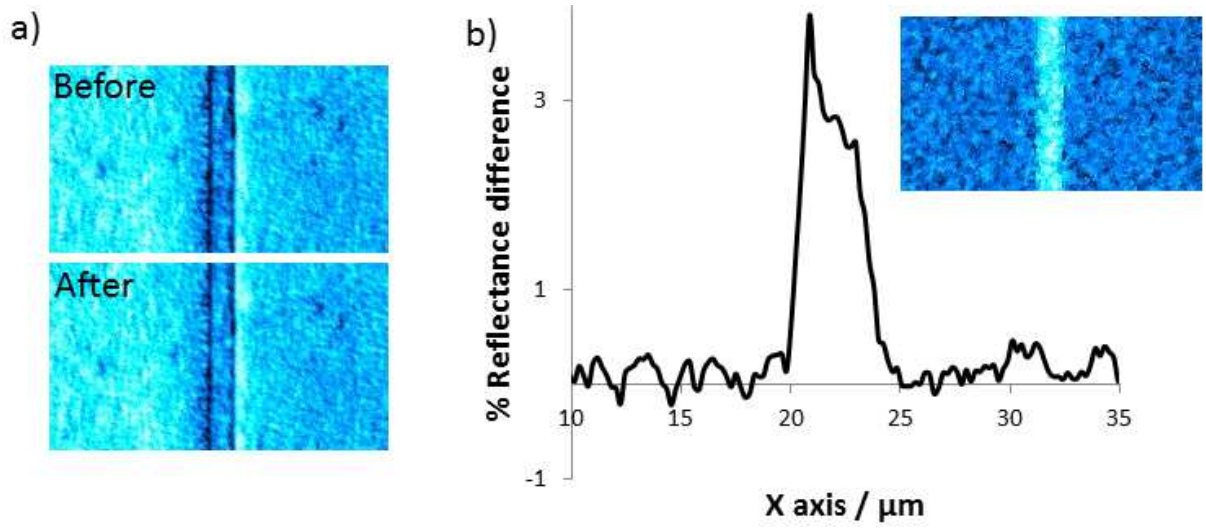

Figure 2.26: a) Far-field images of a film ($\approx$ 250 nm) of $[Fe(Htrz)_2(trz)]BF_4$ on a gold wire (thickness 250 nm, length 1 mm, width 8 μm, Si substrate) at 378 K before and after applying a 190 mA current pulse to the wire. b) Image and average cross section of the reflectance difference between the two images in (a), i.e. the reflectance change induced by the heating of the wire.

before scanning the sample. The tip was completely retracted from the sample before any temperature change was applied to the sample either with the heater stage or with a gold wire.

The constant height NSOM reflectivity scans revealed a strong difference between the reflectance on the wire and the reflectance on the Si substrate (figure 2.27). This contrast is clearly related to the tip-sample distance difference since it was not observed in NSOM experiments with feedback (figure 2.24). The main consequence of the abrupt change of the tip-sample distance is that the high frequency spatial components observed on the wire are lost on the Si substrate where the different sub-wavelength features are no longer distinguishable (figure 2.27). The NSOM images were normalized as described in the previous experiment. An increase of the NSOM reflectance after the current pulse was observed only on the wire (see panel d). This increase (ca. 10%) is three times larger than in far-field (ca. 3%). To confirm this finding this experiment was repeated on a new sample (see figure 2.28). The far-field reflectance difference between the two spin states was around 6 % for the new sample, while in near-field the reflectance on the wire increased 30 % after the current pulse. The difference is at least 4-5 times higher than for the far-field data. In addition, brighter and darker points on the sample with a resolution of ca. 300 nm can be observed. We can conclude that NSOM images at constant height are much more sensible to the spin transition than far-field or even feedback NSOM measurements. In addition constant height scans do not degrade the sample and give high resolution spatial information of the reflectance of the sample.

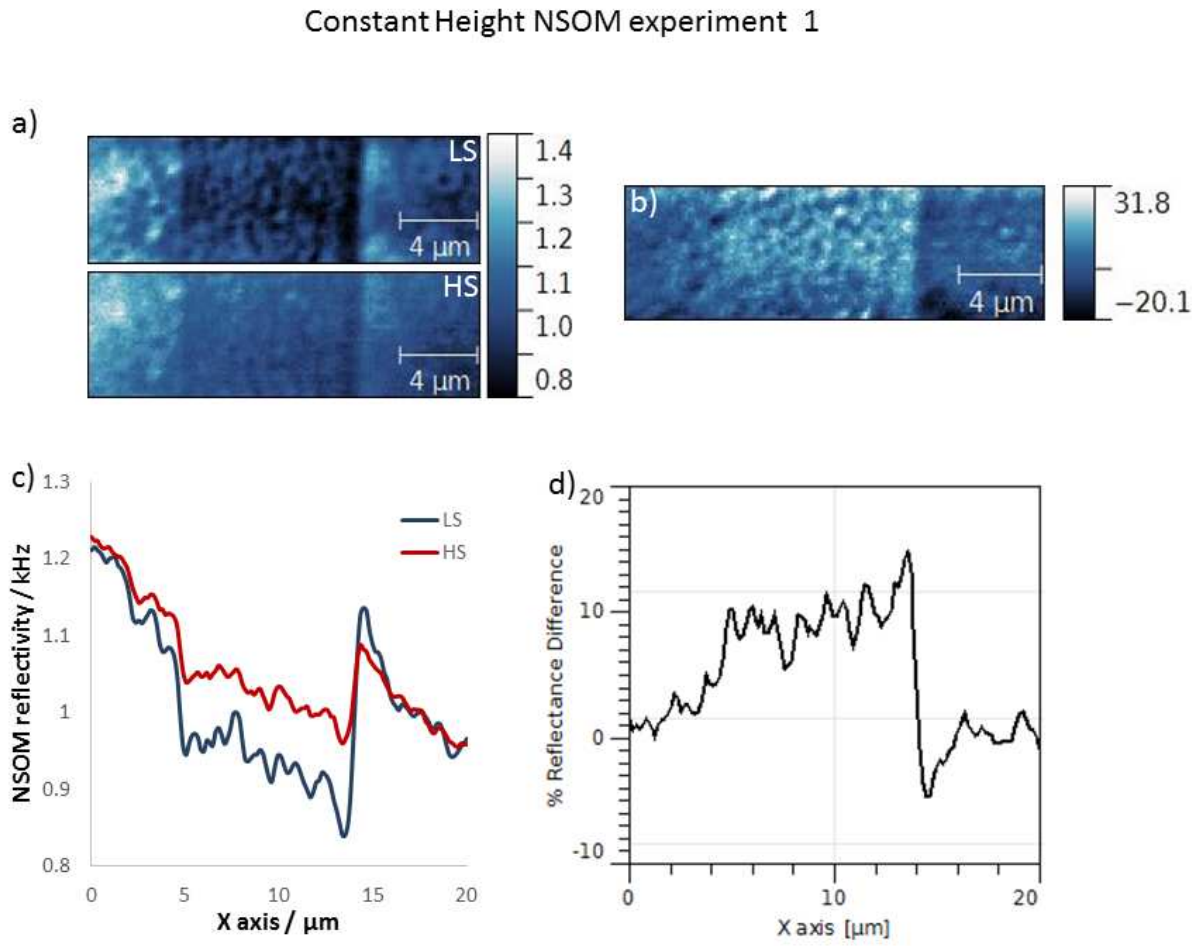

Figure 2.27: a) Constant height NSOM reflectivity images of $[Fe(Htrz)_2(trz)]BF_4$ deposited on a gold wire (thickness = 250 nm, length = 1 mm, width = 8 μm). The two images were acquired at 378 K before (LS) and after (HS) applying a 190 mA current pulse through the wire. c) Average cross section of the images shown in (a). b) Image and d) average cross section of the reflectance difference between the two images in (a), i.e. the reflectance change induced by the heating of the wire.

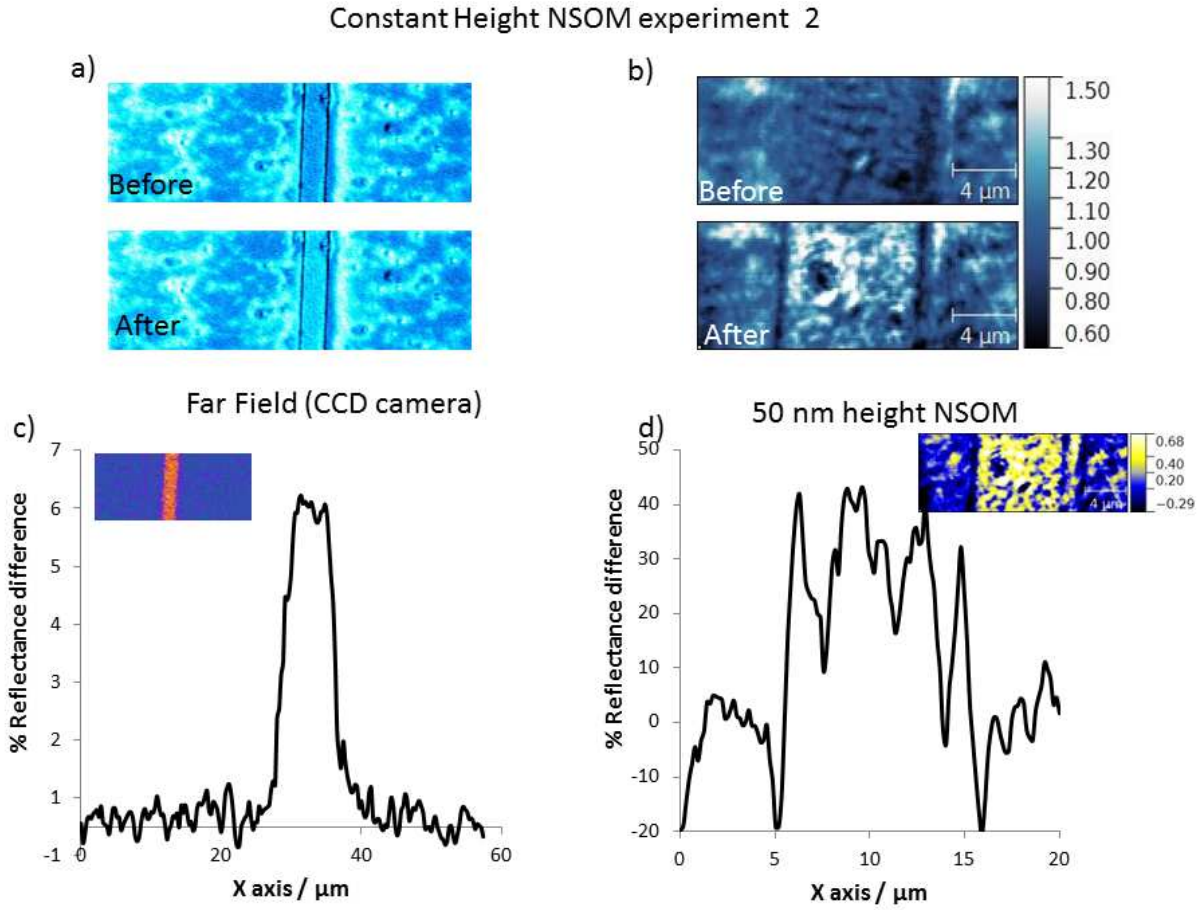

Figure 2.28: a) Far-field and b) constant height NSOM reflectivity images of $[Fe(Htrz)_2(trz)]BF_4$ deposited on a gold wire (thickness 250 nm, length 1 mm, width 8 μm). The images were acquired at 378 K before and after applying a 190 mA current pulse through the wire. Image and average cross section of the reflectance difference between the two images in (a) are shown in c). Image and average cross section of the reflectance difference between the two images in (b) are shown in d).

2.5.0.2 NSOM tip as heating device

Up to now we have used the NSOM tip to analyze the optical properties of the samples with high spatial resolution with the aim to infer information about the spin state change locally. However, the NSOM tip can be used not only to detect the spin state of the sample, but also to manipulate it locally. For example, by increasing the intensity of the laser beam injected into the NSOM fiber we can heat the sample above the spin transition temperature and transform a small volume from the LS to the HS state. Indeed, the metal coating at the end of the tip produces multiple reflections at the metallized sides. Such reflections increase the total amount of light absorbed by the metal coating (from 8% at normal light incidence to 20 - 30 %) and thus it can increase the temperature of the metallic film up to several hundreds of degrees [161]. Even though the heated volume depends on many parameters (tip and sample properties, etc), it was shown that local heating on the sample surface can be achieved with sub-wavelength resolution [162]. This technique opens up therefore the possibility to switch the spin state of a single SCO nanoparticle, which can be used, for example, in a memory device. In our experiments heating with the NSOM tip can replace the nanowire heaters. Of course, laser heating is less well controlled when compared to Joule heating with the metallic nanowire, but it provides more flexibility in the experiments. A specific problem with the nanowire approach is that the presence of the wire significantly modifies the surface topography. When heating with the NSOM tip it is possible to work on a flat area of the sample, increasing the stability of the feedback and decreasing the probability of moving the particles around with the tip.

To explore this idea in a first step we determined the laser power needed to trigger the spin transition in the $Fe(Htrz_2(trz))BF_4$ film we used in the previous NSOM reflectivity experiments. To this aim, the sample was scanned with different light intensities while keeping the temperature of the sample stage at 395 K. The power of the laser at the entrance of the tip fiber was adjusted using a variable neutral density filter and controlled with an optical power meter (PM100D from Thorlabs). The spin state of the sample was determined from far-field reflectance images taken before and after each scan. (N.B. The experimental set-up is the same as described in the section 2.5.) Figure 2.29 (a) shows the reflectance change of the sample in the scan area plotted as a function of the laser power measured at the entrance of the tip fiber. One can note that there exists a threshold laser power (ca. 2 mW) below which the spin state of the sample does not change. This observation is not surprising since the thermal spin transition in this compound is very abrupt (see figure 2.22). Above this threshold value the reflectance increases gradually until a saturation value. The gradual variation is at first sight difficult to conceal with the abrupt spin transition. We believe that this gradual increase of the reflectance can be observed if several particles transit during the laser heating. Heat will diffuse in an

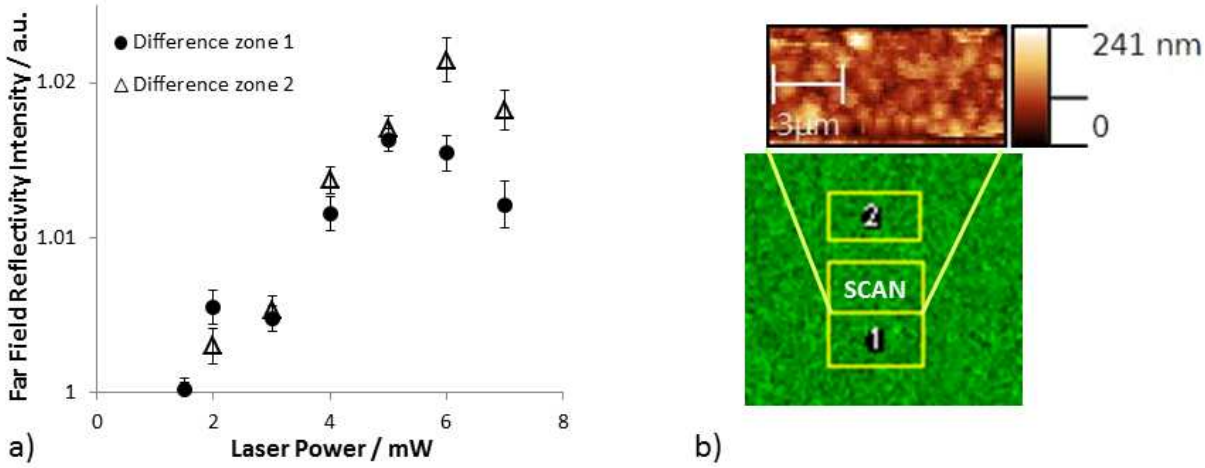

Figure 2.29: a) Reflectivity intensity difference between the scanned area and two reference areas (zones 1 and 2) following NSOM scans with different laser intensities on a film of $[Fe(Htrz)_2(trz)]BF_4$. The sample temperature was kept at 395 K. b) Topography image of the scanned area, which is indicated in the far-field image below together with the two reference areas.

inhomogeneous manner and thus the particles will change their spin state at different laser intensities.

Figure 2.30 shows far-field reflectivity images taken after scanning with the laser power indicated in each picture. The area scanned by the NSOM tip is indicated by the yellow rectangles. With increasing power one can observe more and more bright dots in and near the scanned area, which correspond to particles transformed to the HS state. It may seem surprising that particles out of the scanned area change their spin state, but we have to note that nucleation of the HS phase may occur even if the particle is only partially heated. In addition the positioning of the scanned area within the far-field image is perhaps not perfectly accurate. The images show that different particles do not transit for the same laser intensity. It is difficult to correlate these images with the topography image, because the contrast in NSOM and AFM is often different. In addition in the present case further complications arise from the facts that the illumination and heat diffusion conditions are different for each particle. Above 5 mW the number of particles in the high spin state was not significantly increased. The dark dot that appears after the scan performed with 6 mW is most probably a damage done to the sample by the tip during an engage. In fact, when the tip approaches to the sample to achieve the tip-sample contact, it can tap harder on the sample until the feedback is properly established.

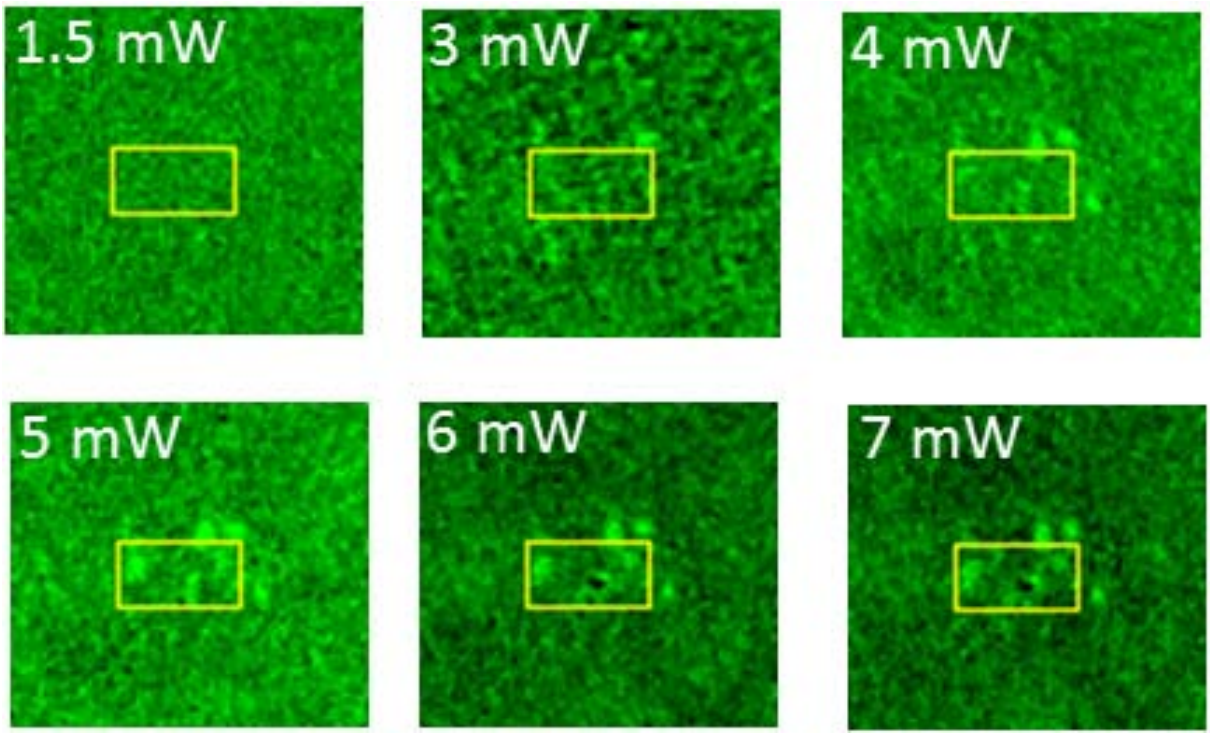

Figure 2.30: Far-field reflectivity images taken of a thin film ($\approx$ 300 nm) of $[Fe(Htrz)_2(trz)]BF_4$. Each image was taken after scanning with an NSOM tip. A blue laser (488 nm) was injected into the NSOM fiber with the power indicated in each image. The yellow rectangles mark the scanned area (10 X 5 μm^2).

2.6 Conclusions

In this chapter we have described a novel experimental set-up, which we implemented to investigate the optical properties of spin crossover thin films with high spatial resolution. To our knowledge, this is the first proven case where the spin state of SCO nanomaterials was imaged with submicrometric spatial resolution [3]. We explored in this chapter NSOM reflectivity and NSOM with fluorescence contrast enhancement and both methods allowed us to observe the spin transition in SCO films. Since most NSOM experiments were carried out in AFM feedback we had also access to spin-state dependent AFM topography data. However, within our experimental conditions, which are far from optimal for high resolution AFM topography measurements, we could not observe significant surface topography changes in the films upon the spin transition.

To overcome the severe experimental constraints imposed by the necessity to carry out a series of NSOM scans at different temperatures in a quantitative manner, we put in place an original experimental strategy based on local heating of the sample by a metallic nanowire. Indeed, the wear of the tip and the sample during several scans associated with various unwanted thermal effects (sample drift, tip heating, etc.) are very difficult to handle when using conventional SPM heating stages. The fast local heating with the nanowires proved to be very successful and allowed us to observe the spin transition as a function of the temperature even during a single scan. We believe that this approach may find a general interest in the SPM community for several reasons. First of all, the sample drift is negligible and probe heating can be minimized. (In particular convection effects become negligible.) In addition, sample thermalization is instantaneous (at the time scale of an SPM scan) and the fact that the temperature difference is confined to the wire provides a reference area near the wire, which can be useful to control the evolution of the tip-sample interaction. Finally, the fact that the wire is heated by an electrical current and its temperature is monitored through its electrical resistance provides a useful means to integrate and synchronize the nanoheater with the rest of the set-up.

Another important aspect of our experimental approach is the simultaneous use of

[3]We are aware that since 2010 several papers claimed that molecular spin states were identified by scanning tunneling microscopy (STM) [91, 163–165]. Even if these reports are extremely interesting, in our opinion in none of these papers there is an irrefutable proof that the changes observed by the STM are related to the spin state switching phenomena. The three main factors behind the difficulties of interpretation are the high fragility of the measuring STM junctions, the difficulties in their characterization by any other means than the tunnelling spectra and the impossibility to connect the molecules to the electrodes without changing their properties. In addition STM is basically limited to the investigation of (sub)monolayer samples on conducting surfaces. In another approach, parallel with our work, the teams of Hauser and Zewail [10] published an electron microscopy study wherein they were able to follow spin state changes in a single nanoparticle. Their approach is very complementary to our SPM based approach with different advantages and drawbacks. Finally, we must recall that we have also published in our team an NSOM-AFM investigation on bulk single crystals [93], but the technical challenges and scientific objectives are very different to those in the the case of nanometric thin films.

far-field optical detection and the SPM. The former appears indispensable to monitor in-situ the spin-state of the sample. In fact, the spin transition in certain samples is not very robust and needs to be followed continuously during the long SPM experiments. In addition, in some cases the SPM probe itself can also influence the properties of the sample (either reversible or irreversible), which can be often detected by far-field optics.

NSOM experiments were first carried out in luminescence mode on thin films of $[Fe^{II}(hptrz)]_3(OTs)_2$ (ca. 60 nm) doped with Rhodamine 110. We could successfully observe the spin transition in this sample through the variation of the luminescence intensity in the near-field. However, these observations remained rather qualitative due mainly to photobleaching problems. For this reason, we turned to NSOM reflectivity measurements where photobleaching effects are not expected. Reflectivity provides in many cases a weaker contrast between the HS and LS states than luminescence and indeed for thin films of $[Fe^{II}(hptrz)]_3(OTs)_2$ it was not possible to implement this approach. On the other hand, for films of $[Fe(Htrz)_2(trz)]BF_4$ particles (ca. 300 nm) we observed a significant variation of the reflectivity in both far-field and near-field, the HS state being much more reflective. NSOM reflectivity experiments on this sample were carried out both in AFM feedback and in constant height mode. Both gave similar results, but the later proved to be more reproducible because it leads to less sample damage. On the whole, NSOM proved to be useful to achieve high spatial resolution (ca. 200-300 nm in our experiments) imaging of the spin transition in nanometric thin films and clearly there is no fundamental obstacle to further increase this resolution by using tips with smaller apertures. On the other hand the acquisition of a series of quantitative scans remain a challenge due to experimental difficulties to achieve stable measurements over long periods and also for more fundamental reasons which concern the interpretation of the NSOM signal, in particular the discrimination of far-field contributions.

Besides the high resolution imaging of the spin transition, NSOM proved to be useful also to manipulate the spin state of $[Fe(Htrz)_2(trz)]BF_4$ particles through local laser heating. It is possible to produce a transition from the LS to the HS state in a single nanometric object. It would be possible therefore to use this technique to perform laser witting on the surface with submicrometric resolution, in particular if a more homogeneous SCO film and a sharper tip is used.

A very interesting perspective of the work presented here is the use of spin crossover thin films for micro- and nano-scale thermal imaging purposes. In particular, the large thermal hysteresis loop associated with the spin transition in the compound $[Fe(Htrz)_2(trz)]BF_4$ provides an unparalleled scope for imaging transient heating phenomena with high spatial resolution thanks to the long-lived metastable states within the hysteresis region. The high resolution imaging of transient heating by a current pulse is clearly demonstrated, for example, in figure 2.27. This promising application of SCO films is currently investigated in our team in the frame of the thesis of Olena Kraieva.

Chapter 3

Mechanical Properties

The mechanical properties play a key role in the spin-transition behavior of SCO solids. Indeed, many interesting cooperative phenomena [34, 94] can be rationalized only by taking into account the volume misfit of the HS and LS states and the associated elastic interactions between the SCO centers [166]. In addition, recently developed, promising applications of SCO materials as microactuators [167] require also a detailed knowledge of the mechanical properties, such as the Young's modulus and mechanical strain. Taking into account their central role in the SCO phenomenon, it is thus rather surprising to realize that the elastic constants of spin-transition materials have been determined only in a few occasions, using nuclear inelastic scattering [168], high-pressure X-ray diffraction [169, 170], and Brillouin spectroscopy [171]. In addition most of these measurements were carried out in either in the HS or LS forms and the spin-state dependence of elastic moduli has been reported only very recently [168]. However, we know that the LS to HS transition involves a drastic increase of the metal-ligand bond lengths (up to 10%) [172]. This softening of the coordination bonds has been clearly observed by vibrational spectroscopies and by ^{5}7Fe Mössbauer spectroscopy [173]. This latter method gives access to the Debye temperature, which can be roughly related to the bulk modulus by a square-root relationship $K^{1/2} \sim \Theta_D$. The available scarce Mössbauer data suggests a typical variation of $1.6 > K_{LS}/K_{HS} > 1.2$. This variation is not huge, but possibly detectable using an AFM. For these reasons we decided to explore AFM mechanical modes for imaging the spin transition through the variation of elastic moduli. While this approach may seem somewhat indirect it provides two important advantages: the possibility of quantitative analysis and (potentially) very high spatial resolution.

The quantitative imaging of mechanical properties using an SPM is a significant challenge even today due to the difficulties to quantify tip-sample interactions and the contact geometry. In our case these difficulties are further amplified by the need for temperature dependent and non-destructive (reversible) measurements as well as the relatively weak contrast between the elastic moduli of the two spin states. We start this

Mode	Measured Property	Reference
AFM Nanoindentation	H, E, Adh, plasticity, Dissipation, Deformation	[174, 175, 181, 182, 185, 186]
Force Modulation	Dissipation and stiffness (Qualitative)	[187–190]
Contact Resonance	E, G, E', E'', Loss Tangent	[191–197]
Tapping	Dissipation (Qualitative)	[198–208]
Loss Tangent Measurement	Loss Tangent	[190, 209, 210]
Bimodal Techniques	E, Loss Tangent, Dissipation	[211–213]
Force Volume Mode	H, E, Adh, Dissipation, Deformation	[138, 214]
Quantitative Imaging	H, E, Adh, Dissipation, Deformation	[215, 216]
Peak Force Tapping	H, E, Adh, Dissipation, Deformation	[137, 217]
Lateral Force Microscopy	Friction coefficient, G	[176, 177, 180]

Table 3.1: AFM modes that give information about the mechanical properties of the sample. E is the Young's modulus, E' is the storage modulus, E'' is the loss modulus, H is hardness, Adh is adhesion and G is the shear modulus.

chapter with a broad survey of the different AFM mechanical modes with special emphasis on the techniques we had access during the thesis work. The next part is devoted to our preliminary tests on electron beam irradiated Polymethyl-methacrylate (PMMA) samples, which were used to test and optimize the different measurement protocols. Finally the AFM mechanical studies of SCO films through the thermal spin transition are presented.

3.1 Analysis principles

As applications in micro-systems grow, there has been an increasing interest in studying the mechanical properties of nano- and micro-materials. Addressing this need several AFM modes have been developed in the last years that are able to determine the hardness (H) [174], the plasticity [175], the coefficient of friction [176, 177], the shear modulus (G) [178–180] and the Young's modulus (E) [138, 181, 182]. If both E and G are measured, it is also possible to determine the Poisson's ratio [183]. The most common AFM modes to obtain the mechanical properties are listed in table 3.1. (N.B. Several other approaches were also proposed - the interested reader can consult the recent review of Passeri et al. [184].)

Adhesion and plasticity are not really interesting for the study of SCO materials since the first is more related to the chemical properties of the material and the second refers to an irreversible process, so the same area can not be probed more than once. Among the main elastic moduli, the bulk modulus cannot be accessed by AFM and the shear modulus can be measured only under special circumstances. On the other hand, the Young's modulus can be obtained in almost any AFM system and on a variety of

samples directly from a force-distance curve. In this work we focused on this property.

In the next sections a description of the different modes we had access to is presented. For a better understanding, the modes are separated in two families: the dynamic AFM modes, which are basically tapping mode based, and the force curve based modes.

3.1.1 Dynamic AFM modes

Techniques based on dynamic AFM modes have the ability to make fast and less invasive measurements. However, quantifying the physical properties of the sample is difficult, since a direct relationship between the observables and the forces is not obvious to deduce.

In AC mode, one can use either the amplitude A_1, the frequency f_1 or the phase to control the feedback loop. The phase ϕ_1 or the amplitude are free to vary depending on the tip-sample interactions, which translates in a qualitative manner the mechanical properties of the sample.

3.1.1.1 Tapping mode and its variants

Depending on the parameter that is used to make the feedback loop slight differences in the interaction between the probe and the sample are observed. In the following paragraphs we discuss briefly each of them.

a) Amplitude modulation

As already stated in section 1.2.1.2 in AM-AFM the amplitude of the oscillation of the tip (A_1) is maintained constant by a feedback loop. When the tip enters in interaction with the material, this latter will exert a force on the tip, so the frequency of oscillation of the tip will be delayed or advanced from that of the excitation force. This phase difference ($\Delta\phi$) will depend, among others, on the mechanical properties of the sample surface. As a consequence this mode receives the name of "phase imaging".

The phase angle ϕ can be obtained as function of the driving frequency ω as follows:

$$\tan(\phi) = \frac{\omega\omega_0}{Q(\omega^2 - \omega_0^2)} \tag{3.1}$$

where ω_0 is the resonant frequency and Q is the quality factor of the vibrating cantilever. (This latter is defined as $Q = \frac{\omega_0}{\Delta\omega}$, where $\Delta\omega$ is the half-power bandwidth.) If the tip is far from the sample (i.e. ω_0), there is no interaction between the tip and the sample, thus the probe phase angle is 90°, by convention. As the probe approaches to the sample, the long-range attractive forces acting on the probe will decrease the resonance frequency. Subsequently the driving frequency becomes larger than the resonant frequency and there-

fore $\phi > 90°$. When the tip is near the sample the resonant frequency becomes larger than the driving frequency consequently $\phi < 90°$. Therefore it is possible to obtain qualitative information about the adhesive forces and the viscoelastic properties [218, 219].

b) Frequency modulation

When the oscillation amplitudes are small in FM-AFM, the frequency shift is proportional to the force gradient of the tip sample interaction [203]. Since the topography of the sample is obtained at a constant frequency by adjusting the tip - sample distance, the topography image is made at a constant force gradient. The record of the drive amplitude over the course of a scan provides a second image where the variations in the drive amplitude are proportional to the dissipated energy by nonconservative tip-sample interactions (viscoelasticity, dissipative forces) [204].

c) Phase modulation

In PM-AFM the scan is performed by adjusting the phase difference, so it is not performed at a constant force gradient as in FM-AFM. On the other hand, PM-AFM mode is more stable than AM-AFM and FM-AFM modes [207]. Jumps normally observed in the two other modes are minimized [208]. As in the previous case the dissipation channel is given by the amplitude signal and it is defined as:

$$A = \frac{A_0}{\left(1 - \left(\frac{f_d}{f_0}\right)^2\right) + \left(\frac{f_d}{Qf_0}\right)} \tag{3.2}$$

These methods are very interesting to observe contrasts due to differences in the viscoelastic properties of the sample. They are particularly attractive to study composite materials, since the change in the phase or amplitude, depending if the study is made in AM or in FM/PM mode, may indicate the spatial distribution of the different materials more reliably than the topography.

The observable quantities in dynamic modes are averaged over many cycles of oscillation, therefore it is not straightforward to obtain an analytical relationship between observables and forces. Nevertheless, a few quantitative methods, such as the loss tangent or the multifrequency modes, have been developed. Both of them are discussed with more details below.

3.1.1.2 Loss tangent mode

Proksch related the phase angle in amplitude modulation mode with the loss tangent [210], which is a dimensionless parameter that measures the ratio of energy dissipated (E'')

to energy stored (E') in one cycle of a periodic deformation:

$$\tan(\delta) = \frac{E''}{E'} \tag{3.3}$$

The measurement is done in two pass. First, the topography is saved. In the second pass the cantilever moves at a preset height Δz above the surface, where the frequency and amplitude is measured by operating the cantilever in phase locked loop.

An attractive feature of the loss tangent is that it is independent of the indenter tip contact area. The loss tangent can be determined as follows:

$$\tan\delta = \frac{\sin\phi_1 - \frac{\omega_0 A_1}{\omega_s A_s}}{Q\frac{A_1}{A_s}\left(1 - \frac{\omega_0^2}{\omega_s^2}\right) - \cos\phi_1} \tag{3.4}$$

where A is the amplitude and the subindex 1 and s means the first pass, second pass respectively.

There is a controversy about the effectiveness of this method. In a recent work it was reported that loss tangent values obtained by this method do not give reliable information [209]. This study reveals that this method gives higher loss tangent values and an incorrect trend between different materials, most probably due to a complicated frequency response form the material and long range adhesive tip-sample interaction forces. An important remark is that this method calculates the cantilever loss tangent which is not necessarily equivalent to the material loss tangent.

3.1.1.3 Bimodal methods

Bimodal methods normally work in the repulsive regime (intermittent contact mode). They profit from the fact that the cantilever-tip ensemble is a mechanical system that has a number of discrete oscillations which are determined by the boundary conditions. Therefore two different excitation signals can be sent to the tip, with two separated feedbacks loops, so the tip is forced to oscillate at two vibrational modes of the cantilever simultaneously. Typically the first and the second flexural resonances are used, although others work as well.

In most common set-ups an output signal of the first mode (either the amplitude or the frequency shift) is used to image the topography, while the other flexural mode is used to measure the mechanical, electrical or magnetic properties of the sample [211]. Several bimodal configurations have been developed due to the diversity of observables. The most common bimodal approaches are presented in table 3.2, which specifies also the feedback mode (amplitude modulated or frequency modulated) for each flexural mode and the material properties that can be measured quantitatively.

In the so-called AM-FM mode, the amplitude of the lower cantilever resonance is

Mode name	Feedback mode 1	Feedback mode 2	Material Property
Bimodal AM	AM	open	Loss tangent
AM-FM	AM	FM	Loss tangent, stiffness, Young's modulus
Bimodal FM	FM	open	Dissipation, stiffness, Young's modulus

Table 3.2: Bimodal AFM configurations

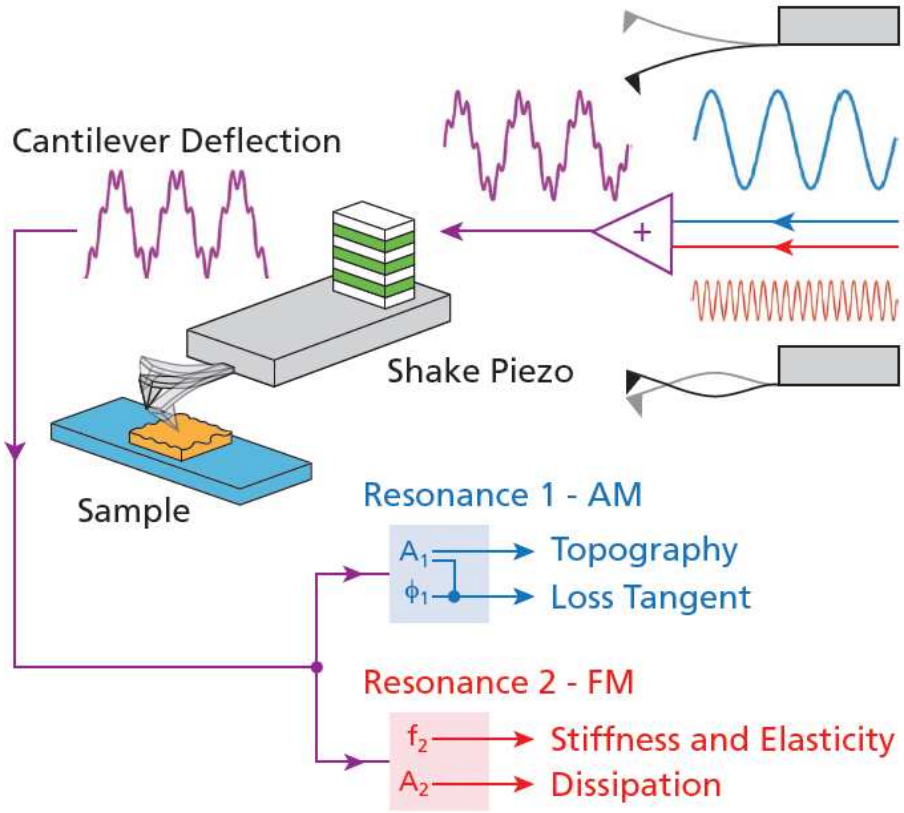

Figure 3.1: Schematic representation of the AM-FM mode, where two separated excitation signals are sent to the tip (blue and red) [220].

maintained at a constant value A_0 (AM-AFM), while in the second vibrational mode, the drive frequency is adjusted to keep the phase at 90 degrees, on resonance (FM-AFM). The topography and the loss tangent are obtained in the AM mode, while the FM mode is used to probe the stiffness and the dissipation, as shown in figure 3.1.

The force applied by the tip was derived by Garcia et al. [211]:

$$F_{ts} \approx \frac{k_2 A_{02}}{Q A_2} \cos \phi_2 \tag{3.5}$$

where the subindex 2 is associated to the second oscillation mode signal and 0 refers to the free oscillation of the tip. Q is the quality factor and k is the spring constant of the cantilever. The Young's modulus (E) can be calculated using one of the tip-sample interaction models described in sec 3.1.3. The tip-sample contact area ($r_c = R(d - d_0)$)

is obtained with a calibration sample of known Young's modulus.

The advantage of this approach is that it is as fast as single frequency tapping mode (up to some tens of Hz), while providing more quantitative information. In contrast to force curves based methods, AM-FM can probe a large range of E values using the same probe, as each flexural mode is associated to a different frequency and thus different spring constant. However, if there is a complicated interaction between the tip and the sample then equation 3.5 may be no longer valid.

3.1.2 Force curves based methods

One of the most commonly applied methods to study the elastic moduli is indentation, where a hard tip with known mechanical properties applies a pressure on the sample. The applied pressure is determined as a function of the indented depth or the residual indentation area to obtain the Young's Modulus or hardness respectively. In nanoindentation small tip sizes and loads are used, so the indentation area may only be a few square micrometers or some nanometers as it is the case of AFM nanoindentation, where the tip radius only measures some tens of nanometers and the applied force can be in the order of some pN for softer samples e.g. cells and some μN for harder samples, e.g. silicon wafers.

3.1.2.1 Force spectroscopy

Force-distance curves (often called force spectra) allow a quantitative determination of several physical and mechanical properties of a material such as dissipated energy, adhesion and Young's modulus, as shown in figure 3.2. When the tip approaches to the sample van der Waals forces attract the tip until it jumps into the surface deflecting downwards a distance proportional to the attractive forces. If it continues to approach the tip will deflects upwards. When the sample is not infinitely hard, the tip will deform it and the resulting curve will be the applied force as function of the deformation of the sample. The Young's modulus and the deformation can be obtained from the slope of this latter part of the curve as shown in the figure. When the tip is retracted the tip will not disengage until the applied force is higher than the adhesion forces. The energy dissipation can be obtained from the area between the approach and retract curves.

As already discussed, the force spectra are recorded by moving the cantilever towards and away from the sample while measuring both the Z-piezo extension and the cantilever deflection (presented in section 1.2.1.1). As mentioned before, most AFM systems measure the cantilever deflection by detecting a laser beam reflected by the backside of the cantilever. As the tip approaches to the sample the system measures the deviation of the laser to the center of the photo-detector, which is measured in volts versus the height position of the piezoelectric translator. This needs to be transformed into a force-distance curve. Once the deflection sensitivity (S) is known, the applied force F and the

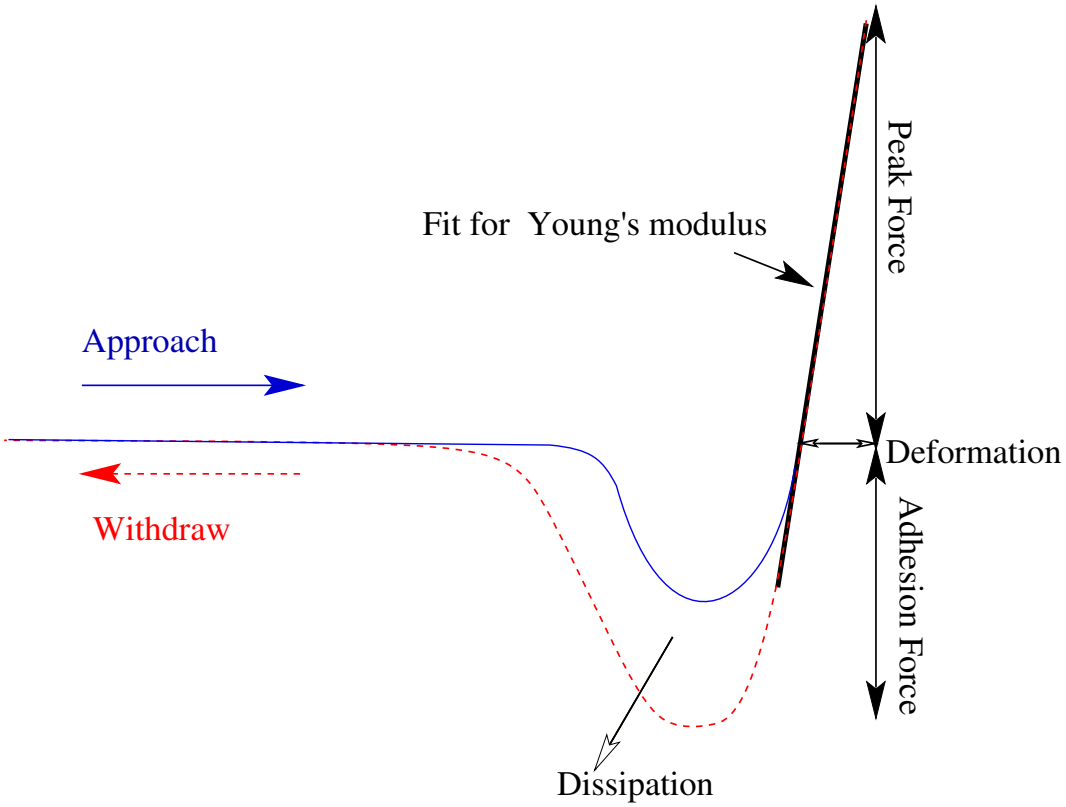

Figure 3.2: Typical force-distance curve obtained with and AFM.

tip position d can be calculated as follows:

$$F = kDS \tag{3.6}$$

$$d = z - DS \tag{3.7}$$

where D is the cantilever deflection (measured in Volts), k is the cantilever spring constant and z is the vertical scanner position. This latter can be determined using scanner sensors, such as optical interferometers, or a standard calibration sample (typically a Si grating).

In the next paragraphs a brief description of the methods to measure the deflection sensitivity and the spring constant are presented.

Deflection sensitivity calibration

The deflection sensitivity depends on the type of cantilever, but also on the optical path and alignment of AFM detection laser. For this reason it will be slightly different each time the cantilever is mounted. Hence it is necessary to determine it each time a tip is placed on the system - even if it is the same tip.

The deflection sensitivity can be obtained from a force-distance curve performed on a hard substrate (silicon or sapphire). In this case the tip does not indent the material

and a good relation between the deviation of the laser beam and the deflection of the cantilever can be made. The repulsive contact region where the deflection rises steeply upwards is linear for a hard surface. If no long-range forces are acting and the tip and sample are infinitely hard, the slope of the contact part of the force curve gives directly the deflection sensitivity $S = \Delta z/\Delta D$. The defection of the cantilever can then be determined in nanometers $Z_c = DS$.

This calibration process can damage the tip, hence it should be done at the end of the experiment. Alternatively if the spring constant of the cantilever is precisely known (which is often not the case) one can use the thermal tuning method (see next section) to obtain S. The accurate determination of S is very important since a small error in S leads to a huge uncertainty on the value of d. Indeed, this latter value is usually very small (a few nm), but it is obtained as a difference of two relatively large values, as shown by equation 3.7.

Spring constant calibration

Assuming that the cantilever deflection is always very small, the applied force can be calculated using Hooke's law $F_{ts} = kZ_c$, provided we know the spring constant of the cantilever.

The spring constant can be determined if the exact shape of the cantilever and the Young's modulus of the material is known. The problem is that the thickness of the material is the smallest dimension of the cantilever and if it is not precisely measured the error on k would be very high. Therefore, several alternative methods have been developed to obtain k [221–223]. Among these methods, two are commonly used due to their simplicity: thermal tuning and Sader's method. Both methods are equally reliable and offer similar uncertainty on rectangular cantilevers, typically about 5% [223].

Thermal tuning

The measurement using the thermal tuning (or thermal noise) method is based on the fact that a harmonic oscillator in equilibrium with its surroundings will oscillate in response to thermal noise, where the amplitude of the oscillations depends only on the spring constant of the cantilever at a given temperature. Hutter and Bechhoefer proposed that if we approximate the cantilever to an oscillator with only one degree of freedom, the spring constant of the cantilever could be related to its thermal energy using the equipartition theorem, resulting [222]:

$$\frac{1}{2}k\left\langle Z_c^2\right\rangle = \frac{1}{2}k_BT \tag{3.8}$$

where $\langle Z_c\rangle$ is the mean squared displacement of the cantilever.

Later, Butt and Jaschke added a correction to this formula [224], since the cantilevers do not act as perfect simple harmonic oscillators. In addition, the optical lever deflection detection scheme results in a further error because it detects the cantilever inclination rather than its true displacement; therefore the energy of each oscillatory mode varies slightly from $\frac{1}{2}k\langle Z_c\rangle$. They proposed to take into account these effects simply by a correction factor:

$$k = 0.817\frac{k_B T}{\langle Z_c^2\rangle} \tag{3.9}$$

In order to isolate the contribution due to thermal oscillations from other noise sources, the data is examined in the frequency domain. In the limit of small damping, the power spectral density can be fitted using a Lorentz function. Other noise sources will add a background to this thermal response. After subtracting this background the area below the peak at the resonance frequency of the cantilever is then a measure of the power of the cantilever oscillations. Since the integral of the power spectrum (P) equals the mean square of the fluctuations in the time-series data, the estimate of the spring constant becomes:

$$k = 0.817 k_B T/P \tag{3.10}$$

Sader method

Let's consider a rectangular cantilever where L denotes the length, w the width and t the thickness of the cantilever. If $L >> w >> t$, Sader's formula for the spring constant of a rectangular cantilever is [225]:

$$k_c = 7.5246\rho_f w^2 L Q f_0^2 \Gamma_i(\mathrm{Re}) \tag{3.11}$$

where ρ_f is the density of the surrounding medium, Q is the quality factor, f_0 is the resonant frequency and Γ_i is the imaginary component of the hydrodynamic function which depends on the Reynolds number Re. This latter depends on the viscosity (η_f) and density (ρ_f) of the medium and is given by $\mathrm{Re} = 2\pi\rho_f f_0 w^2/4\eta_f$. Details on the hydrodynamic function can be found in Sader's publications [225].

3.1.2.2 From force spectroscopy to spectral imaging

In an effort to combine force spectroscopy and imaging with nanometric resolution different methods have been developed. The main difference between these methods is the way the probe is moved along the sample surface. In any case, the key issue is to achieve reasonable imaging time while obtaining proper and detailed spectral data from

each sampled point.

a) Force Volume Mapping

The force-volume method (also called force mapping) was proposed by Radmacher et al. [226]. It consists in collecting a matrix of force curves across the sample surface that are individually analyzed, allowing spatial reconstruction of the topographic maps. This avoids the problem of lateral forces associated with contact-imaging, since the tip is completely detached from the surface before moving to the next point, as shown in figure 3.3. In this way it is possible to make a map of the elasticity of the material and the topography of the surface can be recovered from the zero-force contact point from each force curve, see figure 3.2. However, the big drawback of this mode is that the required time to acquire each force curve is too long. Force curves can be obtained at best at a rate of 100 Hz [137]. In other words, a scan of only 128 x 128 points can take several hours.

b) Quantitative Imaging QI^{TM}

Quantitative Imaging (QI) was developed by the company JPK to collect force curves with a higher speed than the force volume method. The obvious aim is to increase the resolution of the images. The faster acquisition of force curves is achieved by moving the tip laterally at the end of the retraction as well as at the beginning of the approach phases. In other words, vertical and lateral movements are not completely dissociated (see figure 3.3). Nevertheless, during the acquisition of the force-distance curve the tip does not move laterally, which is important to obtain accurate data. Thanks to the fast data transfer on-line data analysis is possible to some extent. In addition, all force-distance curves are saved for posterior analysis. Thanks to the software OpenFovea developed by the Longo et al. [227] it is possible to treat thousands of curves in a few minutes and obtain the mechanical property maps. It should be noted that similar approaches have been recently developed by other AFM companies and they are usually touted as "Fast Force Mapping".

c) Peak Force Tapping

The Peak Force Tapping (PFT) method associated with Quantitative Nanomechanical Analysis (QNM) was developed in 2009 by Veeco Instruments (currently owned by Bruker), but somewhat similar approaches are used by other companies as well. As in the previous cases the tip and the sample are intermittently brought together, so they are in contact for short periods of time, eliminating lateral forces. Here also the tip does not move laterally while making the force-distance curve. In contrast, it moves faster

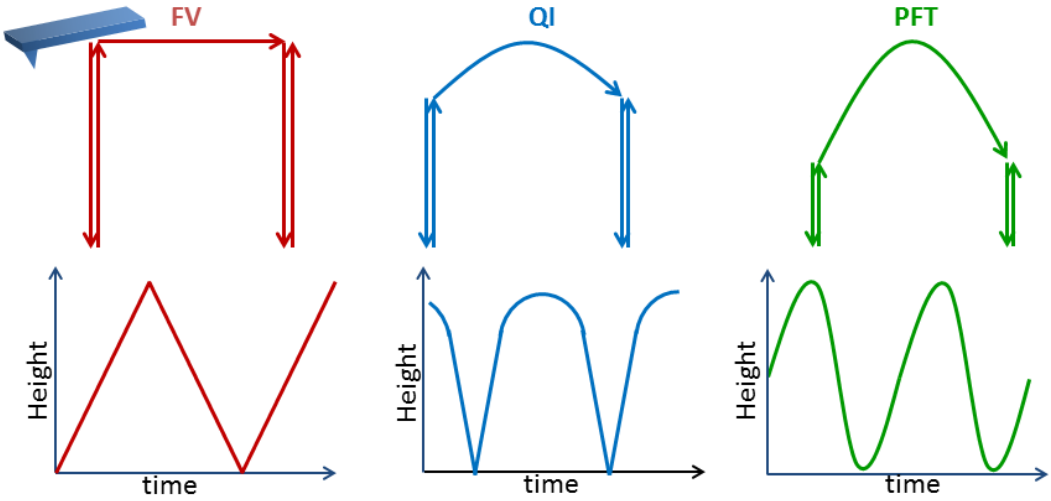

Figure 3.3: Schematic representation of the tip movement in force volume (FV), quantitative imaging (QI) and peak force tapping (PFT). The arrows show the movement of the tip.

when moving from one point to the next. In fact, the approach and retract to the sample as function of the time is a sinusoidal function [137]. In each oscillation cycle a whole force-distance curve is acquired. In this mode force curves can be acquired at frequencies between 1 - 10 kHz. It is important to notice that this frequency is much lower than the resonance frequency of the cantilever. Overall, this method combines the advantages of AC modes (fast and soft imaging) and contact modes (good force control) and it provides thus a good compromise for mapping mechanical properties.

This technique, similar to the other force spectroscopy based approaches, has been applied to quantify the elastic properties of soft as well as moderately hard nanomaterials with a elastic modulus lower than ca. 100 GPa [217]. Usually measurements are carried out at 2 kHz with typical peak to peak amplitudes in air of 300 nm. The key parameters to optimize the tracking are the peak force setpoint and the gains, which differ a lot from regular tapping mode.

3.1.3 Tip-sample interaction models

Since the force between two surfaces depends on both the material properties and the geometry of the contact, several models have been developed to calculate the Young's modulus. The difference between one model and the other is basically the forces that they take into account. All these models have in common that they are only valid for elastic deformations of the material. It is possible to determine when a plastic deformation is being made in the sample, through the force-distance curve, as shown in figure 3.4. With a good control on the applied force it is relatively easy to stay below the yielding point. It is worth to note that not only the magnitude of the applied force, but also the

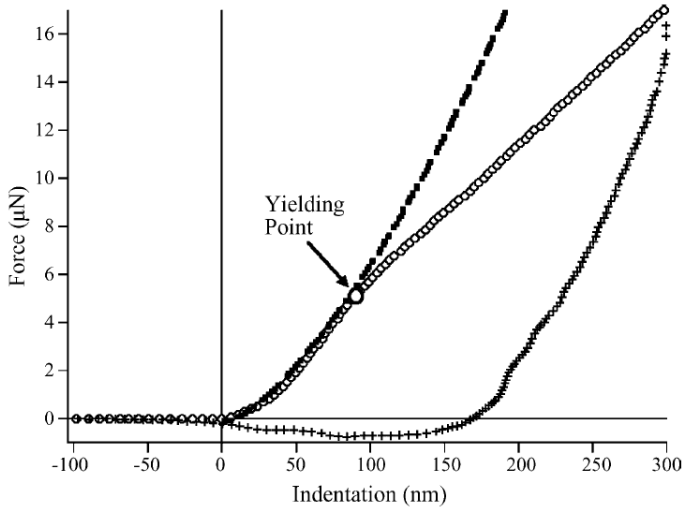

Figure 3.4: Force-distance curve in air on PBMA at 30° C. The approach curve (open circles) is fitted using the Hertz model (dashed line). [138]

indentation velocity may have an influence. Another important thing to consider when AFM nanoindentation measurements are performed is that an elastic deformation should not lead to hysteresis, but friction can produce it. When the tip gets into contact with the sample and the piezoelectric translator keeps approaching, the tip may slide over the sample surface due to the tilt in the cantilever. Indeed, the probe is not placed parallel to the surface, but it has an inclination of 7-20° to assure that the tip is the first thing to touch the sample.

A few important models that have been proposed to describe the tip-sample interaction are listed below.

- **Hertz Model**: Describes the elastic interaction between two geometrical objects. In AFM mechanics the tip is usually approximated by a sphere in contact with an infinite plane [224, 228].

- **Derjaguin Muller & Toporov model (DMT)**: It is similar to the Hertz model, but it takes into account the adhesion forces outside the contact area. It is valid for stiff and small contacts, where $F_{adh} << F_{ts}$ [229].

- **Johnson Kendall Roberts model (JKR)**: Defines the interaction between objects that have a small Young's modulus and large adhesion and contact area. The tip is approximated by a cone in this case. It is a good model to analyze soft biological samples [230].

- **Tatara Model**: It describes the contact mechanics of a finite sized object which has similar dimensions than the tip. In this case the deformation is symmetrically

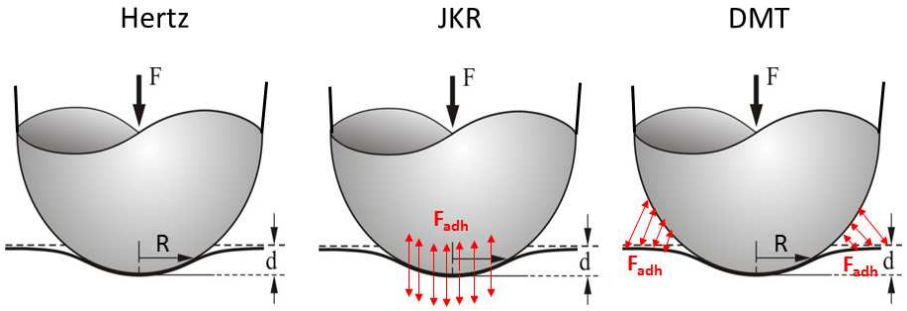

Figure 3.5: Model of a spherical tip in contact with a flat surface

generated on both sides of the sample, one in contact with the tip and the other in contact with the substrate. It is proposed to study nanoparticles [231].

- **Bottom effect cone correction (BECC)**: This model was recently introduced by Gabara and Chadwick to eliminate the influence of the stiffness of the substrate in the case of soft samples [232].

In this work we used the Hertz and DMT models to calculate the Young's modulus, since they appear the most adequate for our samples. The type of contact is very important in these models. In AFM two geometries are normally used, either a sphere or a cone in contact with a plane. Indentations deeper than ca. 2 nm produced irreversible damages to the SCO materials we tested. A good approximation of the shape of the tip in the case of such small indentations is a sphere that gets into contact with a flat surface, as shown in figure 3.5. In the following we discuss only this geometry.

3.1.3.1 Hertz model

Hertz analyzed the stresses at the contact of two elastic solids. In this model the adhesion of the sample is neglected and it is assumed that there are no other forces than elastic stress. Therefore, this model can only be applied when the surface forces are much smaller than the maximum applied force. The force between the tip and the sample is given by:

$$F_{ts} = \frac{4}{3} E * \sqrt{R(d - d_0)^3} \tag{3.12}$$

where E^* is the reduced elastic modulus, R is the radius of the tip and $d - d_0$ is the sample deformation.

The reduced Young's modulus is defined by:

$$E^* = \left[\frac{1 - \nu_s^2}{E_s} + \frac{1 - \nu_{tip}^2}{E_{tip}} \right]^{-1} \tag{3.13}$$

where ν_s is the Poisson's ratio of the sample, ν_{tip} is the Poisson's ratio of the tip, E_s is the

Young's modulus of the sample and E_{tip} is the Young's modulus of the tip. In the case of soft samples, $E_s << E_{tip}$ and the second term in equation 3.13 can be neglected. The Poisson's ratio is often not known, but a good estimation can be made in most cases.

3.1.3.2 Dejarguin Müler and Toporov model (DTM)

This model uses the geometry of the Hertz model, but it assumes in addition that long-rage adhesion forces act outside the contact area. The forces involved in the tip-surface interaction are described by:

$$F_{ts} = \frac{4}{3}E^*\sqrt{R(d-d_0)^3} + F_{adh} \tag{3.14}$$

where F_{adh} is the adhesion force. This latter as well as the sample deformation are determined from the force spectra, as shown in figure 3.2. On the other hand, a further calibration is needed to determine the tip radius.

Tip size calibration

Knowing the tip dimensions accurately is essential to calculate the Young's modulus and several methods have been developed to this aim. For small indentations of around 1 nm, were the tip is approximated to a sphere, the radius of the tip is usually estimated by two different methods using either a so-called "tip characterizer" or a reference sample with known Young's modulus. The tip characterizer consists of a rough, hard surface (e.g. Si or SiO_2). The topography image of this surface depends both on its roughness and on the size of the tip. This latter is obtained by deconvolution. An important drawback of this method is that it might damage the tip. Another option is to use a reference sample with an E value near to that of the sample. Since the Young's moduli of the samples studied in this thesis fall between 1-10 GPa, we used a Polystyrene calibration sample ($E = 2.7$ GPa, $\nu = 0.35$) to determine the tip radius.

3.2 Preliminary tests

Variable temperature quantitative AFM imaging of samples with unknown elastic properties (i.e. our SCO samples) is very challenging. For this reason we started this work with test measurements on PMMA (polymethyl methacrylate) films, with well documented properties. The aim of these tests was to evaluate the efficiency of different AFM methods which were available for us locally (i.e. tapping, contact and peak force tapping (PFT)), to better understand their advantages and disadvantages and to develop our own methodology for thermomechanical measurements on SCO compounds.

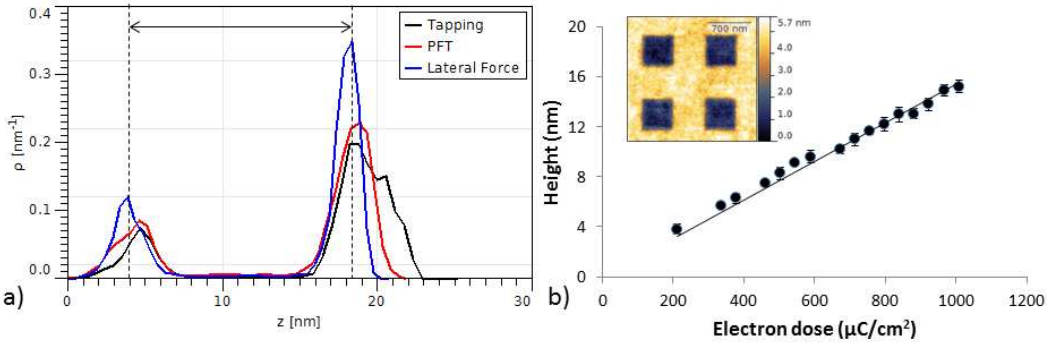

Figure 3.6: a) Height distribution histogram of the patterns generated by e-beam irradiation on a PMMA film (dose = 1050 μC/cm^2) obtained by different AFM modes. b) Plot of the depth of the patterns vs the electron dose. The straight line is a linear fit.

As a test sample a layer ($\approx$ 300 nm) of PMMA was used. Square patterns (250 x 250 nm) were engraved in the films by a focused electron beam using different doses (70 - 2500 μC/cm^2). (These samples were prepared by Franck Carcenac at the LAAS-CNRS using a RAITH e-beam lithography machine.)

3.2.1 Tests in ambient conditions

All measurements presented in this section were performed in ambient air at room temperature unless otherwise stated. Topography measurements were carried out in amplitude modulation tapping (both repulsive and attractive regimens), PFT and contact modes using a Dimension Icon (Bruker) instrument and appropriate tips (Arrow^{TM} NC (Nanoworld), MPP-11120 (Bruker) and SNL (Bruker), respectively). Mechanical properties were inferred from phase images (tapping mode), QNM images (PFT mode) and lateral force images (contact mode).

PMMA is most commonly used as a positive resist for e-beam lithography. The electron beam causes scission of the polymer chains, hence it becomes softer and more soluble in the developer. The irradiated zones can be identified as sunken areas in the sample topography. Since the number of affected polymer chains is proportional to the electron dose, the depth of the irradiated patterns is expected to increase with the dose. Indeed, topography AFM images show a nearly linear augmentation of the the depth as a function of the dose (figure 3.6). No difference was observed in the topographic images between the different modes, tips and acquisition settings.

In phase imaging mode a contrast between the irradiated and non irradiated zones is observed in both attractive and repulsive modes as shown in figure 3.7. Phase imaging is related to inelastic interactions between the tip and the sample, i.e. it is a measurement of the dissipated energy and reflects the difference in the viscoelastic properties of different points of the surface. The phase interactions can be very different in the attractive (non-

contact) and repulsive (intermittent contact) regimens. In the attractive regimen the phase angle values inside the square were found lower than outside, while the opposite trend was observed in the repulsive regimen (figure 3.7 a-d). When the tip is in the attractive regimen $\omega < \omega_0$, as already stated in section 3.1.1. The phase lag will be higher between the excitation and the response of the cantilever when the interfacial adhesion forces are stronger and therefore the difference between ω and ω_0 will increase. Taking into account equation 3.1 we can conclude that higher adhesive forces will lead to lower phase angles. This is exactly what we observed in the case of PMMA, where the irradiated areas should present a higher adhesion than the rest of the sample. On the other hand, in the repulsive regimen the harder the surface is, bigger will be the force that exerts the material on the tip. Hence both ω and the phase angle will increase. Since the PMMA is softer inside the irradiated zone the phase value should be lower. However in our AFM images exactly the opposite can be observed. This inversion of the phase has been already reported for high oscillation amplitudes [218] and it has been associated to an increase in the energy dissipation caused by viscous damping when the oscillation amplitude increases. Even if the interpretation of these results seems difficult there is a clear relationship between the viscoelastic properties of the sample (i.e. the dose) and the change of the phase angle in each case. Taking into account that the e-beam irradiation changes only slightly the viscoelastic properties of PMMA we can conclude that phase imaging is a sensitive technique to detect changes of these properties. One evident drawback of this method is that it is very dependent of the contact area, hence different topographic slopes will give different phase angles. In the case of our sample important phase angle changes are clearly observed around the edges of the irradiated zones. However, these changes are not related to a change in the mechanical properties of the sample, but to a difference in the sample topography. In other words, if the interpretation of phase imaging results difficult for flat samples, it becomes even worst for rough samples. Nevertheless, it is an interesting tool to study composites since it can reveal details that can not be observed in topography images.

Tapping studies were also performed in phase modulation mode using a Nanonics Multiview 2000 instrument (for more details see section 2.1). In this case the phase channel will show the feedback error and the energy dissipation will be observed in the amplitude channel. This system only works in the repulsive regimen. As stated in section c), a change in the amplitude can be associated to a change in dissipation. Figure 3.8 shows the results obtained with the irradiated PMMA sample. Similar to amplitude modulation imaging, there is an artifact around the border of the irradiated area, which is related to the topography. A difference in the amplitude signal is observed between the irradiated and non irradiated zones in the sample, although a clear tendency with the electron dose was not obtained. It may be worth noting that the contrast in the amplitude channel was better for higher gains and shorter probes.

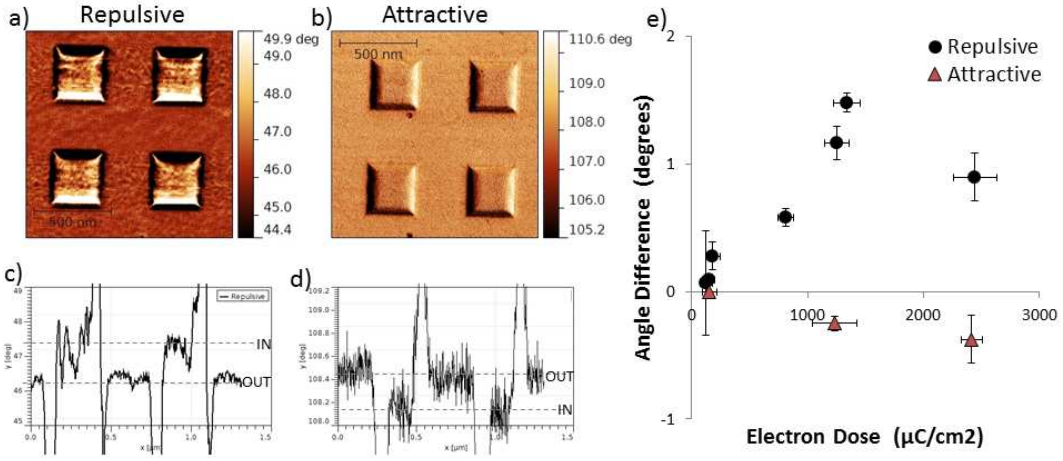

Figure 3.7: (a,b) Phase images of square patterns fabricated by e-beam irradiation on a PMMA film, a) repulsive regimen, b) attractive regimen. Panels c) and d) show the average cross-sections of images (a) and (b), respectively. e) Plot of the phase angle difference between the irradiated and non-irradiated regions as a function of the dose.

On the whole tapping mode appears as a fast, sensitive, non-invasive and easy-to-implement approach to detect changes in viscoelastic properties, but the data interpretation and quantification remains delicate.

PFT-QNM images were obtained using a RTESPA tip ($k \approx 40$ N/m). Deflection sensitivity was calibrated on a silicon wafer and the spring constant was obtained by thermal tuning. The radius of the tip (4.5 nm) was determined with a tip characterizer (titanium roughness sample, Bruker). The maximum force was set to 40 nN and the DMT model was used to calculate the Young's modulus. The Poisson ratio of PMMA (0.3) was taken from reference [233].

Figure 3.9 shows the images acquired around the irradiated patterns for different channels, including topography, Young's modulus, adhesion and deformation. A few representative force-distance curves are also shown. A difference between the irradiated and non-irradiated zones was observed in all detection channels, though the uncertainty is rather high in the case of the deformation data. It must be remarked that the signal in the deformation and adhesion channels is deteriorated due to optical interference phenomena. This is a well-known artifact in force spectroscopy (see more details in appendix A). In addition artifacts occur around the borders of the irradiated areas due to the change in the contact area. A plot of the adhesion force and the Young's modulus as a function of the electron dose is presented in figure 3.10. From this plot, we can conclude that the PMMA becomes softer and more adhesive as the electron dose increases. These results are congruent with the expected properties of the sample. In particular we must underline the high sensitivity of the Young's modulus measurement: changes of only a few percent can be quantified. This provides a significative advantage over phase imaging in tapping mode

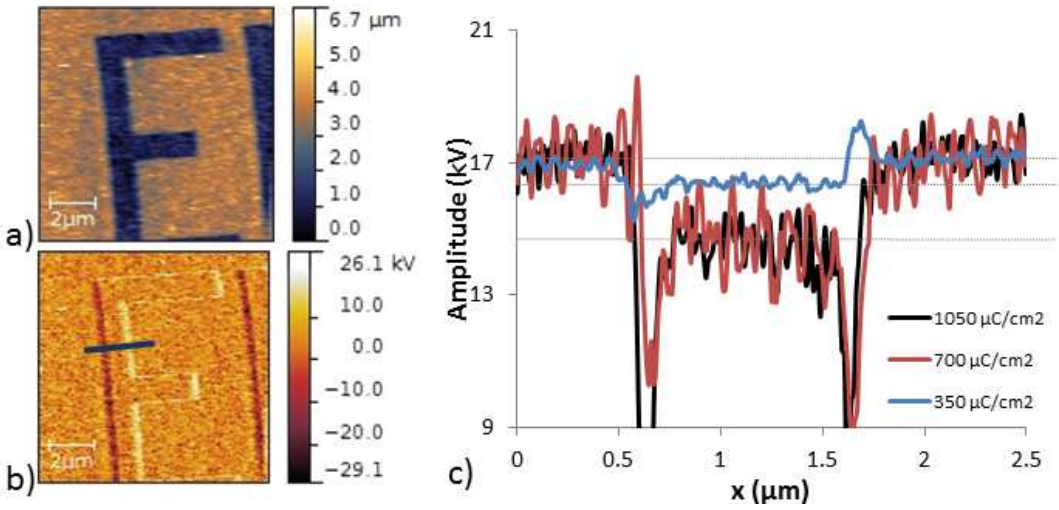

Figure 3.8: a) PM-AFM topography of a PMMA film where the letter E was obtained by electron beam irradiation, b) The amplitude channel of the same scan. c) Cross section of the letter E (indicated by a blue line in (b)) for different doses.

since we measure a material property, which can be determined also by other methods and compared with the AFM data. In addition PFT-QNM remains reasonably fast and non-invasive, even in comparison with tapping mode. (A Young's modulus map with a resolution of 256 X 128 points can be obtained in less than ten minutes.) One should note also that the Young's modulus obtained for the PMMA (ca. 3 GPa) by PFT-QNM corresponds well to the literature data. However, we remarked that this value increases along successive scans. This artifact, which is related to the change of the tip radius, will be examined more in detail in section 3.3.

Exploratory studies were also performed in Lateral Force Microscopy mode using an SNL contact tip (k = 0.36 N/m). LFM is performed in contact mode. It consists in recording the lateral deflection of the cantilever, which provides information about the friction coefficient between the tip and the sample. Obviously a measurement of the friction coefficient is possible if the deflection sensitivity is calibrated in the lateral direction. By convention, negative (positive) values refer to the left-hand (right-hand) side of the photodetector. Figure 3.11 shows LFM images and the corresponding cross-sections obtained on the PMMA test sample around an irradiated pattern. A clear contrast is observed between the irradiated and the non-irradiated zones. From these data we can infer that the friction coefficient is higher inside the irradiated zone. To be noted that during the trace acquisition (i.e. scan from left to right) the tip deflects more to the right inside the irradiated zone resulting in an increase of the LFM signal. In the retrace curves (i.e. scan from right to left) the contrast inverses, but this is expected since the tip is deflected in the opposite direction. Figure 3.11 shows also the lateral deflection change as a function of the electron dose. A clear tendency is observed, the friction coefficient

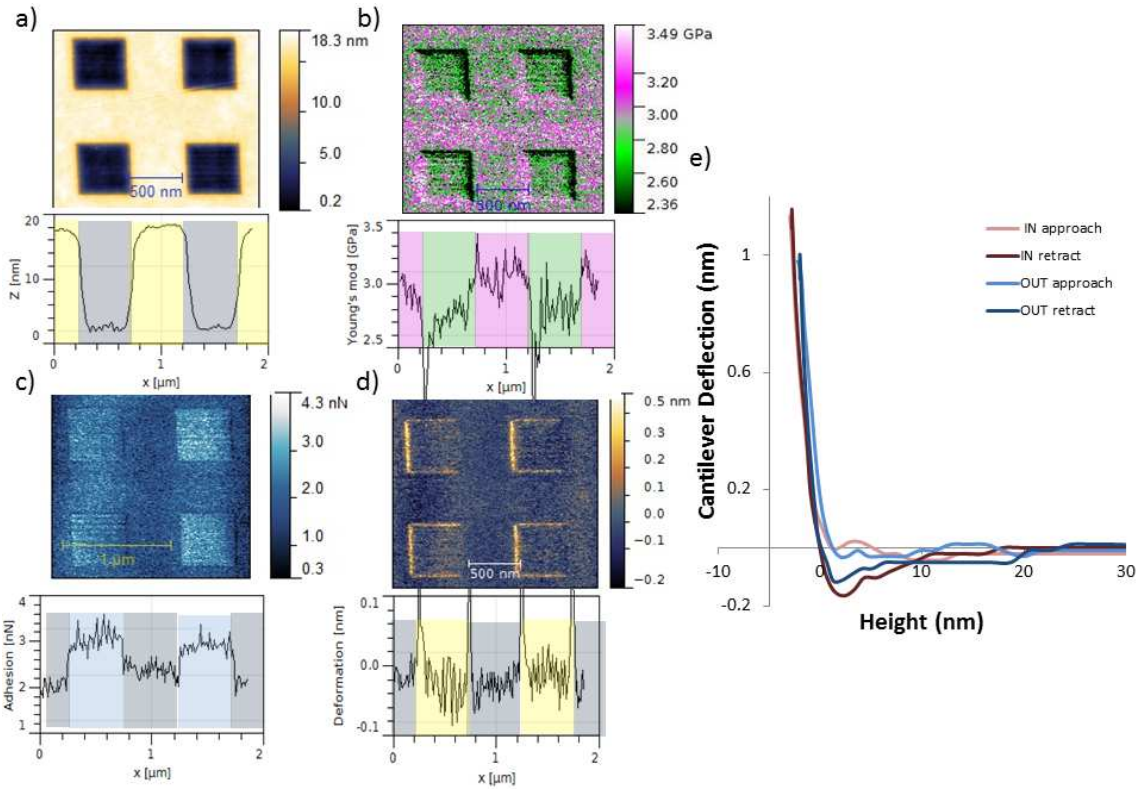

Figure 3.9: PFT-QNM images of a thin film of PMMA with squares made by electron beam irradiation. For each image a cross section across the squares is also shown. a)Topography, b) Young's modulus, c) adhesion and d) deformation. e) Selected representative force-distance curves recorded inside (red) and outside (blue) of the squares.

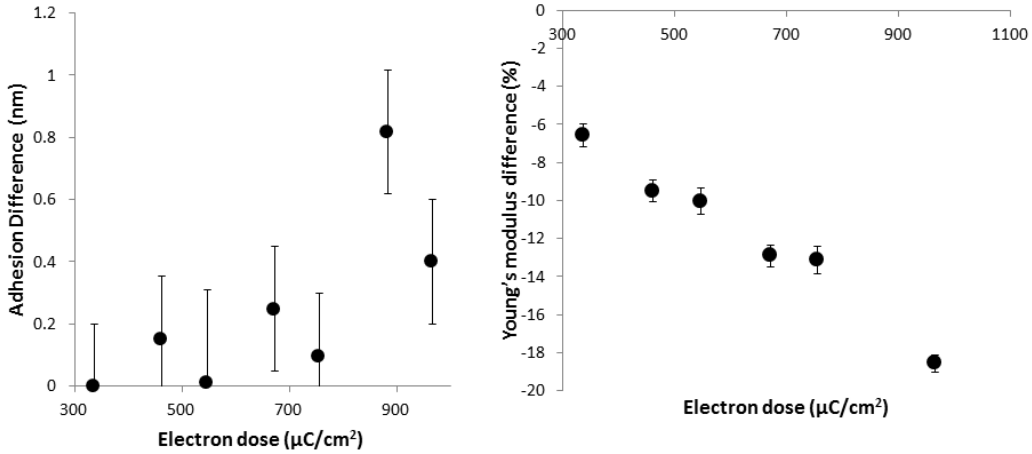

Figure 3.10: Variation of the adhesion force and the Young's modulus as a function of the dose for a thin film of PMMA irradiated by an electron beam. (The difference is obtained by subtracting the data obtained after irradiation from the initial values.)

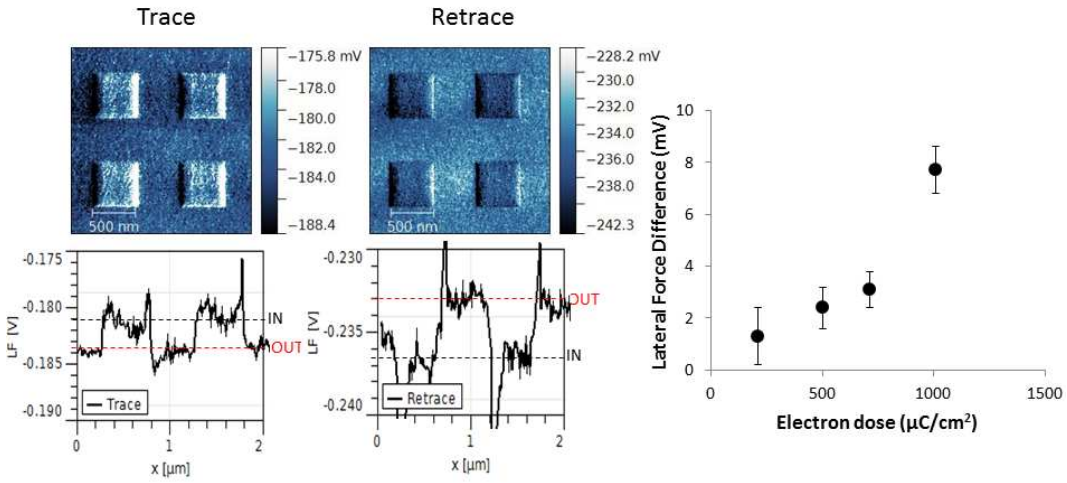

Figure 3.11: LFM images of a section of squares patterned by e-beam in a PMMA film. The corresponding cross-sections for the trace and retrace signals are also shown in the images. The lateral force difference between the irradiated and non-irradiated zone is also plotted as a function of the electron dose.

is higher for higher electron doses. We can explain this by the higher adhesion of the irradiated zone, which must lead to higher friction coefficients.

These tests revealed that each mode provides a useful (and complementary) contrast between the irradiated and non-irradiated zones of the test sample. Among them PFT-QNM and LFM can provide quantitative information about the sample mechanical properties, but the former gives more detailed and better defined data and introduces less damage to the sample. Further studies were therefore restricted to this mode.

3.2.2 Variable temperature tests

As already discussed in the precedent chapter, changing the sample temperature during SPM measurements adds considerable difficulties to the data acquisition and even more importantly to the data analysis. In the case of the mechanical property studies an obvious problem is related to the fact that the properties of the probe (spring constant, resonant frequency, etc) change with the temperature. To evaluate the importance of these issues we have carried out variable temperature measurements using the PMMA test sample. A film of PMMA (280 nm) was spincoated on the same nanowire heater which was used in our NSOM studies (for details see section 2.2.1). As discussed before, using this nanoheater the evolution of the sample properties can be studied more conviniently as a function of the temperature when using an SPM.

Before the measurements on the PMMA we have first investigated the effect of temperature on the properties of the AFM probe. Two experiments were carried out. First, a silicon substrate was heated in ambient air using a heating stage, while the

Temperature (K)	Deflection sensitivity (nm/V)	Spring constant (N/m)
297	127	94
313	128	90
343	122	89
373	123	94

Table 3.3: Deflection sensitivity of the detection system and spring constant of the probe at different temperatures.

probe (MPP11120, Bruker) was also heated using an internal circuit and the deflection sensitivity was determined for different temperatures (from 297 K to 373 K). In the second experiment only the retracted probe was heated in air and the spring constant of the cantilever was measured using the thermal tuning method. The results are compiled in table 3.3. In the investigated temperature range (297-373 K) we observed no substantial change in the properties of the probe. For this reason, this effect will be neglected in the following experiments.

In figure 3.12 the Young's modulus map of a PMMA film spin coated on a gold nanowire (Si substrate) are presented for 1 mA and 28 mA current passing through the nanowire. The nanowire is very well delineated and the heat is well confined on the nanowire. The Young's modulus, calculated using the DMT model, is virtually constant for applied currents between 0 mA and 25 mA. As we approach to the melting point of PMMA the Young's modulus decreases from 3.4 to 0.8 GPa between 413 and 473 K (i.e. 25-28 mA). The variation of the elastic modulus with the temperature reproduces the data reported elsewhere for bulk PMMA [234] (figure 3.12 (g)). The thermal expansion of PMMA is clearly observed for currents higher than 12 mA, but the height of the film decreases near 28 mA, probably because the material melts. An image of the topography recorded at room temperature before and after heating with 28 mA is shown in figures 3.12 e and f, revealing a flow of the material in the heated area (i.e. on the nanowire).

Further tests were performed on PMMA spin coated on nanowires (5 wires, each with a width=0.5 μm, thickness=50 nm and length=80μm), but this time on a glass substrate (figure 3.13). The heat conductivity of glass is much lower than that of silicon, hence on glass substrates the heat spreads laterally over a larger area. In consequence the change of elasticity is not restricted to the heating wires. For this reason a larger sample area was scanned to observe the change of Young's modulus as a function of the distance to the wires. In this case the Young's modulus was calculated using the Hertz model, but this has not changed the result, we obtained the same value for E (3.0 GPa). Figure 3.13 shows the variation of E in the direction perpendicular to the nanowires for two current values (0 and 13 mA). As expected the Young's modulus difference between the two curves (i.e. between room temperature and high temperature) is not restricted to the wires, but also observed until at least 5 μm away from the nanowires. This result

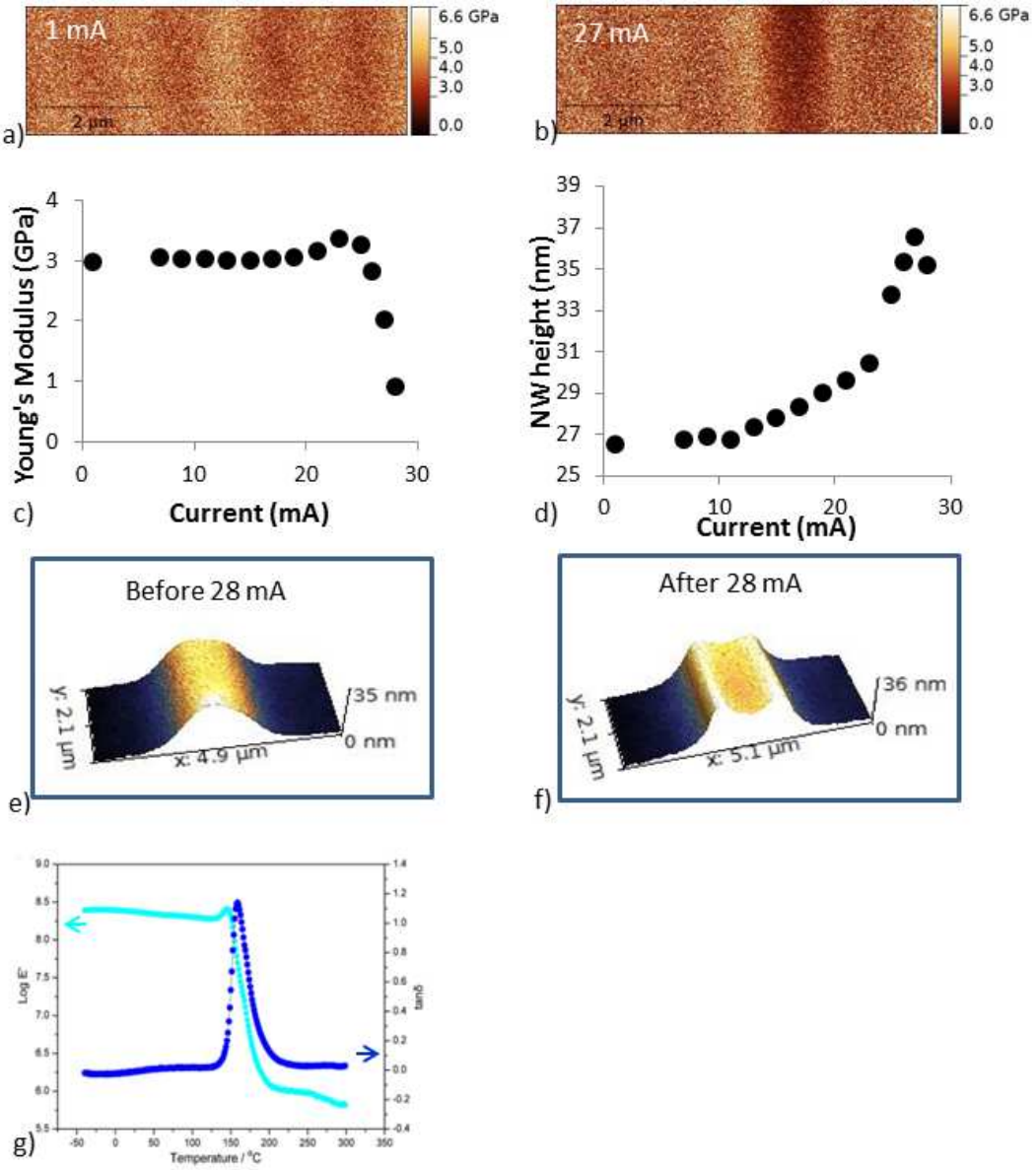

Figure 3.12: Young's modulus maps for a film (300 nm) of PMMA spin coated on a gold nanowire (Si substrate) for an applied current of a) 1 mA and b) 27 mA. Plots of the c) Young's modulus and d) the height of the PMMA film on the wire as a function of the temperature. Topography of the PMMA film at room temperature d) before and e) after applying 28 mA through the nanowire g) Temperature dependence of the storage modulus and loss tangent for bulk PMMA [234].

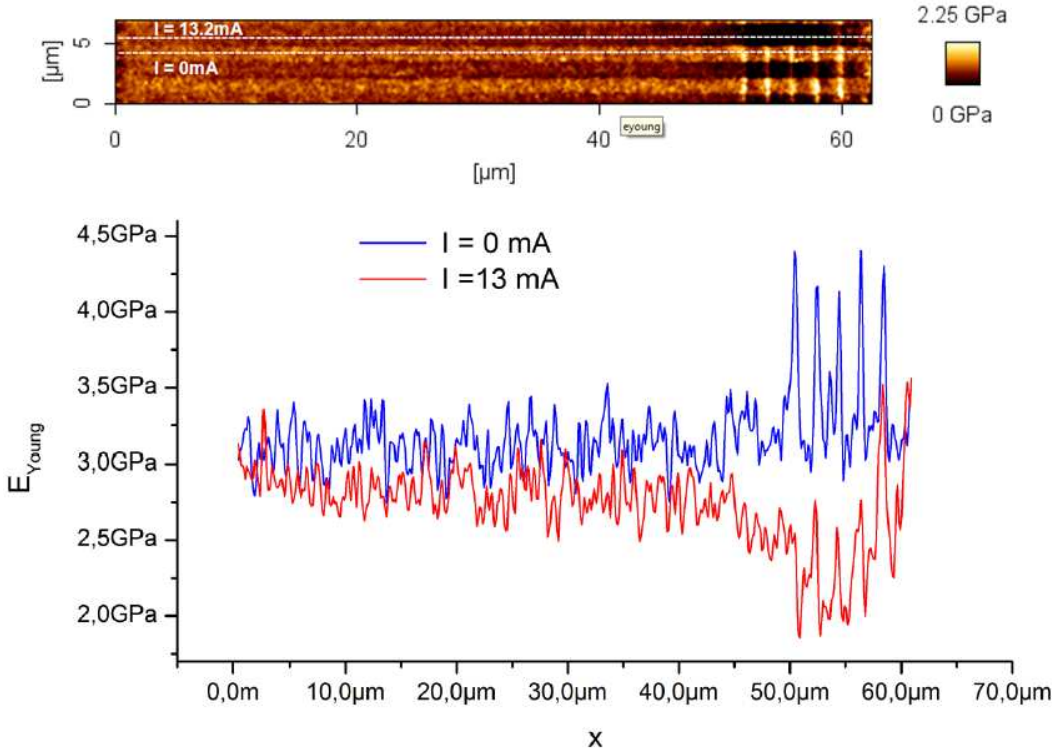

Figure 3.13: Young's modulus map of a PMMA film spin coated on five nanowires (patterned on a glass substrate) for different applied currents (0 and 13.2 mA). Cross-section of the two white lines shown in the Young's modulus map. The radius of the tip was 4 nm and the maximum applied force was 20 nN.

contrasts with those obtained for Si substrates where a few hundred nanometers away from the wires no heating occurs.

In summary these variable temperature mechanical measurements on PMMA proved that PFT-QNM can be used to follow physical phenomena, which lead to a change of the sample stiffness. In a not too large temperature range the properties of the probe remain reasonably constant. The local heating approach using nanowires allows for an easier observation of the temperature effects and help also the data treatment. In the rest of this chapter all the experiments were performed on gold nanowires patterned on Si substrates, since their heat confinement is tighter.

3.3 $[Fe^{II}(hptrz)]_3(OTs)_2$ thin films

The study of mechanical properties of crystals or nanoparticles is delicate, since small movements of the particles may lead to large errors in the Young's modulus measurement. To avoid this problem we decided to work on spin crossover thin films. As described in detail in the previous chapter $[Fe^{II}(hptrz)]_3(OTs)_2$ films doped with Rhodamine 110 were spin coated on gold nanowires (silicon substrate) and analyzed using PFT-QNM. (N.B. We

have also carried out measurements on the $[Fe(Htrz)_2(trz)]BF_4$ nanoparticle films, but up to now we could not obtain well reproducible mechanical data on this sample. We attribute this to problems related to the low adherence of the particles on the substrate. Preliminary data were also acquired with composite films of $[Fe^{II}(hptrz)]_3(OTs)_2$ in PMMA matrix (see appendix B))

AFM analysis were performed at room temperature in air using a Dimension Icon instrument (Bruker) and reflective Al-coated Si probes (MPP11120, Bruker). These latter are characterized by a nominal resonance frequency of 300 kHz, a spring constant of 40 $N{\cdot}m^{-1}$ and a tip radius of 8 nm. AFM images (typically 8 μm X 4 μm, 256 pixels X 128 pixels) were recorded at a scan rate of 0.3 Hz in peak force tapping mode at 2 kHz modulation with quantitative nanomechanical analysis (QNM). The peak force setpoint (25 nN) was chosen to achieve ca. 1-2 nm sample deformation. The deflection sensitivity of the photodetector was determined on a silicon sample, while the spring constant of the cantilever was obtained by thermal tuning. Both parameters were found to be nearly independent of the temperature in the investigated range (see section 3.2.2 for details). A polystyrene calibration sample (Bruker PSFILM, E = 2.7 GPa, Poisson's ratio = 0.35) was used to determine the tip radius by means of the Derjaguin Müller Toporov model, as implemented in the software of the AFM instrument. The Poisson ratio used for the SCO material was 0.4. This value is just an estimation and does not take into account the possible difference between the two spin states. Nevertheless, we should note that the calculated values of E are not very sensitive to small changes of ν. The spin-transition curves of a sample were constructed using 28 AFM images, which were acquired during a period of ca. 6 h. This implies a non-negligible sample drift, which becomes especially critical when investigating non-homogenous samples and/or rough surfaces. For this reason the AFM images must be systematically aligned, which was achieved using the 2D cross-correlation method described by Quintero et al [9].

Briefly this method consists of aligning two or more images of the same scene. Our routine compensates automatically any drift of the sample obtained during the experiments. It receives a stack of images (in TIFF format) and asks from the user two inputs: (1) a section of interest or feature in the 1st image of the stack that will be tracked during the alignment process and (2) at least three reference points present in all the images of the stack which would be used later for fine tuning of the alignment. Once these parameters are defined by the user, the routine executes the normalized 2D cross-correlation process between the feature and the rest of the images of the stack following equation 3.15:

$$CCR(u,v) = \frac{\sum_{x,y}\left[f(x,y) - \bar{f}_{u,v}\right]\left[t(x-u,y-v) - t\right]}{\sum_{x,y}\{\left[f(x,y) - \bar{f}_{u,v}\right]^2 \sum_{x,y}\left(t(x-u,y-v) - \bar{t}\right)^2\}^{0.5}} \tag{3.15}$$

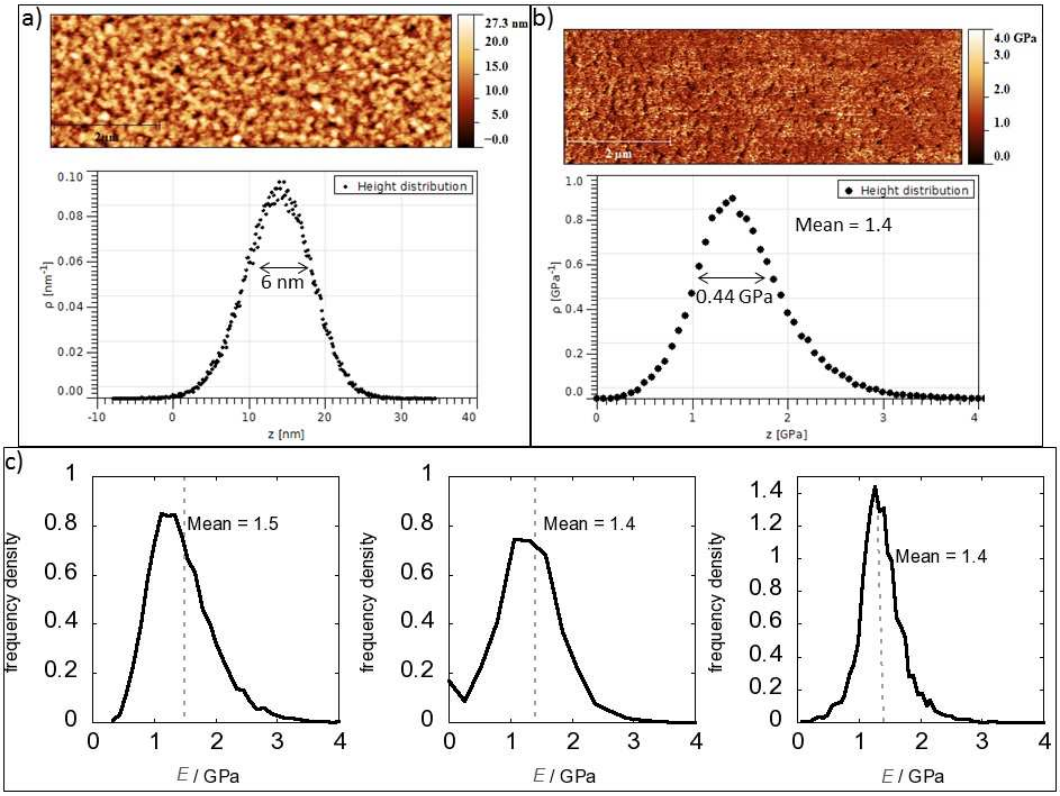

Figure 3.14: PFT-QNM images and associated data histograms for a $[Fe^{II}(hptrz)]_3(OTs)_2$ thin film at room temperature. a) Topography and b) Young's modulus. c) Histograms of the Young's modulus of different samples of the same compound deposited in the same way on similar substrates. Measurements and data treatment were done using the same protocol, but with a different AFM tip in each case.

where $CCR(u, v)$ is the crosscorrelation, $f(x, y)$ is the image to be analyzed, t is the feature, $\bar{t}$ is the mean value of the selected feature and $\bar{f}_{u,v}$ is the mean value of $f(x, y)$ in the region under the feature.

First the sample topography and stiffness were investigated at room temperature. Although the film is very homogeneous, it has a roughness of approximately 6 nm due to the polycrystalline nature of the sample, which is deduced from the width of the height distribution peak (see figure 3.14 (a)). This topography produces an inherent error in the determination of E of 0.4 GPa, as inferred from the width of the Young's modulus distribution in figure 3.14 (b). At room temperature the Young's modulus of the compound is $E = 1.4 \pm 0.4$ GPa. This was calculated using the DMT model. To test the reproducibility of E we performed four measurements in the same experimental conditions, but using in each case a different tip and a different sample. The obtained value was consistently the same as shown in figure 3.14 (c). This proves that our experimental approach provides an excellent precision for the measurement of the Young's modulus.

On the other hand, the accuracy of this Young's modulus value is more difficult to

evaluate. The obtained value of the Young's modulus (ca. 1.4 GPa) seems reasonable in comparison with the few reported values of elastic moduli in SCO materials (typically a few GPa. [4, 168–170]). However, it is very important to keep in mind that several factors can influence the measured absolute values of the Young's modulus of such thin films, such as the approximations inherent to the contact mechanics model (tip radius, shape, etc.), the experimental uncertainties, the presence of adsorbed molecules on the surface, as well as the roughness and even the thickness of the film [138].

This uncertainty in the absolute value of E will affect to a lower degree, however, the measured variation of the Young's modulus between the two spin states (which is our main interest), since the same error will be propagated through the whole series of scans. Hence, the variation of the elastic moduli between the two spin-states should be a more robust observable.

In a first time scans in PFT mode were performed for an applied current of 1 mA (295 K, LS state) and 21 mA (342 K, HS state) in order to obtain a preliminary idea of the expected changes. Figure 3.15 shows images and cross-sections in the two spin states of the material for five different AFM channels (topography, Young's modulus, adhesion, deformation and dissipation). The deformation of the sample is very similar over the whole imaged surface and for both temperatures. A similar deformation means similar contact area, which is obviously a very useful feature for quantitative analysis. In all channels, except the dissipation, the signal changes between the two measurements (if any) are observed only on the area heated by the wire. Indeed, far from the wires the sample remains at room temperature and we do not expect thus any change in its properties. We believe that the dissipation data reflects more artifacts due to laser interference than the material properties. It may be worth noting that interference effects are also visible in the adhesion and Young's modulus channels.

From only two images it is impossible to conclude about the effects of the spin transition because these are convoluted with ordinary thermal effects, such as thermal expansion. Hence a series of data at different temperatures must be acquired both in heating and cooling to deconvolute these different phenomena, to check their reversibility and also the eventual presence of thermal hysteresis. However, for a quantitative study of the mechanical properties during the course of several scans, the wearing of the tip becomes a critical issue. For example, studies of the wear of different tips have been made by Vahdat et al. in tapping mode [235]. In this study, the authors show that the radius of the silicon tip changes from the first scan, and after nine scans the radius is doubled. We have decided to carry out a similar test on our sample. Figure 3.16 (a) shows the variation of the Young's modulus observed over 17 successive scans on the same sample area and in the same conditions. The radius of the tip increases from scan to scan due to wear of the tip, producing the wrong impression that the Young's modulus increases with time. Figure 3.16 (b) shows the efficiency of this approach. In order to avoid this, we

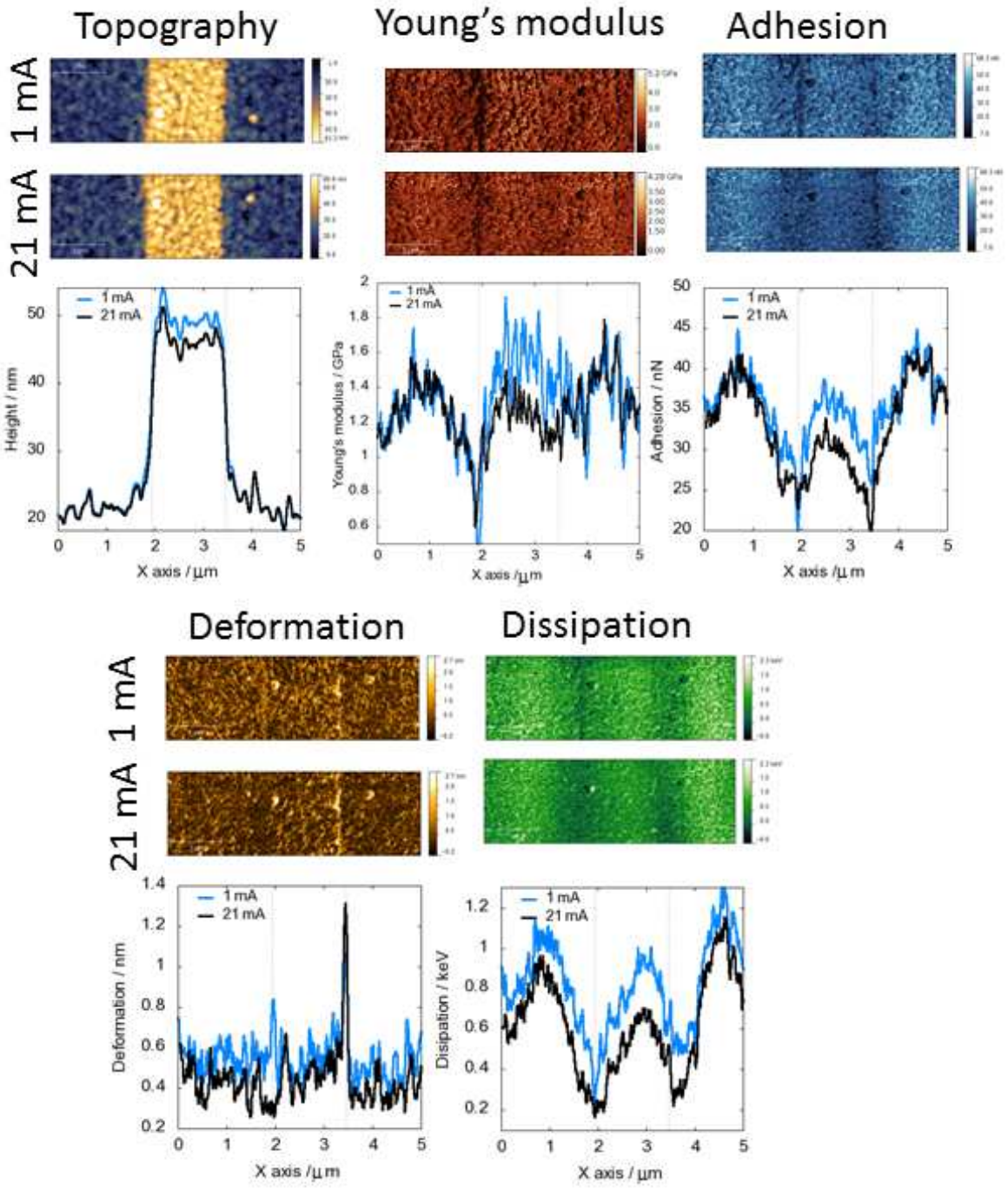

Figure 3.15: AFM maps and the corresponding average cross-sections of the topography, Young's modulus, adhesion, deformation and dissipation of a $[Fe^{II}(hptrz)]_3(OTs)_2$ thin film (40 nm) spin coated on a gold wire. Data are plotted for two different currents (1 and 21 mA) flowing in the wire.

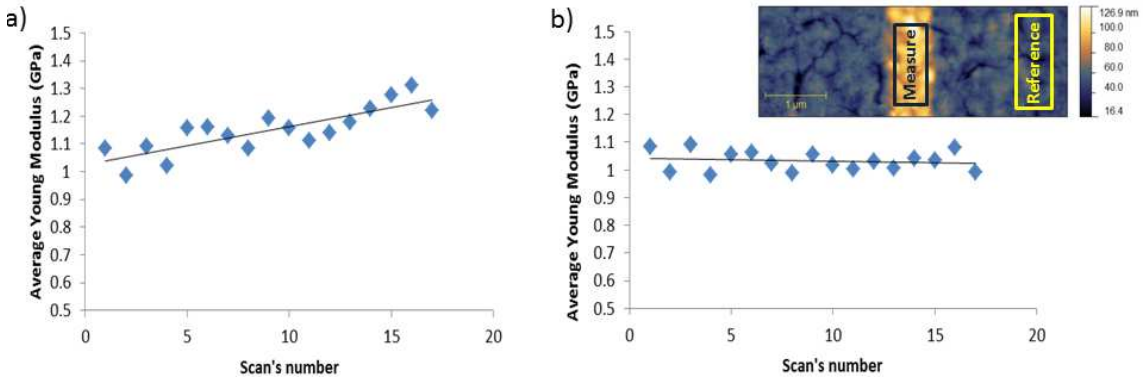

Figure 3.16: Topography image of the $[Fe^{II}(hptrz)]_3(OTs)_2$ thin film sample showing the measurement and reference areas. The plots show the Young's modulus of the measurement area for successive scans without (a) and with (b) the tip radius correction. See the main text for details.

selected a reference area far from the wire and we corrected the tip radius for each scan such a way that the Young's modulus of the reference area was kept constant. In order to acquire a large number of images without the need to carry out a complete tip calibration procedure after each image, we propose to scan always a reference area (next to the area of interest) that would have the same properties in each scan. This information can be used to recalculate the radius of the tip for each scan and obtain quantitative values in each image.

As mentioned above, in this type of measurements oscillations coming from optical interference may be present. This interference is produced because the laser beam is not only reflected by the cantilever, but it traverses the cantilever or "leaks" around its borders and finally reflected on the sample as well (more details can be found in appendix A). It is possible to decrease the interference by assuring a good laser alignment and using highly reflective probes, but in our experimental conditions it was not possible to avoid it completely. When the oscillations are very marked, it is difficult to determine the variations in the adhesion and the dissipation. Therefore we only focused on the variation of the Young's modulus as a function of the temperature.

Figure 3.17 shows the AFM topographic images of a 70 nm thick film of $[Fe(hptrz)_3](OTs)_2$ doped with Rhodamine 110 deposited on a heater made of two parallel Au nanowires. AFM scans were performed in PFT mode for different currents in the wires. In the topography images we observe no substantial change (Figure 3.17 a-b). Though the spin transition is known to induce a spontaneous strain, in our thin layer the associated expansion is expected to be less than 1 nm which remains difficult to detect owing to the non-negligible sample roughness. On the other hand, it is important to notice the absence of any significant sample degradation in the topography scans. The map of the Young's moduli (E) was obtained using the DMT model. The observed values

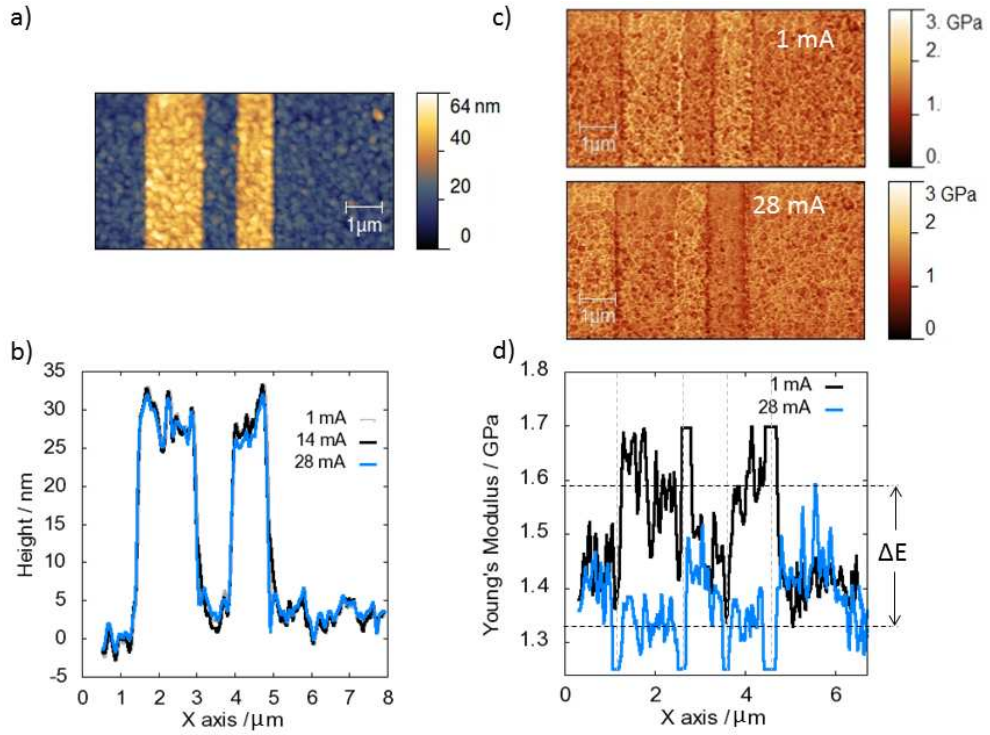

Figure 3.17: AFM study of a thin film (70 nm) of the compound $[Fe(hptrz)_3](OTs)_2$ doped with Rhodamine 110 and spin-coated on two gold microwires. a) AFM topography image. b) Average cross sections of the topography for different currents flowing in the wires (1, 14 and 28 mA), c) Young's modulus maps and d) average cross sections of the Young's modulus for $I = 1$ mA and 28 mA. The two dotted horizontal lines indicate the Young's modulus change ΔE of the film due to Joule heating. The dashed vertical lines show the edges of the wires where measurement artifacts may occur.

of E are not exactly the same above and next to the wires, which is probably related to the fact that the stiffness of gold (79 GPa) and that of the substrate (for SiO_2 $E \approx 75$ GPa) are different and/or the film thickness is not exactly the same on the nanowire and on the SiO_2 substrate. The most important finding here is that an increase of the current to 28 mA in the wires leads to a very substantial decrease of the Young's modulus by ca. 30% (Figure 3.17 c-d). This change is clearly linked to the current increase because no change is observed away from the wires and upon switching the current level back from 28 to 1 mA, the changes are perfectly reversible. These observations have been reproduced several times on the same sample, even two months after the first experiment, as well as on other samples using different wire geometries.

The decrease of the Young's modulus for increasing currents in the wires (i.e., for increasing temperatures) is expected to occur chiefly due to the LS to HS spin transition in the film, since the HS form of the material has a lower stiffness. However, ordinary thermal expansion may also contribute to this effect. It is therefore necessary to correlate the AFM data with independent measurements of the spin-state change of the material.

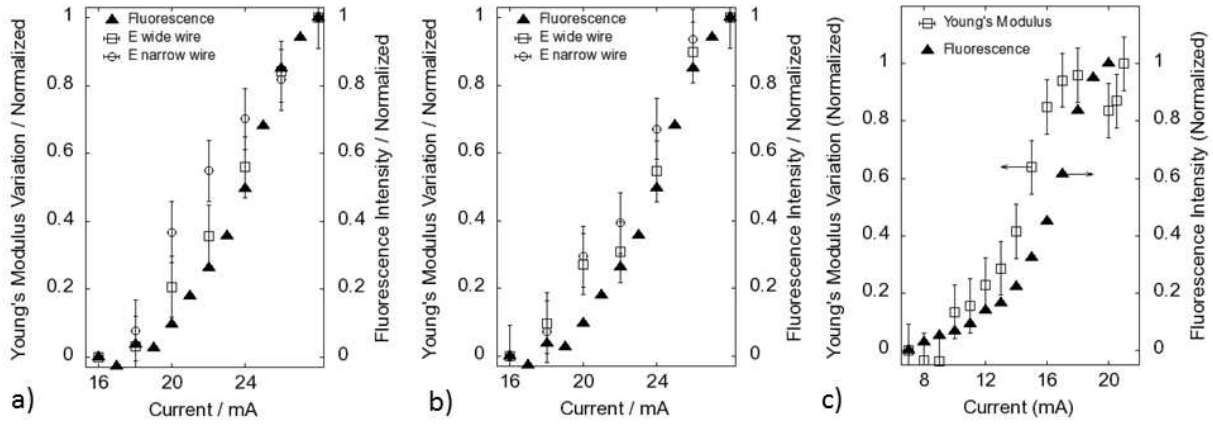

Figure 3.18: Normalized variations of the Young's modulus and that of the fluorescence intensity of a thin layer of $[Fe(hptrz)_3](OTs)_2$ doped with Rhodamine 110 as a function of the current applied to the nanowire heaters. Figures a) and b) show two data series on the same sample (the double wire device), but acquired in one week interval. Figure c) show data for the single wire device. The error bars represent the standard deviations of the measured data points.

As already explained in chapter 2 this can be achieved with this sample by recording fluorescence images as a function of temperature (i.e. applied current). Figure 3.18 shows the (normalized) variation of the fluorescence intensity and that of the Young's modulus of the material as a function of the current applied to the wires. Data are shown for the double wire device (depicted in figure 3.17) and also for the single wire device (depicted in figure 3.15). In each case we observed an increase of the fluorescence intensity for increasing currents, which is an unambiguous indication of the spin transition. The good correlation of fluorescence with the Young's modulus changes proves that the change of this latter arises chiefly as a result of the spin transition. (N.B. Some difference between the fluorescence and the Young's modulus curves can be observed, but one should note that the fluorescence data were obtained in far-field with a spatial resolution, which is comparable with the width of the wires. This means that these data integrate possibly unheated sample area as well explaining their shift towards higher temperatures. It may be worth noting also that different wires produce the spin transition at different current values, which is simply related to the fact that their resistance is different.)

By calibrating the wire resistance against temperature (see section 2.2.1), it is also possible to plot the Young's modulus changes as a function of the temperature. As shown in Figure 3.19 the spin transition is centered around 313 K, which corresponds well to our previous results on these films (See section 2.2.2). The initial room-temperature value of the Young's modulus is reproduced after a full thermal cycle, within the experimental uncertainty, providing evidence that the observed changes are not linked to a sample degradation or instrumental drift. When going from the low spin to the high spin state

the Young's modulus decreases from ca. 1.7 GPa to 1.3 GPa. To our knowledge this is the first time that the Young's modulus and its spin state dependence has been determined for a spin crossover material. For the lack of literature data we can not make really meaningful comparisons, but we can note that the variation of the Young's modulus observed by AFM ($E_{LS}/E_{HS} = 1.33 \pm 0.04$) correlates well with the change of Debye temperature extracted from Mössbauer data for a few SCO compounds (see the introduction of section 3).

One of the key aspects of the present study is that the sample stiffness can be determined with a high spatial resolution. To illustrate this point, figure 3.20 shows the Young's modulus of a film of $[Fe(hptrz)_3](OTs)_2$ as a function of the current intensity in a wire for different regions of interest (ROI) of the film. We were interested in determining the size at which we can still observe the Young's modulus variation. We show that it is possible to follow spin transition on an area of 70 x 70 nm^2. It might be possible to observe the spin transition at lower spatial resolutions, but more resolved images are necessary. We must stress that the spatial resolution of the Young's modulus and the spatial resolution of the thermal spin transition curve is obviously not the same, since this latter is extracted from a series of AFM images, while the former refers to a single image. Nevertheless, the spin transition curves can be retrieved even for very small sample areas.

Another approach to analyze the spatial resolution is based on the fact that the heat is spatially strongly confined to the wire. For example, one can analyze the Young's modulus data in the direction perpendicular to the nanowire. For this purpose, we fixed the size of the ROIs to 70 nm along the x axis (i.e., perpendicular to the wire length). For each ROI selected above the wire, we observe similar changes as in figure 3.17: an increase of E by ca. 400 MPa when going from the HS to the LS phase. As can be expected, this change is fairly homogeneous over the whole surface of the wire. In the immediate proximity of the wire, there is still a small change in the Young's modulus of about 100 MPa. However, more than 200 nm away from the wire we observed no changes. Indeed, one expects that the heat generated in the wires flows away in the direction of the substrate (z axis), since the thermal conductivity of the latter is several orders of magnitude higher than that of the compound. For a more-quantitative discussion, the heat distribution in the devices (both the single wire and the double wire device) has been calculated using finite element simulations by means of COMSOL Multiphysics. (These calculations have been performed by Olena Kraieva and the numerical details have been published in reference [156].) Figure 3.21 shows the results of the simulations as well as ther comparison with our AFM results. Overall there is an excellent agreement between the heat distributions derived from the COMSOL simulations and the Young's modulus distributions inferred from the AFM data. Incidentally we can remark on the basis of this result that this type of thermomechanical measurements might be also used for high spatial resolution thermometry purposes.

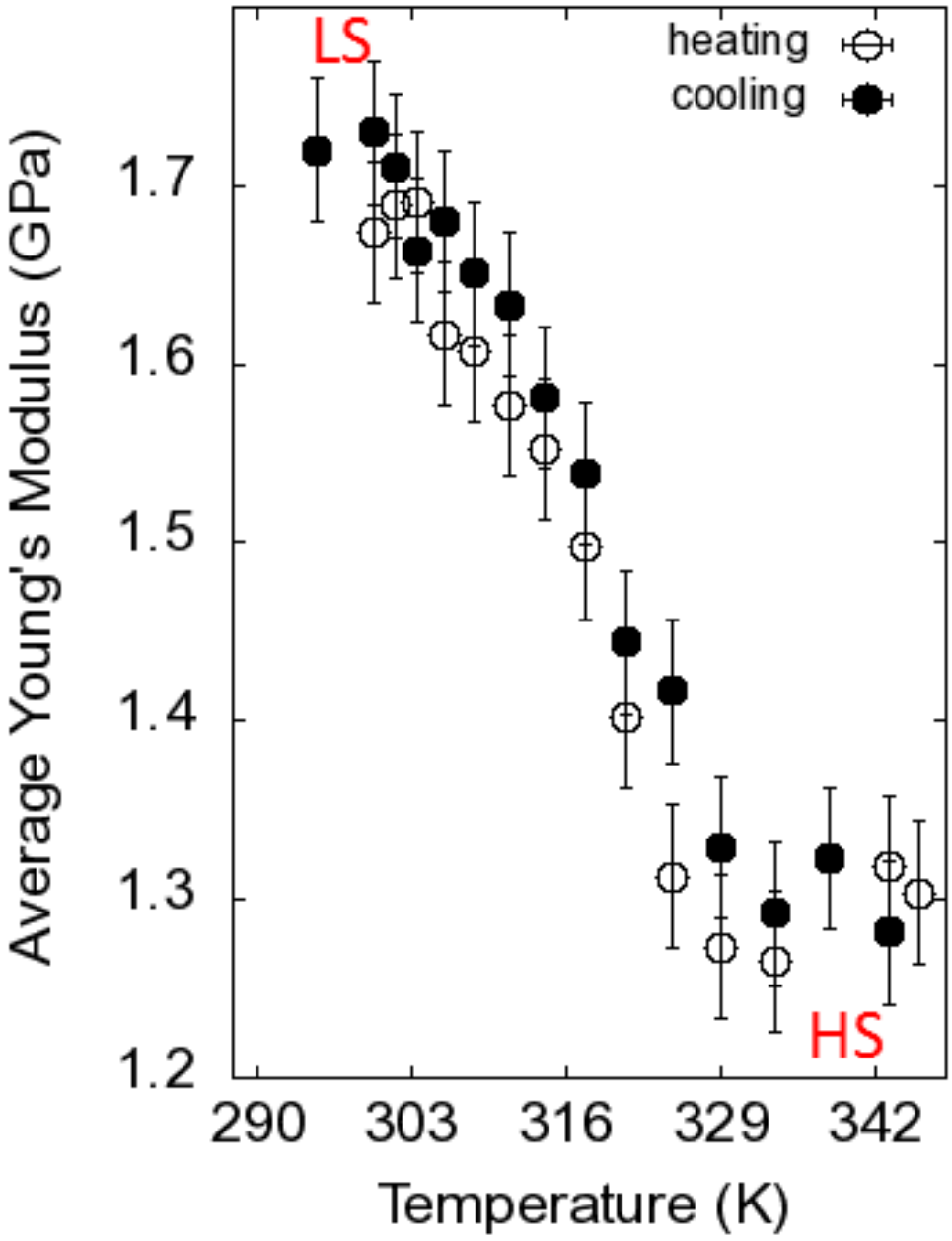

Figure 3.19: Averaged Young's modulus of a thin layer (40 nm) of $[Fe(hptrz)_3](OTs)_2$ (doped with Rhodamine 110) as a function of the temperature for the heating and cooling modes. The error bars represent the standard deviations of the measured data points.

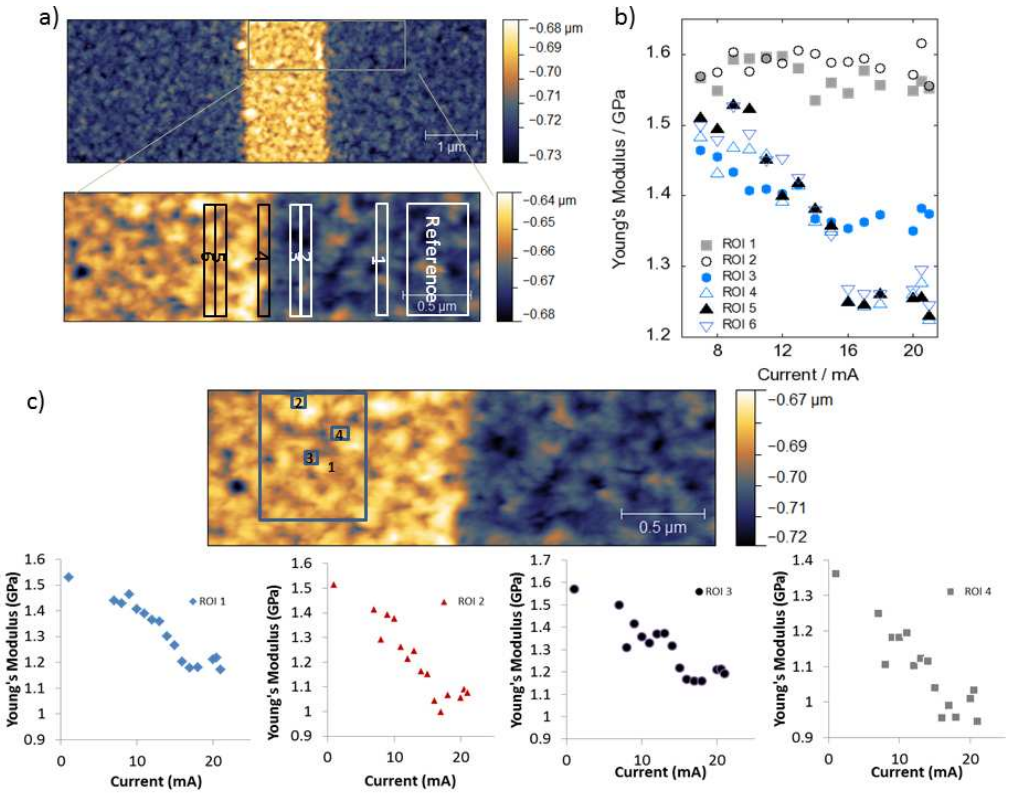

Figure 3.20: a) Topography maps of a $[Fe(hptrz)_3](OTs)_2$ thin film (40 nm) spin-coated on a gold wire. The selected regions of interest (ROI) of 70 nm widths as well as the reference area are shown in the images. b) Variation of the Young's modulus for the different ROIs as function of the current intensity in the wire. c) Young's modulus variation for areas of different sizes shown in the AFM topography image. The large square (1) is ca. 500 x 700 nm^2, while the small squares (2-4) measure ca. 70 x 70 nm^2. It is possible to follow the spin transition at such small sizes.

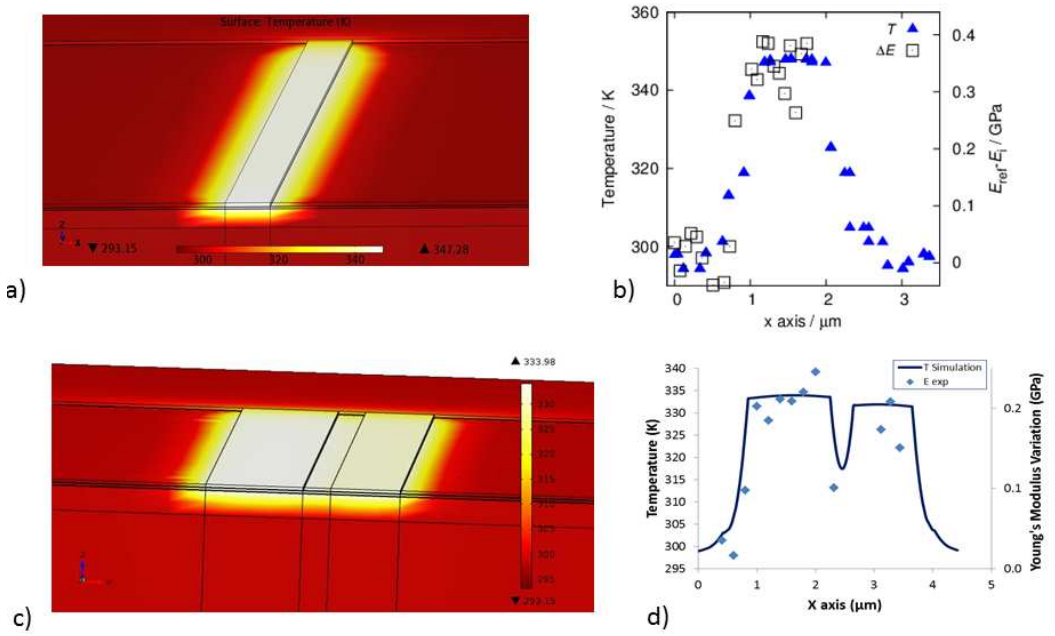

Figure 3.21: 3D model of the temperature distribution in our nanoheater devices simulated by COMSOL for a) the single nanowire device (width = 1 μm, thickness = 50 nm and length = 80 μm, 20 mA current) and c) for the double wire device (widths = 1 μm and 500 nm, thickness = 50 nm and length = 80 μm, 32 mA current). b) and d) Cross sections of the calculated temperature distribution and that of the experimentally determined Young's modulus change ($E_{ref} - E_{\mathrm{ROI}}$) along the x axis for a current of 20 mA and 32 mA, respectively.

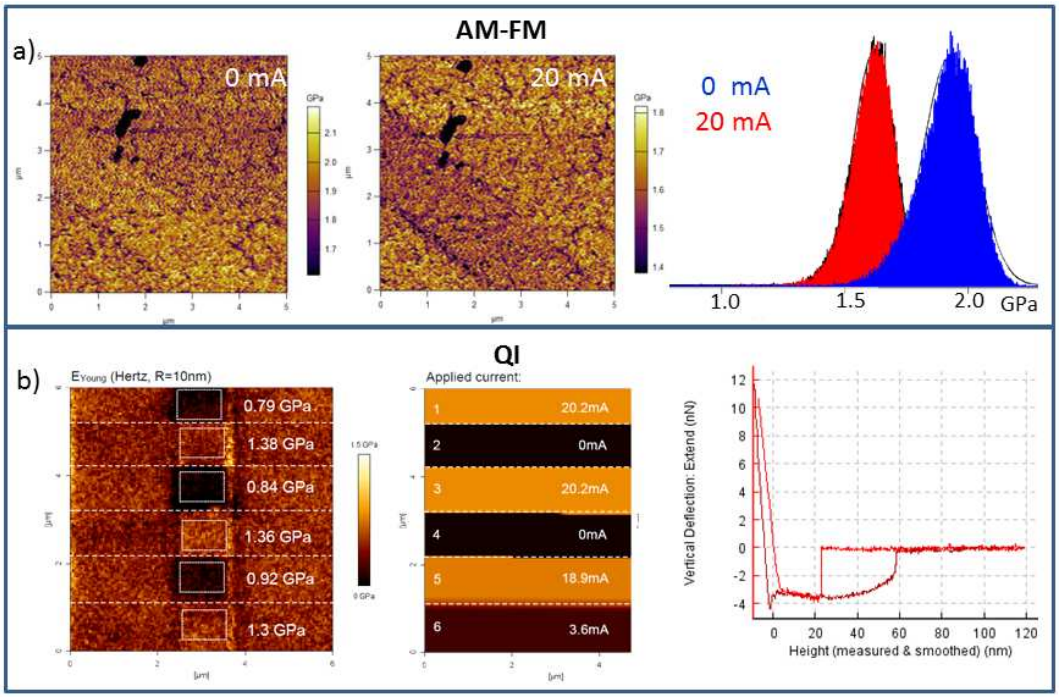

Figure 3.22: a) Young's modulus maps and distribution histograms obtained by AM-FM for a thin film (thickness = 40 nm) of $[Fe^{II}(hptrz)]_3(OTs)_2$ on a nanowire heater system for 0 and 20 mA currents. b) Young's modulus map of the same film obtained in QI mode. During image acquisition the current flowing in the wire was successively switched on and off as indicated. A representative force-distance curve is also shown.

As already stated the Young's modulus value depends on the choice of the contact model, the Poisson ratio and the geometry of the tip, which are all delicate to validate. In addition the results may also depend on the choice of the tip, the AFM instrument and/or the imaging mode. In order to further approve our results, a few additional tests were performed in Quantitative Imaging mode (using a NanoWizard 3 AFM at JPK Instrument), and in AM-FM mode (using a Cypher AFM at Asylum Research office). The tests were performed as part of demos in the respective companies, hence the results presented below are preliminary. Nevertheless, they provided several interesting conclusions. In each case we used the contact mechanics model implemented in the software: DMT for the Cypher and Hertz for the NanoWizard.

These tests were performed on similar samples than used in our PFT measurements. Figure 3.22 shows a summary of the main findings. AM-FM data were collected in the LS (0 mA) and HS (20 mA) states of the $Fe(hptrz)]_3(OTs)_2$ film. The Young's modulus distribution histograms in the two cases reveal mean values of 1.4 GPa (HS) and 1.8 GPa (LS) in excellent agreement with the PFT data. In addition the images show the same confinement of the Young's modulus change to the heated area, as observed previously. The QI data were collected in a single AFM scan by turning successively on and off the

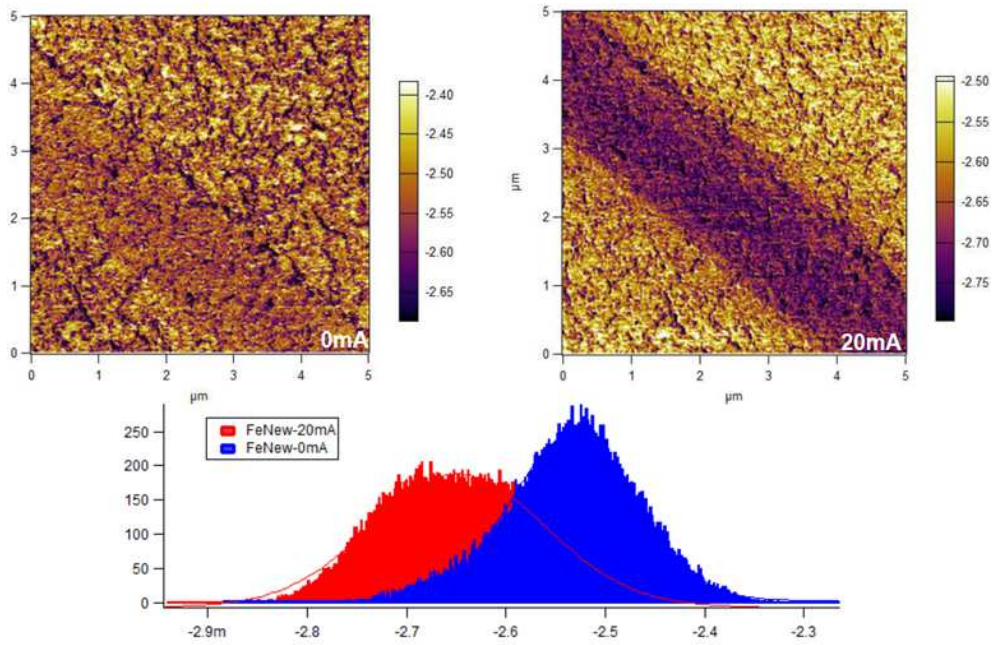

Figure 3.23: Loss tangent images and histograms for a thin layer of $[Fe^{II}(hptrz)]_3(OTs)_2$ on a nanowire heater system, for 0 mA and 20 mA currents.

current in the wire as shown in figure 3.22 (b). A reproducible change of E between 0.7 GPa (HS) and 1.4 GPa (LS) was observed. From the force-distance curves obtained in QI mode it can be inferred that a thin layer of liquid was present on the sample at the moment of the measurement (Figure 3.22), which might explain the lower E values when compared to the other data. Although these are preliminary results, it is important to remark that the order of magnitude of E is the same for all measurements and in all cases the Young's modulus in the HS state is lower than in the LS state.

During the experiments with the Cypher, the loss tangent images of the sample were also obtained for 0 and 20 mA currents, as shown in figure 3.23. The contrast between the material on the wire and on the substrate is higher for 20 mA. The loss tangent values are negative which is of course physically impossible. Unfortunately we were only able to do this experiment once, so the results could be improved. Nevertheless, the contrast between the HS and the LS states is remarkable.

3.4 Conclusions

In this chapter we described a novel approach, AFM thermomechanical measurements, to detect and image the spin transition phenomenon in nanometric thin films. This approach is based on the fact that the spin transition involves a significant change of the stiffness of the material.

Based on a few preliminary tests, we have chosen the peak force tapping mode for

quantitative nanoscale thermomechanical measurements. Using this method in conjunction with a nanowire heating device, we have been able to image the Young's modulus change of the spin crossover complex $[Fe^{II}(hptrz)]_3(OTs)_2$ between the two spin states. When going from the low-spin to the high-spin state we observed, for the first time, a decrease of the modulus from 1.7 GPa to 1.3 GPa, i.e. a change of ca. 25-30%, which can be rationalized by taking into account the softening of the metal-ligand bonds in the HS state.

The most important asset of our approach is that it allows the spin-transition phenomenon to be followed with a nanometric spatial resolution. Actually, we believe that among the various SPM techniques this type of mechanical measurements provide the highest resolution to this aim[1]. This opens up a unique possibility for the investigation of the spin transition in different nano-objects. In addition, the nanoscale imaging of spatially localized events, such as formation of the phase boundaries and their motion, also becomes possible. Indeed, the spin transition encompasses various phenomena occurring at different length scales (both nanometric and micrometric), which have been studied, up to now, chiefly by diffraction-limited optical microscopy. On the other hand, our results also highlight that the AFM studies of thin spin crossover layers can offer an interesting alternative for high-resolution imaging of surface temperature variations, which is currently a great concern in many fields of science and technology.

Beyond the nanoscale detection of the spin transition, merely the fact that we determined the Young's modulus of a spin crossover film is an important new result. For example, the knowledge of the Young's modulus (and its variation) is an indispensable input for the design of microactuator devices based on spin crossover complexes and also for the theoretical modeling of the spin transition. In addition to the Young's modulus (stiffness) other material properties (adhesion, dissipation, loss tangent, etc.) were also extracted in the two spin states and provide additional and previously unknown information about these systems.

Peak force tapping is one of the force curve based methods, which are probably the most appropriate for quantitative mechanical studies. Nevertheless, we proved that other methods such as phase imaging, loss tangent imaging, multifrequency (AM-FM) imaging and lateral force microscopy can also provide useful and sometimes complementary information. Among them AM-FM appears as a very interesting method for future work due to its very high imaging speed compared to force curve based methods, while providing similar quantitative data. Future work should also address in more detail the validity range of contact mechanical models for different SCO samples and it would be also very interesting to test the possibility of (thermo)mechanical addressing the spin state of these materials.

[1]STM cannot be used on insulating films.

Chapter 4

Imaging and manipulation of SCO single crystals

The spin crossover phenomenon has been deeply characterized using Mössbauer spectroscopy, X-ray diffraction, as well as magnetic and optical methods. However, the in situ observations of the nucleation, the evolution of the phase boundaries and the associated changes of the microstructure have been reported very recently in spin crossover solids. Nevertheless, much remains unknown concerning the nucleation and growth kinetics for cooperative SCO systems.

In the frame of the thesis of Salma Bedoui in the team, the spatial and temporal dynamics of the spin transition was deeply investigated in single crystals of the molecular spin crossover compound [Fe^{II}(bapbpy)$(NCS)_2$] (bapbpy = N-(6-(6-(pyridin-2-ylamino)pyridin-2-yl)pyridin-2-yl)pyridin-2-amine) showing first order spin transition [78–81]. By means of far-field optical microscopy the heterogeneous nucleation of different spin domains and their propagation was observed and the velocity of the domain barrier was found to be a few micrometers per second. The formation of one stable nucleus during the phase transition was found a scarce and extremely reproducible process, which occurred at predetermined locations (micro-structural defects). For this reason the transformation kinetics strongly depends on the crystal quality and differs from one crystal to another. In good quality crystals a single nucleation event occurs at a predetermined place (usually at a corner or edge) followed by the formation of a well defined phase boundary, which propagates through the whole crystal. The possibility to modulate or even to control the spatiotemporal dynamics was also demonstrated by either ablating microstructural defects in the crystal or by locally heating it with a laser pulse. Comparative studies of a non-cooperative compound of the same family, the [Fe(Meta'Me2(bapbpy)$(NCS)_2$] were also carried out. In line with the very gradual character of the SCO in this compound, the spin crossover process occurs in a homogenous manner without discernible domain formation.

However, there are many open questions that can be studied with higher spatial resolution techniques, such as: How the nucleation and growth phenomena depend on the morphology and structure of the sample? What is the minimum size where phase separation can still be observed? What is the size and the nature of the phase boundary? To answer some of these questions the existing experimental methods are not sufficient and we need new technics able to detect the spin transition with high spatial resolution.

In the continuity of the previous work in our team we decided to explore the possibilities provided by AFM techniques to image and to manipulate the spin transition in single crystals. Unfortunately the compound $[Fe^{II}(bapbpy)(NCS)_2]$ displays spin transition at low temperatures which we can not access with our AFM set-ups. For this reason we decided to work with the $[Fe(bbpya)(NCS)_2]$ complex from the same family. This latter compound exhibits an abrupt spin transition above room temperature which makes it an interesting candidate for AFM studies.

In this chapter we present an AFM imaging of the spin transition in $[Fe(bbpya)(NCS)_2]$. The synthesis and the main properties of the sample will be presented at first, followed by optical far-field microscopy imaging of its spin transition. Important electrostatic and thermal interactions between the sample and the AFM probe were observed. These will be discussed in the next section. Afterwards, the change in the topography of the crystals due to spin transition is presented in different experimental conditions.

4.1 Sample description

Inspired by their earlier investigation of the compound $[Fe(bapbpy)(NCS)_2]$ (**2**), where bapbpy is the ligand N-(6-(6-(pyridin-2-ylamino)pyridin-2-yl)pyrindin-2-yl)pyridin-2-amine [236](Figure 4.1 a), Zheng et. al. have synthesized a new SCO compound, the $[Fe(bbpya)(NCS)_2]$ (**1**), where bbpya is the ligand N,N-bis(2,2'-bipyrid-6-yl)amine (figure 4.1 b).

Magnetic susceptibility and differential scanning calorimetry measurements were performed by Zheng et. al. on powder samples and revealed that the spin transition in $[Fe(bbpya)(NCS)_2]$ occurs around 410 K (figure 4.2). This is one of the highest transition temperatures reported in the literature for a SCO compound. Intriguingly, the SCO is rather gradual between approx 350 - 500 K, but still a clear hysteresis is observed with $T^{\uparrow}_{1/2} = 418K$ upon warming and $T^{\downarrow}_{1/2} = 403K$ upon cooling. These results were corroborated by differential scanning calorimetry measurements where anomalies were found in both warming and cooling modes at $T^{\uparrow}_{1/2} = 434K$ and at $T^{\downarrow}_{1/2} = 415K$, respectively. Unfortunately the crystal structure was only determined at room temperature (i.e. in the LS state).

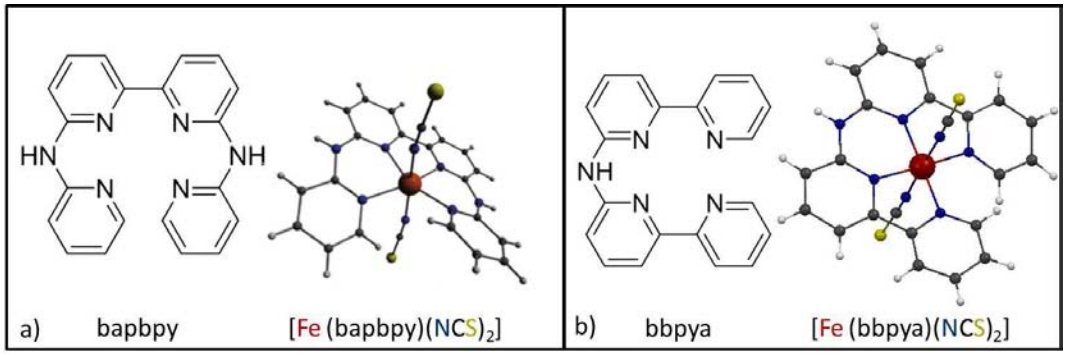

Figure 4.1: Structures of the spin transition compounds a)[Fe(bapbpy)$(NCS)_2$] and b)[Fe(bbpya)$(NCS)_2$].

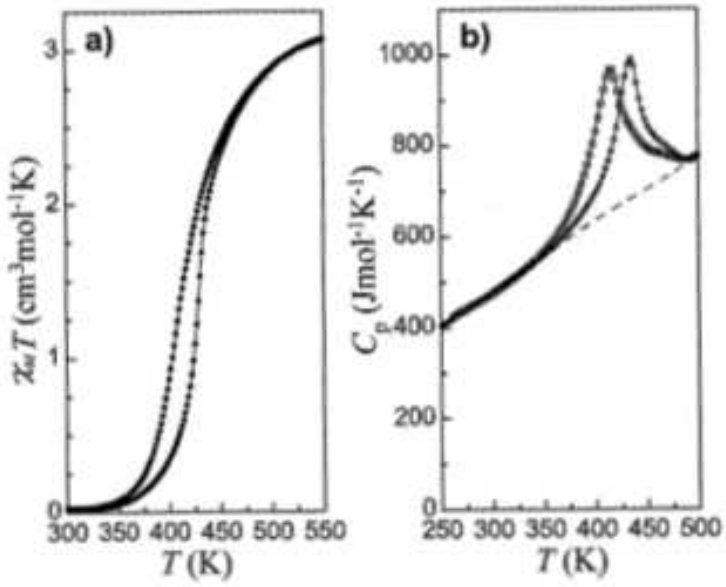

Figure 4.2: Thermal variation of $\chi_M T$ (a) and the molar heat capacity (b) for [Fe(bapbpy)$(NCS)_2$] measured at 10 K min^{-1} upon warming (empty circles) and cooling (empty squares) [237].

4.2 Preliminary sample characterization

In this work we investigated [Fe(bbpya)$(NCS)_2$] single crystals of ca. 40 μm of width, 20 μm thickness and a length that can vary from 0.8 to 1.8 mm. The crystals were carefully chosen under an optical microscope so they present an adequate size to perform AFM studies (they should be twice as long as the width of the cantilever to observe the influence of the tip on the crystal) and the less possible visible defects on the surface. (The crystals were grown by Sipeng Zheng in the group of Sylvestre Bonnet at the University of Leiden.)

4.2.1 Raman Spectroscopy

Since the properties of large single crystals can be significantly different when compared to powder samples and some differences may also occur from crystal to crystal, the spin transition of the crystals was first checked by means of variable temperature Raman spectroscopy. In fact, the structural changes which accompany the spin transition phenomenon are in general clearly manifested in the vibrational spectra of SCO molecules. We acquired Raman spectra by means of a LabramHR (Horiba Jobin Yvon) confocal micro-spectrometer equipped with a Peltier-cooled CCD detector (Andor DU420) and an Olympus BXFM optical microscope. A HeNe laser operating at 632.8 nm was used as an excitation source. The laser beam was focused on a spot of approximately 2 μm via a 50x long-working-distance objective (NA=0.5), which also served to collect the scattered photons. The confocal hole was kept at 1000 μm. The Rayleigh scattering was removed by an edge filter and the Raman spectra were recorded between 1200 and 2200 cm^{-1} with acquisition times between 10 and 30 s. The spectral resolution was set to ca. 3 cm^{-1}. The long axis of the needle shaped crystals was perpendicular to the laser polarization direction. The sample was enclosed in a Linkam THMS600 liquid nitrogen cryostat equipped with a glass window. Before the experiment the sample chamber was purged by dry nitrogen for 30 min at 403 K in order to remove traces of solvents.

Figure 4.3 a, shows selected representative Raman spectra of a crystal of the compound [Fe(bbpya)$(NCS)_2$] at three different temperatures (433, 453 and 513 K). The spectrum at 433 K shows relatively intense peaks between 1250 and 1650 cm^{-1} and two isolated peaks between 2050 and 2200 cm^{-1}. These latter correspond to the CN stretching modes of the thiocyanate ligands. Since they are isolated from the other peaks and are relatively intense, they can be used to study the spin transition in analogy with the compound **2**, which was previously investigated in detail by Bedoui et al. [79]. In the case of compound **1** the Raman peak at 2076 (2113) cm^{-1} probes the HS (LS) state. To follow the spin transition we recorded the Raman spectra of compound **1** at different temperatures while increasing the temperature from 353 to 533 K. To avoid any artifacts

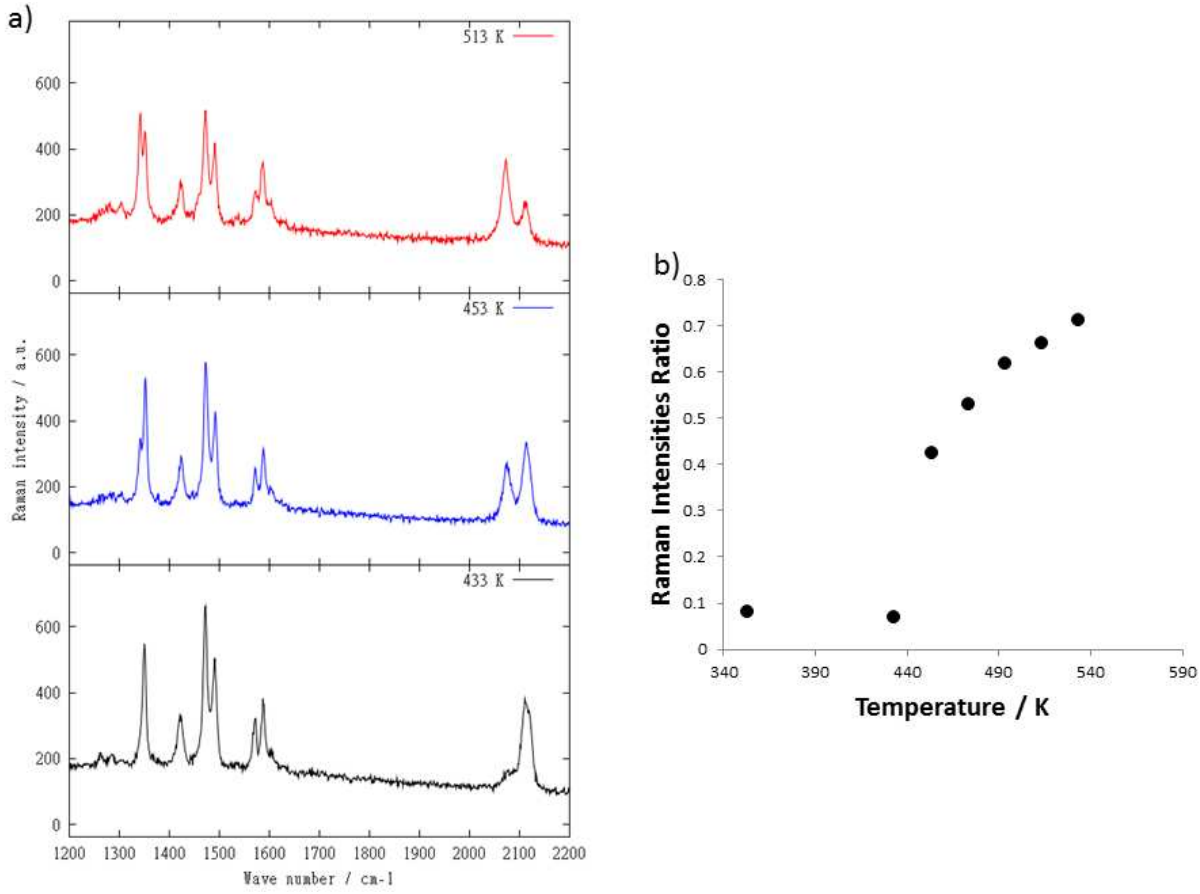

Figure 4.3: a) Raman spectra of a single crystal of [Fe(bbpya)$(NCS)_2$] at 433, 453 and 513 K. b) Ratio of the CN stretching intensities in the heating mode.

that may affect the intensity of the peaks, we have followed the intensity ratio of the CN stretching modes. The ratio between two peaks of the same spectrum was obtained by $Ratio = \frac{I_{HS}}{I_{HS}+I_{LS}}$, where I_{HS} and I_{LS} are the maximum intensities of the peaks at 2076 and 2011 cm^{-1}. To our surprise the crystals of compound **1** present a two-step thermal spin transition, which was not detected for the powder sample. An abrupt transition in the crystals is observed between 433 and 453 K from the LS state to an intermediate phase (IP), which consists of ca. 50/50 % HS and LS molecules. This first step is followed by a very gradual conversion to the HS state, as shown in figure 4.3 b. The transformation of the crystal to the pure HS state can not be obtained because for temperatures higher than 533 K ($n_{HS} \approx 0.75$) sample decomposition was observed. For this reason, in the following experiments only the transition between the LS and the IP phases will be discussed. It may be worth to note also that somewhat similar differences were previously reported also in compound **2** between the powder and the single crystal samples, the latter showing more abrupt transitions and a better defined plateau between the two steps of the spin transition [77].

4.2.2 Optical microscopy studies

For the investigation of the spatio-temporal dynamics of the spin transition, the good reproducibility of this latter is indispensable. Unfortunately the quality of many SCO crystals degrades dramatically during the transition due to auto-split, cleavage and other failures. As a matter of fact, the availability of good quality crystals displaying a robust and well reproducible spin transition is the main bottleneck for this type of study. (In our case the number of available samples is further restricted by the relatively small temperature range accessible by our AFM.) In order to test the reproducibility of the spin transition curve in the compound [Fe(bbpya)$(NCS)_2$], we used conventional far-field optical microscopy. As already stated in chapter 2 SCO compounds present a drastic change of their optical properties at the spin transition temperature. In the case of **1** the optical density in the visible range decreases when going from the LS to the HS state. This property can be used to follow in a quantitative way the spin transition by an optical microscope. Optical microscopy images of several crystals were recorded in bright-field either in transmission or in reflectivity modes using an Olympus BX51 microscope equipped both with a color CMOS camera (IDS UI-1250ML) and a thermoelectrically cooled CCD camera (Andor Ikon-M with 13 μm pixel size). A 50 X objective (numerical aperture NA = 0.5, working distance WD = 10.6 mm) was used. The sample was illuminated by a halogen lamp (400 to 700 nm), but in certain cases the spectral range was reduced using a band-pass filter (650 $\pm$ 25 nm). The temperature of the sample was controlled by means of a Linkam THMS600 cryostat.

The overall shape of the transition curves is the same for the different crystals we investigated, but the fine details vary from crystal to crystal. In each case we observed a very abrupt spin transition, which was complete in less than 0.1-0.5 K. The spin transition occurs always with a hysteresis of ca. 1.5-8 K width, which is centered around approx. 435-440 K. When compared to **2** in this sample it was much more difficult to find crystals which preserve their integrity over successive thermal cycles. We observed in many cases self-cleavage and also pronounced thermosalient phenomena ("jumping crystals"). In fact during the transition the crystals always changed in a perceptible manner their size and shape, which can explain these phenomena. Nevertheless, we succeeded to find several robust crystals, which displayed reasonably well reproducible SCO. Perhaps not surprisingly, these latter were usually small and thin needles. The spatio-temporal development of the transition was found globally very similar to that observed for **2**. Briefly, nucleation occurs usually at the apex of the crystals and the well defined phase boundary moves from one end of the crystal to the other. The forward and reverse transitions follow spatially the opposite way. In many cases we observed a slow-down or even the trapping and successive re-acceleration of the phase boundary, which is certainly linked to the presence of microstructural defects. It is important to note that it was possible

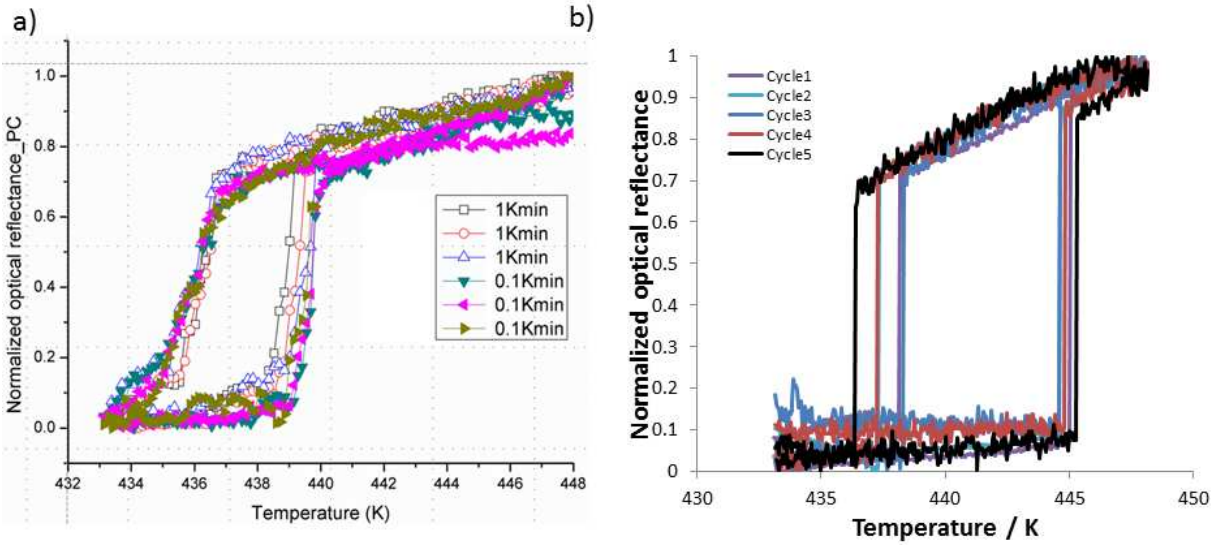

Figure 4.4: Optical reflectance of two different crystals of **1** recorded over several successive thermal cycles. The temperature rates were 1K/min and 0.1 K/min for (a) and 0.5 K/min for (b).

to block the position of the phase boundary if the heating (or cooling) was stopped in the middle of the hysteresis region and the sample temperature was slightly decreased (or increased).

Figures 4.4, 4.5 and 4.6 show a few typical transition curves and optical microscopy images of **1** recorded across the spin transition. The spin transition curves in figure 4.4 (a) were acquired at different rates (0.1 and 1 K/min) during six successive thermal cycles. One can observe an increase of the reflectance around 439 K due to the transition from the LS to the IP phase, while the reverse transition occurs around 436 K. The quality of this sample is relatively low which is reflected by the fact that the transition is not very abrupt and the hysteresis is rather narrow. Nevertheless, it shows a good reproducibility, which is nearly independent of the heating and cooling rates (within the investigated range). For comparison, the spin transition of a higher quality crystal is depicted in figure 4.4 (b). In this case the transition occurs in a virtually discontinuous manner and it is completed in less than 0.1 K. The hysteresis in this sample is somewhat larger and centered at a higher temperature, but the exact values of the transition temperatures are difficult to define because they change slightly between every cycle.

Selected snapshots of the nucleation and growth process are shown for two crystals in figures 4.5 and 4.6. In both cases there is a single nucleation point at the apex of the crystals. It is interesting to remark the very well defined and nearly constant orientation of the phase boundary with respect to the orientation of the crystal. This phenomenon has already been observed by Sy et al. [66] in another SCO sample. They explained the specific orientation of the phase boundary by the existence of a HS/LS interface which

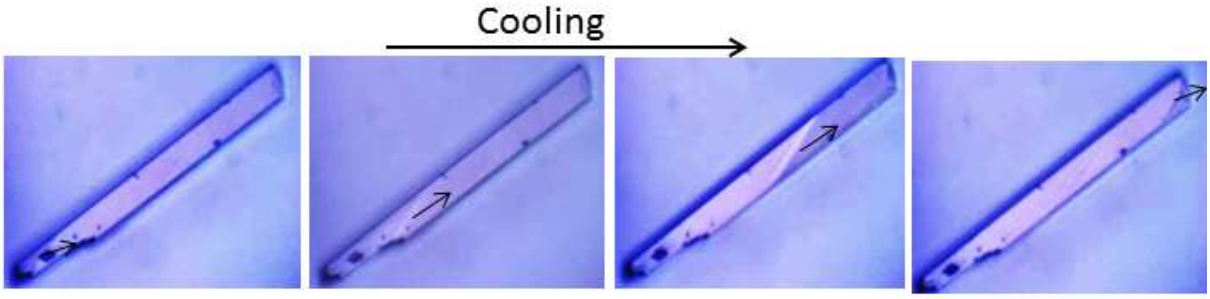

Figure 4.5: Far-field optical microscopy snapshots (transmission mode) of the spin transition of a [Fe(bbpya)$(NCS)_2$] crystal in the cooling mode. The low temperature (LS) phase has higher optical density.

minimizes the elastic strain at the phase boundary.

4.3 AFM

Optical microscopy has proven that crystals of **1** have on the whole adequate spin transition properties (such as size, spin transition temperature, reproducibility, etc) to study their spatio-temporal dynamics using atomic force microscopy. However, the high temperatures at which transition occurs increases unfortunately the heat transfer between the sample (and/or the heating stage) and the probe even if this latter is heated. In the following section we will describe this effect and the associated problems in detail.

AFM experiments discussed in this chapter were performed using a SmartSPM (AIST-NT) in tapping mode using a silicon tip with aluminium coating on the backside of the cantilever (Rtespa, Bruker, frequency = 300 kHz, k = 40 N·m^{-1}), unless otherwise indicated.

4.3.1 Probe-sample interactions

As already mentioned the crystals move during the spin transition, therefore it is necessary to fix them to the surface. A small drop of Epoxy glue was homogeneously spread over the surface of the Si substrate. Crystals of **1** were then placed one by one on the substrate with the help of a needle. The sample temperature was controlled with a heating state provided by the AFM company. All experiments were carried out in air. The AFM probe was approached to the crystals either vertically at a fixed lateral position or laterally at a constant height. The spin state of the crystal was followed in-situ by conventional far-field optical microscopy using a 10 X Mitutoyo objective (NA = 0.28). The crystals were illuminated with a halogen lamp and the reflected light was captured using a CMOS camera.

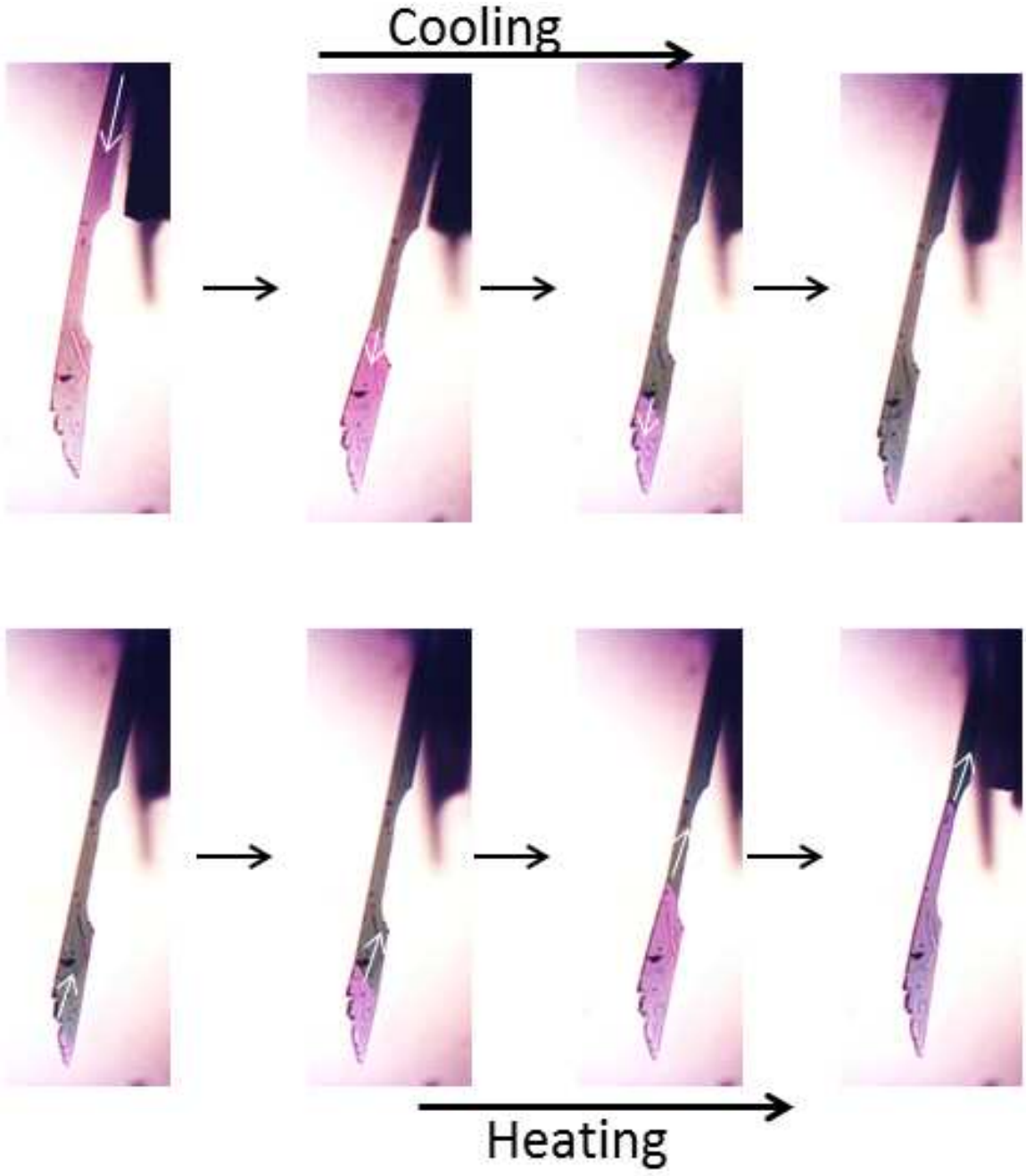

Figure 4.6: Far-field optical microscopy snapshots (transmission mode) of the spin transition of a [Fe(bbpya)$(NCS)_2$] crystal in the heating and cooling modes. The low temperature (LS) phase has higher optical density.

In a first experiment the temperature of the crystal was increased to 433 K (*LS* state) at a rate of 10 K/min and an approach was performed on the crystal in order to calibrate the tip-sample distance. Then, the tip was retracted 500 μm and the temperature was increased to 448 K. As mentioned before at this temperature the sample is in the intermediate phase (*HS-LS*). Following sample thermalization, the tip-sample distance was decreased in small steps (10 μm) and a snapshot of the sample was taken after each step. As shown in figure 4.7 at ca. 70 μm tip-sample separation, the nucleation of the *LS* phase (characterized by a dark contrast) was observed in the crystal under the AFM probe. As the tip further approached to the crystal the *LS* domain has progressively grown towards the other end of the crystal. When the tip is engaged on the sample surface the *LS* phase progressed ca. 90 μm, which corresponds to approx 50 % of the length of the crystal. When retracting the probe the opposite phenomenon occurs, but the approach and retract curves present a wide hysteresis of ca. 50 μm. This hysteresis reflects obviously the bistability of the sample. This experiment was reproduced three times on the same sample with the same result and it was also confirmed using other crystals. Interestingly if the tip is maintained at a certain height the phase boundary remained at the same position (for at least 2 hours). However, the elastic strain produced on the crystal provokes an irreversible damage (cracks) around the phase boundary after ca. 15-20 minutes.

This experiment reveals that the AFM probe strongly influences the spin state of the crystal even at large distances. The most obvious hypothesis to explain this finding is heat transfer between the sample and the probe, i.e. the probe which is colder than the sample brings this latter to the low temperature (*LS*) phase. On one hand this thermal interaction is a huge difficulty for the imaging of the spin transition. On the other hand it is an exciting finding which opens perspectives for the manipulation of the spin transition in a reversible and spatially localized manner. In order to further explore this possibility we have carried out a few other experiments.

In a second experiment the tip-surface distance was calibrated as previously and the temperature was fixed again at 448 K. However, in this case the tip was kept at a constant height from the substrate (100 μm) and the sample was moved laterally, i.e. parallel to the length of the cantilever (Y axis). As the tip approached to the crystal, the nucleation of the *LS* phase was observed at the extremity of the crystal near to the cantilever, as shown in figure 4.8. The distance between the tip and the nucleation point was of 490μm. As the tip further approaches to the crystal the new phase propagates through it, i.e. the volume of the *LS* phase increases. The phase boundary moves ca. 0.85 μm for every micrometer the tip approaches or retracts from the crystal. As in the previous case a hysteresis is observed (ca. 80 μm.). We have also carried out experiments (not shown here) where the tip moved from one side to the other of the crystal. In such a case the phase boundary follows the movement of the tip in a more direct way. The

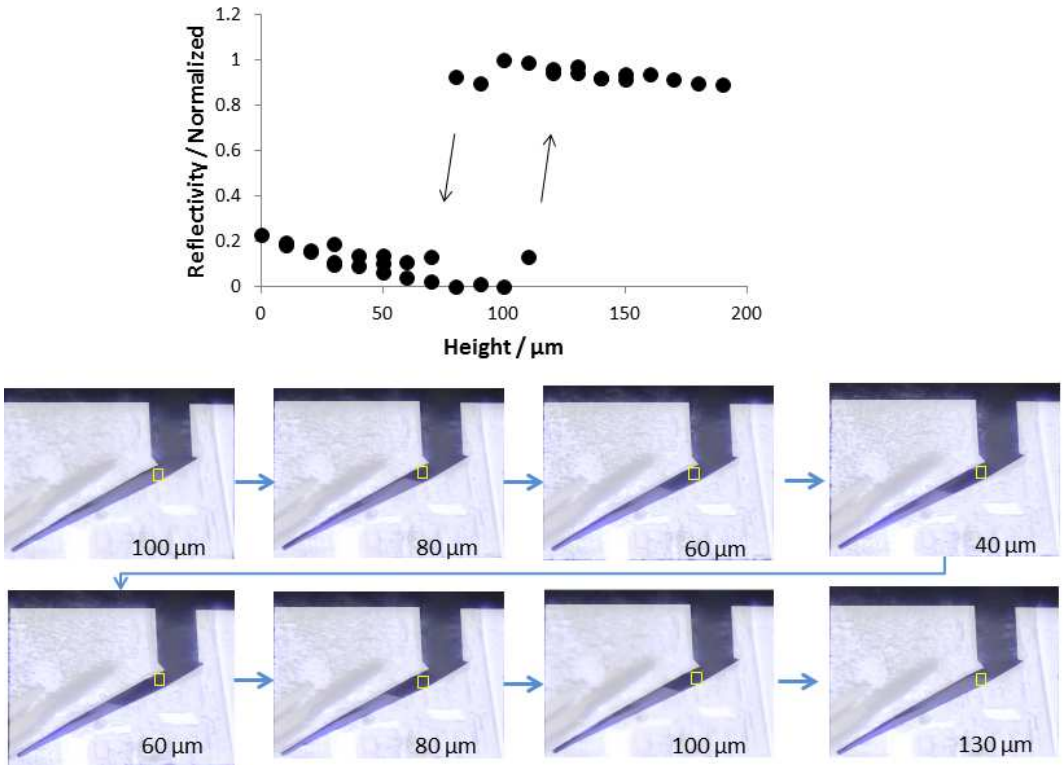

Figure 4.7: Plot of the vertical distance between the tip and the crystal surface vs the normalized reflectance of a [Fe(bbpya)$(NCS)_2$] crystal in the area marked in the images below. Arrows indicate increasing and decreasing tip-sample distance. A few selected images corresponding to this plot are shown below. The tip-sample distance is indicated in each image. The experiment was performed at 448 K. The size of the images is 300 X 300 μm^2.

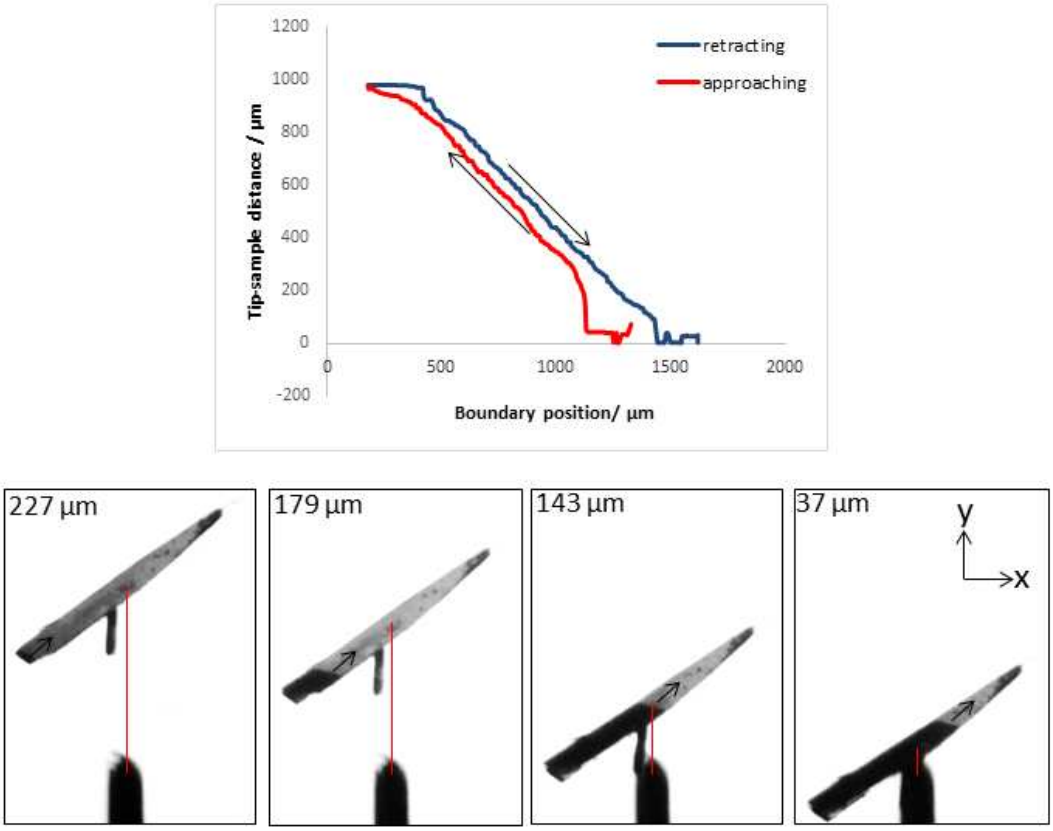

Figure 4.8: Distance between the phase boundary and the nucleation point in crystal of **1** as a function of the tip-sample distance for the experiment shown in the images. The tip-substrate distance (100 μm) and the sample stage temperature (448 K) are kept constant and the tip approaches the sample in the Y direction. Arrows in the plot indicate the approach and the retract of the tip. The tip-sample distance is indicated in each image. The size of the images is 290 x 450 μm^2.

volume of the crystal that is transformed to the *LS* state was found to depend not only on the tip-sample distance, but of course also on the temperature of the sample. Depending on the choice of the crystal as well as on the experimental details, in particular where and how the crystal is approached by the tip, we observed different behaviors, such as multiple nucleation points and thus several domains with sometimes different boundary angles and propagation directions. Another interesting observation is that if the tip approaches to the crystal far from a natural nucleation point (i.e. far from a corner or a defect in the crystal), the transition is more difficult to induce.

In order to better understand the nature of the tip-sample interaction, similar experiments were performed on a crystal, but using different AFM probes (Rtespa (Bruker), HQCSC17 and HQNSC15 (Micromash), etc). Each probe consists of a sharp Si tip attached to a cantilever, which is held by a silicon chip. (The scheme of a probe can be depicted in figure 3.1.) Figure 4.9 shows the reflectivity as function of the tip-surface distance for two different probes (Rtespa and HQCSC17 with a cantilever length of 125

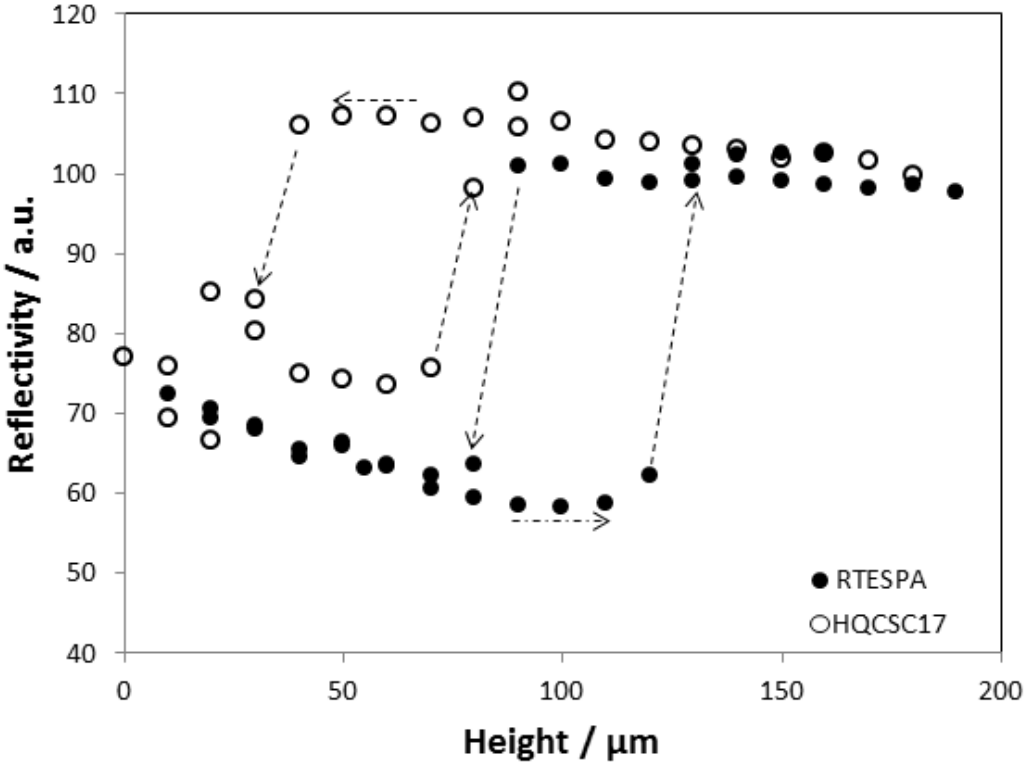

Figure 4.9: Reflectance of a crystal of compound **1** as a function of the tip-sample vertical distance for two different tips measured both in approach and retract modes.

and 450 μm, respectively). In these experiments the tip moves in the Z axis and basically we observe the same phenomenon as previously in figure 4.7. The interesting finding here is that longer cantilevers produce a switch to the LS state at shorter tip-sample distances. From this result we can infer that not only the tip-sample distance, but also the distance between the crystal and the chip has an influence on the probe-sample interaction. To confirm this conclusion we also made experiments using silicon chips without any cantilever or tip and the spin transition was also observed when approaching only the bare chip. Nevertheless, this does not mean that the tip has no effect at all. For example, when using long cantilevers (450 μ m) we observed nucleation at two different points, near the end of the tip as well as close to the chip. Let us note also that preliminary experiments suggest that the interaction between the probe and the sample is significantly more important when using probes made of conducting materials (Si or metal) when compared to insulating materials such as glass or plastic.

4.3.2 Investigation of the heat transfer between the probe and the sample

As already mentioned, the most probable cause of this long-range interaction between the probe and the crystal is a local heat transfer. When a silicon tip approaches

to a hot surface, there is normally a thermal interaction between the tip and the sample that is not negligible. In general there are three different modes of heat transfer in air: conduction, convection and radiation. The relative importance of heat transfer modes depends on the operating temperatures, the dimensions and the distance of the objects as well as on the conditions of air flow (open/closed space and cavities). At low operating temperatures (< 573 K) micro-scale heat transfer by radiation in air is small compared to that by conduction or convection over a wide range of dimensions [238]. Therefore only heat conduction and convection in air will be considered in the following. Heat conduction in air becomes relatively important (in our experimental conditions) when the air gap between the sample and the tip is only a few tens of microns. Heat convection plays a role in carrying heat and mass from the hot surface to the colder probe and environment at larger distances [239]. It is important to remark that micro-scale heat convection is not zero [240].

The different heat transfer modes at this scale can be analyzed with good accuracy using finite elements simulations. From an experimental point of view a powerful approach would be to repeat our measurements under vacuum and also using probes made of materials with very different thermal properties. Unfortunately, at this moment of the thesis work, these experimental tools were not available and a proper numerical modeling would have taken too much time. We have therefore decided to use an experimental approach, which was readily available. In fact, temperature changes can be measured locally using the nanowire heater system presented in section 2.2.1 by simply measuring the electrical resistance of the nanowire. In these experiments a clean gold nanowire (thickness = 50 nm, width = 1 μm, length = 40 μm) on a silicon substrate was used. The substrate was heated using the AFM heater stage. The current applied to the nanowire was controlled using a source-meter (Keithley model 2611A). In each experiment the distance to the nanowire was calibrated by performing an initial approach to the sample as well as a scan to locate the nanowire in the X - Y directions. We always assured that the end of the tip was on the middle of the nanowire. The resistance of the nanowire was measured while applying 0.5 mA current to it, unless otherwise indicated.

In the first experiment the tip was located at a constant distance (200 μm) above the nanowire and the resistance of the nanowire was measured for different temperatures. The temperature was changed using either the heater stage (i.e. by heating a large surface) or the nanowire (i.e. by heating only a tiny surface area). Each measurement was performed both in the presence and in the absence of the AFM probe. For this the probe holder with the probe was manually removed and replaced three times for each temperature and the average resistance value was taken. In each case, the resistance was measured after the temperature of the system was fully stabilized. Figure 4.10 shows the results of this experiment. As expected the relation between the resistance of the wire and its temperature is nearly linear (in particular in the absence of the probe). The presence

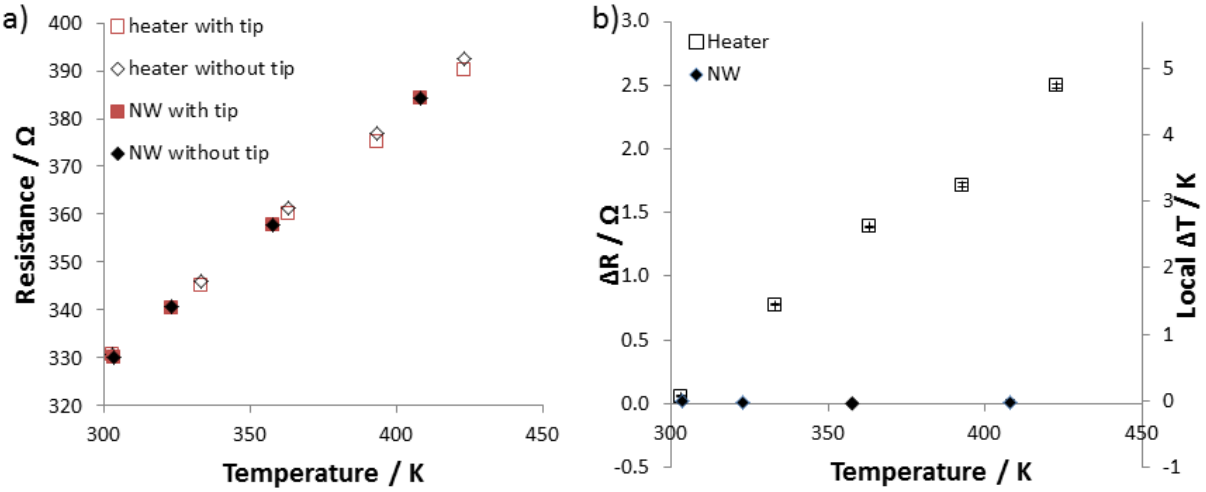

Figure 4.10: a) Electrical resistance as function of the temperature of a gold nanowire heated either with a heater stage (open symbols) or by injecting a current into the nanowire (closed symbols). Resistance was measured both in the presence of an AFM tip (located at 200 μm above the wire) (square symbols) and in its absence (diamond symbols). b) The difference between the resistance measured with and without the tip as a function of the temperature. Open and closed symbols correspond to heating by the heating stage or by directly the nanowire (NW), respectively.

or absence of the probe has strictly no influence on the resistance of the nanowire when only this latter is heated (figure 4.10 (b)). However, when the sample is heated using the heating stage we observed a clear effect of the probe. In the presence of the probe the resistance is systematically lower. This resistance difference (i.e. with and without the probe) increases linearly with the temperature. From this data we can deduce that even when the tip is at 200 μm from the surface the average temperature of the wire decreases by as much as 5 K (at 423 K) when the heater stage is used. We must insist that we measured the mean temperature of the wire and locally the effect of the probe can be even higher than 5 K. Hence, it is not surprising that the SCO crystals change their spin state from HS to LS even before the tip is in contact with the surface. In other words when the probe approaches to the crystal, it starts to affect (reduce) the temperature of the crystal locally already from large distances (i.e. 200 μm). The presence of the probe favors thus the low temperature (LS) phase. The thermal effect of the probe (ca. 5 K) may seem rather small, but we must recall that the spin transition is extremely abrupt in sample **1** and due to the hysteresis it is not necessary to heat the whole sample, but only a small volume (i.e. the nucleation volume).

In the next step we carried out similar experiments in which the temperature was kept constant and the tip-sample distance was changed. Figure 4.11 (a) shows the resistance of a gold nanowire (NW) as a function of the tip - NW distance at room temperature. No significant variation of the resistance is observed. On the contrary, when we repeat the

same experiment at 423 K the resistance decreases monotonously when the tip approaches the NW 4.11 (b). From the NW resistance we can infer that for a tip-sample separation of 200 (50) μm the temperature of the NW is 8 (15) K below that of the heating stage. The large gap (200 μm) at which the heat transfer occurs indicates that thermal convection is present in the system. One way to diminish the thermal convection phenomena is to reduce the size of the heated area by several orders of magnitude. This will affect the Grashof number [239, 241], which governs the convection heat transfer process, diminishing the convection effect. In fact the nanowire heater system reduces the heated area by three orders of magnitude. If the main heat transfer mechanism in our case is thermal convection this highly reduced area should lead to a drastical decrease of heat transfer. However, if thermal conduction dominates the heat transfer we can expect less dramatic changes. We thus repeated the previous experiment, but instead of heating with the stage, we directly heated the nanowire by an applied current of 5 mA, which corresponds to 427 K. The result of the experiment is shown in figure 4.11 (b). It shows that there is no considerable heat transfer ($\Delta T < 1$ K) between the tip and the wire even when the tip is engaged on the sample surface. However, a closer look on these data (figure 4.12) reveals that the temperature on the wire decreases a few tenths of a degree for tip - sample distances smaller than 40 μm, as expected for conductive heat transfer in air. The influence of the tip - NW distance on the nanowire temperature was also investigated for different applied currents. The range of applied currents (1-5 mA) corresponds to NW temperatures between 313 and 427 K. As shown in figure 4.12, almost independently of the initial temperature of the NW, the approach of the tip to the nanowire leads to a similar resistance (i.e. temperature) change of this latter. In each case, the temperature of the wire decreases only a few tenths of a degree even when the tip is engaged. This small thermal effect slowly increases with the current applied to the tip (figure 4.12 (b)).

We have seen above in figure 4.8 that the probe has an influence on the spin state of the crystals of **1** even when these latter are laterally several micrometers away from the tip. In order to better understand this result, we repeated this experiment using the gold nanowires instead of the SCO crystals in order to determine the lateral temperature distribution. The tip was placed 100 μm above the surface which was maintained at 423 K using a heater stage. The sample was moved parallel to the cantilever (Y axis) using the stepper motors. (N.B. The AIST probe holder is built in such a way that the angle between the probe and the sample is of 20°.) Figure 4.13 shows the resistance of the nanowire as a function of its lateral distance to the tip. Remarkably the lowest temperature (resistance) value was observed in the middle of the probe and not near the tip, supporting our hypothesis of a heat transfer dominated by thermal convection in the system.

The different experiments with the nanowires evidence clearly an important heat transfer due to convection phenomena between the AFM probe and the sample. This can

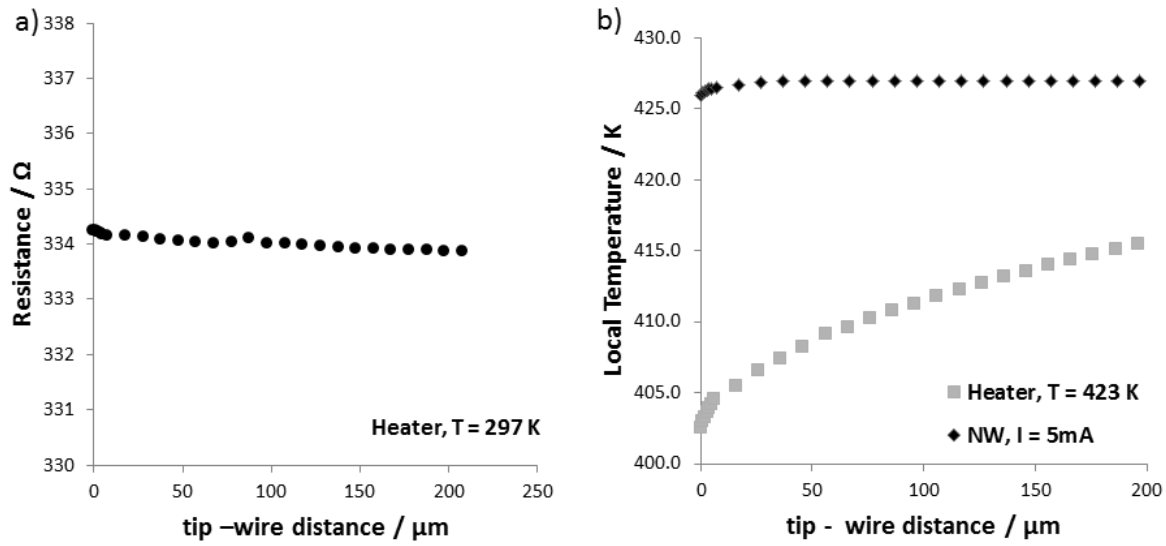

Figure 4.11: a) Resistance of a gold nanowire (thickness = 50 nm, width = 1 μm, length = 40 μm, glass substrate) as a function of the distance between the nanowire and the AFM tip. The temperature of the sample stage was maintained at 297 K. b) Variation of the temperature of the NW (obtained from the resistance of the wire) as a function of the distance between the nanowire and the AFM tip. Squares correspond to the experiment where the whole sample stage was kept at 423 K. Diamonds indicate another experiment were only the nanowire was heated to 427 K.

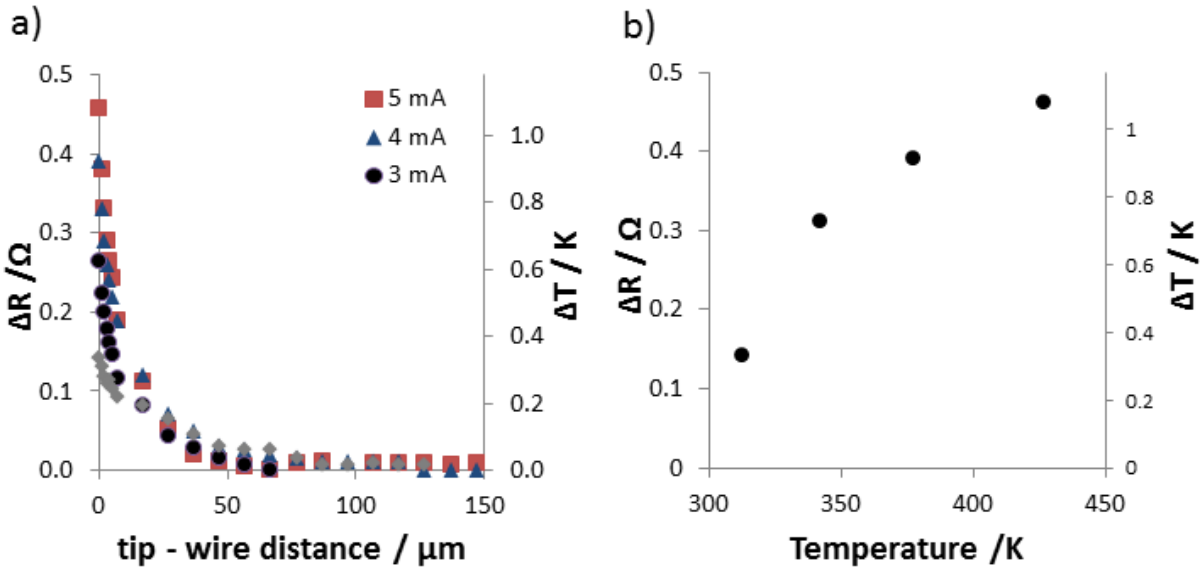

Figure 4.12: a) Resistance difference (ΔR = R_{max} - R) as a function of the distance between a gold nanowire (thickness = 50 nm, width = 1 μm, length = 40 μm, glass substrate) and the AFM tip for different currents applied to the wire. b) Resistance difference (ΔR = R_{max} - R_{min}) as a function of the nanowire temperature (i.e. applied current). The temperature difference corresponding to the resistance changes is also shown for both figures.

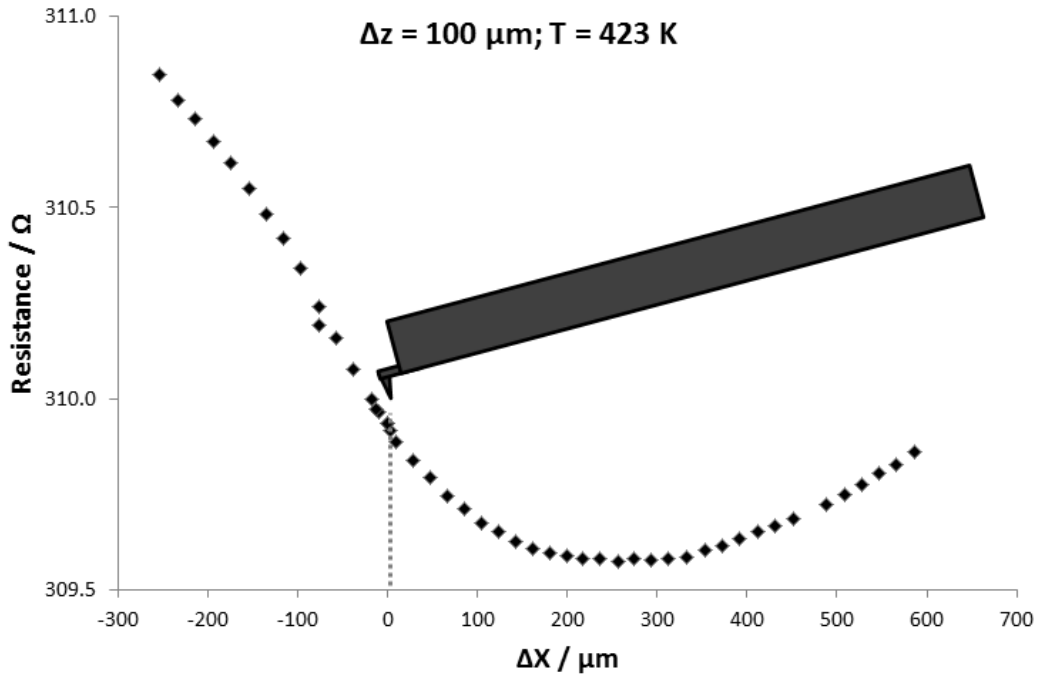

Figure 4.13: Resistance as a function of the position of the wire relative to the tip at a constant tip height ($\approx$ 100 μm) and temperature (423 K).

of course explain the influence of the probe on the spin state of our samples. However, this observation does not exclude the existence of other types of probe-sample interactions. In particular, we observed that electrostatic effects also occur in the experiments. A very obvious manifestation of these latter was repeatedly observed when the crystals were not glued to the surface. In such case, as the tip approached to the crystals we observed them moving and in some cases the crystals even "jumped" towards the probe and stuck to it. An example of this phenomenon is shown in figure 4.14. We observed this phenomena in crystals of all sizes and shapes. (It is interesting to note that the force needed to pull crystals of ca. 100 - 200 μm length 30 μm away from the surface is ca. 0.9 - 1.4 nN.) Another interesting observation concerns the relationship between these electrostatic effects and the spin transition. In fact, electrostatic phenomena were observed most often during the spin transition and in particular after several spin transition events (i.e. after several heating-cooling cycles). Trying to better understand this phenomena we applied different voltages at different distances between the tip and the sample. However, we did not observed any effect on the spin state of the crystals nor we were able to make them move. We believe a triboelectric effect occurs during the spin transition, i.e. most probably the crystal is charged due to friction between the different HS and LS domains in the crystal and/or due to the formation of cracks in the crystal. To further investigate these phenomena we performed Electrostatic Force Microscopy (EFM) measurements (see details on EFM in reference [121]). In EFM the tip scans the surface topography during

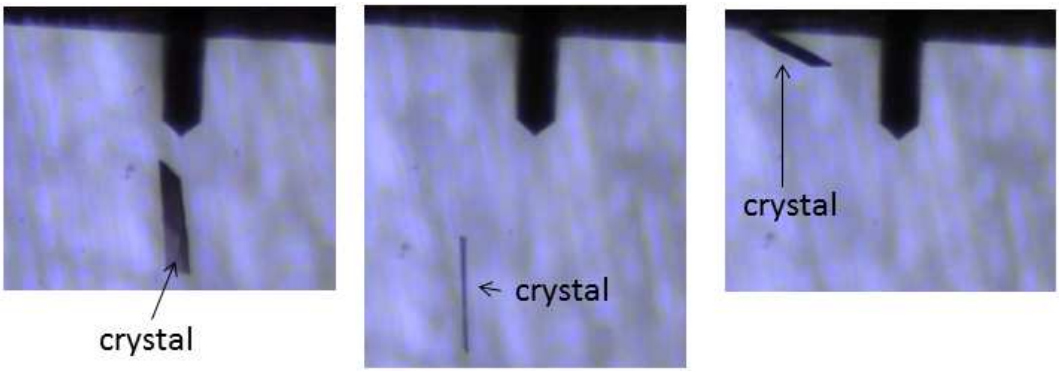

Figure 4.14: Selected optical images of a crystal of compound **1** that show the crystal is moving towards the probe. The probe was moved towards and away form the crystal while keeping its height constant (30 μm). The temperature of the sample holder was fixed at 448 K.

the trace in AC mode. Then, the tip is retracted from the surface and the retrace is performed at a constant tip-surface distance while applying a voltage between them. The amplitude of the oscillation of the tip will be modified depending on the electrostatic forces between the probe and the substrate. We performed EFM measurements at room temperature on crystals of **1** after two or three thermal cycles. The tip was lifted 100 nm above the surface for each measurement. Charges on the crystal were found after two thermal cycles in the crystal, although they are not uniformly distributed (i.e. most of the crystal is not charged even after four thermal cycles). Figure 4.15 shows EFM images after 2 and 3 cycles for the same zone. Images were taken for two different applied voltages (+10 and -10 V). Darker and brighter areas can be found in all images, which correspond most probably to differently charged areas. From the images we can infer that some areas are indeed charged, since we observe an inversion of the contrasts between the images taken for +10 and for -10 V. After cycling the crystal once more we observed an increase in the amplitude of the EFM signal, confirming the hypothesis that the crystal accumulates charges during the spin transitions.

4.3.3 Variable temperature topography studies

Unfortunately NW heaters can not be used to heat micrometric single crystals. Other methods and hints must be therefore considered in order to avoid, or at least reduce, unwanted thermal effects between the AFM probe and the crystals. Possible ideas include (i) the use of a vacuum chamber, which would completely eliminate convection and significantly reduce conduction effects, (ii) the use of very long cantilevers which can reduce convection effects, and (iii) heating the AFM probe to the same temperature as the sample stage. Since we had no equipment to carry out these measurements under vacuum we tested the two latter solutions. The use of long cantilevers has brought effectively some

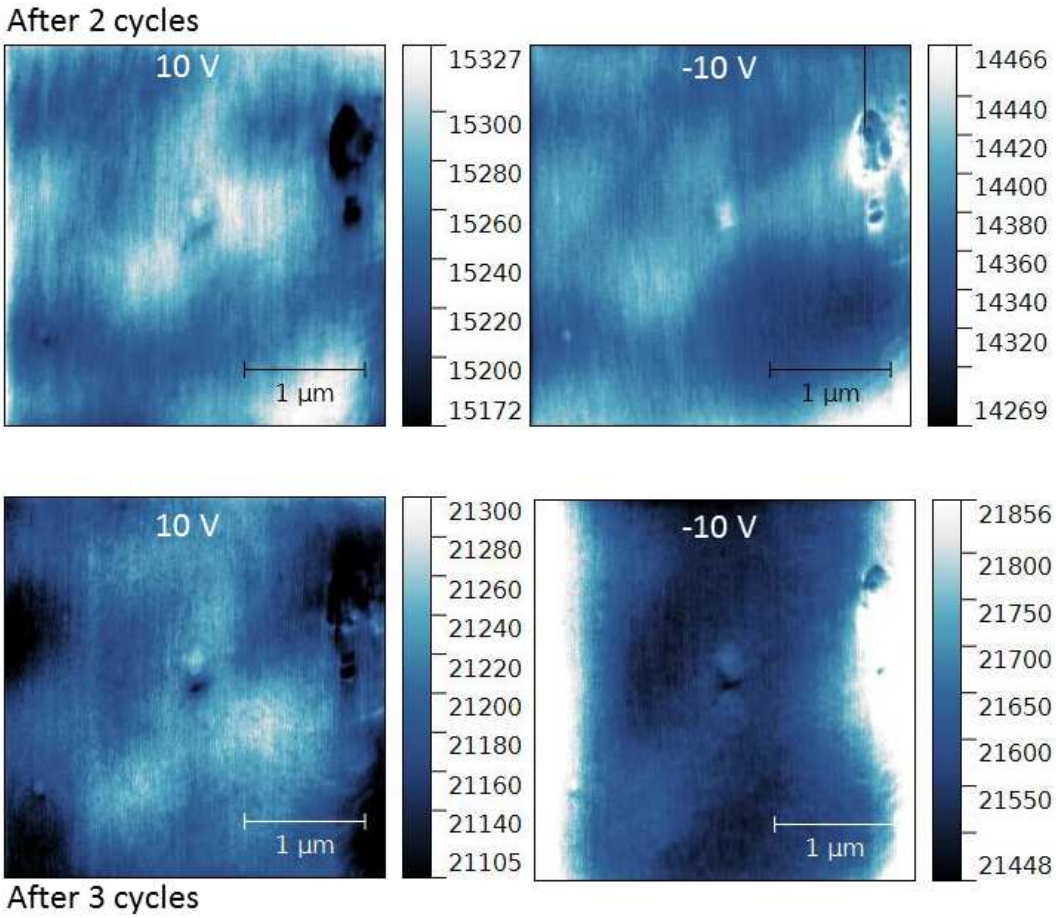

Figure 4.15: EFM images on the same zone of a crystal of **1** following 2 and 3 thermal cycles. The images were recorded at room temperature for two different tip-sample voltages (+10 V, -10V). The tip was lifted 100 nm from the surface to perform the scans.

improvement, but this approach is very restrictive in terms of spring constants and this in particular for tapping mode. For this reason most of the measurements were carried out by heating the AFM probe. Since the tip is made of silicon it can be heated by Joule effect in order to decrease the thermal difference between the tip and the sample. It is important to note that the cantilever and especially the chip are not heated to the same temperature as the tip for simple geometry reasons. Hence this approach can only reduce, but not completely eliminate heat transfer problems. In addition to tip heating we also purged the sample chamber by a gentle nitrogen flux, which also contributed to the temperature stabilization of the system.

Taking into account the promising results obtained previously on single crystals of the SCO compound Fe(pyrazine)[$Pt(CN)_4$] in topography mode [93] we decided to focus in a first time on this mode. Indeed topography images are very straightforward to obtain and should reflect the structural changes associated with the spin transition. Other than observing structural changes, topography images can help us also to observe defects (such as thin cracks) which are not visible in the optical microscope. Such information can be useful to better understand the spatio-temporal dynamics. For example, the propagation of the new phase tends to stop or slow down due to defects in the crystals. These defects are sometimes only visible using more resolved techniques as atomic force microscopy.

At first, topography images were acquired at room temperature on several crystals of **1** in order to get familiarized with the sample. For typical AFM scan sizes, the surface of the crystals are relatively smooth with a roughness of a few nanometers, as shown in figure 4.16. The topography is clearly different for each crystal. This is not very surprising since probably we are observing different crystallographic planes and also crystals with different growth and thermal history.

Images at different temperatures were recorded using a Dimension Icon (Bruker) instrument in non-contact mode. The advantage of using this system is that the tip can be heated and the sample chamber can be purged. Far-field optical images were also recorded systematically between the AFM scans. Figure 4.17 (a) shows optical reflectivity images of a crystal of compound **1** in the LS and IP phases. In these images we can observe that the crystal elongates along its long axis, while it is compressed in the other direction when going from the LS to the IP phase. The color change confirms the spin transition. Somewhat unexpectedly the surface area (determined by ImageJ) is actually ca. 0.4 % larger in the LS state (1395 μm^2) than in the IP (1389 μm^2). Selected AFM images for the two phases are presented in figure 4.17 (b). Thanks to the tip heating strategy we succeeded to acquire AFM images not only in the LS, but also in the high temperature phase. The AFM images show several distinguishable features that help us to locate different points on the crystal during the spin transition and measure the distance between them. This way we followed the expansion/contraction of the crystal as a function of the temperature. Figure 4.17 (c) shows a few examples for this type of measurements. Each

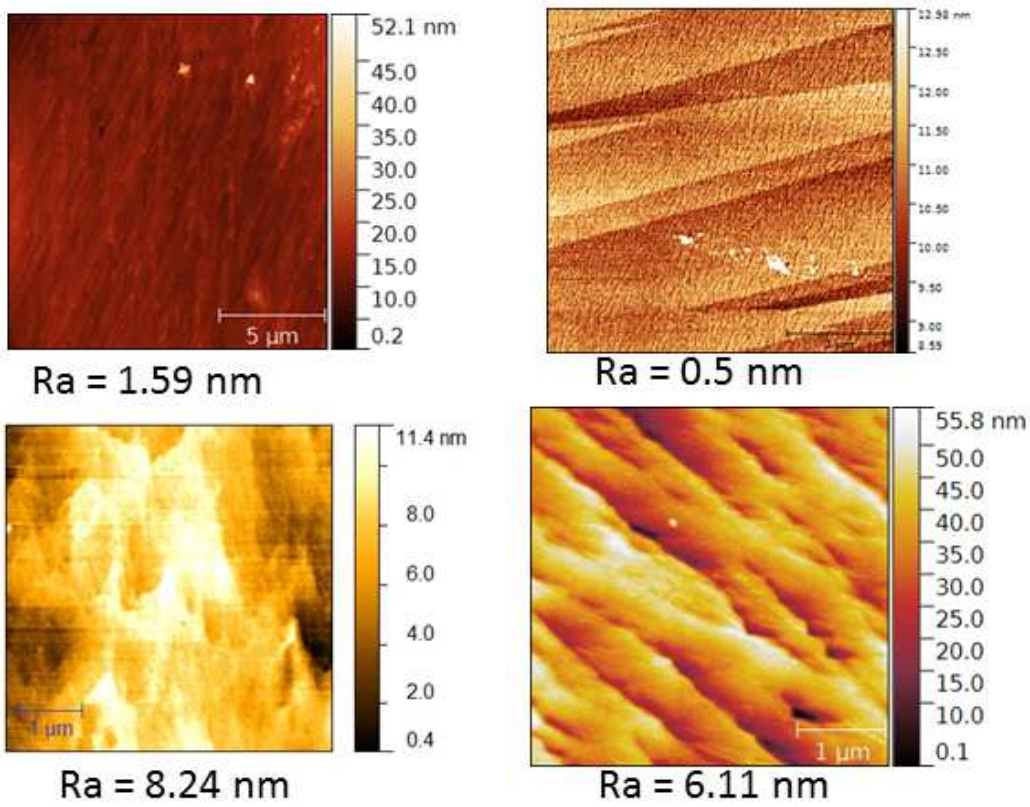

Figure 4.16: Tapping topography images for four different crystals of **1** at room temperature.

plot corresponds to a distance between selected features on the surface (indicated by white lines in the topography images) as a function of the temperature measured both in the heating (closed circles) and cooling (open circles) modes. The first important observation is that the thermal variation of the distances between the features is reversible in each case. This proves that the observed movements correspond to the expansion/compression of the crystal and not to the degradation of its surface. It is worth noting that a crack appeared on the crystal after the spin transition, which is visible both in the optical and the AFM images. Apart from this the topography of the surface appears very similar in both phases. This contrasts the case of Fe(pyrazine)[$Pt(CN)_4$] wherein a significant surface reconstruction was observed between the HS and LS forms [93]. Since the crack observed in the AFM image is closely parallel to the long axis of the crystal, we measured distances parallel (lines 1 and 4) and perpendicular (lines 2 and 3) to the crack. From figure 4.17 (c) it is clear that lines 1 and 4 retract by ca. 2.4 %, while lines 2 and 3 elongate by ca. 3.1% when going from the LS to the IP phase. In other words, these data indicate that the crystal elongates perpendicular to the crack and compresses in the other direction in good agreement with the optical microscopy observations. It will be necessary to compare these results also with crystallography data, but unfortunately up to now we have not been able to determine the crystal structure of this compound in the high temperature phase.

Certain crystals after being thermally cycled several times (7-9 times from 433 K to 448 K) present a peculiar feature, which consist of several nearly parallel dark lines in the optical images. An example is shown in figure 4.18 (a). AFM topography images recorded at room temperature revealed that these lines are actually nearly periodic, "sawtooth-liked" topography features with peak to peak distances of ca. 2-3 μm and peak to valley distances of ca. 50-70 nm. After a few weeks at room temperature these features disappeared and the crystal became once again flat. These topographic features are reminiscent to those observed earlier for crystals of compound **2** during the transition between the LS and intermediate (HS-LS-LS) phases [79]. In the case of this latter compound these undulations were attributed to a twinning process, the LS phase being non-merohedraly twinned. Interestingly during the spin transition the formation of twin domains was also accompanied by the formation of a parallel spin domains. These latter, distinguished by Raman spectroscopy, of course disappeared at the end of the transition. In the case of our compound the LS phase is not twinned, but apparently the twin-like features are related to the thermal spin transition since we observed them only after a few transition cycles. To further investigate this hypothesis we carried out a series of experiments with a crystal presenting this feature.

Figure 4.19 (a) shows far-field optical images of a crystal of compound **1** recorded at 448 K with the AFM tip engaged at two different locations on the crystal. In these conditions a part of the crystal is in the LS phase (on the right from the AFM tip) and

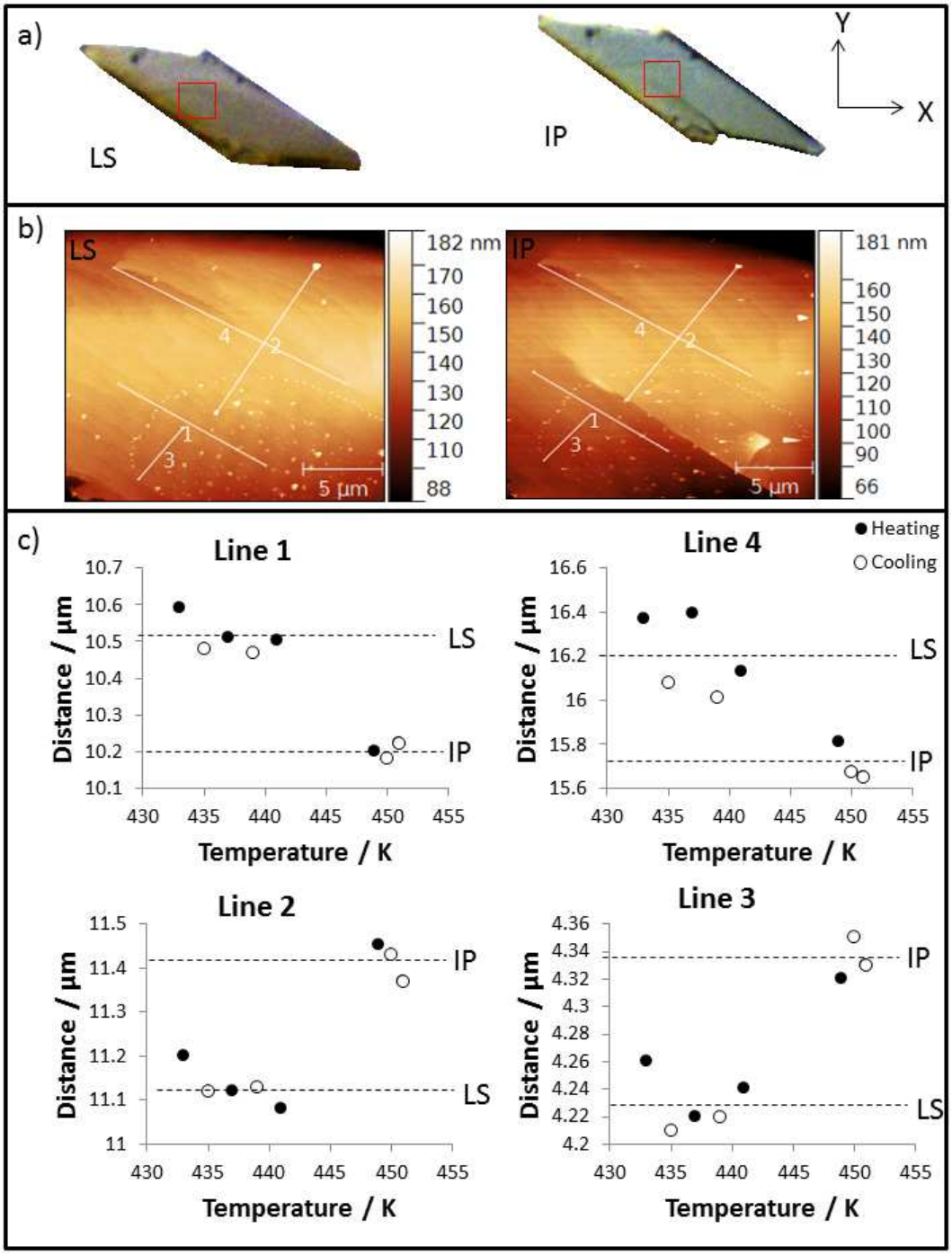

Figure 4.17: a) Optical and b) AFM images of a crystal of **1** in the *IP* and *LS* phases. c) Variation of the length of the white lines in (b) as a function of the temperature in the heating and cooling modes.

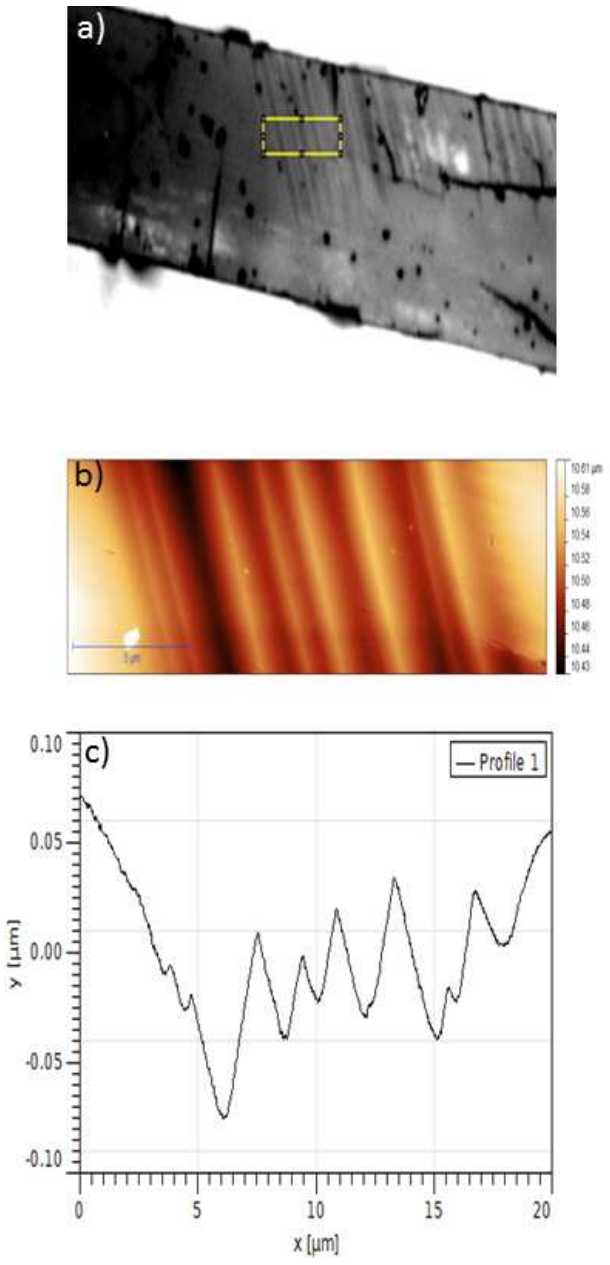

Figure 4.18: a) Optical image, b) AFM topography image and c) topography cross-section of a crystal of **1** recorded at room temperature following 9 thermal cycles across the spin transition. The yellow rectangle in the optical image indicates the area of the AFM scan.

the rest is in the IP phase as inferred from the optical contrasts. In addition, several dark lines appear on the crystal. The spatial frequency of these lines is higher than previously, but actually in each experiment we observed slightly different line densities between 0.1-0.5 μm^{-1}. One can remark that the orientation of these lines parallels the shape of the cantilever, but this might just be a coincidence, since the orientation of the phase boundary in the absence of any AFM tip was already observed similar. When displacing the AFM tip along the crystal these lines move with the tip as shown in the figure. When imaging the topography of this region by the AFM, which was not obvious due to the fact that the lines move with the probe, we could observe similar sawtooth-like features as in figure 4.18. When the tip is retracted the whole crystal is transformed to the IP phase and the lines disappear. It may be worth to note that this experiment was carried out in contact mode using a very long (450 μm) cantilever, which allowed us (as mentioned already in section 4.3.2) to reduce heat transfer between the probe and the sample and thus record images during the spin transition. Nevertheless, the control of the sample temperature and its spin state was extremely difficult. To improve the stability and reproducibility of the experiment we changed the experimental set-up by adding an additional optical path to the system, which allowed us to focus a laser beam ($\lambda = 633$ nm) on the sample surface. This oblique laser beam was aligned so as to irradiate the sample surface near the AFM tip and it was used to locally heat the sample. This way we disposed an independent and local temperature control.

Figure 4.20 compiles the results of an experiment using this laser heating method. In the absence of the laser beam (i.e. 0.0 mW in the images) we observe basically the same phenomena as reported above. The crystal is partially transformed to the LS phase and there are lines around the tip. When the laser is turned on (1.0 mW) the laser-induced heating brings the crystal to the IP phase. As a consequence the lines in the optical images disappear and the topography becomes flat. As shown in figure 4.20 (b) the switching between these two topographies could be repeated several times. We have also repeated this experiment at a different location of the same crystal (figure 4.21). For this experiment we reduced the laser intensity to 0.5 mW because long exposure to 1.0 mW led to some surface degradation. On the whole the same effects were observed in this part of the crystal as well, the only notable difference is the change of the orientation of the "sawtooth" lines.

These experiments prove that the peculiar twin-like topography in this sample is strongly related to the spin transition. As mentioned before, this latter is accompanied by a significant volume and structural change. It is plausible that the elastic strain during the transition is accommodated by the formation of these topographic features. In other words, similar to the famous martensitic transitions, the elastic energy is minimized by these microstructures. This explanation may seem difficult to conceal with the fact that in some cases the sawtooth topography was also observed at room temperature (i.e. far from

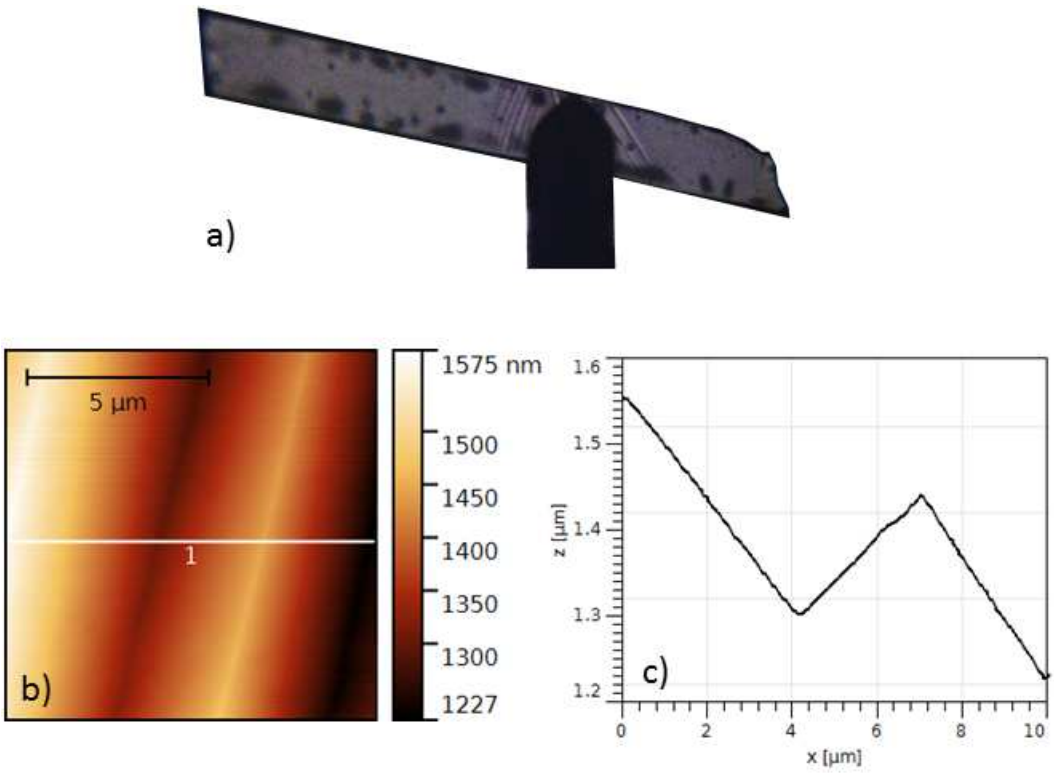

Figure 4.19: a) Optical images, b) AFM topography image and c) topography cross-section of a crystal of **1** recorded at 448 K with the tip engaged on the surface of the crystal. AFM topography was acquired in contact mode using a HQ CSC17 Micromasch probe ($k = 0.18$ N/m, length = 450 μm).

the spin transition). It is possible that some plastic deformation occurs in the system, which is frozen-in when the sample is cooled to room temperature and this metastable structure relaxes over a rather long period (several weeks).

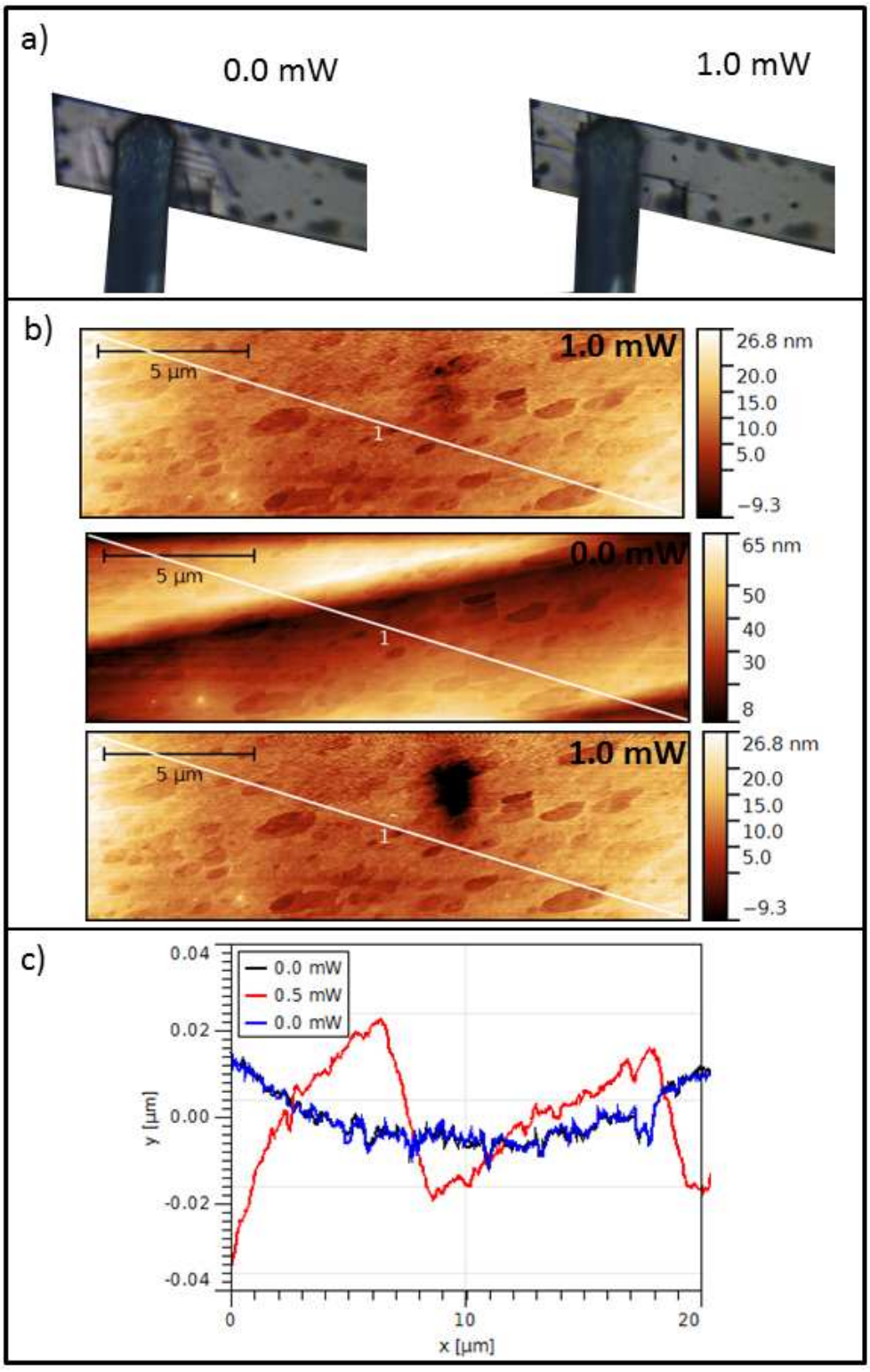

Figure 4.20: a) Optical images, b) AFM topography images and c) topography cross-sections of a crystal of **1** recorded at 448 K with the tip engaged on the surface of the crystal. Images were acquired while turning successively on (0.0 mW) and off (1.0 mW) a laser beam (633 nm) focused near the tip. AFM topography was acquired in tapping mode using a FESPA (Bruker) probe.

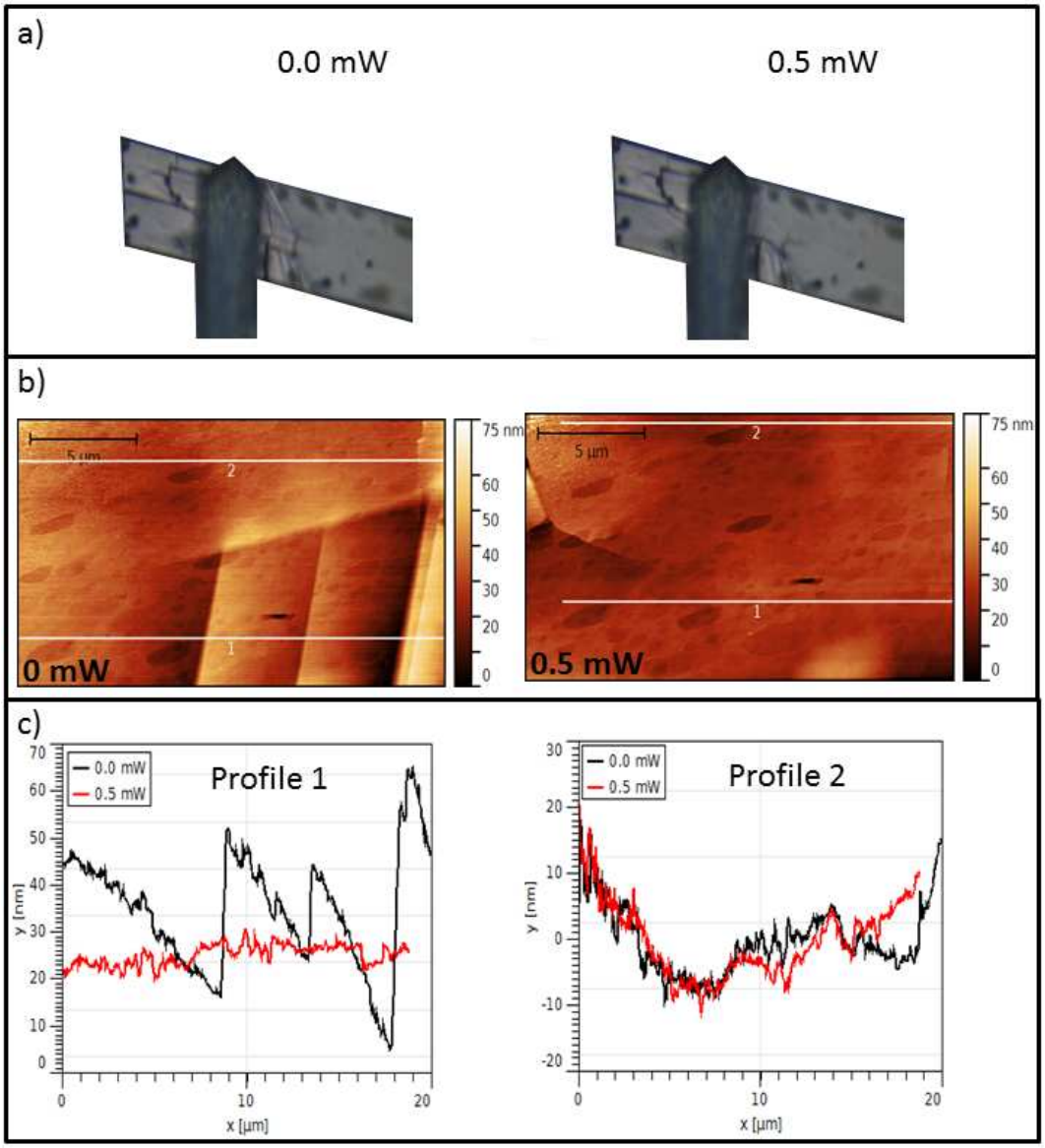

Figure 4.21: a) Optical images, b) AFM topography images and c) topography cross-sections of a crystal of **1** recorded at 448 K with the tip engaged on the surface of the crystal. Images were acquired while turning successively on (0.0 mW) and off (0.5 mW) a laser beam (633 nm) focused near the tip. AFM topography was acquired in tapping mode using a FESPA (Bruker) probe.

4.4 Conclusions

Contrary to the previous chapters which were devoted to the SPM investigation of nanocrystalline spin crossover samples (thin films, nanoparticles), here we described AFM studies of surfaces of macroscopic single crystals. The principal objective of this work was the observation and manipulation of the phase separation in the course of a first-order transition, which we could accomplish only partially. Nevertheless, several important findings could be obtained and a number of technical issues, in particular heat transfer effects, were clarified.

In a first time we investigated the spin transition properties of single crystals of $[Fe(bbpya)(NCS)_2]$ using conventional optical microscopy and Raman spectroscopy. These measurements revealed that actually the spin transition in this compound occurs in two steps, which was not observable in the case of the powder samples. The second step of the transition being very gradual and incomplete, we characterized more deeply the first step between the low spin and the intermediate (HS-LS) phases. This first step of the transition is extremely abrupt and is associated with nucleation and growth phenomena, which were found fairly similar to those reported for the $[Fe(bapbpy)(NCS)_2]$ complex from the same family of compounds.

AFM studies of **1** proved to be very difficult due to severe heat transfer between the sample and the probe. We have investigated the details of the heat exchange and using our nanowire heaters we provided evidence that the most important contribution comes from thermal convection phenomena in our experimental conditions. Due to these convection effects the probe affects the sample temperature at distances as large as a few hundreds of micrometers. We were able to overcome partially these problems by heating the not only the sample, but also the AFM probe. This allowed us to obtain AFM topography images in the two phases and even in the course of the spin transition. Further technical improvements are still possible, but we believe the real solution would be to establish a homogeneous temperature over the whole system, including the sample stage, the sample, the probe and the medium around them. In our opinion this can be achieved only if the AFM images are acquired in liquid medium. This will of course further restrict the working temperature range.

The analysis of AFM topography images recorded in the low spin and intermediate phases revealed a very anisotropic volume change. This latter correlated well with optical microscopy data, but further confirmation using high temperature x-ray diffraction will be necessary. Even more interestingly during thermal cycling we observed the emergence of a peculiar sawtooth-like topography on the sample surface. We have shown that this topographic feature appears during the spin transition and we tentatively explained this phenomenon as a way for the system to reduce the excess elastic energy arising from the volume misfit of the HS and LS molecules during the spin transition. During these

measurements we put in place a new set-up for local laser heating of the sample. This set-up allows also the collection and analysis of laser light scattered locally by the sample and thus Raman spectroscopic maps could be acquired simultaneously with the AFM images. This represents an important perspective for this work as Raman maps may allow to confirm if the observed sawtooth topography corresponds or not to spin domains.

Tip-sample thermal interactions represent a serious obstacle to acquire AFM images during the spin transition. On the other hand, we recognized that the open-up very interesting perspectives to manipulate and control locally the spatio-temporal dynamics. In particular we have shown that by simply moving the AFM probe with respect to the sample, we can induce the spin transition at different possible nucleation points and finely control the position of the phase boundary, which are very difficult or even impossible to achieve when the whole sample is heated. Further improvements are possible if the experiments are carried out in vacuum, i.e. based only on thermal conduction effects. Let us note finally that electrostatic phenomena were also observed during the spin transition. There is no accepted theory or unequivocal experimental proof in the literature which could account for electric fields effects on the spin state of SCO compounds, but we can not exclude that these latter might have some role in our observations.

General Conclusions and Perspectives

The research presented in this thesis was motivated by the recent development of nanosized materials (thin films, nanoparticles, etc.) of transition metal complexes displaying molecular spin state switching phenomena. Bistable spin crossover nanoobjects are appealing for a variety of applications, but a lot of efforts are still needed to analyze and understand the different physical and chemical phenomena governing their properties.

In this work we demonstrated that spin crossover phenomena can be studied and triggered by means of scanning probe microscopy with nanometric spatial resolution. We showed that scanning probe microscopy can be used to follow the thermal spin transition in nanoscale SCO materials through the analysis of different kinds of tip-sample interactions including the detection (or generation) of evanescent electromagnetic waves by an apertured fiber tip, the analysis of elastic deformation induced by a sharp silicon tip. Additionally, we proved that SCO phenomena in bulk can also be followed by observing changes of features in the sample topography as a function of the temperature. In addition, the possibility to trigger and even finely control the spin transition by local heat exchange between the sample and the probe was also put in evidence.

Scanning probe microscopy techniques have been used in the past two decades to investigate phase change phenomena in different materials, such as ferroelectrics, polymers and magnetic materials. In most cases, however, SPM imaging across the phase change phenomena remained qualitative. Quantitative imaging of a material property which can be controlled by independent means has been rarely reported even in other fields. The main obstacle in any quantitative SPM approach is the analysis of the interactions between the SPM probe and the sample, all the more that both can change their properties during the SPM measurements. In addition, the phase change must be triggered by some external stimuli, which can also perturb the SPM analysis. In the case of SCO compounds the most convenient way to induce the spin transition is thermal excitation. We observed at several instances that the wear of the tip and the sample during successive scans as well as various unwanted thermal effects (sample drift, heat exchange between the sample and the probe, etc.) are very difficult to handle when using conventional SPM heating stages.

To overcome (or at least minimize) these problems we implemented a novel experimental strategy to study SCO films based on the localized heating of the sample by a Joule-heated metallic wire. This original approach allowed us to achieve very fast and tightly controlled temperature changes as well as to significantly reduce thermal drift and thermal exchange with the probe. Scans over the non-heated area allowed also to correct (or at least to detect) tip and/or sample degradation. These latter were also monitored in most cases in-situ by means of high sensitivity optical microscopy coupled to the SPM. We believe that this nanoheater strategy is not only interesting for the SCO field, but can find a more general application within the SPM community.

Perhaps somewhat unexpectedly AFM thermo-mechanical measurements proved to be the most powerful approach for the quantitative imaging of the spin transition. We succeeded to indent SCO thin films in a non-destructive manner and from the temperature dependence of the indentation data we could extract the Young's modulus of the films in the two spin states. This information is very relevant on its own, but even more importantly it can be used to monitor the spin state change with unparalleled spatial resolution. These measurements were carried out using a relatively recent AFM mode - the Peak Force Tapping, which belongs to the family of fast force mapping techniques. Preliminary tests using other mechanical modes were also made and it was shown that multifrequency AC imaging can provide similar results, but at an even faster imaging rate.

Even if the SCO is associated with a significant volume change, surface topography AFM images were not useful to follow the spin transition in thin film samples. (N.B. This simple approach deserves, however, further efforts in the future.) On the other hand, very interesting surface topography changes were observed during the SCO in single crystal samples. The topography differences between the two spin states were analyzed and they correlate well with the change of the crystal shape. Even more importantly, intriguing transient topography changes were also observed during the spin transition in the form of surface undulations around the phase boundary. We suggested these undulations are formed in order to minimize the significant elastic stress and strain near the phase boundary.

Nanoscale optical imaging of SCO films provided also useful contrast between the high spin and low spin phases both in fluorescence and reflectance modes. The former uses fluorescent probes incorporated in the film, while the latter probes directly the refractive index change of the SCO sample. Reflectivity measurements proved to be more robust, in particular in constant height NSOM mode. In the case of the investigated samples the quantification of the spin state changes observed in NSOM was difficult (both in fluorescence and in reflectivity). A possible solution to this problem would be to work in transmission mode, but this would request samples with rather specific optical properties. (I.e., a thin sample with a high optical density change upon the SCO in the UV spectral

region is needed.) Generally speaking, samples with appropriate properties are crucial not only for NSOM, but also for any other SPM technique and future work must focus more on this issue.

Beside the detection of spin state changes in a small sample volume, we have shown that an SPM tip can be also used to trigger the spin transition locally. We tested high resolution photothermal laser writing using NSOM tips and we succeeded in switching the spin state of individual nanoparticles. In another (simple) approach, a cold Si probe was used to induce the high spin to low spin transition in a single crystal. We have shown that the tip can induce the nucleation of the LS phase and allows also the fine control of the position of the phase boundary. This finding opens up interesting possibilities to investigate the properties of the phase boundary. Clearly there are many other ways to use an SPM probe to manipulate the spin state of matter with nanometric resolution, such as using specific thermal probes or mechanical effects, which remain to be explored. These tools are appealing since they can allow to perform nanometric write/errase operations and can therefore give access to new devices, such as nanoscale memories. For example, we have shown in this work that the thermal memory observed in some SCO compounds provides an unprecedented scope for imaging transient thermal events with a high spatial resolution.

Finally we must note that other SPM methods provide also exciting perspectives for the SCO field. Notably it would be interesting to explore the possibilities provided by magnetic force microscopy (MFM) and nanoscale vibrational spectroscopy methods, such as tip enhanced Raman and FTIR spectroscopies.

Appendix A

SPM Artifacts

An ideal AFM image is an accurate representation of a sample surface or sample properties. Every part of an image that differs from the sample surface or properties is an artefact. As with any analytical technique, SPM is not free of artifacts. Here some common artifacts which were found during this work are presented.

A.1 AFM artifacts

A.1.1 Tip shape issues

The most known and probably the most studied of these artifacts are the so-called "tip-artifacts", which originate from the finite-sized tip. This problem often arises when imaging features from 50 to 500 nm. In this case the shape of the SPM tip has a drastic effect on the images that are acquired (figure A.1). This is one area where having reproducible probes is an advantage, if the tip shape is well characterized, so that the images can be better interpreted and the obvious artifacts identified. Topography images are always a combination of the tip shape and the true surface topography. Obviously the sharper and narrower tip produces the most accurate representation of the surface. This artifact will depend on the cone angle of the main pyramid that forms the tip and the radius of the tip end.

When something contaminates the tip, such as a particle that glues to the tip, strange repetitive shapes are introduced to the image. In order to diagnose this issue a new sample with known features must be scanned or the tip must be replaced. It might be possible to clean the tip, but it is better to simply change the probe. In addition to the repetitive shapes, tip contamination can lead to twinned features, as shown in figure A.2.

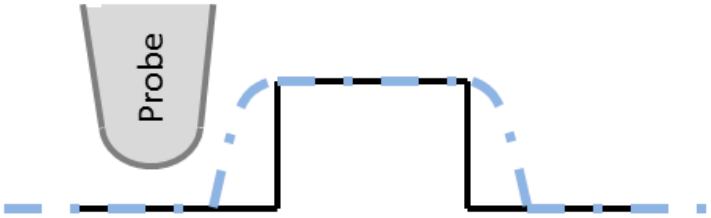

Figure A.1: Scheme of an AFM probe scanning a small square. The doted line represents the topography image obtained with the probe. The black line represents the real topography.

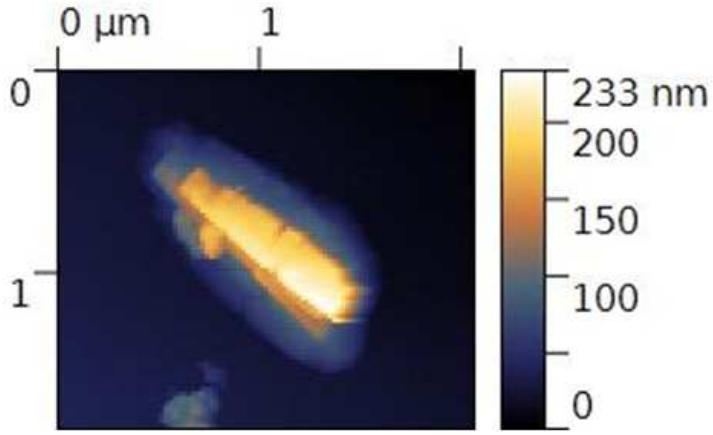

Figure A.2: AFM topography Image of a SCO crystal of [Fe(Pyrazine)Pt(CN)$_4$] made with a contaminated probe.

A.2 Oscillations

Oscillations in AFM data can come from several sources, including electrical interference, mechanical vibrations, acoustic noise and optical interference. There are some practical rules that can be used to infer the origin of oscillations in AFM data. For example, if the periodicity of the oscillations appears to increase as scan rate is diminished, the oscillations come from some fixed frequency interference. This sort of interference may come from an acoustic source in the room, or from mechanical vibrations or electrical interference transmitted to the microscope. By measuring the frequency of the oscillations, one can often get a clue of what is causing the interference. For example, 60 Hz (or 50 Hz where appropriate) oscillations are usually electrical in origin. The frequency of these oscillations is determined using the following:

$$\frac{2scansize(nm)}{oscilationperiod(nm)} \cdot scanfrequency(Hz) \tag{A.1}$$

The factor 2 comes from the fact that tip travels twice the scan size (forward and reverse) each cycle. In when the scan angle is affected, the oscillation features will rotate with respect to the sample accordingly.

When changing the scan rate does not change the periodicity of the oscillations, then they have a fixed spatial frequency. This is the case for optical interference artifacts, which are produced when the ambient laser light (i.e., light passing around or even through the cantilever, and then reflecting off the surface) interferes with laser light reflecting from the cantilever. This is a common problem with all the commercial AFMs based on an optical detection system, in which a laser source with coherent output is used. Although the artifacts described in this work are more frequent in contact mode on highly reflective surfaces, they occasionally appear in non-contact mode images, as in tapping mode. Although optical interferences could be essentially eliminated using other AFM modes, such as phase detection and frequency modulation, in many AFM applications in materials science, such as force curve mapping (adhesion maps acquisition) and friction analysis, the contact mode is required. In this work, these artifacts are presented as regularly spaced (1-2 μm), sine-shaped stripes along the whole image, as shown in the adhesion images shown in figure A.3. In this figure the topography and adhesion images are shown for different scan and sample angles. When the scan angle is zero we observe parallel lines in the adhesion image which are formed parallel to the wire shown in the topography (figure A.3 a). If only the scan angle is rotated, the parallel lines in the adhesion map continue to be parallel to the wire (figure A.3 b). From this result we can determine that the lines are not result of electrical interference, mechanical vibrations or acoustic noise. However, if the sample is rotated 90 degrees, the parallel lines in the adhesion map are no longer parallel to the wire, but they are rotated 90 degrees, as shown

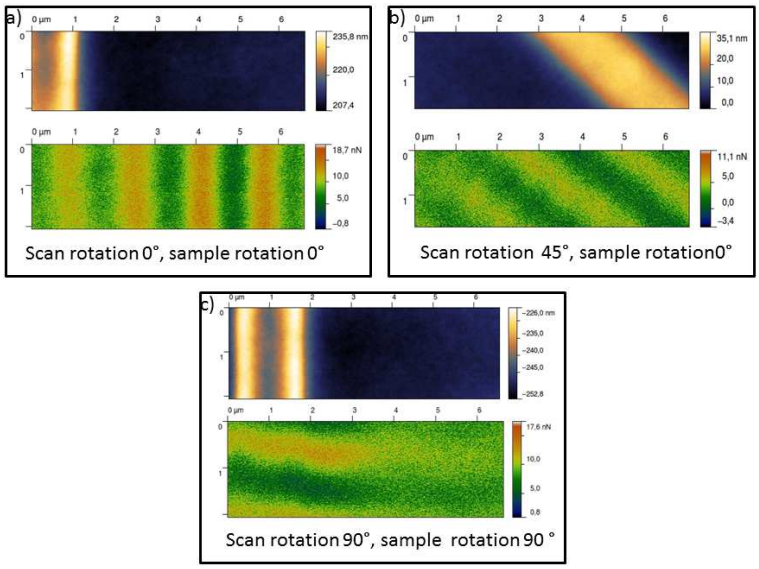

Figure A.3: Topography and adhesion images of a thin film of $[Fe^{II}(hptrz)]_3(OTs)_2$ spin coated on a nanowire device for different scan angles and sample angles.

in panel c. This is a clear indication that the lines are an artifact, which is related to the detection system. In this case it is result of optical interference produced by the optical deflection system. As this effect depends on the reflection of a part of the laser beam on the surface, it will be more pronounced on highly reflective and smooth surfaces. Although other authors have noted this phenomenon, no results about their influence either on surface roughness measurements or on image contrast (which is the basis of some AFM modes) have been reported. Moreover, in order to remove these artifacts from images, the fast Fourier transform technique (FFT) has been used, improving the results of the usual flattening routines. However, real information can be lost during this process.

A.3 NSOM artifacts

Topography artifacts are normally observed in NSOM when imaging steep slopes or edges on a sample. Sometimes topography artifacts can modify or even completely obscure the optical information contained in the data, namely due to the fact that the variations of the sample refractive index and topographic variations can lead to the same effects on the NSOM data. An example of this effect is the luminescence on the borders of a nanowire as shown in figure 2.17.

Regular oscillations on the NSOM signal can be also observed. This oscillations are normally related to mechanical vibrations or acoustic noise that are transmitted through the fiber tip, as shown in figure A.4. This artifact is normally found when the tip is not well attached to a surface so it oscillates due to external noises.

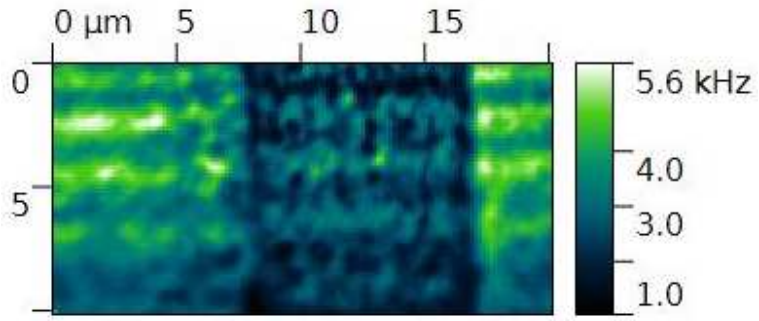

Figure A.4: NSOM image of $[Fe(Htrz)_2(trz)]BF_4$ nanoparticles deposited on a gold wire. The image was obtained with a loose fiber tip.

Appendix B

Mechanical studies on a SCO composite

One of the interest to use AFM for mechanical measurements is the possibility to analyze heterogeneous samples with high spatial resolution. In this context phase imaging is very interesting since it allows to observe differences in the mechanical properties of the material. Contrary to force based curves this method takes into account all forces (i.e. adhesive and repulsive forces). Therefore it is easier to observe the location of the different compounds in a composite. In order to investigate this possibility we have prepared mixtures of PMMA and $[Fe^{II}(hptrz)]_3(OTs)_2$.

The Young's modulus of the PMMA do not change between 293 K and 343 K, whereas the elastic modulus of the $[Fe(hptrz)]_3(OTs)_2$ changes due to spin transition (more details are presented in sections 3.2 and 3.3. If the mechanical properties of the forming parts do not change when the composite is prepared, the contrast between the two compounds will be grater in high spin than in low spin. Phase images performed in tapping mode and force curves carried out in Quantitative Imaging mode show a clear contrast between both compounds. The phase images are very different, depending on the setpoint and amplitude of the cantilever. The brighter points in the phase images with a setpoint of 60% are related to the lower points in the topography, but the rest do not have any relation with the topography. Although the middle image (Amp=50, setpoint=60%) can be consider a mixture of the other two images, it is hard to make a relation between the different phases and determine without doubt which is the PMMA and which is the SCO compound.

Conversely Quantitative Images give a better idea of the different materials, once again there is no clear relation between the adhesion or the stiffness to the topography image. The contrast in the adhesion image is bigger than in the stiffness image, probably because the tip probes a bigger volume of the sample while only the adhesion of the surface is detected. Nevertheless, in general it is possible to determine from the images that the

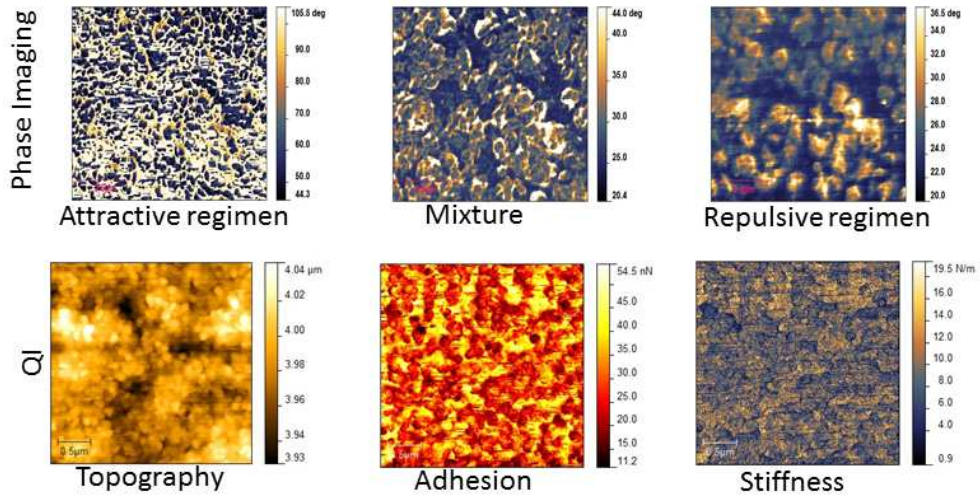

Figure B.1: Images obtained by phase imaging and QI modes of $[Fe^{II}(hptrz)]_3(OTs)_2$ and PMMA composite, the phase channel is presented for different amplitudes and setpoints, below the topography, adhesion and stiffness obtained in QI.

harder parts of the material are also more adhesive. Since PMMA's elastic modulus is higher than the Young's modulus from the SCO compound we can determine that the yellow parts in the adhesion corresponds to PMMA polymer and red parts to the adhesion correspond to SCO particles.

A thin film of this compound was deposed on a NW heater, to measure the Young Modulus as function of the temperature (current) on the NW. In figure B.2 the height of the NW is plotted as function of the current passing through it. For currents bigger than 14 mA a decrease of the height of the NW is observed. Even though the thickness of the film is lower the Young's modulus do not increase, but slightly decrease for high currents (> 14 mA). This could be due to two different reasons, the melting point of the composite is lower than the melting point of the PMMA (≈ 433 K), or the temperature reached by the NW with this material is higher than with $[Fe(hptrz)]_3OTs_2$. A complete analysis of the NW in order to determine the reached temperature at different currents with this materials would be necessary to solve this question. Although since the spin transition curve was not obtained by any other method like Raman or plasmon. We decided to stop the analysis with this compound.

The study of the mechanical properties of SCO composites will be continued as the part of the analysis of the thesis of Dolores Manrique, where it is very important to determine the Young's Modulus in the high spin state and in the low spin state to determine the work done by SCO micro- and nano-actuators. As part of this research the influence of the substrate for very thin layers, must be also investigated, to continue the work in nanoactuators, but also to continue the study of the mechanical properties of SCO nanoparticles.

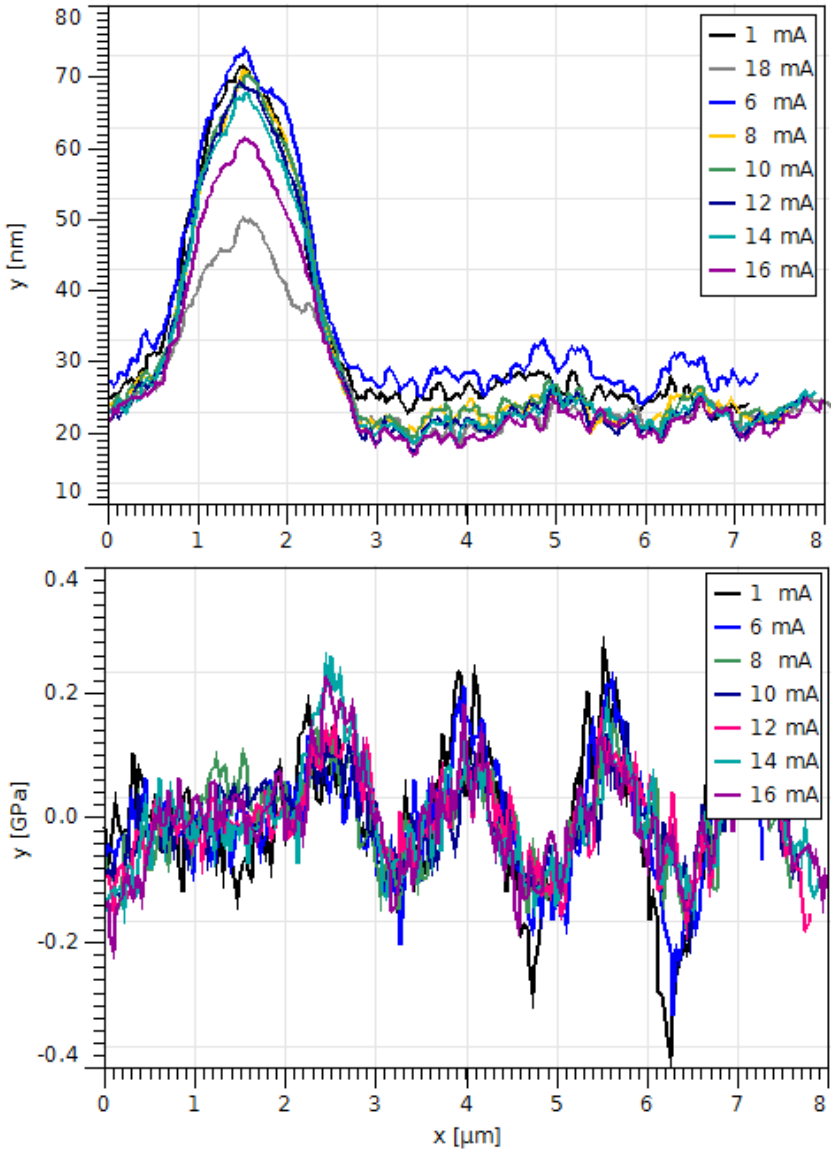

Figure B.2: Cross sections of a thin layer of $[Fe^{II}(hptrz)]_3(OTs)_2$ and PMMA composite spin coated in a nanowire device of (top) the topography and (bottom) the Young's modulus for different applied currents.

Appendix C

Etudes à hautes résolutions spatiales du phénomène de conversion de spin par microscopies à sonde locale

C.1 Introduction

Les matériaux à transition de spin sont des complexes inorganiques qui présentent une transformation de phase entre l'état haut spin (HS) et l'état bas spin (BS). Comme dans un grand nombre de matériaux, la stabilité des phases et la cinétique de la transition dépendent de la taille du système. En particulier, il a été montré que la température de transition (ou plus généralement le diagramme de phase) et le caractère complet de la transformation sont fortement affectés à l'échelle nanométrique. Les études expérimentales et théoriques qui permettent de comprendre les mécanismes physiques sous-jacents sont très récents et demandent encore de confirmation. D'un autre côté, les propriétés exceptionnelles des nanomatériaux à transition de spin font d'eux des matériaux très intéressants pour un grand nombre d'applications technologiques. En effet, le changement d'état de spin de ces nano-objets à transition de spin (nanoparticules, couches minces, nanostructures, ect.) est accompagné par différentes modifications des propriétés du matériau, comme par exemple, les propriétés magnétiques, optiques, électriques et mécaniques. Cette modification des propriétés permet un large éventail d'applications dans les domains de la nanoélectronique, la spintronique, la nanophotonique et les systèmes nanomécaniques. Par exemple, ils ont été proposés comme éléments outils pour

des capteurs de gaz [1, 2], micro- et nano- actuateurs (MEMS, NEMS)[3, 4], des pigments activables thermiquement [5], des guides d'ondes photonique [6], des filtres Thz commutables [7] et des nanothermomètres [8, 9].

Les méthodes expérimentales usuelles utilisées pour caractériser les matériaux massifs à transition de spin (magnétométrie, diffraction des rayons-X, calorimétrie, spectroscopie Mössbauer, spectroscopies électronique et vibrationnelle), ne sont pas toujours adaptées pour étudier les matériaux à transition de spin à l'échelle nanométrique. Cela est due en général à la faible quantité de matière sondé. De ce fait, de nouvelles techniques de caractérisations doivent être développées. En particulier, il est nécessaire de pouvoir développer un outil ayant une haute résolution spatiale et une grande sensibilité afin d'être capable de détecter le changement d'état de spin dans une très petite quantité de matière qui, idéalement, est un nano-objet unique isolé. Au delà de leur haute résolution et/ou de leur grande sensibilité, ces systèmes expérimentaux permettent aussi d'avoir des informations sur les propriétés du matériau, qui sont difficiles d'accès par les techniques conventionnelles ou non significatives à d'autres échelles de tailles. Les techniques de microscopie optique en champ lointain ont déjà été utilisées avec succès pour observer le changement d'état de spin dans un nano-objet unique. Par exemple, les nanoparticules uniques à transition de spin sont étudiées avec de la fluorescence, du spectroscopie Raman et de la microscopie à contraste interférentiel. D'autre part, des couches minces d'épaisseurs nanométriques de matériaux à transition de spin ont été analysées par différentes méthodes photoniques (ellipsométrie, résonance des plasmons de surface, etc.).

Dans le but de dépasser la résolution spatiale des méthodes optiques en champ lointain, nous pouvons utiliser des faisceaux d'électrons ou des rayons-X, ce qui permet de connaître la structure et d'obtenir des informations spectroscopiques avec une très haute résolution spatiale. Dans le cas des matériaux à transition de spin relativement fragiles, des précautions doivent être cependant prisent du fait de la nature invasive de ces techniques: chauffage de l'échantillon et dommages causés par les radiations. Ces problèmes ont largement été diminués dans une très récente étude qui utilise une microscope électronique afin de suivre la transition de spin dans des nanoparticules uniques [10]. Une autre approche possible que nous avons exploré au cours de cette thèse est basée sur les

microscopies à sonde locale. Bien que les microscopies à sonde locale ont déjà été utilisés pour étudier la transition de phase dans différents métaux, l'étude des matériaux à transition de spin à l'aide de ces techniques est . En effet, seul la microscopie par effet tunnel a été utilisé dans ce domaine mais, cette microscopie est plus adaptée dans le cadre d'une étude sur une molécule unique que sur des nanomatériaux qui sont les objects de notre travail. Effectivement, le principal objectif de ce travail est d'explorer l'utilisation possible de microscopie à sonde locale pour caractériser et manipuler l'état de spin de matériaux à transition de spin à l'échelle nano et micrométrique. Nous nous sommes concentrés sur deux méthodes de microscopie à sonde locale: la microscopie optique en champ proche et la microscopie à force atomique. Cette dernière a été utilisé pour obtenir des images topographiques de l'échantillon et pour cartographier ses propriétés mécaniques.

C.1.1 Introduction au phénomène de la transition de spin

Le phénomène de TS peut être expliqué par la théorie du champ de ligands (LFT). D'autre part, cette théorie est également un outil important pour comprendre les propriétés optiques des composés à TS (plus de détails peuvent être trouvés dans l'article de Hauser [46] Lorsque l'ion Fe(II) est complexé à six atomes donneurs, il adopte une configuration octaédrique qui entraîne la levée de dégénérescence des 5 orbitales d en niveaux de symétrie t_{2g} triplement dégénérés et en niveaux de symétrie e_g doublement dégénérés de plus haute énergie (Figure C.1). La différence d'énergie (10 Dq) qui sépare les deux niveaux t_{2g} et e_g est directament liée au champ cristallin. Les six électrons du fer(II) peuvent alors se répartir de deux façons différentes selon les valeurs relatives du champ de ligand et de l'énergie d'appariement des électrons, Π. Si 10Dq > Π c'est l'état bas-spin (BS, $^1A_1$), diamagnétique et si 10Dq < Π, c'est l'état haut spin (HS, $^5T_2$), paramagnétique. Le diagramme de Tanabe-Sugano de la Figure C.1 montre, pour un ion de configuration d^6 dans un environnement octaédrique, qu'un état $^5T_2$ (état HS), est stabilisé par les champs faibles alors que l'état $^1A_1$ (état BS), est stabilisé par les champ forts. Ainsi, pour des complexes ayant une éclatement du champ cristallin 10Dq proche de Π, le système peut passer d'un état à l'autre sous l'effet d'une perturbation extérieure comme la température, une pression, une irradiation lumineuse ou l'application d'un champ magnétique ou électrique.

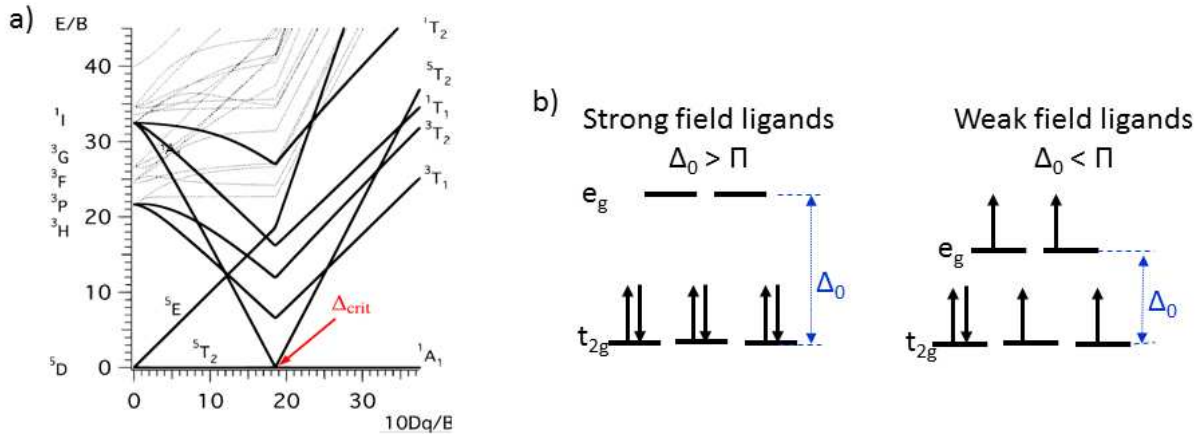

Figure C.1: a) Diagramme de Tanabe-Sugano pour un ion $3d^6$ dans un champ électrostatique octaédrique. b) Configurations électroniques Haut Spin (champ crystallin faible) et bas spin (champ crystallin fort) pour un ion $3d^6$ (Fe(II), Co(III)).

C.1.2 Introduction à la microscopie à sonde locale

La microscopie à sonde locale est une branche de la microscopie qui a été créé pour accéder à des résolutions au delà de la diffraction optique. Cela consiste à avoir une pointe fine qui balaye toute la surface de l'échantillon avec une précision nanométrique ou subnanométrique. Ceci peut être comparer au fait de toucher la surface avec son doigt. Avec cette technique, il est possible d'obtenir des images à trois dimensions de la surface d'un solide avec une résolution atomique. Parmi cette variété de technique de microscopie à sonde locale, deux approches semblent particulièrement adaptées pour l'étude des composés à transition de spin: (1) la microscopie optique en champ proche (NSOM en anglais) puisque l'indice de réfraction des matériaux à transition de spin change durant la transition et (2) les différents modes mécaniques de la microscopie à force atomique (AFM en anglais) puisque l'élastisité varie d'un état de spin à un autre.

En AFM, la force entre la pointe et l'échantillon est gardée constante grâce à une boucle d'asservissement qui contrôle la déflexion du levier. Il y a deux modes principaux de microscopie à force atomique: (1) le mode contact, où la déflexion du levier est contrôlée par une boucle de rétroaction et (2) le mode tapping, où la pointe est forcée d'osciller à sa fréquence de résonance, et la boucle de rétroaction garde soit l'amplitude, soit la phase, soit la fréquence constante.

Le NSOM a été développé dans le but de dépasser la limite de diffraction optique.

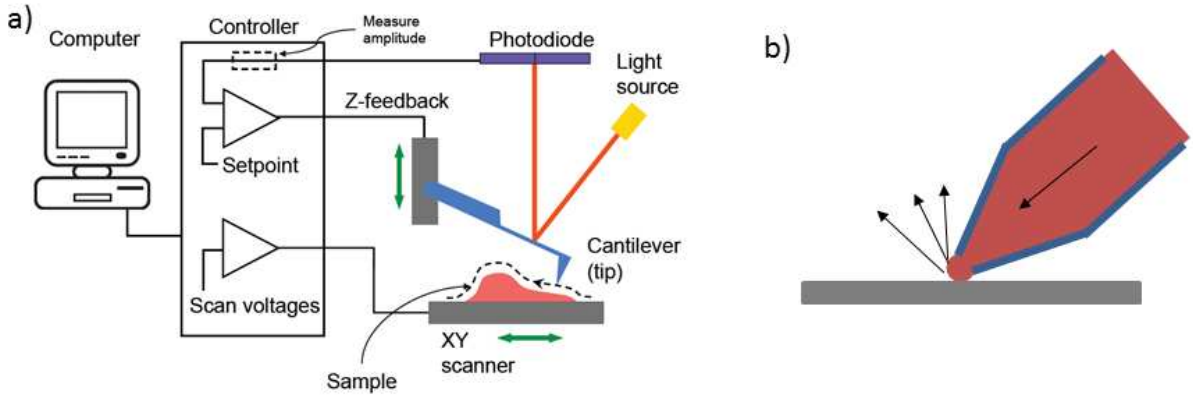

Figure C.2: a) Modèle d'AFM utilisant un système de mesure de déflexion par faisceau optique. b) NSOM configuration en réflection: on excite l'échantillon à travers l'ouverture de la pointe en champ proche et on collecte la lumière réfléchie en champ lointain.

Cette limite peut être dépassée en réduisant la source d'illumination lumineuse à un volume plus petit que sa longueur d'onde. Cependant, le champ proche est étroitement confiné à la surface de la matière, ainsi, sa détection n'est pas facile et a besoin d'actuateurs de précision nanométrique, c'est-à-dire, capables de bouger un capteur ou une source de lumière à quelques nanomètres de l'échantillon.

C.2 Microscopie optique en champ proche (NSOM)

C.2.1 Méthodologie

Afin de surmonter les contraintes expérimentales fortes imposées par la nécessité de procéder à une série de mesures par microscopie optique en champ proche (NSOM) à différentes températures et de manière quantitative, nous mettons en place une stratégie expérimentale originale basée sur un chauffage local de l'échantillon par un nanofil métallique (Voir Figure C.3). En effet, l'usure de la pointe et de l'échantillon au cours de mesures successives NSOM associées à divers effets thermiques indésirables (dérive de l'échantillon, chauffage de la pointe, etc.) sont très difficiles à appréhender lorsque l'on l'utilise des techniques de chauffage classiques en microscopie à sonde locale. Le chauffage local rapide avec les nanofils s'avére très concluant, ce qui nous permet d'observer la transition de spin en fonction de la température même au cours d'un seul et unique balayage. Nous pensons que cette approche peut trouver un intérêt général dans la communauté de la

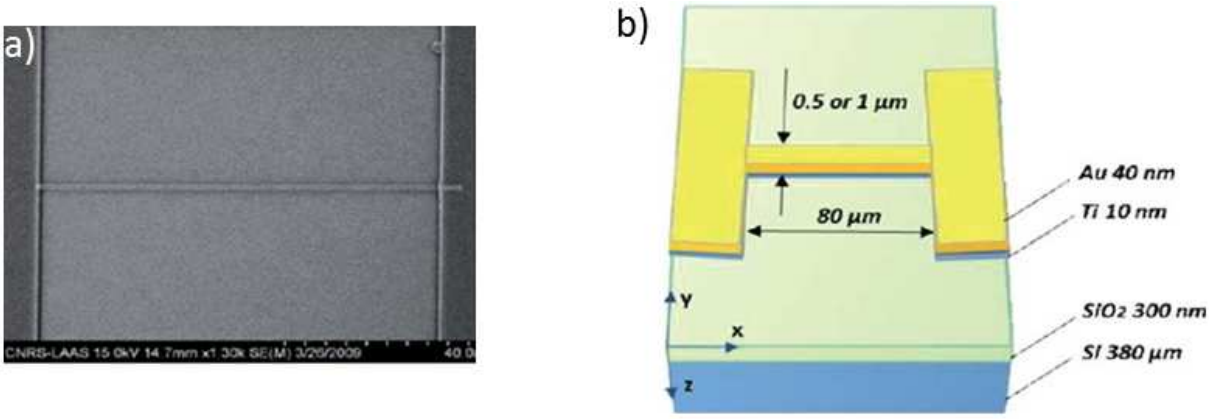

Figure C.3: a) Image effectuée par microscopie electronique à balayage et b) représentation schématique d'un dispositif de nanofil chauffant d'or de dimension 50 nm × 1 μm × 80 μm.

.

microscopie à sonde locale pour plusieurs raisons. Tout d'abord, la dérive de l'échantillon est négligeable et le chauffage de la sonde peut être minimisé. En outre, la thermalisation de l'échantillon est très rapide et la différence de température est confinée au niveau du fil, fournissant ainsi une zone de référence proche du fil. Cette zone peut être utile pour contrôler l'évolution de l'interaction pointe-échantillon. Enfin, la possibilité de chauffer la fil par un courant électrique et de contrôler sa température au travers de sa résistance électrique donnent des moyens utiles d'un intégration et de synchronisation du nanofil chauffant avec l'autre partie de l'installation.

C.2.2 Détection de la fluorescence en NSOM

Les premières experiences de NSOM sur le composé $[Fe^{II}(hptrz)]_3(OTs)_2$ ont été réalisées en utilisant la fluorescence. L'échantillon a été irradié avec de la lumière bleue (488 nm) provenant d'un laser argon (Melles Griot) couplé à la fibre de la pointe. Lorsque la pointe est proche de l'échantillon, des ondes évanescentes générée à proximité du sommet de la pointe excitent un très petit volume des fluorophores. La lumière émise par l'échantillon est ensuite collectée par un objectif de Mitutoyo (grossissement 50x, N.A.=0.55). Ensuite la lumière est filtrée par un miroir dichroïque (Semrock FF510-Di02) et un filtre passe bande centré autour de 550 nm. Le signal est détecté par un tube photomultiplicateur (PMT). En guise de protection, un filtre coupe bande centré autour

de 488 nm est placé en face du tube photomultiplicateur. Des mesures de NSOM ont été ensuite réalisées en parallèle de l'acquisition de la topographie par microscopie à force atomique (AFM).

La figure C.4 montre des images de microscopie en champ lointain et en champ proche à température ambiante. La figure C.4 b présente une comparaison de l'intensité de fluorescence entre les données du champ proche et celles du champ lointain en fonction de la température. Les données des mesures en champ lointain sont tracées à la fois pour l'aire balayée et une autre surface "vierge" qui n'a pas été balayée en champ proche. Durant le chauffage amenant l'échantillon de la température ambiante à 343 K, l'intensité de fluorescence en champ lointain diminue de manière assez monotone, mais le changement le plus important semble se produire entre 303 K et 343 K. Au cours du refroidissement, l'intensité de fluorescence reste constante jusque 313 K avant d'augmenter pour atteindre sa valeur initiale à température ambiante. La courbe observée présente un cycle d'hystérésis. Ces résultats peuvent être attribués à la transition de spin de l'échantillon. La différence entre l'intensité en champ lointain à l'intérieur et à l'extérieur de la surface balayée reste négligeable dans cette expérience. Il y a donc une assez bonne correspondance entre la dépendance en température du signal fluorescent en champ proche et en champ lointain, en particulier au début du cycle thermique. A la fin du cycle, la différence entre les données champ proche et champ lointain augmente considérablement. Cette différence est probablement associée à un changement des propriétés de la pointe. Nous pouvons tout de même conclure que la transition de spin est détectable au travers du signal fluorescent en champ proche.

C.2.3 Réflectivité en NSOM

Dans le but d'effectuer des mesures NSOM à hauteur constante autour du fil d'or, l'approche de la pointe vers l'échantillons a toujours été réalisée sur le fil. Ensuite, la pointe est retractée de $60nm$ du fil avant le balayage de l'échantillon. La pointe est complétement rétractée de l'échantillon avant qu'un quelconque changement de la température ne soit appliqué à l'échantillon soit par le système de chauffage de l'AFM soit à l'aide du fil d'or. Après avoir chauffé le matériel sur le fil par effet Joule, des mesures NSOM doivent montrer une augmentation de la réflectivité au niveau du fil. D'un autre côté, les propriétes

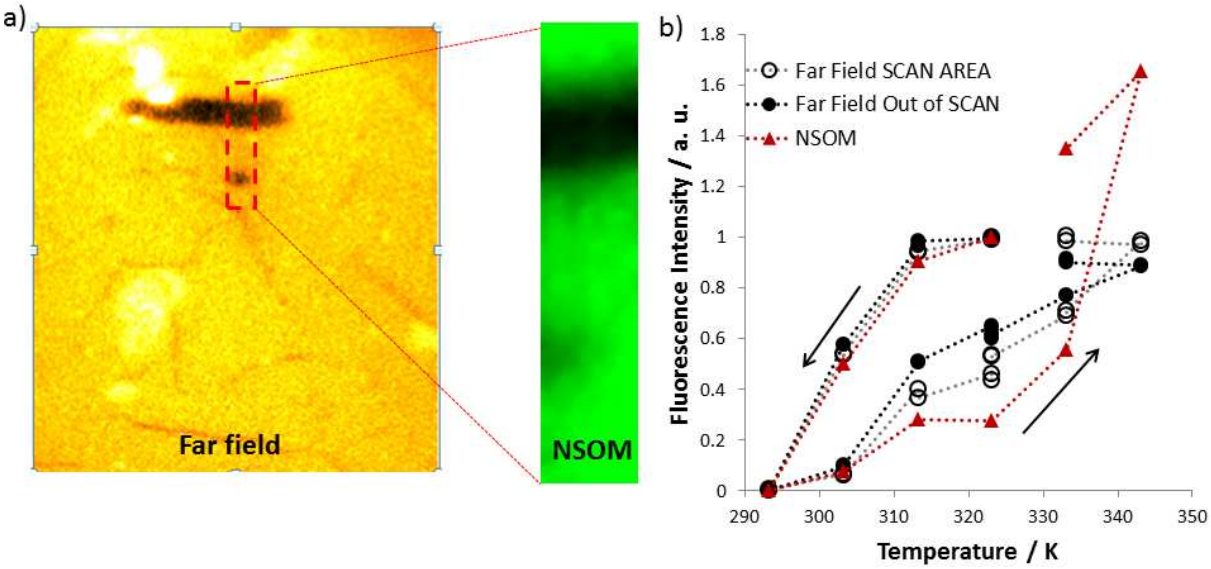

Figure C.4: a) Intensité de fluorescence en champ lointain et en champ proche d'une couche ($\approx$ 150 nm) de $[Fe^{II}(hptrz)]_3(OTs)_2$ enduit par centrifugation sur du silicium. b) Evolution de l'intensité de fluorescence avec la température pour la même couche en champ lointain et en champ proche. Les données en champ lointain sont représentées à la fois pour la surface balayée (repérée par un rectangle rouge dans a)) et une autre surface qui n'a pas été balayée en champ proche.

optiques sur le substrat de silicium doivent être identiques puisque la température du matériau n'est pas modifiée par le courant appliqué. En s'appuyant sur cette hypothèse et des données en champ lointain, nous avons normalisé les images NSOM au moyen d'une surface de référence choisie loin du fil. Une augmentation de la reflectance NSOM après l'application d'un pulse de courant a été observée uniquement sur le fil. Cette augmentation (env. 10%) est trois fois plus importants qu'en champ lointain (env. 3%). Afin de confirmer ce résultat, nous avons répété l'expérience sur un nouvel échantillon (voir figure C.5). La différence de réflectance en champ lointain entre les deux états de spin est d'environ 6% pour le nouvel échantillon, tandis que la réflectance en champ proche sur le fil augmente d'environ 30% après l'application du pulse de courant. La différence est au moins 4-5 fois plus importante que pour les données champ lointain. De plus, on a pu observer des points plus clairs et plus sombres avec une résolution d'environ 300 nm. Nous pouvons conclure que les images NSOM effectuées à hauteur constante sont beaucoup plus sensibles à la transition de spin que des mesures en champ lointain. De plus, un balayage à hauteur constante ne dégrade pas l'échantillon et donne des informations sur la réflectance de l'échantillon avec une résolution spatiale élevée.

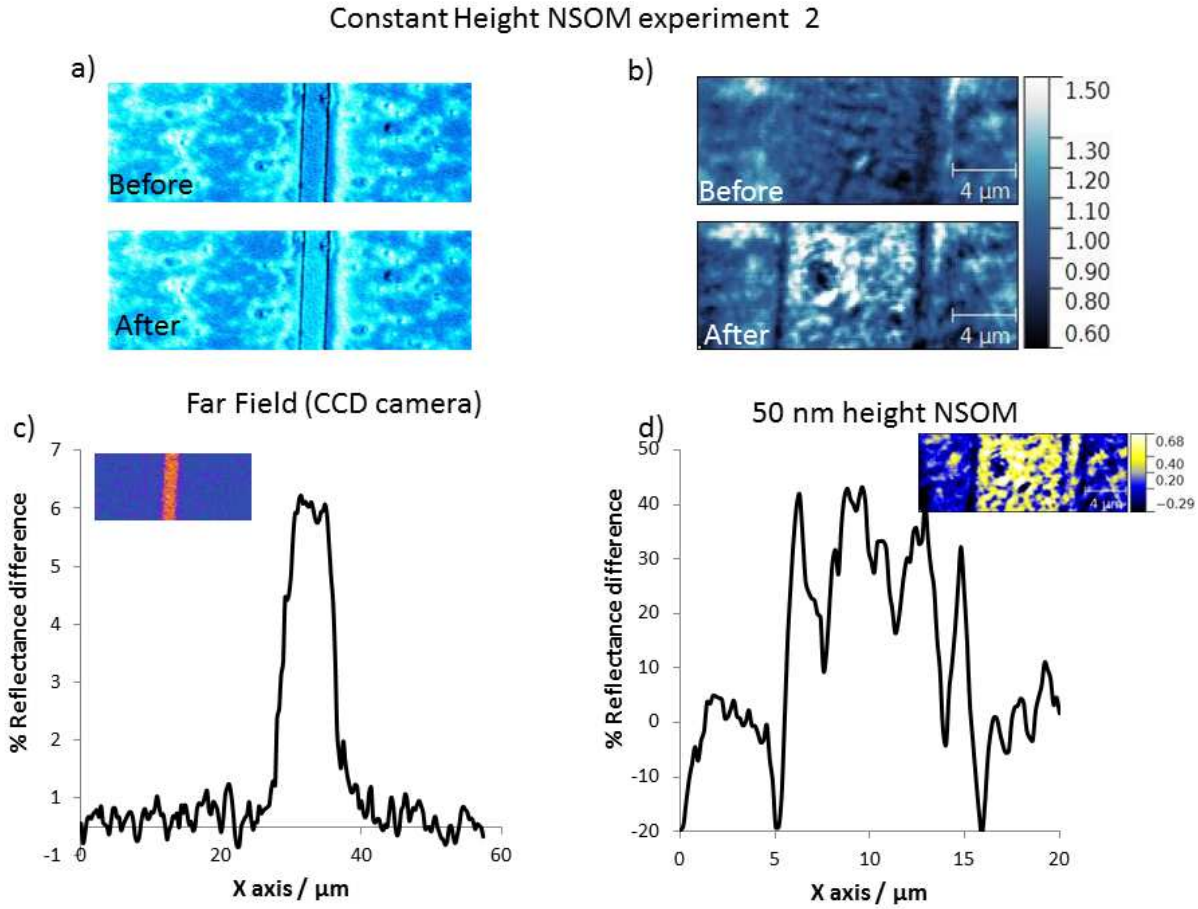

Figure C.5: Images de la réflectivité a) en champ lointain et b) en NSOM (avec hauteur constante) du composé $[Fe(Htrz)_2(trz)]BF_4$ dopé avec Rhodamine 110 déposé sur un fil d'or (épaisseur $250nm$, longueur $1mm$ et largeur $8\mu m$). Les images ont été obtenues à la température de $378K$ avant et après l'application d'un courant pulsé de $190mA$ au travers du fil d'or. Les images et les profils moyens de la différence de réflectance entre les deux images en a) (b)) sont montrées dans c) (d)).

C.2.3.1 Utilisation de la pointe NSOM comme dispositif de chauffage

La pointe NSOM peut être utilisée non seulement pour détecter l'état de spin de l'échantillon, mais aussi pour le manipuler localement. En augmentant l'intensité du faisceau laser injecté dans la fibre NSOM, nous pouvons chauffer l'échantillon au dessus de sa température de transition et transformer un petit volume de l'état LS vers l'état HS. En effet, la lumière absorbée par le métal dont le bout de la pointe est induite, augmente la température du film métallique de plusieurs centaines de degrés du fait de la réflexion multiple au niveau de la partie métallique[161]. Même si le volume chauffé est dépendant de nombreux paramètres (propriétes thermiques de la pointe et de l'échantillon...), nous avons pu tout de même montrer que le chauffage local de la surface de l'échantillon peut être réalisé avec une résolution sub-longueur d'onde. Par conséquence, cette technique ouvre la possibilité de changer l'état de spin d'une unique nanoparticule à transition de spin et pourra être utilisée, par exemple, dans des dispositifs de stockage d'information. La figure C.6 montre des images de la réflectivité en champ lointain prises sur des nanoparticules de $[Fe(Htrz)_2(trz)]BF_4$ après balayage en champ proche avec un laser dont la puissance est indiquée sur chaque image. La surface balayée par la pointe NSOM est indiquée par les rectangles jaunes. Avec l'augmentation de la puissance du laser, on peut observer des points de plus en plus clairs à l'intérieur et proche de la surface balayée, ce qui correspond à des nanoparticles transformées dans l'état HS par effet photothermique. Il peut paraître surprenant que des nanoparticules situées en dehors de l'aire balayée changent d'état de spin, cependant il nous paraît important de noter que la nucléation de la phase HS peut se produire même si la particule n'est chauffée que partiellement. De plus, le positionnement de la surface balayée à l'intérieur de l'image en champ lointain n'est peut être pas parfait. Les images montrent que les différentes particules ne changent pas d'état de spin pour une même intensité de laser. Il est difficile de corréler ces images avec celles de la topographie, du fait d'une différence de contraste entre les images NSOM et AFM. De plus, dans le cas présent, d'autres complications existent du fait que les conditions d'illumination et de diffusion de la chaleur sont différentes pour chaque particule. Au dessus de $5mW$, l'augmentation du nombre de particules dans l'état HS n'est pas significative. Les points sombres qui apparaissent après le balayage effectué avec une puissance de laser de $6mW$ correspondent très probablement à une dégradation de l'échantillon par la pointe lors de

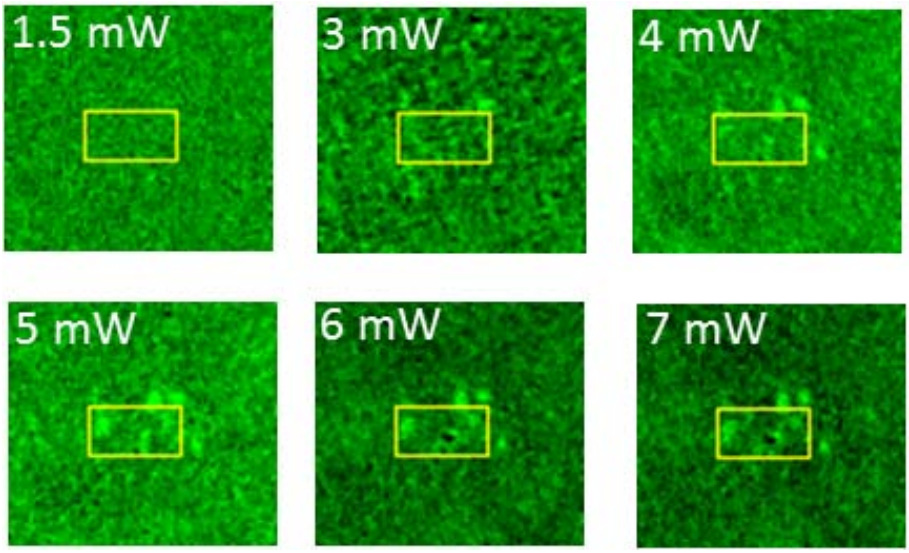

Figure C.6: Images de la réflectivité en champ lointain prises sur un film mince ($\approx$ 300 nm) de $[Fe(Htrz)_2(trz)]BF_4$. Chaque image a été prise après un balayge avec la pointe NSOM. un laser bleu ($488nm$) a été incorporé dans la fibre NSOM. La puissance fournie par le laser à l'échantillon est indiquée sur chaque image. Les rectangles jaunes repèrent les surfaces balayées par la pointe (10 X 5 μm^2).).

l'engagement de celle-ci.

C.3 Propriétés méchaniques

Les propriétés mécaniques jouent un rôle clé dans le comportement de la transition de spin dans les solides. En effet, beaucoup de phénomènes coopératifs intéressants [34, 94] peuvent être rationalisés seulement en considérant la variation de volume entre les états haut spin et bas spin et des interactions élastiques associées [166]. De plus, des applications récentes et prometteuses des matériaux à transition de spin en tant que microactuateurs [167] requièrent aussi une connaissance détaillée des propriétés mécaniques comme le module de Young et la contrainte mécanique. Si on prend en compte leurs rôles majeurs dans la transition de spin, il est alors plutôt surprenant de réaliser que les constantes élastiques des matériaux à transition de spin ont été déterminées dans seulement quelques études, en utilisant la diffusion inélastique nucléare [168], la diffraction des rayon X sous haute pression [169, 170], et la spectroscopie Brillouin [171]. De plus, la plupart de ces mesures ont été effectuées soit dans la forme HS ou BS et la dépendance d'état de spin du module élastique à seulement été reporté très récemment [168]. Cependant, on

sait que les transitions BS vers HS impliquent une augmentation drastique des distances métal-ligand (jusqu'à 10%)[172]. Cet affaiblissement des liaisons de coordination a été clairement observé par spectroscopie vibrationnelle et par spectroscopie Mössbauer du ^{57}Fe[173]. Cette dernière méthode donne accès aux températures de Debye qui peuvent être reliées au module de bulk $K^{1/2} \approx \theta_D$. Les données Mössbauer disponibles suggèrent une variation typique de $1.6 > K_{LS}/K_{HS} > 1.2$. Cette variation n'est pas grande, mais peut être détectable en utilisant l'AFM. Pour ces raisons nous avons décidé d'explorer les modes mécaniques en utilisant l'AFM. Alors que cette approche peut paraitre en assez indirecte, elle possède deux avantages : l'accès à une analyse quantitative et une très haute résolution spatiale.

C.3.1 Études des couches minces du composé $[Fe^{II}(hptrz)]_3(OTs)_2$

Les analyses AFM ont été réalisées à température ambiante dans l'air en utilisant un appareil "Dimension Icon (Bruker)" et une sonde de Si avec une couche métalique d'Al (MPP11120, Bruker). Les images AFM (généralement 8 μm $\times$ 4 μm) on été enregistrées avec une vitesse de balayage de 0.3 Hz dans le mode "peak force tapping" avec une analyse nanomechanique quantitative (QNM). La force maximale appliquée (25 nN) a été choisi pour atteindre une déformation de l'échantillon de ca. 1-2 nm. La sensibilité de la déflection du photodétecteur a été déterminée sur un échantillon de silicium, alors que la constante de ressort du levier a été obtenue en enregistrant son bruit thermique. Ces deux paramètres sont pratiquement indépendants de la température sur la plage étudiée. Un échantillon de calibration de polystyrène (Bruker PSFILM, E = 2.7 GPa, coefficient de Poisson = 0.35) a été utilisé pour déterminer le rayon de la pointe en utilisant le modèle de Derjaguin Müller Toporov. Le coefficient de Poisson (ν) utilisé pour le complexe à transition de spin était de 0.4. Cette valeur n'est qu'une estimation et ne prends pas en compte la possible différence entre les deux états de spin. Néanmoins, il est important de noter que les valeurs calculées de E ne sont pas vraiment sensibles aux faibles changements de ν. Les images AFM ont été systématiquement alignées en utilisant une méthode de corrélation 2D [9].

La figure C.7 montre que les images AFM topographiques d'un film de 70 nm d'épaisseur de $[Fe(hptrz)_3](OTs)_2$ dopé avec de la Rhodamine 110 déposé sur un système chauffant composé de nanofil d'or. Les balayages AFM on été réalisés pour différents courants appliqués aux fils. Sur les images topographiques nous n'avons pas observé de changement significatif (Figure C.7 a-b). Bien que la transition de spin est connu pour induire une déformation spontanée, dans notre couche mince l'expansion associée est attendue en dessous de 1 nm, ce qui reste difficile à détecter à cause de la rugosité de l'échantillon qui est non négligeable. D'autre part, il est important de remarquer l'absence de dégradation de l'échantillon sur les images topographiques. La cartographie du module de Young (E) a été obtenue en utilisant le model DMT. Les valeurs observées de E ne sont pas exactement les mêmes sur et à coté des fils ce qui est probablement lié au fait que la dureté de l'or (79 GPa) et celle du substrat ($E \approx 75$ GPa pour le SiO_2) sont différentes et /ou l'épaisseur du film n'est pas exactement la même sur les nano-fils et sur le substrat de SiO_2. La découverte la plus importante dans cette configuration est qu' une augmentation du courant jusqu'à 28 mA dans les fils entraine une diminution substantielle du module de Young de ca. 30% (Figure C.7 c-d). Ce changement est clairement lié à l'augmentation du courant car ce phénomène n'est pas observé hors des fils et lorsque le courant est diminué de 28 à 1 mA le changement est parfaitement réversible. Ces observations ont été reproduites à plusieurs reprises sur le même échantillon : deux mois après la première expérience et aussi sur d'autres échantillons en utilisant des fils de géométrie différente.

La diminution du module de Young lorsque le courant est augmenté dans les fils (i.e., pour une augmentation de température) est attendue à cause de la transition de spin BS vers HS dans le film, car la forme HS du matériau possède une plus faible rigidité. Cependant, l'expansion thermique ordinaire peut aussi contribuer à cet effet. C'est pourquoi il est nécessaire de corréler les résultats AFM avec des mesures indépendantes du changement d'état de spin du matériau. Cela peut être effectué avec cet échantillon en enregistrant des images de fluorescence en fonction de la température (i.e. du courant appliqué). La figure C.8 montre la variation de l'intensité de la fluorescence et le module de Young du matériau en fonction du courant appliqué dans les fils. Des résultats ont été obtenu pour le dispositif à deux fils (décrite FigureC.7) et aussi pour celui à un fil. Dans tout les cas, nous avons observé une augmentation de l'intensité de fluorescence

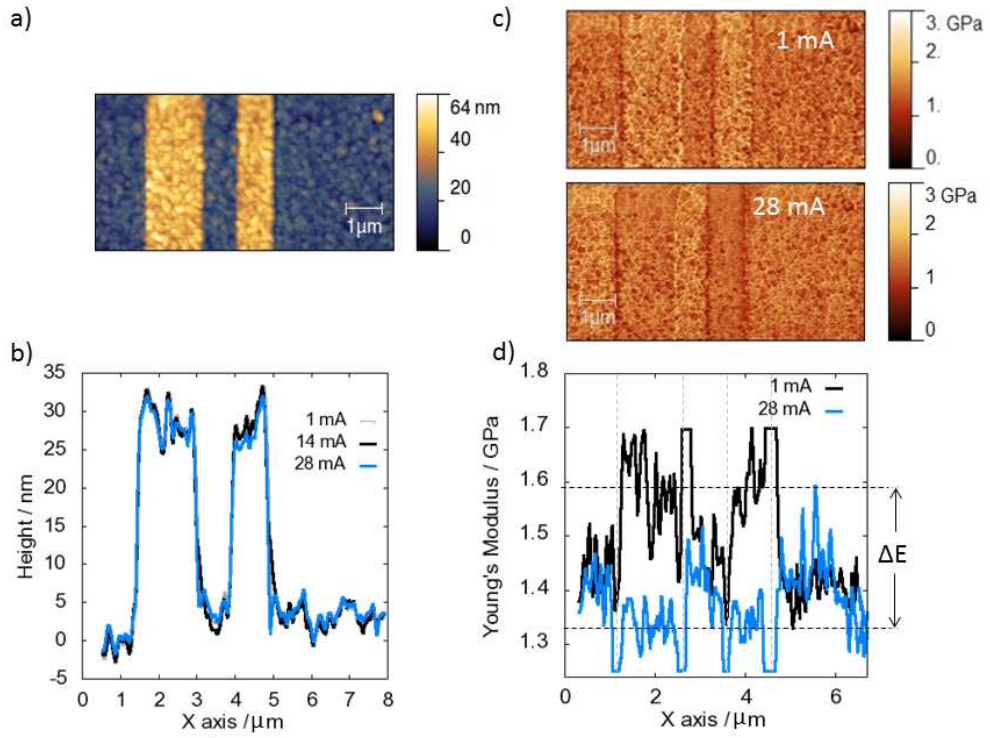

Figure C.7: Étude AFM d'un film mince (70 nm) du composé $[Fe(hptrz)_3](OTs)_2$ dopé avec la Rhodamine 110 et déposé sur deux microfils d'or. a) Image AFM topographique. b) moyenne du plan de coupe de la topographie pour différentes intensités de courant dans les fils (1, 14 et 28 mA), e) cartographie du module de Young d) moyenne du plan de coupe du module de Young pour $I = 1$ et 28 mA. Les deux lignes en pointillées horizontales indiquent un changement du module de Young (ΔE) des films à cause du chauffage par effet Joule. Les lignes en tirets verticaux montrent les extrémités des fils où des artefacts liés à la mesure peuvent apparaitre.

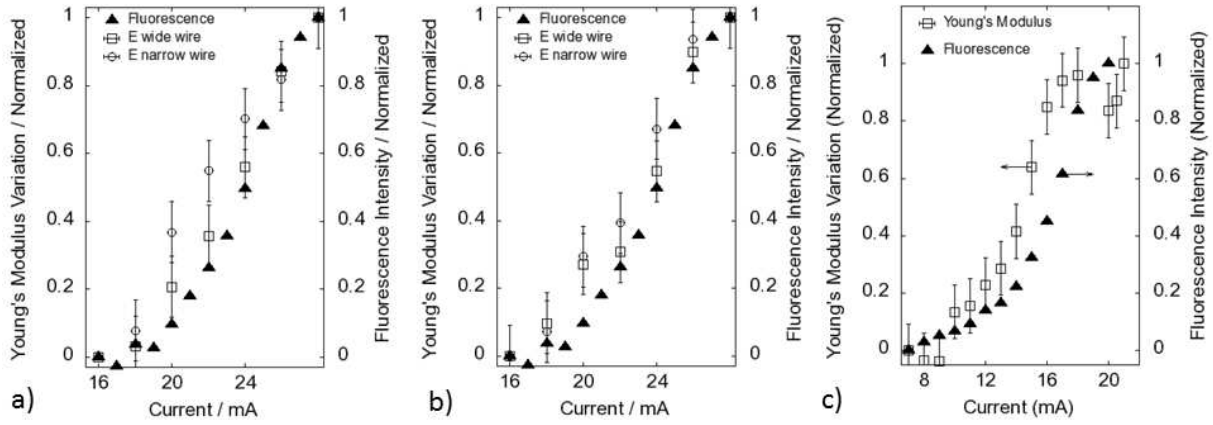

Figure C.8: Variation normalisée du module de Young et de l'intensité de fluorescence d'un film mince de $[Fe(hptrz)_3](OTs)_2$ dopé avec de la Rhodamine 110 en fonction du courant appliqué dans les nanofils chauffants. Les figures a) et b) montrent deux séries de données pour le même échantillon et c) pour un échantillon différent.

avec une augmentation du courant, ce qui indique sans ambigüité la transition de spin. La bonne corrélation de la fluorescence avec le changement de module de Young prouve que le changement de ce dernier provient de la transition de spin.

En calibrant la résistance avec la température, il est aussi possible de tracer le changement du module de Young en fonction de la température. Comme observé sur la Figure C.9 la transition de spin est centrée autour de 313 K, ce qui correspond bien aux résultats dejà publiés sur ces films. La valeur initiale du module de Young à température ambiante est retrouvée après un cycle thermique complet, avec l'incertitude expérimentale, donnant la preuve que les changements observés ne sont pas liés à une dégradation de l'échantillon ou une dérive instrumentale. Lors du passage HS vers BS le module de Young diminue de ca. 1.7 GPa à 1.3 GPa. À notre connaissance c'est la première fois que le module de Young et sa dépendance avec l'état de spin ont été déterminés pour un matériau à transition de spin. À cause de l'absence de donnés dans la littérature nous ne pouvons pas faire de comparaison, mais on peut noter que la variation du module de Young observée par AFM ($E_{BS}/E_{HS} = 1.33 \pm 0.04$) correspond bien avec le changement de la température de Debye extraite des données du Mössbauer pour plusieurs composés à transition de spin.

Un des aspects clef de l'étude présentée est le fait que la rigidité de l'échantillon peut être déterminée avec une haute résolution spatiale. Nous avons démontré qu'il est

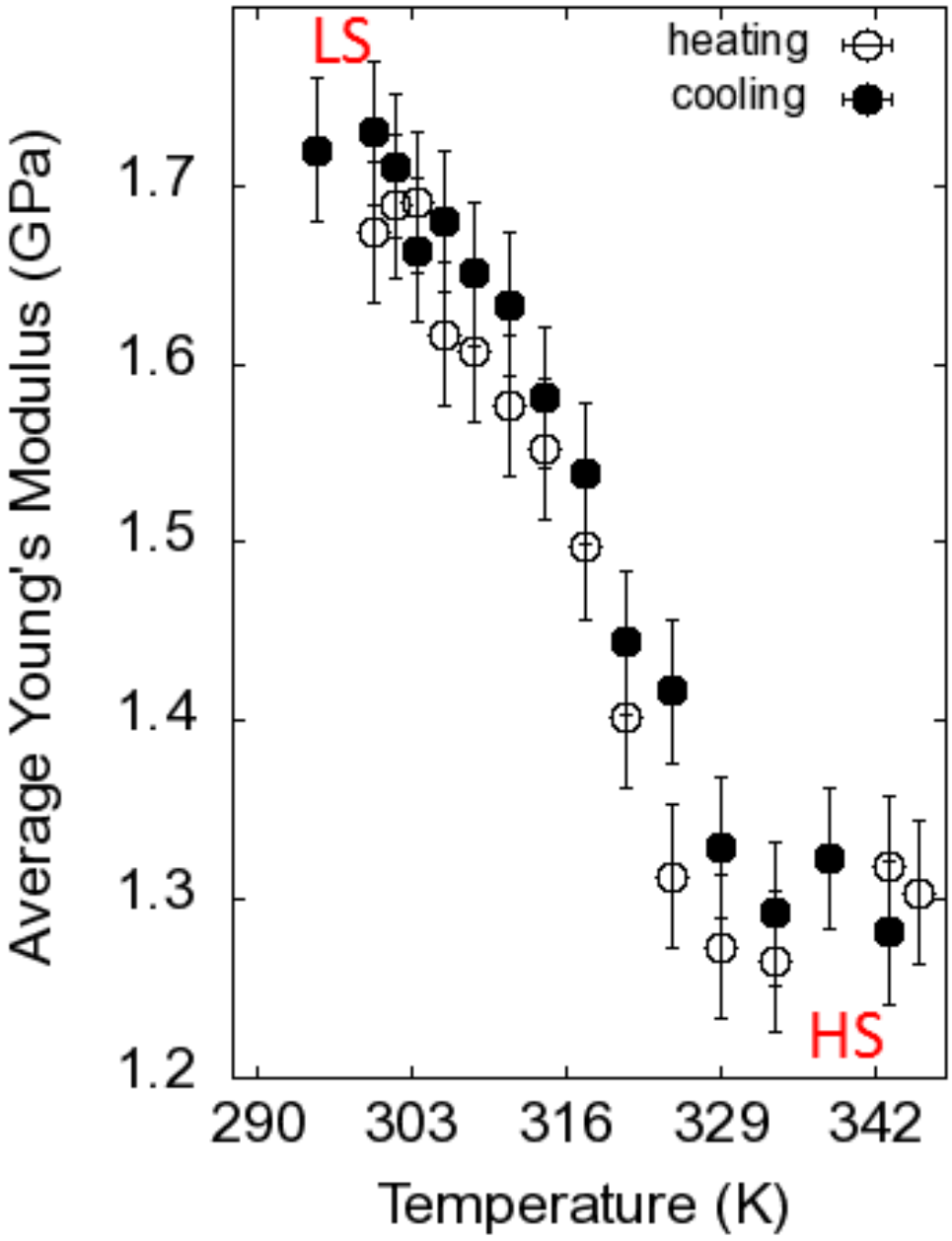

Figure C.9: Moyenne des modules de Young d'une couche mince (40 nm) de $[Fe(hptrz)_3](OTs)_2$ (dopée avec la Rhodamine 110) en fonction de la température pour les modes de chauffage et refroidissement.

possible de suivre la transition de spin d'une surface de 70 x 70 nm^2. Il pourrait même être envisageable d'observer la transition de spin à plus haute résolution spatiale, mais des images mieux résolues sont nécessaires. Nous devons insister sur le fait que la résolution spatiale du module de Young et la résolution spatiale des courbes à transition de spin avec la température ne sont évidement pas les mêmes, car ces dernières sont extraites d'une série d'image AFM, alors que le premier provient d'une seule image. Néanmoins, les courbes de transition de spin peuvent être obtenues même pour des petites zones de l'échantillon.

C.4 Imagerie et manipulation de monocristaux à transition de spin

Dans la continuité du travail réalisé par Salma Bedoui au sein de notre équipe durant sa thèse [78–81], nous avons décidé d'explorer des possibilités fournies par les techniques d'AFM pour imager et manipuler la transition de spin dans les mono-cristaux. Nous avons choisi de travailler avec le complexe [Fe(bbpya)$(NCS)_2$] (**1**). Ce composé dispose d'une transition de spin abrupte au dessus de la température ambiante faisant de lui un candidat intéressant pour les études AFM.

C.4.1 Interactions sonde-échantillon

Les cristaux se déplacent durant la transition de spin, par conséquent, il est nécessaire de les fixer à la surface. Une petite goutte de colle Epoxy a été répandue de manière homogène à la surface du substrat de silicium. Les cristaux de **1** ont alors été placés un par un sur le substrat à l'aide d'une aiguille. Toutes les expériences ont été effectuées à l'air libre. La transition de spin a été suivie in-situ par microscopie optique en champ lointain conventionnelle utilisant un objectif Mitutoyo x10 (NA = 0.28). Les cristaux ont été irradiés avec une lampe halogène et la lumière réfléchie a été capturée à l'aide d'une caméra CMOS.

La température du cristal a été progressivement augmentée jusqu'à 433 K (état BS) à un taux de chauffage de 10 K/min et une approche a été réalisée sur le cristal dans le

but de calibrer la distance pointe-échantillon. Alors, la pointe a été éloignée à 500 μm et la température a été augmentée jusqu'à 448 K. A cette température, l'échantillon est dans la phase intermédiaire (HS-BS). La pointe a été maintenue à une hauteur constante du substrat (100 μm) et l'échantillon a été déplacé latéralement, i.e. parallèlement à la longueur du levier (Y axis). Quand la pointe a été approchée du cristal, la nucléation de la phase BS a été observée à l'extrémité du cristal près du levier, comme montré dans la figure C.10. Nous atribuons ce phénomene à un tranfert thermique par convection entre la sonde AFM et l'échantillon. La distance entre la pointe et le point de nucléation était de 490 μm. Quand la pointe s'approche davantage du cristal, la nouvelle phase se propage à travers celui-ci, i.e. le volume de la phase BS augmente. Pour chaque micromètre où la pointe s'approche ou s'éloigne du cristal, les parois du domaine se déplace d'environ 0.85 μm. Comme dans le cas précédent, un hystérésis est observé (ca. 80 μm). Nous avons également effectué des expériences où la pointe se déplace d'un côté à l'autre du cristal. Dans de tels cas, la frontière du domaine suit le mouvement de la pointe de manière plus directe. Le volume du cristal qui a transité vers l'état BS a été trouvé dépendant non seulement de la distance pointe-échantillon, mais également de la température de l'échantillon. En fonction du choix du cristal ou des détails expérimentaux, en particulier l'endroit et la manière dont la pointe s'approche du cristal, nous avons observé différents comportements, tels que de multiples points de nucléation et donc, plusieurs domaines avec quelques fois différents angles et directions de propagation. Une autre observation intéressante est que si la pointe approche le cristal loin du point de nucléation naturel (i.e. loin du coin ou d'un défaut du cristal), la transition est plus difficile à induire.

C.4.2 Études de la topographie à température variable

Malheureusement, le contrôleur de température NW ne peut pas être utilisé pour chauffer les monocristaux micrométriques. D'autres méthodes et astuces doivent donc être considérées dans le but d'éviter, ou du moins, de réduire les effets thermiques non désirés entre la sonde AFM et les cristaux. Des idées possibles incluent (i) des mesures sous vide, qui éliminerait complètement la convection et réduirait significativement les effets de conduction thermique, (ii) l'utilisation de très longs leviers qui pourraient réduire les effets de convection, et (iii) chauffer la sonde AFM à la même température que l'échantillon.

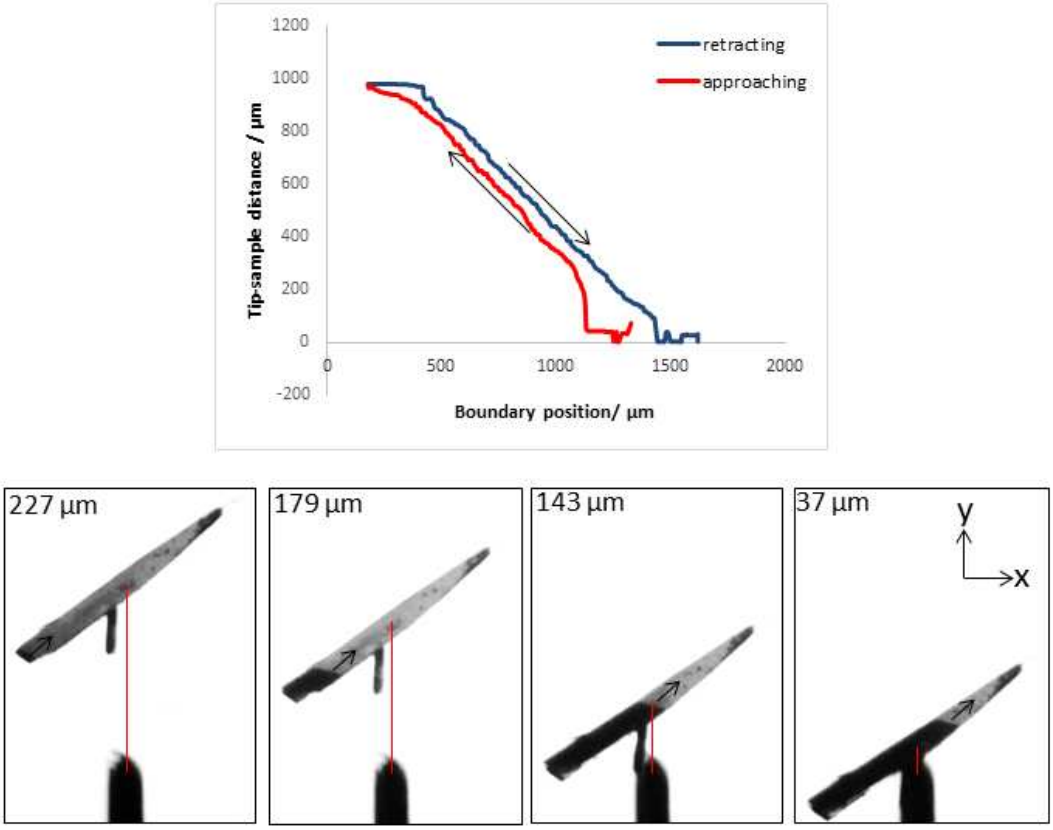

Figure C.10: Deplasment du parois HS/BS le cristal du composé **1** en fonction de la distance pointe-échantillon pour l'expérience montrée dans les images. La distance pointe-substrat (100 μm) et la température de l'échantillon (448 K) sont gardées constantes et la pointe approche l'échantillon dans la direction Y. Les flèches sur la figure indiquent l'approche et le retrait de la pointe. La distance pointe-échantillon est indiquée dans chaque image. La taille de l'image est 290 x 450 μm^2.

Puisque nous n'avons pas d'équipement pour réaliser ces mesures sous vide, nous avons testé les deux dernières solutions. L'utilisation d'un long levier a effectivement apporté quelques améliorations, mais cette approche est très restrictive en terme de constante de ressort, en particulier pour le mode tapping. Pour cette raison, une grande partie des mesures ont été réalisées en chauffant la sonde AFM par effet Joule.

Des images à différentes températures ont été enregistrées via l'appareil "Dimension Icon" (Bruker) en mode non-contact. Des images optiques en champ lointain ont aussi été enregistrées systématiquement entre les scans AFM. La figure C.11 (a) montre des images de réflectivité optique d'un cristal du composé **1** dans la phase BS et IP (1389 μm^2). Les images AFM sélectionnées sont présentées dans la figure C.11 (b).

Les images AFM montrent plusieurs caractéristiques (repères) distinguables qui nous aide à localiser différents points sur le cristal durant la transition de spin et à mesurer les distances entre eux. De cette manière, nous avons suivi l'expansion/contraction du cristal en fonction de la température. La figure C.11 (c) montre quelques exemples pour ce type de mesures. Chaque courbe correspond à une distance entre des repères sélectionnées sur la surface (indiqué par des lignes blanches sur les images de topographie) en fonction de la température mesurée à la fois durant le chauffage (cercles pleins) et durant le refroidissement (cercles vides). La première observation importante est que la variation thermique des distances entre les repères est réversible à chaque fois. Cela prouve que les déplacements observés correspondent à l'expansion ou à la contraction du cristal après la transition de spin, ce qui est visible à la fois dans les images optiques et d'AFM. Excepté cela, la topographie de la surface apparaît comme très similaire dans les deux phases. Puisque la fissure observée dans les images AFM est presque parallèle à l'axe long du cristal, nous avons mesuré les distances parallèles (lignes 1 et 4) et perpendiculaires (ligne 2 et 3) à la fissure. De la figure C.11 (c), il est clair que le cristal s'allonge perpendiculairement à la fissure (3.1%) et se contracte dans l'autre direction (2.4%) en bon accord avec les observations de la microscopie optique. Il sera nécessaire de comparer ces résultats avec les données cristallographiques, mais malheureusement jusqu'à maintenant, nous n'avons pas été capable de déterminer la structure cristalline de ce composé dans la phase haute température.

La figure C.12 regroupe les résultats d'une expérience utilisant la méthode de

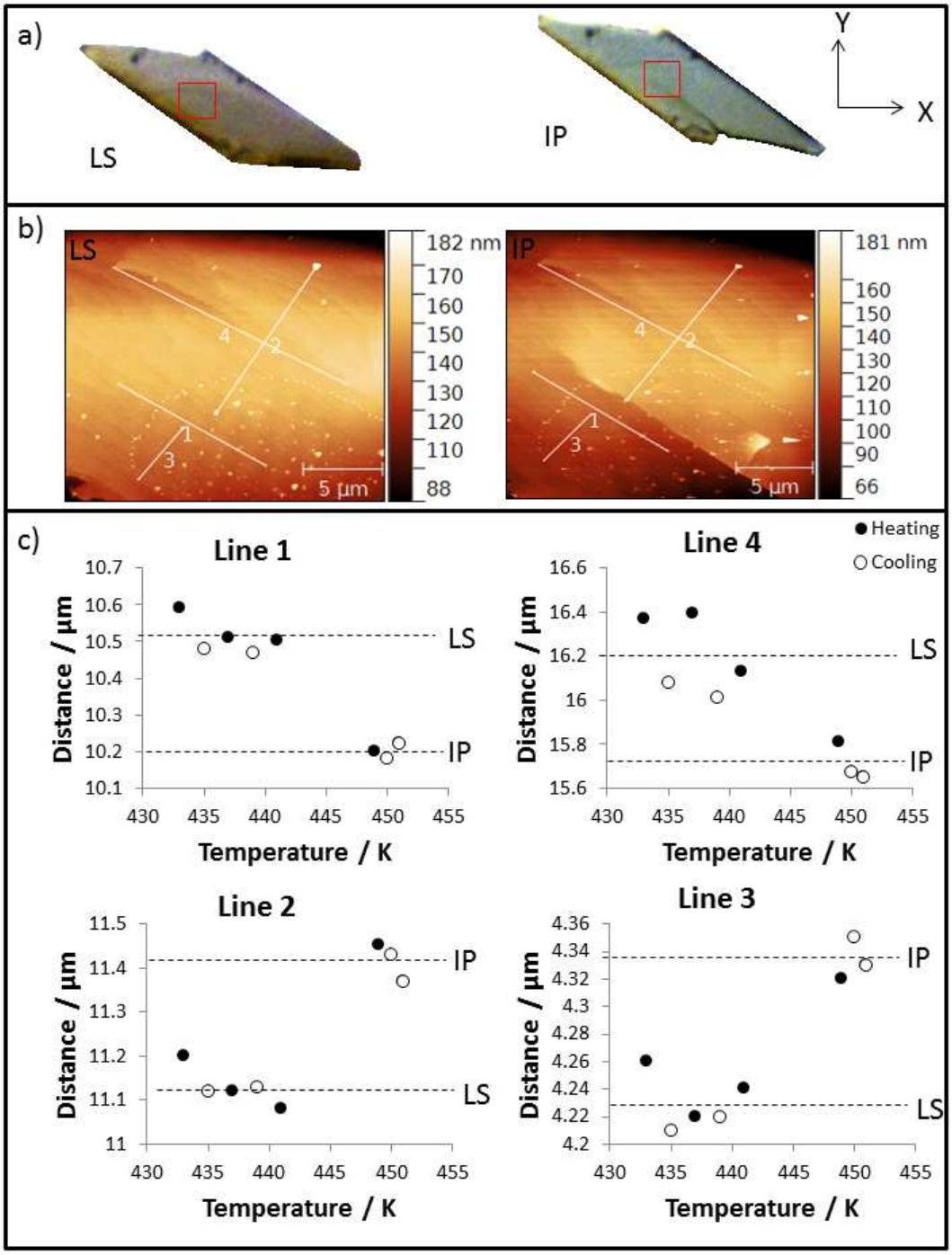

Figure C.11: Images optiques a) et AFM b) d'un cristal du composé **1** dans les phases PI et BS. c) Variation de la longueur des lignes blanches de b) en fonction de la température lors du chauffage et du refroidissement.

chauffage laser. En l'absence de faisceau laser (i.e. 0.0 mW dans les images), nous observons une topographie en dents de scie. Le cristal transite partiellement dans l'état BS et il y a un mélange de phases autour de la pointe. Quand le laser est allumé (1.0 mW), le chauffage induit par le laser amène le cristal dans la phase PI. En conséquence, les lignes dans les images optiques disparaissent et la topographie devient plate. Comme montré dans la figure 4.20 (b), la transition entre ces deux topographies pourrait être répété plusieurs fois.

Ces expériences prouvent que la topographie de surface dans cette échantillon est fortement liée à la transition de spin. Cette dernière est accompagnée par un changement significatif du volume et de la structure. Il est plausible que les déformations élastiques durant la transition soient accompagnées par la formation de ces repères topographiques. En d'autres mots, de manière similaire aux fameuses transitions martensitiques, l'énergie élastique est minimisée par ces microstructures. Cette explication pourrait sembler difficile à concilier avec le fait que dans quelques cas la topographie en dents de scie a aussi été observée à température ambiante (i.e. loin de la transition de spin). Cependant il est possible que des déformations plastiques apparaissent dans le système, et restent gelés quand l'échantillon est refroidi à température ambiante et cette structure métastable relaxe sur une plus longue période (plusieurs semaines).

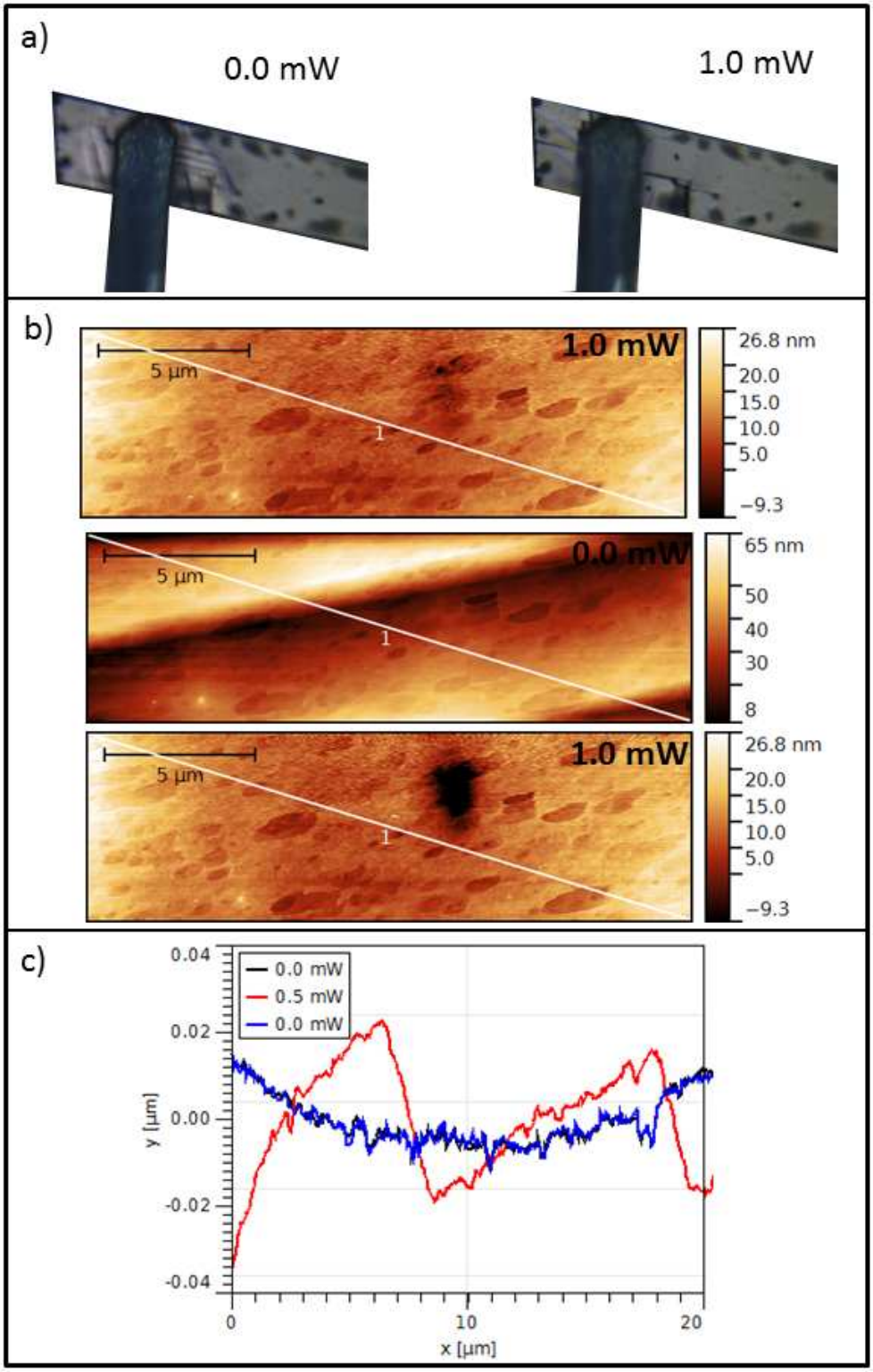

Figure C.12: a) Image optique, b) topographie AFM et c) coupe transversale de l'image de topographie d'un cristal du composé **1** enregistré à 448 K avec la pointe engagée sur la surface du cristal. Les images ont été obtenues en allumant (1.0 mW) et éteignant (0.0 mW) successivement le faisceau laser (633 nm) focalisé près de la pointe.

C.4.3 Conclusions

Dans ce travail nous avons démontré que le phénomène de la transition de spin (TS) peut être étudié et déclenché par de la microscopie en champ proche (AFM en anglais) avec une résolution spatiale nanométrique. Nous avons montré que la AFM peut être utilisée pour suivre la transition de spin thermique dans des nanomatériaux à TS à travers l'analyse de différents types d'interactions pointe-échantillon, incluant la détection (ou la génération) d'ondes électromagnétiques évanescentes par une pointe de fibre optique et l'analyse des déformations élastiques induites par une pointe de silicium pointue. De plus, nous avons prouvé que le phénomène du TS dans les matériaux massifs peut aussi être suivi en observant les changements des caractéristiques de la topographie de l'échantillon en fonction de la température. Enfin, la possibilité de déclencher et même de finement contrôler la transition par un chauffage localisé à l'aide de la pointe a été également mis en évidence.

Les techniques de AFM ont été employés ces deux dernières décennies pour étudier les phénomènes de changement de phase dans différents matériaux. Dans la plupart des cas, toutefois, l'imagerie AFM pendant le changement de phase est restée qualitative. L'imagerie quantitative d'une propriété d'un matériau qui peut être contrôlée par des stimuli externes a rarement été publiée, même dans d'autres domaines. L'obstacle principal dans toute approche AFM est l'analyse des interactions entre la sonde AFM et l'échantillon, et cela d'autant plus que les deux peuvent changer de propriétés durant les mesures. De plus, le changement de phase doit être déclenché par des stimuli extérieurs, qui peuvent également perturber les analyses AFM. Dans le cas de composés à TS, la manière la plus aisée d'induire la transition est par excitation thermique. Nous avons observé à plusieurs occasions que l'usure de la pointe et de l'échantillon durant des scans successifs ainsi que les effets thermiques non-désirés (dérive de l'échantillon, échange de chaleur entre l'échantillon et la pointe, etc.) sont très difficiles à gérer en se servant de dispositifs de chauffage AFM conventionnels. Pour éliminer (ou du moins minimiser) ces problèmes nous avons implémenté une stratégie expérimentale originale pour étudier les films à TS. Cette strategie est basée sur un chauffage local de l'échantillon par effet Joule sur un fil métallique. Cette approche nous a permis d'obtenir des changements de température très rapides et contrôlés ainsi que de réduire significativement la dérive ther-

mique et les échanges thermiques avec la pointe. Des scans sur les parties non-chauffées de l'échantillon nous ont aussi permis de corriger (ou du moins de détecter) la dégradation de la pointe et/ou de l'échantillon. Cette dernière a été également surveillée dans la plupart des cas in-situ par des moyens de microscopie optique à haute sensitivité couplée à la AFM. Nous pensons que cette stratégie de nano-chauffage est intéressante non seulement pour le domaine de la TS, mais pourra trouver des applications plus générales dans la communauté AFM. Peut-être de manière inattendue, les mesures thermo-mécaniques par microscopie à force atomique (AFM) ont prouvées être les plus efficaces pour l'imagerie quantitative de la transition de spin. Nous avons réussi à indenter des couches minces de SCO d'une manière non-destructive et de la dépendance en température des données d'indentation nous avons pu extraire le module de Young des films dans les deux états de spin. Cette information est déjà très pertinente en soi, mais elle peut en plus être utilisée pour surveiller l'évolution du changement d'état de spin avec une résolution spatiale sans égale. Ces mesures ont été effectuées à l'aide d'un mode AFM relativement récent - le Peak Force Tapping, qui appartient à la famille des techniques de cartographie de force rapide. Des tests préliminaires à l'aide d'autres modes mécaniques ont aussi été réalisés et il a été prouvé que l'imagerie AC multifréquence peut prodiguer des résultats similaires, mais avec un taux d'imagerie encore plus rapide.

Même si la TS est associée à un changement de volume significatif, la topographie de surface des images AFM n'ont pas été utiles pour suivre la transition de spin dans des échantillons de films minces. (N.B. Cette approche simple mérite, toutefois, des efforts plus poussés dans le futur.) D'un autre côté, des changements de topographie de surface très intéressants ont été observés pendant la TS dans des échantillons de monocristaux. Les différences de topographie entre les deux états de spin ont été analysées et elles sont bien corrélées avec le changement de la forme du cristal. Encore plus important, d'étranges changements de topographie temporaires ont été observés durant la transition de spin sous la forme d'ondulations de surface autour de la bordure de phase. Nous suggérons que ces ondulations sont formées afin de minimiser des constraintes élastiques près des bordures de phase.

L'imagerie optique à l'échelle nanométrique de films de TS a également prodigué un contraste utile entre les phases haut spin et bas spin à la fois en fluorescence et en

réflectance. Le premier se sert d'éléments fluorescents incorporés dans le film, alors que le dernier teste directement le changement d'indice optique de l'échantillon. Les mesures de réflectivité ont été plus robustes, en particulier en mode de hauteur constante NSOM. Dans le cas des échantillons étudiés, la quantification des changements d'état de spin observés en NSOM était difficile (à la fois en fluorescence et réflectivité). Une solution possible à ce problème serait de travailler en transmission, mais cela demanderai des échantillons avec des propriétés optiques spécifiques (c.a.d, une couche mince avec un grand changement de densité optique lors de la TS dans la région des UV). De manière générale, des échantillons avec des propriétés appropriées sont cruciaux non seulement pour la NSOM, mais également pour n'importe quelle autre technique AFM et ces travaux futurs devront se centrer plus sur cette question.

En plus de la détection de changements d'état de spin dans un petit volume, nous avons montré qu'une pointe AFM peut également être utilisée pour déclencher cette transition localement. Nous avons testé l'écriture photothermique avec un laser à haute résolution en utilisant des pointes NSOM et nous avons réussi à faire transiter des particules à TS individuelles. Dans une autre approche simple, une pointe de Si froide a été utilisée pour induire la transition de haut spin vers bas spin dans un seul monocristal. Nous avons montré que la pointe peut induire la nucléation de la phase BS et permet un contrôle fin de la position des bordures de phase. Clairement, il y a bien d'autres manières d'utiliser une pointe AFM pour manipuler l'état de spin avec une résolution nanométrique, tel qu'utiliser des pointes thermiques spécifiques ou des effets mécaniques, qui restent encore à explorer. Ces outils sont intéressants car ils permettent de faire des opérations de lecture/écriture nanométriques et ainsi donnent accès à de nouveaux dispositifs, comme des mémoires à échelle nanométrique. Par exemple, nous avons montré dans ce travail que la mémoire thermique observée dans certains composés SCO prodigue une méthode sans précédent pour imager des effets thermiques transitives avec une haute résolution spatiale.

Finallement, nous pourrons noter que d'autres méthodes AFM nous font également espérer des perspectives intéressantes pour le domaine de la TS. Notamment il serait intéressant d'explorer les possibilités offertes par la microscopie à force magnétique (MFM) et des méthodes spectroscopiques vibrationnelles, comme le Raman ou les spectroscopies FTIR en champ proche.

Bibliography

[1] Carlos Bartual-Murgui, Amal Akou, Christophe Thibault, Gábor Molnár, Christophe Vieu, Lionel Salmon, and Azzedine Bousseksou. Spin-crossover metal–organic frameworks: promising materials for designing gas sensors. *Journal of Materials Chemistry C*, 3(6):1277–1285, January 2015.

[2] Amal Akou, Il'ya A. Gural'skiy, Lionel Salmon, Carlos Bartual-Murgui, Christophe Thibault, Christophe Vieu, Gábor Molnár, and Azzedine Bousseksou. Soft lithographic patterning of spin crossover complexes. part 2: stimuli-responsive diffraction grating properties. *J. Mater. Chem.*, 22(9):3752–3757, February 2012.

[3] María D. Manrique-Juárez, Sylvain Rat, Lionel Salmon, Gábor Molnár, Carlos M. Quintero, Liviu Nicu, Helena J. Shepherd, and Azzedine Bousseksou. Switchable molecule-based materials for micro- and nanoscale actuating applications: achievements and prospects. *Coordination Chemistry Reviews*, 2015.

[4] Helena J. Shepherd, Gábor Molnár, William Nicolazzi, Lionel Salmon, and Azzedine Bousseksou. Spin crossover at the nanometre scale. *Eur. J. Inorg. Chem.*, 2013(5-6):653–661, 2013.

[5] Jean-Fran¸cois Létard, N. Daro, and O. Nguyen. Nanoparticules d'un composé à transition de spin, 2005-08-12.

[6] Gautier Félix, Khaldoun Abdul-Kader, Tarik Mahfoud, Il'ya A. Gural'skiy, William Nicolazzi, Lionel Salmon, Gábor Molnár, and Azzedine Bousseksou. Surface plasmons reveal spin crossover in nanometric layers. *J. Am. Chem. Soc.*, 133(39):15342–15345, October 2011.

[7] P. Mounaix, E. Freysz, J. Degert, N. Daro, J.-F. Létard, P. Kužel, V. Vigneras, and L. Oyenhart. One-dimensional tunable photonic crystals with spin crossover material for the terahertz range. *Applied Physics Letters*, 89(17):174105, October 2006.

[8] Lionel Salmon, Gábor Molnár, Djelali Zitouni, Carlos Quintero, Christian Bergaud, Jean-Claude Micheau, and Azzedine Bousseksou. A novel approach for fluores-

cent thermometry and thermal imaging purposes using spin crossover nanoparticles. *Journal of Materials Chemistry*, 20(26):5499, 2010.

[9] Carlos M. Quintero, Il'ya A. Gural'skiy, Lionel Salmon, Gábor Molnár, Christian Bergaud, and Azzedine Bousseksou. Soft lithographic patterning of spin crossover complexes. part 1: fluorescent detection of the spin transition in single nano-objects. *J. Mater. Chem.*, 22(9):3745–3751, February 2012.

[10] Renske M. van der Veen, Oh-Hoon Kwon, Antoine Tissot, Andreas Hauser, and Ahmed H. Zewail. Single-nanoparticle phase transitions visualized by four-dimensional electron microscopy. *Nat Chem*, 5(5):395–402, May 2013.

[11] L. Cambi and A. Gagnasso. *Atti. Accad Naz. Lincei*, 13:809, 1931.

[12] W. A. Baker and H. M. Bobonich. Magnetic properties of some high-spin complexes of iron(II). *Inorg. Chem.*, 3(8):1184–1188, August 1964.

[13] A. H. Ewald, R. L. Martin, I. G. Ross, and A. H. White. Anomalous behaviour at the $^6A_1$-$^2T_2$ Crossover in Iron (III) Complexes. *Proc. R. Soc. Lond. A*, 280(1381):235–257, July 1964.

[14] Andreas Hauser. Light-induced spin crossover and the high-spin $\rightarrow$ low-spin relaxation. In P. Gütlich and H. A. Goodwin, editors, *Spin Crossover in Transition Metal Compounds I*, number 233 in Topics in Current Chemistry, pages 259–324. Springer Berlin Heidelberg, January 2004.

[15] Muin S. Haddad, Wayne D. Federer, Michael W. Lynch, and David N. Hendrickson. Spin-crossover ferric complexes: unusual effects of grinding and doping solids. *Inorg. Chem.*, 20(1):131–139, January 1981.

[16] Hiroki Oshio, Kenji Kitazaki, Junichi Mishiro, Noriyuki Kato, Yonezo Maeda, and Yoshimasa Takashima. New spin-crossover iron(III) complexes with large hysteresis effects and time dependence of their magnetism. *J. Chem. Soc., Dalton Trans.*, 6:1341–1347, January 1987.

[17] Sabine Schenker, Andreas Hauser, and Raylene M. Dyson. Intersystem crossing dynamics in the iron(III) spin-crossover compounds [fe(acpa)2]PF6 and [fe(Sal2tr)]PF6. *Inorg. Chem.*, 35(16):4676–4682, January 1996.

[18] R. Carl Stoufer, Darwin W. Smith, Emilie A. Clevenger, and Thomas E. Norris. Complexes of cobalt(II). i. on the anomalous magnetic behavior of some six-coordinate cobalt(II) complexes. *Inorg. Chem.*, 5(7):1167–1171, July 1966.

[19] Jacqueline Zarembowitch and Olivier Kahn. Magnetic properties of some spin-crossover, high-spin, and low-spin cobalt(II) complexes with schiff bases derived from 3-formylsalicylic acid. *Inorg. Chem.*, 23(5):589–593, February 1984.

[20] Juan Faus, Miguel Julve, Francisco Lloret, Jose A. Real, and Jorunn Sletten. Dimethylvioluratobis(phenanthroline)cobalt(II), a novel spin-crossover octahedral co(II) complex. synthesis, crystal structure and magnetic properties of [co(dmvi)(phen)2]ClO4.cntdot.3H2O. *Inorg. Chem.*, 33(24):5535–5540, November 1994.

[21] Katja Heinze, Gottfried Huttner, Laszlo Zsolnai, and Peter Schober. Complexes of cobalt(II) chloride with the tripodal trisphosphane triphos: Solution dynamics, spin-crossover, reactivity, and redox activity. *Inorg. Chem.*, 36(24):5457–5469, November 1997.

[22] Philipp Gütlich, Bruce R. McGarvey, and Wolfgang Klaeui. Temperature-dependent $^{5}t_{2}(o_{h}) \rightleftharpoons {}^{1}a_{1}(o_{h})$ spin equilibrium in a six-coordinate cobalt(iii) complex. investigation by ^{31}p nmr in solution. *Inorg. Chem.*, 19(12):3704–3706, December 1980.

[23] Gil Navon and Wolfgang Kläui. Cobalt-59 NMR of a cobalt(III) spin-crossover compound. *Inorg. Chem.*, 23(17):2722–2725, August 1984.

[24] Wolfgang Kläui, Werner Eberspach, and Philipp Guetlich. Spin-crossover cobalt(III) complexes: steric and electronic control of spin state. *Inorg. Chem.*, 26(24):3977–3982, December 1987.

[25] J. H. Ammeter, R. Bucher, and N. Oswald. High-spin-low-spin equilibrium of manganocene and dimethylmanganocene. *J. Am. Chem. Soc.*, 96(25):7833–7835, December 1974.

[26] Mary E. Switzer, Richard Wang, Michael F. Rettig, and August H. Maki. Electronic ground states of manganocene and 1,1'-dimethylmanganocene. *J. Am. Chem. Soc.*, 96(25):7669–7674, December 1974.

[27] P. Greig Sim and Ekk Sinn. First manganese(III) spin crossover, first d4 crossover. comment on cytochrome oxidase. *J. Am. Chem. Soc.*, 103(1):241–243, January 1981.

[28] Lilia Kaustov, Merav E. Tal, Alexander I. Shames, and Zeev Gross. Spin transition in a manganese(III) porphyrin cation radical, its transformation to a dichloromanganese(IV) porphyrin, and chlorination of hydrocarbons by the latter. *Inorg. Chem.*, 36(16):3503–3511, July 1997.

[29] Dost M. Halepoto, David G. L. Holt, Leslie F. Larkworthy, G. Jeffery Leigh, David C. Povey, and Gallienus W. Smith. Spin crossover in chromium(II) complexes and the crystal and molecular structure of the high spin form of bis[1,2-bis(diethylphosphino)ethane]di-iodochromium(II). *J. Chem. Soc., Chem. Commun.*, 18:1322–1323, January 1989.

[30] Michio Sorai, Yohko Yumoto, Halepoto Dost M., and Leslie F. Larkworthy. Calorimetric study on the spin-crossover phenomenon between 3T1 and 5E in trans-bis[1,2-bis(diethylphosphino) ethane]diiodochromium(II), [CrI2(depe)2]. *J. Phys. Chem. Solids*, 54(4):421–430, April 1993.

[31] E. König and K. Madeja. Unusual magnetic behaviour of some iron(II)–bis-(1,10-phenanthroline) complexes. *Chem. Commun. (London)*, 3:61–62, January 1966.

[32] E. König and G. Ritter. Temperature dependence of Debye-Waller factors at a cooperative high-spin ($^5T_2$) $\rightleftharpoons$ low-spin ($^1A_1$) transition in dithiocyanatobis(2,2'-bipyridyl)iron(II). *Physics Letters A*, 43(6):488–490, April 1973.

[33] Christian Janot. Effet Mossbauer et applications à la physique du solide. *Pure App. Chem.*, 48(1):53–64, 1976.

[34] Edgar König, Gerhard Ritter, and S. K. Kulshreshtha. The nature of spin-state transitions in solid complexes of iron(II) and the interpretation of some associated phenomena. *Chem. Rev.*, 85(3):219–234, June 1985.

[35] Azzedine Bousseksou, Gábor Molnár, and Galina Matouzenko. Switching of Molecular Spin States in Inorganic Complexes by Temperature, Pressure, Magnetic Field and Light: Towards Molecular Devices. *European Journal of Inorganic Chemistry*, 2004(22):4353–4369, November 2004.

[36] P Gütlich, V Ksenofontov, and A Gaspar. Pressure effect studies on spin crossover systems. *Coordination Chemistry Reviews*, 249(17-18):1811–1829, September 2005.

[37] John J. McGarvey and Ian Lawthers. Photochemically-induced perturbation of the ^1A ^5T equilibrium in Fe(II) complexes by pulsed laser irradiation in the metal-to-ligand charge-transfer absorption band. *J. Chem. Soc., Chem. Commun.*, 16:906–907, January 1982.

[38] S. Decurtins, P. Gütlich, C. P. Köhler, H. Spiering, and A. Hauser. Light-induced excited spin state trapping in a transition-metal complex: The hexa-1-propyltetrazole-iron (II) tetrafluoroborate spin-crossover system. *Chem. Phys. Lett.*, 105(1):1–4, March 1984.

[39] S. Decurtins, P. Gutlich, K. M. Hasselbach, A. Hauser, and H. Spiering. Light-induced excited-spin-state trapping in iron(II) spin-crossover systems. optical spectroscopic and magnetic susceptibility study. *Inorg. Chem.*, 24(14):2174–2178, July 1985.

[40] A. Hauser. Reversibility of light-induced excited spin state trapping in the $Fe(ptz)_6(BF_4)_2$, and the $Zn_{1-x}Fe_x(ptz)_6(BF_4)_2$ spin-crossover systems. *Chemical Physics Letters*, 124(6):543 – 548, 1986.

[41] Y. Qi, E. W. Müller, H. Spiering, and P. Gütlich. The effect of a magnetic field on the high-spin α low-spin transition in $[Fe(phen)_2(NCS)_2]$. *Chem. Phys. Lett.*, 101(4–5):503–505, October 1983.

[42] A. Bousseksou, N. Negre, M. Goiran, L. Salmon, J.-P. Tuchagues, M.-L. Boillot, K. Boukheddaden, and F. Varret. Dynamic triggering of a spin-transition by a pulsed magnetic field. *Eur. Phys. J. B*, 13(3):451–456, February 2000.

[43] A. Bousseksou, J. Nasser, J. Linares, K. Boukheddaden, and F. Varret. Ising-like model for the two-step spin-crossover. *J. Phys. I*, 2(7):1381–1403, July 1992.

[44] C. P. Slichter and H. G. Drickamer. Pressured-induced electronic changes in compounds of iron. *J. Chem. Phys.*, 56(5):2142–2160, March 1972.

[45] H. Spiering, E. Meissner, H. Köppen, E. W. Müller, and P. Gütlich. The effect of the lattice expansion on high spin $\rightarrow$ low spin transitions. *Chem. Phys.*, 68(1–2):65–71, June 1982.

[46] Andreas Hauser. Ligand field theoretical considerations. In P. Gütlich and H. A. Goodwin, editors, *Spin Crossover in Transition Metal Compounds I*, number 233 in Topics in Current Chemistry, pages 49–58. Springer Berlin Heidelberg, January 2004.

[47] Satoru Sugano, Yukito Tanabe, and Hiroshi Kamimura. *Multiplets of transition-metal ions in crystals*, volume 33. Academic Press, 1970.

[48] Philipp Gütlich and Harold A. Goodwin. Spin Crossover—An overall perspective. In P. Gütlich and H. A. Goodwin, editors, *Spin Crossover in Transition Metal Compounds I*, number 233 in Topics in Current Chemistry, pages 1–47. Springer Berlin Heidelberg, January 2004.

[49] Nicolás Moliner, M. Carmen Muñoz, Sylvie Létard, Lionel Salmon, Jean-Pierre Tuchagues, Azzedine Bousseksou, and José Antonio Real. Mass effect on the equienergetic high-spin/low-spin states of spin-crossover in 4,4‘-bipyridine-bridged

iron(II) polymeric compounds: Synthesis, structure, and magnetic, mössbauer, and theoretical studies. *Inorg. Chem.*, 41(26):6997–7005, December 2002.

[50] P. Gütlich. *Struct. Bonding.* (**Berling**), 44:83, 1981.

[51] M. Sorai and S. Seki. Phonon coupled cooperative low-spin 1A1high-spin 5T2 transition in [fe(phen)2(NCS)2] and [fe(phen)2(NCSe)2] crystals. *J. Phys. Chem. Solids*, 35(4):555–570, 1974.

[52] S. K. Kulshreshtha and R. M. Iyer. Nature of the high-spin (5T2) α low-spin (1A1,) transition in [fe(bipy)2(NCS)2]. *Chem. Phys. Lett.*, 108(5):501–504, July 1984.

[53] S. K. Kulshreshtha, R. M. Iyer, E. König, and G. Ritter. The nature of spin-state transitions in fe(II) complexes. *Chem. Phys. Lett.*, 110(2):201–204, September 1984.

[54] R. Carl Stoufer, Daryle H. Busch, and Wayne B. Hadley. UNUSUAL MAGNETIC PROPERTIES OF SOME SIX-COÖRDINATE COBALT(II) COMPLEXES[1]-ELECTRONIC ISOMERS. *J. Am. Chem. Soc.*, 83(17):3732–3734, September 1961.

[55] J. R. Sams, J. C. Scott, and T. B. Tsin. Tris [2-(2'-pyridyl)benzimidazole]iron(II) complexes. Some new examples of $^5T_2$ $^1A_1$ spin equilibria. *Chem. Phys. Lett.*, 18(3):451–453, February 1973.

[56] Edgar König and K. Madeja. $^5T_2$-$^1A_1$ equilibriums in some iron(II)-bis(1,10-phenanthroline) complexes. *Inorg. Chem.*, 6(1):48–55, January 1967.

[57] E. König and G. Ritter. Hysteresis effects at a cooperative high-spin ($^5T_2$)$\rightleftharpoons$ low-spin ($^1A_1$) transition in dithiocyanatobis (4, 7-dimethyl-1, 10-phenanthroline) iron (II). *Solid State Comm.*, 18(3):279–282, 1976.

[58] V. V. Zelentsov. *Sov. Sci. Rev. B Chem.*, 81:543, 1981.

[59] Galina S. Matouzenko, Jean-François Létard, Sylvain Lecocq, Azzedine Bousseksou, Laurence Capes, Lionel Salmon, Monique Perrin, Olivier Kahn, and André Collet. Two-step spin crossover in a mononuclear compound [fe(DPEA)(bim)]$(ClO_4)_2$·0.5 H_2O[DPEA = (2-aminoethyl)bis(2-pyridylmethyl)amine, bim = 2,2-bisimidazole] - crystal structure, magnetic properties, mössbauer spectroscopy, and photomagnetic effects. *Eur. J. Inorg. Chem.*, 11:2935–2945, 2001.

[60] Harald Romstedt, Andreas Hauser, and Hartmut Spiering. High-spin $\rightarrow$ low-spin relaxation in the two-step spincrossover compound [fe(pic)3]Cl2EtOH (pic = 2-picolylamine). *J. Phys. Chem. Solids*, 59(2):265–275, February 1998.

[61] Jose Antonio Real, Helene Bolvin, Azzedine Bousseksou, Ary Dworkin, Olivier Kahn, Francois Varret, and Jacqueline Zarembowitch. Two-step spin crossover in the new dinuclear compound [fe(bt)(NCS)2]2bpym, with bt = 2,2'-bi-2-thiazoline and bpym = 2,2'-bipyrimidine: experimental investigation and theoretical approach. *J. Am. Chem. Soc.*, 114(12):4650–4658, June 1992.

[62] Azzedine Bousseksou, Gábor Molnár, Lionel Salmon, and William Nicolazzi. Molecular spin crossover phenomenon: recent achievements and prospects. *Chem. Soc. Rev.*, 40(6):3313–3335, May 2011.

[63] Andreas Hauser. Light-induced spin crossover and the high-spin → low-spin relaxation. In P. Gütlich and H. A. Goodwin, editors, *Spin Crossover in Transition Metal Compounds I*, number 234 in Topics in Current Chemistry, pages 155–198. Springer Berlin Heidelberg, January 2004.

[64] Andreas Hauser. Intersystem crossing in the [Fe(ptz)6](BF4)2 spin crossover system (ptz=1-propyltetrazole). *The Journal of Chemical Physics*, 94(4):2741–2748, February 1991.

[65] W. Nicolazzi and S. Pillet. Structural aspects of the relaxation process in spin crossover solids: Phase separation, mapping of lattice strain, and domain wall structure. *Phys. Rev. B*, 85(9):094101, March 2012.

[66] Mouhamadou Sy, Francois Varret, Kamel Boukheddaden, Guillaume Bouchez, Jerome Marrot, Santoshi Kawata, and Sumio Kaizaki. Structure-Driven Orientation of the High-Spin-Low-Spin Interface in a Spin-Crossover Single Crystal. *Angewandte Chemie-International Edition*, 53(29):7539–7542, July 2014. WOS:000339564800022.

[67] Miguel Paez-Espejo, Mouhamadou Sy, François Varret, and Kamel Boukheddaden. Quantitative macroscopic treatment of the spatiotemporal properties of spin crossover solids based on a reaction diffusion equation. *Physical Review B*, 89(2):024306, January 2014.

[68] A. Slimani, K. Boukheddaden, F. Varret, M. Nishino, and S. Miyashita. Properties of the low-spin high-spin interface during the relaxation of spin-crossover materials, investigated through an electro-elastic model. *Journal of Chemical Physics*, 139(19):194706, November 2013. WOS:000327714900037.

[69] Cristian Enachescu, Masamichi Nishino, Seiji Miyashita, Kamel Boukheddaden, François Varret, and Per Arne Rikvold. Shape effects on the cluster spreading process of spin-crossover compounds analyzed within an elastic model with Eden and Kawasaki dynamics. *Physical Review B*, 91(10):104102, March 2015.

[70] S. Pillet, V. Legrand, M. Souhassou, and C. Lecomte. Kinetics of light-induced first-order phase transformation in molecular solids: $Fe(btr)_2(ncs)_2{\cdot}h_2o$. *Physical Review B*, 74(14):140101, October 2006.

[71] Nolwenn Huby, Laurent Guérin, Eric Collet, Loic Toupet, Jean-Claude Ameline, Hervé Cailleau, Thierry Roisnel, Takeshi Tayagaki, and Koichiro Tanaka. Photoinduced spin transition probed by x-ray diffraction. *Physical Review B*, 69(2):020101, January 2004.

[72] S. Pillet, J. Hubsch, and C. Lecomte. Single crystal diffraction analysis of the thermal spin conversion in [fe(btr)(2)(NCS)(2)](h2o): evidence for spin-like domain formation. *European Physical Journal B*, 38(4):541–552, April 2004. WOS:000222354700002.

[73] Jelena Jeftic, Roland Hinek, Silvia C. Capelli, and Andreas Hauser. Cooperativity in the iron(II) spin-crossover compound [fe(ptz)(6)](PF(6))(2) under the influence of external pressure (ptz = 1-n-propyltetrazole). *Inorganic Chemistry*, 36(14):3080–3087, July 1997.

[74] Y. Ogawa, S. Koshihara, K. Koshino, T. Ogawa, C. Urano, and H. Takagi. Dynamical aspects of the photoinduced phase transition in spin-crossover complexes. *Physical Review Letters*, 84(14):3181–3184, April 2000.

[75] A. Goujon, F. Varret, K. Boukheddaden, C. Chong, J. Jeftić, Y. Garcia, A. D. Naik, J. C. Ameline, and E. Collet. An optical microscope study of photo-switching and relaxation in single crystals of the spin transition solid [fe(ptz)6](BF4)2, with image processing. *Inorganica Chimica Acta*, 361(14-15):4055–4064, October 2008.

[76] Jelena Jeftic, Nieves Menéndez, AndréWack, Epiphane Codjovi, Jorge Linarès, Antoine Goujon, Gérard Hamel, Stefan Klotz, Gérard Syfosse, and François Varret. A helium-gas-pressure apparatus with optical-reflectivity detection tested with a spin-transition solid. *Measurement Science and Technology*, 10(11):1059, November 1999.

[77] Sylvestre Bonnet, Gábor Molár, Jose Sánchez Costa, Maxime A. Siegler, Anthony L. Spek, Azedine Bousseksou, Wen-Tian Fu, Patrick Gamez, and Jan Reedijk. Influence of Sample Preparation, Temperature, Light, and Pressure on the Two-Step Spin Crossover Mononuclear Compound [Fe(bapbpy)(NCS) $_2$]. *Chemistry of Materials*, 21(6):1123–1136, March 2009.

[78] Salma Bedoui, William Nicolazzi, Sipeng Zheng, Sylvestre Bonnet, Gábor Molnár, and Azzedine Bousseksou. Impact of single crystal properties on nucleation and growth mechanisms of a spin transition. *Polyhedron*, 87:411–416, February 2015.

[79] S. Bedoui, G. Molnár, S. Bonnet, C. Quintero, H. J. Shepherd, W. Nicolazzi, L. Salmon, and A. Bousseksou. Raman spectroscopic and optical imaging of high spin/low spin domains in a spin crossover complex. *Chemical Physics Letters*, 499(1):94–99, 2010.

[80] Salma Bedoui, Manuel Lopes, William Nicolazzi, Sylvestre Bonnet, Sipeng Zheng, Gábor Molnár, and Azzedine Bousseksou. Triggering a phase transition by a spatially localized laser pulse: Role of strain. *Phys. Rev. Lett.*, 109(13):135702, September 2012.

[81] Salma Bedoui, Manuel Lopes, Sipeng Zheng, Sylvestre Bonnet, Gábor Molnár, and Azzedine Bousseksou. Laser-induced artificial defects (LIADs): Towards the control of the spatiotemporal dynamics in spin transition materials. *Advanced Materials*, 24(18):2475–2478, May 2012.

[82] Zulema Arcis-Castíllo, Sipeng Zheng, Maxime A. Siegler, Olivier Roubeau, Salma Bedoui, and Sylvestre Bonnet. Tuning the Transition Temperature and Cooperativity of bapbpy-Based Mononuclear Spin-Crossover Compounds: Interplay between Molecular and Crystal Engineering. *Chemistry – A European Journal*, 17(52):14826–14836, December 2011.

[83] Christian Chong, Haritosh Mishra, Kamel Boukheddaden, Stéphane Denise, Guillaume Bouchez, Eric Collet, Jean-Claude Ameline, Anil D. Naik, Yann Garcia, and François Varret. Electronic and structural aspects of spin transitions observed by optical microscopy. the case of [fe(ptz)6](BF4)2. *The Journal of Physical Chemistry B*, 114(5):1975–1984, 2010.

[84] C. Chong, F. Varret, and K. Boukheddaden. Evolution of self-organized spin domains under light in single-crystalline $[\text{Fe}{(\text{ptz})}_{6}]{({\text{BF}}_{4})}_{2}$. *Physical Review B*, 81(1):014104, January 2010.

[85] François Varret, Ahmed Slimani, Kamel Boukheddaden, Christian Chong, Haritosh Mishra, Eric Collet, Jaap Haasnoot, and Sébastien Pillet. The propagation of the thermal spin transition of [fe(btr)2(NCS)2]·h2o single crystals, observed by optical microscopy. *New Journal of Chemistry*, 35(10):2333–2340, September 2011.

[86] François Varret, Christian Chong, Antoine Goujon, and Kamel Boukheddaden. Light-induced phase separation (LIPS) in [Fe(ptz)6](BF4)2 spin-crossover single crystals: Experimental data revisited through optical microscope investigation. *Journal of Physics: Conference Series*, 148(1):012036, February 2009.

[87] A. Slimani, F. Varret, K. Boukheddaden, C. Chong, H. Mishra, J. Haasnoot, and S. Pillet. Visualization and quantitative analysis of spatiotemporal behavior in a first-order thermal spin transition: A stress-driven multiscale process. *Physical Review B*, 84(9):094442, September 2011.

[88] Gábor Molnár, Virginie Niel, José. Real, Leonid Dubrovinsky, Azzedine Bousseksou, and John J. McGarvey. Raman spectroscopic study of pressure effects on the spin-crossover coordination polymers fe(pyrazine)[m(CN) 4]·2h 2 o (m = ni, pd, pt). first observation of a piezo-hysteresis loop at room temperature. *The Journal of Physical Chemistry B*, 107(14):3149–3155, April 2003.

[89] Manuel Gruber, Vincent Davesne, Martin Bowen, Samy Boukari, Eric Beaurepaire, Wulf Wulfhekel, and Toshio Miyamachi. Spin state of spin-crossover complexes: From single molecules to ultrathin films. *Physical Review B*, 89(19):195415, May 2014.

[90] Aaron Hurley, Nadjib Baadji, and Stefano Sanvito. Strategy for detection of electrostatic spin-crossover effect in magnetic molecules. *Physical Review B*, 88(5):054409, August 2013.

[91] Toshio Miyamachi, Manuel Gruber, Vincent Davesne, Martin Bowen, Samy Boukari, Loïc Joly, Fabrice Scheurer, Guillaume Rogez, Toyo Kazu Yamada, Philippe Ohresser, Eric Beaurepaire, and Wulf Wulfhekel. Robust spin crossover and memristance across a single molecule. *Nature Communications*, 3:938, July 2012.

[92] C. Chong, B. Berini, K. Boukheddaden, E. Codjovi, J. Linarès, Y. Garcia, A. D. Naik, and F. Varret. Characterization of spin crossover crystal surface by AFM. *physica status solidi (a)*, 207(5):1227–1231, December 2009.

[93] Manuel Lopes, Carlos M. Quintero, Edna M. Hernández, Víctor Velázquez, Carlos Bartual-Murgui, William Nicolazzi, Lionel Salmon, Gábor Molnár, and Azzedine Bousseksou. Atomic force microscopy and near-field optical imaging of a spin transition. *Nanoscale*, 5(17):7762–7767, August 2013.

[94] O. Kahn and C. Jay Martinez. Spin-transition polymers: From molecular materials toward memory devices. *Science*, 279(5347):44–48, 1998.

[95] Massimiliano Cavallini. Status and perspectives in thin films and patterning of spin crossover compounds. *Phys. Chem. Chem. Phys.*, 14(34):11867–11876, August 2012.

[96] Gábor Molnár, Lionel Salmon, William Nicolazzi, Ferial Terki, and Azzedine Bousseksou. Emerging properties and applications of spin crossover nanomaterials. *Journal of Materials Chemistry C*, 2(8):1360, 2014.

[97] Jean-François Létard, Philippe Guionneau, and Laurence Goux-Capes. Towards spin crossover applications. In *Spin Crossover in Transition Metal Compounds III*, number 235 in Topics in Current Chemistry, pages 221–249. Springer Berlin Heidelberg, January 2004.

[98] Thibaut Forestier, Stéphane Mornet, Nathalie Daro, Taishi Nishihara, Shin-ichiro Mouri, Koichiro Tanaka, Olivier Fouché, Eric Freysz, and Jean-François Létard. Nanoparticles of iron(II) spin-crossover. *Chem. Commun.*, 36:4327–4329, August 2008.

[99] Antoine Tissot, Jean-François Bardeau, Eric Rivière, François Brisset, and Marie-Laure Boillot. Thermo- and photoswitchable spin-crossover nanoparticles of an iron(ii) complex trapped in transparent silica thin films. *Dalton Transactions*, 39(33):7806, 2010.

[100] Akio Nakamoto, Yuuki Ono, Norimichi Kojima, Daiju Matsumura, and Toshihiko Yokoyama. Spin crossover complex film, [fe^{II}(H-trz)₃]-Nafion, with a spin transition around room temperature. *Chemistry Letters*, 32(4):336–337, 2003.

[101] Akio Nakamoto, Yuuki Ono, Norimichi Kojima, Daiju Matsumura, and Toshihiko Yokoyama. Additions and corrections : Spin crossover complex film, [fe^{II}(H-trz)₃]-Nafion, with a spin transition around room temperature. *Chemistry Letters*, 32(5):476, 2003.

[102] Saioa Cobo, Gábor Molnár, José Antonio Real, and Azzedine Bousseksou. Multilayer sequential assembly of thin films that display room-temperature spin crossover with hysteresis. *Angewandte Chemie International Edition*, 45(35):5786–5789, September 2006.

[103] Lionel Salmon, Gábor Molnár, Saioa Cobo, Pascal Oulié, Michel Etienne, Tarik Mahfoud, Philippe Demont, Akira Eguchi, Hiroshi Watanabe, Koichiro Tanaka, and Azzedine Bousseksou. Re-investigation of the spin crossover phenomenon in the ferrous complex [fe(HB(pz)3)2]. *New J. Chem.*, 33(6):1283–1289, June 2009.

[104] S. Shi, G. Schmerber, J. Arabski, J.-B. Beaufrand, D. J. Kim, S. Boukari, M. Bowen, N. T. Kemp, N. Viart, G. Rogez, E. Beaurepaire, H. Aubriet, J. Petersen, C. Becker, and D. Ruch. Study of molecular spin-crossover complex fe(phen)2(NCS)2 thin films. *App. Phys. Lett.*, 95(4):043303, July 2009.

[105] Il'ya A. Gural'skiy, Carlos M. Quintero, Gábor Molnár, Igor O. Fritsky, Lionel Salmon, and Azzedine Bousseksou. Synthesis of spin-crossover nano- and micro-objects in homogeneous media. *Chem. Eur. J.*, 18(32):9946–9954, 2012.

[106] Khaldoun Abdul-Kader, Manuel Lopes, Carlos Bartual-Murgui, Olena Kraieva, Edna M. Hernández, Lionel Salmon, William Nicolazzi, Franck Carcenac, Christophe Thibault, Gábor Molnár, and Azzedine Bousseksou. Synergistic switching of plasmonic resonances and molecular spin states. *Nanoscale*, 5(12):5288–5293, June 2013.

[107] Paul W. Kolb, Danilo B. Romero, H. Dennis Drew, Andrei B. Sushkov, Satish B. Ogale, and Yutaka Moritomo. Near-field evidence for ferromagnetic nanoneedles in $nd_{1/2}sr_{1/2}MnO_3$. *Nano Letters*, 7(6):1449–1453, June 2007.

[108] Yanhong Tang, Yan Wang, Xindong Wang, Shidi Xun, Chongyu Mei, Lixiang Wang, and Donghang Yan. AFM observations of phase transitions in molecularly thin films of a three-ring bent-core compound. *The Journal of Physical Chemistry B*, 109(18):8813–8819, May 2005.

[109] Fei Yang, Ling Xu, Rui Zhang, Lei Geng, Liang Tong, Jun Xu, Weining Su, Yao Yu, Zhongyuan Ma, and Kunji Chen. Direct observation of phase transition of GeSbTe thin films by atomic force microscope. *Applied Surface Science*, 258(24):9751–9755, October 2012.

[110] Justyna Wiedemair, Michael J. Serpe, Jongseong Kim, Jean-Francois Masson, L. Andrew Lyon, Boris Mizaikoff, and Christine Kranz. In-situ AFM studies of the phase-transition behavior of single thermoresponsive hydrogel particles. *Langmuir*, 23(1):130–137, January 2007.

[111] Meng Xu, Shijun Zhang, Jieying Liang, Hui Quan, Jianye Liu, Hongwei Shi, Dali Gao, and Jie Liu. Influences of processing on the phase transition and crystallization of polypropylene cast films. *Journal of Applied Polymer Science*, 131(22):n/a–n/a, 2014.

[112] Magdalena Huefner, Ram Krishna Ghosh, Eugene Freeman, Nikhil Shukla, Hanjong Paik, Darrell G. Schlom, and Suman Datta. Hubbard gap modulation in vanadium dioxide nanoscale tunnel junctions. *Nano Letters*, 14(11):6115–6120, 2014.

[113] Naoyuki Ishida and Simon Biggs. Direct observation of the phase transition for a poly(n-isopropylacryamide) layer grafted onto a solid surface by AFM and QCM-d. *Langmuir*, 23(22):11083–11088, October 2007.

[114] Gerd Binnig, H. Rohrer, Ch. Greber, and E. Weibel. Surface studies by scanning tunneling microscopy. *Physical Review Letters*, 49(1):57–61, 1982.

[115] D. W. Pohl, W. Denk, and M. Lanz. Optical stethoscopy: Image recording with resolution $\lambda/20$. *Applied Physics Letters*, 44(7):651–653, April 1984.

[116] A. Lewis, M. Isaacson, A. Harootunian, and A. Muray. Development of a 500 Å spatial resolution light microscope: I. light is efficiently transmitted through $\lambda/16$ diameter apertures. *Ultramicroscopy*, 13(3):227–231, 1984.

[117] G. Binnig, C. F. Quate, and Ch. Gerber. Atomic force microscope. *Phys. Rev. Lett.*, 56:930–933, Mar 1986.

[118] Yow-Ren Chang, Vijay Krishna Raghunathan, Shaun P. Garland, Joshua T. Morgan, Paul Russell, and Christopher J. Murphy. Automated AFM force curve analysis for determining elastic modulus of biomaterials and biological samples. *Journal of the Mechanical Behavior of Biomedical Materials*, 37:209–218, September 2014.

[119] Dietmar Haba, Josef Kaufmann, Andreas J. Brunner, Katharina Resch, and Christian Teichert. Observation of elastic modulus inhomogeneities in thermosetting epoxies using AFM – discerning facts and artifacts. *Polymer*, 55(16):4032–4040, August 2014.

[120] C. Mathew Mate, Gary M. McClelland, Ragnar Erlandsson, and Shirley Chiang. Atomic-scale friction of a tungsten tip on a graphite surface. *Physical Review Letters*, 59(17):1942–1945, October 1987.

[121] R. J. Barczyński, N. A. Szreder, J. Karczewski, and M. Gazda. Electronic conductivity in the SiO2–PbO–fe2o3 glass containing magnetic nanostructures. *Solid State Ionics*, 262:801–805, September 2014.

[122] D. Courjon and C. Bainier. Near field microscopy and near field optics. *Reports on Progress in Physics*, 57(10):989, October 1994.

[123] Raja Das, Adhish Jaiswal, and Pankaj Poddar. Static and dynamic magnetic properties and interplay of dy 3+ , gd 3+ and mn 3+ spins in orthorhombic DyMnO 3 and GdMnO 3 nanoparticles. *Journal of Physics D: Applied Physics*, 46(4):045301, January 2013.

[124] Shunsuke Yoshizawa, Howon Kim, Takuto Kawakami, Yuki Nagai, Tomonobu Nakayama, Xiao Hu, Yukio Hasegawa, and Takashi Uchihashi. Imaging josephson vortices on the surface superconductor $\mathrm{Si}(111)\text{-}(\sqrt{7}\ifmmode\times\else\texttimes\fi{}\sqrt{3})\text{-}\mathrm{In}$

using a scanning tunneling microscope. *Physical Review Letters*, 113(24):247004, December 2014.

[125] E. P. Smakman, S. Mauger, D. W. Rench, N. Samarth, and P. M. Koenraad. Structural, electronic, and magnetic properties of single MnAs nanoclusters in GaAs. *Applied Physics Letters*, 105(23):232405, December 2014.

[126] M. Alejandra Sánchez, Sergio A. Paniagua, Ignacio Borge, Christian Viales, and Mavis L. Montero. Lewis basicity, adhesion thermodynamic work and coordinating ability on aminated silicon surfaces. *Applied Surface Science*, 317(0):1060 – 1067, 2014.

[127] DongWeon Lee, Adrian Wetzel, Roland Bennewitz, Ernst Meyer, Michel Despont, Peter Vettiger, and Christoph Gerber. Switchable cantilever for a time-of-flight scanning force microscope. *Applied Physics Letters*, 84(9):1558–1560, March 2004.

[128] F. Krok, K. Sajewicz, J. Konior, M. Goryl, P. Piatkowski, and M. Szymonski. Lateral resolution and potential sensitivity in Kelvin probe force microscopy: Towards understanding of the sub-nanometer resolution. *Physical Review B*, 77(23):235427, June 2008.

[129] Wilhelm Melitz, Jian Shen, Andrew C. Kummel, and Sangyeob Lee. Kelvin probe force microscopy and its application. *Surface Science Reports*, 66(1):1–27, January 2011.

[130] L. Zhang, T. Sakai, N. Sakuma, T. Ono, and K. Nakayama. Nanostructural conductivity and surface-potential study of low-field-emission carbon films with conductive scanning probe microscopy. *Applied Physics Letters*, 75(22):3527–3529, November 1999.

[131] Elisabeth Soergel. Piezoresponse force microscopy (PFM). *Journal of Physics D: Applied Physics*, 44(46):464003, November 2011.

[132] P. Guethner, U. Fischer, and K. Dransfeld. Scanning near-field acoustic microscopy. *Appl. Phys. B Photophys. Laser Chem*, B48:89–92, 1989.

[133] Gerhard Meyer and Nabil M. Amer. Optical-beam-deflection atomic force microscopy: The NaCl (001) surface. *Applied Physics Letters*, 56(21):2100, 1990.

[134] A. G Khurshudov, K. Kato, and H. Koide. Wear of the AFM diamond tip sliding against silicon. *Wear*, 203:22–27, 1997.

[135] C. Su, L. Huang, K. Kjoller, and K. Babcock. Studies of tip wear processes in tapping model^{TM} atomic force microscopy. *Ultramicroscopy*, 97(1):135–144, 2003.

[136] Q. Zhong, D. Inniss, K. Kjoller, and V. B. Elings. Fractured polymer/silica fiber surface studied by tapping mode atomic force microscopy. *Surface Science*, 290(1-2):L688–L692, June 1993.

[137] Stefan B. Kaemmer. Introduction to bruker's ScanAsyst and PeakForce tapping AFM technology. *Bruker application note. Bruker Nano Inc., Santa Barbara, CA*, 2011.

[138] Hans-Jürgen Butt, Brunero Cappella, and Michael Kappl. Force measurements with the atomic force microscope: Technique, interpretation and applications. *Surface Science Reports*, 59(1-6):1–152, October 2005.

[139] William A. Ducker and Robert F. Cook. Rapid measurement of static and dynamic surface forces. *Applied Physics Letters*, 56(24):2408–2410, June 1990.

[140] Marcel A. Lauterbach. Finding, defining and breaking the diffraction barrier in microscopy–a historical perspective. *Optical Nanoscopy*, 1(1):1–8, 2012.

[141] E. Synge. A suggested method for extending microscopic resolution into the ultra-microscopic region. *Phil. Mag.*, 6:356–362, 1928.

[142] Lukas Novotny. The history of near-field optics. *Progress in optics*, 50:137, 2007.

[143] Max Born and Emil Wolf. *Principles of Optics: Electromagnetic Theory of Propagation, Interference and Diffraction of Light*. Cambridge University Press, October 1999.

[144] Manuel Nieto-Vesperinas and Emil Wolf. Phase conjugation and symmetries with wave fields in free space containing evanescent components. *Journal of the Optical Society of America A*, 2(9):1429–1434, September 1985.

[145] Lukas Novotny and Bert Hecht. *Principles of Nano-Optics*. Cambridge University Press, 2 edition edition, 2012.

[146] Eugene Hecht. *Optics*. Addison-Wesley, 4 edition edition, 2001.

[147] Reuben M. Bakker, Hsiao-Kuan Yuan, Zhengtong Liu, Vladimir P. Drachev, Alexander V. Kildishev, Vladimir M. Shalaev, Rasmus H. Pedersen, Samuel Gresillon, and Alexandra Boltasseva. Enhanced localized fluorescence in plasmonic nanoantennae. *Applied Physics Letters*, 92(4):043101, 2008.

[148] Zheyu Fang, Xuejin Zhang, Dan Liu, and Xing Zhu. Excitation of dielectric-loaded surface plasmon polariton observed by using near-field optical microscopy. *Applied Physics Letters*, 93(7):073306, 2008.

[149] Y. Gorodetski, A. Niv, V. Kleiner, and E. Hasman. Observation of the spin-based plasmonic effect in nanoscale structures. *Phys. Rev. Lett.*, 101(4):043903, 2008.

[150] Gilad M. Lerman, Avner Yanai, and Uriel Levy. Demonstration of nanofocusing by the use of plasmonic lens illuminated with radially polarized light. *Nano Lett.*, 9(5):2139–2143, 2009.

[151] Il'ya A. Gural'skiy, Carlos M. Quintero, Khaldoun Abdul-Kader, Manuel Lopes, Carlos Bartual-Murgui, Lionel Salmon, Pengxiang Zhao, Gábor Molnár, Didier Astruc, and Azzedine Bousseksou. Detection of molecular spin-state changes in ultrathin films by photonic methods. *J. Nanophotonics*, 6(1):063517–1, 2012.

[152] Amal Akou, Carlos Bartual-Murgui, Khaldoun Abdul-Kader, Manuel Lopes, Gábor Molnár, Christophe Thibault, Christophe Vieu, Lionel Salmon, and Azzedine Bousseksou. Photonic gratings of the metal–organic framework {Fe(bpac)[Pt(CN)4]} with synergetic spin transition and host–guest properties. *Dalton Transactions*, 42(45):16021, 2013.

[153] Hal Edwards, Larry Taylor, Walter Duncan, and Allan J. Melmed. Fast, high-resolution atomic force microscopy using a quartz tuning fork as actuator and sensor. *Journal of applied physics*, 82(3):980–984, 1997.

[154] M. M. Qazilbash, M. Brehm, Byung-Gyu Chae, P.-C. Ho, G. O. Andreev, Bong-Jun Kim, Sun Jin Yun, A. V. Balatsky, M. B. Maple, F. Keilmann, Hyun-Tak Kim, and D. N. Basov. Mott Transition in VO2 Revealed by Infrared Spectroscopy and Nano-Imaging. *Science*, 318(5857):1750–1753, December 2007.

[155] Carlos M. Quintero, Olena Kraieva, Franck Carcenac, Denis Lagrange, Yaremchuk Nina A., Gábor Molnár, and Christian Bergaud. Joule heated metallic microwire devices for sub-micro second t-jump experiments. *MEJ*, submmited.

[156] Olena Kraieva, Carlos M. Quintero, Gábor Molnár, Michel Mortier, Lionel Aigouy, and Christian Bergaud. Investigation of luminophores for high spatial and temporal resolution. In *Thermophysics 2014 - Conference Proceedings*, pages 163–170, Bratislava, Slovakia, oct 2014. Brno University of Technology, Faculty of Chemistry.

[157] Khaldoun Abdul Kader. *Etude du phénomène de la transition de spin dans les couches ultra-minces à l'aide des plasmons de surface*. PhD thesis, Université de Toulouse, Université Toulouse III-Paul Sabatier, 2014.

[158] David K. Teertstra. The Optical Analysis of Minerals. *The Canadian Mineralogist*, 43(2):543–552, April 2005.

[159] Hiroshi Hatano, Yasushi Inouye, and Satoshi Kawata. A Near-Field Scanning Optical Microscope Which Measures Both Constant-Height and Constant-Gap Images. *Japanese Journal of Applied Physics*, 37(8B):L1008, August 1998.

[160] B. Hecht, H. Bielefeldt, Y. Inouye, D. W. Pohl, and L. Novotny. Facts and artifacts in near-field optical microscopy. *Journal of Applied Physics*, 81(6):2492–2498, March 1997.

[161] P. G. Gucciardi, S. Patanè, A. Ambrosio, M. Allegrini, A. D. Downes, G. Latini, O. Fenwick, and F. Cacialli. Observation of tip-to-sample heat transfer in near-field optical microscopy using metal-coated fiber probes. *Applied Physics Letters*, 86(20):203109, May 2005.

[162] C. Triolo, S. Patanè, M. Mazzeo, S. Gambino, G. Gigli, and M. Allegrini. Pure optical nano-writing on light- switchable spiropyrans/merocyanine thin film. *Optics Express*, 22(1):283, January 2014.

[163] Mohammad S. Alam, Michael Stocker, Klaus Gieb, Paul Müller, Marco Haryono, Katja Student, and Andreas Grohmann. Spin-State Patterns in Surface-Grafted Beads of Iron(II) Complexes. *Angewandte Chemie International Edition*, 49(6):1159–1163, February 2010.

[164] Thiruvancheril G. Gopakumar, Francesca Matino, Holger Naggert, Alexander Bannwarth, Felix Tuczek, and Richard Berndt. Corrigendum: Electron-Induced Spin Crossover of Single Molecules in a Bilayer on Gold. *Angewandte Chemie International Edition*, 52(14):3796–3796, April 2013.

[165] Alex Pronschinske, Yifeng Chen, Geoffrey F. Lewis, David A. Shultz, Arrigo Calzolari, Marco Buongiorno Nardelli, and Daniel B. Dougherty. Modification of Molecular Spin Crossover in Ultrathin Films. *Nano Letters*, 13(4):1429–1434, April 2013.

[166] H. Spiering, K. Boukheddaden, J. Linares, and F. Varret. Total free energy of a spin-crossover molecular system. *Phys. Rev. B*, 70(18):184106, November 2004.

[167] Helena J. Shepherd, Il'ya Gural'skiy, Carlos M. Quintero, Simon Tricard, Lionel Salmon, Gábor Molnár, and Azzedine Bousseksou. Molecular actuators driven by cooperative spin-state switching. *Nat Commun*, 4, October 2013.

[168] Gautier Félix, Mirko Mikolasek, Haonan Peng, William Nicolazzi, Gábor Molnár, Aleksandr I. Chumakov, Lionel Salmon, and Azzedine Bousseksou. Lattice dynamics in spin-crossover nanoparticles through nuclear inelastic scattering. *Physical Review B*, 91(2):024422, January 2015.

[169] Thierry Granier, Bernard Gallois, Jacques Gaultier, Jose Antonio Real, and Jacqueline Zarembowitch. High-pressure single-crystal x-ray diffraction study of two spin-crossover iron (II) complexes: Fe (Phen) 2 (NCS) 2 and Fe (Btz) 2 (NCS) 2. *Inorganic Chemistry*, 32(23):5305–5312, 1993.

[170] Helena J. Shepherd, Tatiana Palamarciuc, Patrick Rosa, Philippe Guionneau, Gábor Molnár, Jean-François Létard, and Azzedine Bousseksou. Antagonism between Extreme Negative Linear Compression and Spin Crossover in $[Fe(dpp)_2(NCS)_2]\cdot py$. *Angewandte Chemie International Ed.*, 51(16):3910–3914, April 2012.

[171] J. Jung, F. Bruchhäuser, R. Feile, H. Spiering, and P. Gütlich. The cooperative spin transition in [FexZn1 - x(ptz)6](BF4)2: i. elastic properties — an oriented sample rotation study by brillouin spectroscopy. *Zeitschrift für Physik B Condensed Matter*, 100(4):517–522, December 1996.

[172] Philipp Gütlich, Andreas Hauser, and Hartmut Spiering. Thermal and optical switching of iron(ii) complexes. *Angew. Chem. Int. Ed. Engl.*, 33(20):2024–2054, 1994.

[173] Jean-Pierre Tuchagues, Azzedine Bousseksou, Gábor Molnár, John J. McGarvey, and François Varret. The role of molecular vibrations in the spin crossover phenomenon. In *Spin Crossover in Transition Metal Compounds III*, number 235 in Topics in Current Chemistry, pages 84–103. Springer Berlin Heidelberg, January 2004.

[174] R. Suriano, V. Oldani, C. L. Bianchi, and S. Turri. AFM nanomechanical properties and durability of new hybrid fluorinated sol-gel coatings. *Surface and Coatings Technology*, 264:87–96, February 2015.

[175] Philip Egberts, Robert Gralla, and Roland Bennewitz. Temporal development of indentation plasticity on the atomic scale revealed by force microscopy. *Physical Review B*, 86(3):035446, July 2012.

[176] Diego F. Arias, Diana M. Marulanda, Alejandra M. Baena, and Alfonso Devia. Determination of friction coefficient on ZrN and TiN using lateral force microscopy (LFM). *Wear*, 261(11–12):1232–1236, December 2006.

[177] M. Varenberg, I. Etsion, and G. Halperin. An improved wedge calibration method for lateral force in atomic force microscopy. *Review of Scientific Instruments*, 74(7):3362–3367, July 2003.

[178] O. Piétrement and M. Troyon. Quantitative study of shear modulus and interfacial shear strength by combining modulated lateral force and magnetic force modulation microscopies. *Surface and Interface Analysis*, 31(11):1060–1067, November 2001.

[179] Chengming Jiang, Wenqiang Lu, and Jinhui Song. Shear Modulus Property Characterization of Nanorods. *Nano Letters*, 13(1):111–115, January 2013.

[180] Neng-Kai Chang and Shuo-Hung Chang. Determining Mechanical Properties of Carbon Microcoils Using Lateral Force Microscopy. *IEEE Transactions on Nanotechnology*, 7(2):197–201, March 2008.

[181] Lili L Johnson, R. K Eby, and Mary Ann B Meador. Investigation of oxidation profile in PMR-15 polyimide using atomic force microscope (AFM). *Polymer*, 44(1):187–197, January 2003.

[182] D. Passeri, A. Bettucci, A. Biagioni, M. Rossi, A. Alippi, M. Lucci, I. Davoli, and S. Berezina. Quantitative measurement of indentation hardness and modulus of compliant materials by atomic force microscopy. *The Review of Scientific Instruments*, 79(6):066105, June 2008.

[183] D. C. Hurley and J. A. Turner. Measurement of Poisson's ratio with contact-resonance atomic force microscopy. *Journal of Applied Physics*, 102(3):033509, 2007.

[184] Daniele Passeri, Marco Rossi, Emanuela Tamburri, and Maria Letizia Terranova. Mechanical characterization of polymeric thin films by atomic force microscopy based techniques. *Analytical and Bioanalytical Chemistry*, 405(5):1463–1478, October 2012.

[185] R. Ferencz, J. Sanchez, B. Blümich, and W. Herrmann. AFM nanoindentation to determine Young's modulus for different EPDM elastomers. *Polymer Testing*, 31(3):425–432, May 2012.

[186] Davide Tranchida, Zebene Kiflie, and Stefano Piccarolo. Atomic force microscope nanoindentations to reliably measure the young's modulus of soft matter. *Modern Research and Educational Topics in Microscopy*, 2:737–46, 2007.

[187] P. Maivald, H. J. Butt, S. a. C. Gould, C. B. Prater, B. Drake, J. A. Gurley, V. B. Elings, and P. K. Hansma. Using force modulation to image surface elasticities with the atomic force microscope. *Nanotechnology*, 2(2):103, April 1991.

[188] H. Y. Nie, M. Motomatsu, W. Mizutani, and H. Tokumoto. Local elasticity measurement on polymers using atomic force microscopy. *Thin Solid Films*, 273(1–2):143–148, February 1996.

[189] Veeco Instruments Inc. *Force Modulation Imaging with Atomic Force Microscopy*, 2004.

[190] P.m. McGuiggan and D.j. Yarusso. Measurement of the loss tangent of a thin polymeric film using the atomic force microscope. *Journal of Materials Research*, 19(01):387–395, 2004.

[191] P. A. Yuya, D. C. Hurley, and J. A. Turner. Contact-resonance atomic force microscopy for viscoelasticity. *Journal of Applied Physics*, 104(7):074916, October 2008.

[192] P. A. Yuya, D. C. Hurley, and J. A. Turner. Relationship between Q-factor and sample damping for contact resonance atomic force microscope measurement of viscoelastic properties. *Journal of Applied Physics*, 109(11):113528, June 2011.

[193] Dalia G. Yablon, Anil Gannepalli, Roger Proksch, Jason Killgore, Donna C. Hurley, Jean Grabowski, and Andy H. Tsou. Quantitative Viscoelastic Mapping of Polyolefin Blends with Contact Resonance Atomic Force Microscopy. *Macromolecules*, 45(10):4363–4370, May 2012.

[194] J.P. Killgore, D.G. Yablon, A.H. Tsou, A. Gannepalli, P.A. Yuya, J.A. Turner, R. Proksch, and D.C. Hurley. Viscoelastic property mapping with contact resonance force microscopy. *Langmuir*, 27(23):13983–13987, 2011.

[195] Sara E. Campbell, Virginia L. Ferguson, and Donna C. Hurley. Nanomechanical mapping of the osteochondral interface with contact resonance force microscopy and nanoindentation. *Acta Biomaterialia*, 8(12):4389–4396, December 2012.

[196] Ryan C. Tung, Jason P. Killgore, and Donna C. Hurley. Hydrodynamic corrections to contact resonance atomic force microscopy measurements of viscoelastic loss tangenta). *Review of Scientific Instruments*, 84(7):073703, July 2013.

[197] Ishita Chakraborty and Dalia G. Yablon. Temperature dependent loss tangent measurement of polymers with contact resonance atomic force microscopy. *Polymer*, 55(7):1609–1612, April 2014.

[198] R. Garcia and A. San Paulo. Attractive and repulsive tip-sample interaction regimes in tapping-mode atomic force microscopy. *Physical Review B*, 60(7):4961, 1999.

[199] N. F. Martínez and R. García. Measuring phase shifts and energy dissipation with amplitude modulation atomic force microscopy. *Nanotechnology*, 17(7):S167, 2006.

[200] J. Tamayo. Relationship between phase shift and energy dissipation in tapping-mode scanning force microscopy. *Applied physics letters*, 73(20):2926–2928, 1998.

[201] Javier Tamayo and Ricardo García. Effects of elastic and inelastic interactions on phase contrast images in tapping-mode scanning force microscopy. *Applied Physics Letters*, 71(16):2394, 1997.

[202] Franz J. Giessibl and Hartmut Bielefeldt. Physical interpretation of frequency-modulation atomic force microscopy. *Physical Review B*, 61(15):9968, 2000.

[203] Franz J. Giessibl. Advances in atomic force microscopy. *Reviews of modern physics*, 75(3):949, 2003.

[204] David Martinez-Martin, Carolina Carrasco, Mercedes Hernando-Perez, Pedro J. de Pablo, Julio Gomez-Herrero, Rebeca Perez, Mauricio G. Mateu, Jose L. Carrascosa, Daniel Kiracofe, John Melcher, and Arvind Raman. Resolving Structure and Mechanical Properties at the Nanoscale of Viruses with Frequency Modulation Atomic Force Microscopy. *PLoS ONE*, 7(1):e30204, January 2012.

[205] Yan Jun Li, Naritaka Kobayashi, Hikaru Nomura, Yoshitaka Naitoh, Masami Kageshima, and Yasuhiro Sugawara. High-Speed Phase-Modulation Atomic Force Microscopy in Constant-Amplitude Mode Capable of Simultaneous Measurement of Topography and Energy Dissipation. *Japanese Journal of Applied Physics*, 47(7S2):6121, July 2008.

[206] Takeshi Fukuma, Jason I. Kilpatrick, and Suzanne P. Jarvis. Phase modulation atomic force microscope with true atomic resolution. *Review of Scientific Instruments*, 77(12):123703, December 2006.

[207] Hendrik Hölscher. Theory of phase-modulation atomic force microscopy with constant-oscillation amplitude. *Journal of Applied Physics*, 103(6):064317, March 2008.

[208] Naritaka Kobayashi, Yan Jun Li, Yoshitaka Naitoh, Masami Kageshima, and Yasuhiro Sugawara. High-Sensitivity Force Detection by Phase-Modulation Atomic Force Microscopy. *Japanese Journal of Applied Physics*, 45(8L):L793, August 2006.

[209] Dalia G. Yablon, Jean Grabowski, and Ishita Chakraborty. Measuring the loss tangent of polymer materials with atomic force microscopy based methods. *Measurement Science and Technology*, 25(5):055402, May 2014.

[210] Roger Proksch and Dalia G. Yablon. Loss tangent imaging: Theory and simulations of repulsive-mode tapping atomic force microscopy. *Applied Physics Letters*, 100(7):073106, February 2012.

[211] Ricardo Garcia and Roger Proksch. Nanomechanical mapping of soft matter by bimodal force microscopy. *European Polymer Journal*, 49(8):1897–1906, August 2013.

[212] M. Deniz Aksoy and A. Atalar. Force spectroscopy using bimodal frequency modulation atomic force microscopy. *Physical Review B*, 83(7), February 2011.

[213] Gaurav Chawla and Santiago D Solares. Single-cantilever dual-frequency-modulation atomic force microscopy. *Measurement Science and Technology*, 20(1):015501, January 2009.

[214] Brunero Cappella. Mechanical Properties and Adhesion of a Micro Structured Polymer Blend. *Polymers*, 3(3):1091–1106, July 2011.

[215] L. Chopinet, C. Formosa, M.P. Rols, R.E. Duval, and E. Dague. Imaging living cells surface and quantifying its properties at high resolution using AFM in QI^{TM} mode. *Micron*, 48:26–33, May 2013.

[216] Jpk instruments, (nanowizard 3) qi mode.

[217] P. Trtik, J. Kaufmann, and U. Volz. On the use of peak-force tapping atomic force microscopy for quantification of the local elastic modulus in hardened cement paste. *Cement and Concrete Research*, 42:215–221, 2012.

[218] B. Bhushan and J. Qi. Phase contrast imaging of nanocomposites and molecularly thick lubricant films in magnetic media. *Nanotechnology*, 14(8):886, 2003.

[219] F. Z. Fang, Z. W. Xu, and S. Dong. Study on phase images of a carbon nanotube probe in atomic force microscopy. *Measurement Science and Technology*, 19(5):055501, 2008.

[220] Atomic force microscopy based viscoelastic property measurements with am-fm viscoelastic mapping mode. sponsored by Oxford Instruments Asylum Research. http://www.azom.com/article.aspx?ArticleID=11329.

[221] Christopher T Gibson, D Alastair Smith, and Clive J Roberts. Calibration of silicon atomic force microscope cantilevers. *Nanotechnology*, 16(2):234–238, February 2005.

[222] Jeffrey L. Hutter and John Bechhoefer. Calibration of atomic-force microscope tips. *Review of Scientific Instruments*, 64(7):1868, 1993.

[223] Benjamin Ohler. Cantilever spring constant calibration using laser Doppler vibrometry. *Review of Scientific Instruments*, 78(6):063701, June 2007.

[224] H.-J. Butt and M. Jaschke. Calculation of thermal noise in atomic force microscopy. *Nanotechnology*, 6(1):1, January 1995.

[225] John Elie Sader. Frequency response of cantilever beams immersed in viscous fluids with applications to the atomic force microscope. *Journal of applied physics*, 84(1):64–76, 1998.

[226] M. Radmacher, J. P. Cleveland, M. Fritz, H. G. Hansma, and P. K. Hansma. Mapping interaction forces with the atomic force microscope. *Biophysical Journal*, 66(6):2159–2165, June 1994.

[227] Giovanni Longo, Laura Marques Rio, Charles Roduit, Andrej Trampuz, Alain Bizzini, Giovanni Dietler, and Sandor Kasas. Force volume and stiffness tomography investigation on the dynamics of stiff material under bacterial membranes. *Journal of Molecular Recognition*, 25(5):278–284, May 2012.

[228] Xinghua Shi and Ya-Pu Zhao. Comparison of various adhesion contact theories and the influence of dimensionless load parameter. *Journal of Adhesion Science and Technology*, 18(1):55–68, 2004.

[229] B. V. Derjaguin, V. M. Muller, and Y. P. Toporov. Effect of contact deformations on the adhesion of particles. *Journal of Colloid and interface science*, 53(2):314–326, 1975.

[230] K. L. Johnson, K. Kendall, and A. D. Roberts. Surface Energy and the Contact of Elastic Solids. *Proceedings of the Royal Society of London A: Mathematical, Physical and Engineering Sciences*, 324(1558):301–313, September 1971.

[231] Yoichi Tatara. Large Deformations of a Rubber Sphere under Diametral Compression : Part 1 : Theoretical Analysis of Press Approach, Contact Radius and Lateral Extension. *JSME international journal. Ser. A, Mechanics and material engineering*, 36(2):190–196, April 1993.

[232] Núria Gavara and Richard S. Chadwick. Determination of the elastic moduli of thin samples and adherent cells using conical atomic force microscope tips. *Nature Nanotechnology*, 7(11):733–736, November 2012.

[233] G. N. Greaves, A. L. Greer, R. S. Lakes, and T. Rouxel. Poisson's ratio and modern materials. *Nature Materials*, 10(11):823–837, November 2011.

[234] Jing Han, Guiping Ma, and Jun Nie. A facile fabrication of porous PMMA as a potential bone substitute. *Materials Science and Engineering: C*, 31(7):1278–1284, October 2011.

[235] Vahid Vahdat, David S. Grierson, Kevin T. Turner, and Robert W. Carpick. Mechanics of Interaction and Atomic-Scale Wear of Amplitude Modulation Atomic Force Microscopy Probes. *ACS Nano*, 7(4):3221–3235, April 2013.

[236] Sylvestre Bonnet, Maxime A. Siegler, José Sánchez Costa, Gábor Molnár, Azzedine Bousseksou, Anthony L. Spek, Patrick Gamez, and Jan Reedijk. A two-step spin crossover mononuclear iron(ii) complex with a [HS–LS–LS] intermediate phase. *Chemical Communications*, 43:5619, 2008.

[237] Sipeng Zheng and Faculteit der Wiskunde en Natuurwetenschappen. *Mononuclear spin-transition materials based on the bapbpy scaffold*. Dissertatie, Leiden University, Netherlands, June 2014.

[238] Xin-Gang Liang and Zeng-Yuan Guo. The Scaling Effect on the Thermal Processes at Mini/Microscale. *Heat Transfer Engineering*, 27(4):30–40, May 2006.

[239] J. J. Mahony. Heat Transfer at Small Grashof Numbers. *Proceedings of the Royal Society of London. Series A, Mathematical and Physical Sciences*, 238(1214):412–423, January 1957.

[240] A.M. Leung, J. Jones, E. Czyzewska, J. Chen, and M. Pascal. Micromachined accelerometer with no proof mass. In *Electron Devices Meeting, 1997. IEDM '97. Technical Digest., International*, pages 899–902, December 1997.

[241] Frank P. Incropera and Frank P. Incropera, editors. *Fundamentals of heat and mass transfer*. John Wiley, Hoboken, NJ, 6th ed edition, 2007.

Résumé

Récemment, un grand nombre d'objets de taille nanométrique, incluant les nanoparticules, les films minces, les dispositifs nanostructurés, présentant des phénomènes de commutation impliquant différents états de spin, ont été développé pour des applications dans le domaine des capteurs et des systèmes nanophotoniques, nanoélectroniques et nanomécaniques. En effet, ces nanomatériaux à conversion de spin présentent une dépendance en taille des propriétés physico-chimiques très intéressantes. Même si l'origine du phénomène de conversion de spin est purement moléculaire, le comportement macroscopique de ces systèmes à l'état solide est fortement influencé par les interactions intermoléculaires élastiques. On s'attend donc à ce que les propriétés coopératives et, de manière plus générale, le diagramme de phase, soient très dépendantes de la taille du système. Au delà de la stabilité des phases, les cinétiques de transformation dépendent également de la taille du système. Dans ce contexte, des interactions élastiques fortes conduisent dans de nombreux cas à des transitions de type premier ordre accompagnées par une séparation de phase hétérogène. Les détails du mécanisme de la dynamique spatio-temporelle associée à la transition de spin restent encore inexplorés. L'ensemble de ces phénomènes observés dans les matériaux à transition de spin demande des méthodes de caractérisation possédant une capacité d'imagerie d'une grande résolution spatiale afin d'aller au delà des techniques de microscopie optique en champ lointain habituellement employées. Par conséquence, l'objectif global de cette thèse de doctorat est de développer de nouvelles approches qui permettent de détecter le phénomène de transition de spin avec une résolution spatiale nanométrique. Pour observer la transition de spin thermique dans les films minces, nous avons utilisé pour la première fois la microscopie optique en champ proche (NSOM en Anglais) ainsi que la microscopie à force atomique (AFM en Anglais) en conjonction avec des dispositifs originaux de chauffage à l'échelle du nanomètre, conçus à partir de nanofils et fonctionnant par effet Joule. En utilisant ces techniques, le changement de l'état de spin a pu être observé avec une résolution sub-longueur d'onde au travers des changements des propriétés mécaniques et optiques du matérial. Le NSOM en mode illumination, utilisé soit en mode luminescence ou en mode réflexion fournit un signal utile pour la détection du changement d'état de spin; mais ne permet en revanche qu'une quantification limitée du phénomène en raison de l'instabilité des échantillons. D'un autre côté, les différents modes mécaniques AFM, incluant la spectroscopie de force rapide et l'analyse multifréquentielle, ont permis des mesures quantitatives et reproductibles avec une résolution nanométrique. En particulier, nous avons été capable de mesurer pour la première fois l'augmentation du module d'Young (env. 25-30%) observée lors de la transition de l'état Haut Spin vers l'état Bas Spin et nous avons utilisé cette propriété pour réaliser une imagerie quantitative de la transition de spin. Des mesures AFM ont été faites sur des monocristaux à transition de spin. Nous avons montré que les transferts thermiques entre la sonde et l'échantillon peuvent être utilisés pour manipuler la nucléation et la propagation des phases Haut et Bas Spin dans des cristaux. Par ailleurs, ces interactions sonde-échantillon rendent difficiles l'imagerie AFM de ces phénomènes. Néanmoins, les changements d'ordre topographique de la surface au cours de la transition de spin ont pu être observés et discutés en conjonction avec les résultats de spectroscopie Raman et microscopie optique en champ lointain. L'ensemble de ces résultats ouvre de nouvelles possibilités d'étude et de contrôle/manipulation de ces objets bistables à l'échelle du nanomètre.

Mots-clés: Microscopie à sonde locale, microscopie à force atomique, microscopie optique en champ proche, transition de spin.

Abstract

Recently a variety of nanoscale objects, including nanoparticles, thin films and nanometric assemblies, exhibiting molecular spin-state switching phenomena have been developed for applications in sensors, nanophotonic, nanoelectronic and nanomechanical systems. These spin crossover nanomaterials have been also reported to exhibit interesting size-dependent properties. Indeed, even if the origin of the spin crossover phenomenon is purely molecular, the macroscopic behavior of these systems in the solid state is strongly influenced by elastic interactions between the molecules. These cooperative properties and, in general, the phase diagram are expected to depend strongly on the size of the material. Beyond the phase stability, the transformation kinetics is likely to display also size dependence. Indeed, the strong elastic interactions in these materials lead, in many cases, to first-order phase transitions and phase separation phenomena. Details of the associated spatio-temporal dynamics of spin crossover systems remain largely unexplored. All these size dependent and spatially heterogeneous phenomena in spin crossover materials call for appropriate characterization methods with high spatial resolution imaging capability, but to date only far-field optical microscopy has been used to this aim. Hence, the overall objective of this PHD thesis was to develop new approaches allowing to trigger and detect the spin crossover phenomenon with nanometric spatial resolution. For the detection of the thermally induced spin crossover in thin films, we used for the first time Near-Field Scanning Optical Microscopy (NSOM) and Atomic Force Microscopy (AFM) in conjunction with an original nano-heater device, based on Joule-heated metallic nanowires. Using these techniques the spin-state change in the films was inferred with sub-wavelength resolution through the associated optical and mechanical property changes of the material. Apertured NSOM used either in luminescence or reflectivity mode provided useful signal for detecting the spin-state switching phenomena, but rather limited quantification was possible due to sample stability issues. On the other hand, AFM mechanical modes, including fast force spectroscopy and multifrequency analysis, allowed for quantitative and well-reproducible measurements with nanometric resolution. In particular, we have measured for the first time the increase of the Young's modulus (ca. 25-30 %) when going from the high spin to the low spin state and used this property for quantitative imaging of the spin transition. AFM measurements were also performed on spin crossover single crystals. We have shown that probe-sample thermal interactions can be used to manipulate the nucleation and propagation of the high spin and low spin phases in the crystals. On the other hand, these interactions make for difficulties for the AFM imaging of these phenomena. Nevertheless changes of the surface topography during the spin transition could be observed and discussed in conjunction with far-field optical microscopy and Raman spectroscopy data. The ensemble of these results open up new possibilities for the investigation and manipulation of these bistable objects at the nanoscale.

Key words: Scanning probe microscopy, atomic force microscopy, near-field scanning optical microscopy, spin transition.